

DESIGNING AND INVESTIGATING A NOVEL  
BIODEGRADABLE-NONTOXIC MG-MN-ZN-NA-K  
ALLOYING SYSTEM

by

Murtatha M. Jamel

A Dissertation Submitted in  
Partial Fulfillment of the  
Requirements for the Degree of

Doctor of Philosophy  
in Engineering

at

The University of Wisconsin-Milwaukee

December 2020

# ABSTRACT

## DESIGNING AND INVESTIGATING A NOVEL BIODEGRADABLE-NONTOXIC MG-MN-ZN-NA-K ALLOYING SYSTEM

by

Murtatha M. Jamel

The University of Wisconsin-Milwaukee, 2020

Under the Supervision of Professor Hugo Lopez

Magnesium has been studied extensively due to the promising potential of using magnesium alloys in different applications, especially for biomedical implantation devices and other medical applications. This growing interest is due to the abundance of magnesium metal in the Earth's crust, as well as the fact that magnesium is 37% less dense than aluminum, has good mechanical properties, and is a nontoxic element with good biocompatibility. However, most Mg-based alloys contain alloying elements that are added to improve the mechanical properties but have toxic characteristics. At the same time a number of these alloys are still used in medical applications.

This proposed work focuses on designing and investigating a novel biomedical-biodegradable-nontoxic Mg-Mn-Zn-Na-K alloying system. Each of these alloying elements were selected based on two criteria. First, they fulfil the desired combination of biomedical-biodegradable-nontoxic alloying systems. Second, they improve the mechanical properties and corrosion behavior of relative to un-alloyed magnesium. Additionally, highly controlled melting and rapid cooling systems were developed for this study to reduce the processing defects and attain alloys with optimum properties. Furthermore, this work includes studying the effect of various cooling rates on the performance of pure magnesium made by casting in addition to investigating the effect of alloying elements. The fabrication of the alloys will be followed by four main characterization methods to determine the mechanical properties, corrosion performance, microstructure, and composition of the alloying systems.

The current study intends to develop a roadmap to analyze the effective factors in improving the performance of Mg alloys, starting from the selection of alloying elements and followed by the casting and solidification procedures. While the focus is on biomedical applications, developing casting and alloying systems for Mg alloys could be applied to other applications such as the automotive and aerospace industries due to the light weight and abundance of Mg.

© Copyright by Murtatha M. Jamel, 2020  
All Rights Reserved

*Dedicated to My  
Family  
Grandfather & Grandmother  
Uncle  
Aunties*



# TABLE OF CONTENTS

ABSTRACT .....	II
TABLE OF CONTENTS .....	VI
LIST OF FIGURES .....	IX
LIST OF TABLES .....	XVIII
LIST OF EQUATIONS .....	XIX
CHAPTER 1 .....	1
1. CHAPTER OUTLINE .....	1
1.1. Introduction .....	1
1.2. Background and Progress.....	5
1.3. Research Motivation .....	10
CHAPTER 2 .....	11
2. LITERATURE REVIEW .....	11
2.1. Mg Corrosion .....	14
2.1.1. Corrosion Products .....	18
2.1.2. The Effect of Impurities .....	20
2.1.3. Corrosion Environments .....	23
2.2. Mg Alloying Systems.....	30
2.3. The Effect of Solidification Rate on Mg Properties .....	65
2.4. The Economic Impact .....	68

CHAPTER 3 .....	71
3. RESEARCH.....	71
3.1. <b>Research Selection Process and Expectations</b> .....	<b>71</b>
3.2. <b>Goal and Objectives</b> .....	<b>76</b>
3.3. <b>Outline of the Dissertation</b> .....	<b>77</b>
CHAPTER 4 .....	79
4. RESEARCH METHODOLOGY .....	79
4.1. <b>Design of Experiment</b> .....	<b>80</b>
4.2. <b>Characterization Methods</b> .....	<b>83</b>
4.2.1. Macrographic and Micrographic Characterization .....	84
4.2.1.1. Stereoscope .....	84
4.2.1.2. Optical Microscope .....	84
4.2.2. Structure and Composition Characterizations .....	85
4.2.2.1. SEM and EDS .....	85
4.2.2.2. XRD .....	85
4.2.3. Mechanical Properties.....	85
4.2.3.1. Tensile Testing.....	85
4.2.3.2. Impact testing.....	86
4.2.3.3. Hardness .....	87
4.2.4. Corrosion Performance .....	87
4.2.4.1. Mass loss.....	87
4.2.4.2. pH Monitoring.....	89
4.2.4.3. Electrochemical Cell .....	89
CHAPTER 5 .....	91
5. EXPERIMENTAL WORK .....	91
5.1. <b>Materials and Processes</b> .....	<b>91</b>

5.1.1. Materials .....	92
5.1.1.1. Magnesium.....	92
5.1.1.2. Zinc.....	93
5.1.1.3. Manganese .....	93
5.1.1.4. Sodium.....	93
5.1.1.5. Potassium.....	93
5.1.1.6. Hank’s Balanced Salt Solution.....	94
5.1.2. Samples Preparation .....	95
5.1.2.1. Casting .....	95
5.1.2.2. Grinding and Polishing.....	101
<b>5.2. Results and Discussion.....</b>	<b>102</b>
5.2.1. Microstructure .....	102
5.2.2. Impact and Fracture Mechanism .....	111
5.2.3. Hardness.....	118
5.2.4. Tensile and Fracture Mechanism.....	120
5.2.5. Microstructural Topography and Composition .....	136
5.1.2.1. SEM and EDS .....	136
5.1.2.2. XRD .....	179
5.2.6. Corrosion.....	183
5.2.6.1. Electrochemical Testing .....	186
5.2.6.2. Immersion Testing.....	192
5.2.6.3. Post-Immersion SEM and EDS.....	199
5.2.6.4. Post-Immersion XRD .....	217
<b>CHAPTER 6.....</b>	<b>221</b>
<b>6.1. Conclusion.....</b>	<b>221</b>
<b>6.2. Future Plan .....</b>	<b>225</b>
<b>REFERENCES .....</b>	<b>226</b>

# LIST OF FIGURES

Figure 1: The use of magnesium in Biomedical applications (a) Screws (a) Orthopedic applications (b) Wound closing clips (c) Stents for artery revascularization (d) Structured scaffolds [36].	4
Figure 2: The effect of melting temperature and time on the normalized evaporation rate [45].	8
Figure 3: The effect of pressure on the normalized evaporation amount [45].	9
Figure 4: Ashby diagram of Young's modulus versus density for various materials and alloys [73].	13
Figure 5: Schematic diagram of the biocorrosion process due to the interaction with the solution [80].	16
Figure 6: Schematic diagram of the interaction between Mg and SBF: (a) the degradation of Magnesium substrate surface with solution, (b) the dissolution of Mg(OH) <sub>2</sub> layer, and (c) the formation and precipitate of phosphates [93].	19
Figure 7: The effect of impurities on the corrosion behavior of Mg-based alloys in 3% NaCl solution [21].	21
Figure 8: The corrosion of Mg-based alloys in different biological environments, the corrosion rate differs from one environment to another even for the same alloy [19].	24
Figure 9: The pH change during the corrosion process in two different solutions, 3% NaCl and Simulated Body Fluid at 37 °C [41].	26
Figure 10: The atomic radius of different alloying elements [19].	31
Figure 11: The corrosion morphology of Mg-Dy alloying system after immersion test in 0.9% NaCl solution for 72 hrs (a) 5% Dy (b) 10% Dy (c) 15% Dy (d) 20% Dy [23].	33
Figure 12: The formation of massive corrosion byproducts on the top of Mg-Ca alloy with high content of Ca [42].	35
Figure 13: The tensile strength versus the elongation of different alloying systems of Mg [19].	38
Figure 14: The ultimate tensile strength versus elongation of various Mg alloying systems [20].	42
Figure 15: The microstructure images of Mg-Ca and Mg-Ca-Mn-Zn alloying systems (a) Mg-2Ca, (b) Mg-4Ca, (c) Mg-0.5Ca-0.5Mn-2Zn (c) Mg-0.5Ca-0.5Mn-4Zn [74].	47
Figure 16: The hydrogen gas evolution rate of Mg-Ca and Mg-Ca-Mn-Zn alloying systems in Kokubo solution for duration of 240 hours [74].	48
Figure 17: SEM images of Mg-Ca and Mg-Ca-Mn-Zn alloying systems (a) pure Mg (b) Mg-2Ca, (c) Mg-4Ca, (d) Mg-0.5Ca-0.5Mn-2Zn (e) Mg-0.5Ca-0.5Mn-4Zn (f) Mg-0.5Ca-0.5Mn-7Zn [74].	49
Figure 18: The binary phase diagram of Mg-Zn [126].	52

Figure 19: The binary phase diagram of Mg-Mn [126].	53
Figure 20: The microstructure of Vivo interaction of Mg-Mn-Zn alloying system as implants with the host after 10 weeks of the implantation. The tagged area ‘‘N’’ represents the new bone tissue and ‘‘R’’ is the interaction layer between the implant and the biological surrounding (a) Optical microstructure of the implant and the biological surrounding (b) SEM microstructure of the implant and the biological surrounding, and (c) EDS analysis on the interface phase. [131].	55
Figure 21: The microstructure of Vivo interaction of Mg-Mn-Zn alloying system as implants with the host. The tagged area ‘‘N’’ represents the new bone tissue, ‘‘D’’ is the degradation area due to the interaction between the implant and the biological surrounding, and ‘‘M’’ is the implantation device. Optical images of the cross-sections of Mg-Mn-Zn implants and bones. (a) after 9 weeks of the implantation (b) after 18 weeks of the implantation [132].	56
Figure 22: Isothermal section for the ternary system of Mg-Mn-Zn at 320 °C [133].	58
Figure 23: Microstructure of as-cast Mg-Zn-Mn alloying system. (a) Mg-1Mn-1Zn, (b) Mg-1Mn-.....	59
Figure 24: The microstructure of Mg-Mn-Zn alloying system [30].	61
Figure 25: The binary phase diagrams of (a) magnesium-sodium, (b) potassium-magnesium, (c) sodium-zinc, (d) potassium-zinc, and (e) potassium-sodium.	63
Figure 26: The effect of various cooling rates on the corrosion rates of Mg-0.7Zn-2Y for as-solidified and RS ribbons in 17% NaCl solution with a pH of 6.8 [136].	67
Figure 27: The effect of various cooling rates on the corrosion depth of Mg-0.7Zn-2Y in 17% NaCl solution with a pH of 6.8 [136].	67
Figure 28: The usage of magnesium in different applications [139].	68
Figure 29: The density of Magnesium in comparison with other metals, based on 100 iron. [137].	69
Figure 30: Comparison graph between Mg and Al price [139].	70
Figure 31: The production of Magnesium [16, 139].	70
Figure 32: The selection process of alloying elements for designing the alloying systems	72
Figure 33: Pourbaix diagram for Mg and water at 25°C [22].	73
Figure 34: Research methodology chart.	79
Figure 35: Design of Experiment Chart.	80
Figure 36: The Mg-1Mn-4Zn-4Na-as cast alloying system.	83
Figure 37: Tensile specimen geometry	86
Figure 38: Charpy impact specimen geometry	87

Figure 39: Corrosion setup for mass loss testing .....	88
Figure 40: The electrochemical cell set up for the potentiostat test. ....	90
Figure 41: Preparation chart of 1X Hank's Balanced Salt Solution from 10X. ....	94
Figure 42: Crucibles that was used to melt Mg (a) low carbon steel permanent crucible(b) Mg sacrificial crucible. ....	97
Figure 43: The developed closed melting system .....	99
Figure 44: The developed quenching system.....	100
Figure 45: Quenched magnesium casting (a) side-image of Mg casting (1.5" D x 10" L) (b) Shrinkage pipe at the top of mg casting. ....	101
Figure 46: The macrostructure of pure magnesium at 6.5x (a) cooled in the furnace (slow cooling rate) (b) cooled in the furnace with uninsulated-ends (moderate cooling).....	103
Figure 47: The microstructure of pure magnesium quenched in liquid CO <sub>2</sub> at 500x. ....	103
Figure 48: The grain size-cooling rate curve. ....	104
Figure 49:The microstructure of the alloying systems (a) quenched Mg-1Mn-2Zn at 50x (b) quenched Mg-1Mn-4Zn at 50x (c) quenched Mg-1Mn-2Zn at 200x (d) quenched Mg-1Mn-4Zn at 200x (e) quenched Mg-1Mn-2Zn at 500x (f) quenched Mg-1Mn-4Zn at 500x (g) quenched Mg-1Mn-4Zn, polarized image at 500x (h) quenched Mg-1Mn-4Zn, polarized image at 500x.....	107
Figure 50:The microstructure of the alloying systems (a) quenched Mg-1Mn-4Zn-0.5Na at 50x (b) quenched Mg-1Mn-4Zn-K at 50x (c) quenched Mg-1Mn-4Zn-0.5Na-0.5K at 50x (d) quenched Mg-1Mn-4Zn-0.5Na at 200x (e) quenched Mg-1Mn-4Zn-K at 200x (f) quenched Mg-1Mn-4Zn-0.5Na-0.5K at 200x (g) quenched Mg-1Mn-4Zn-0.5Na at 500x (h) quenched Mg-1Mn-4Zn-K at 500x (i) quenched Mg-1Mn-4Zn-0.5Na-0.5K at 500x (j) quenched Mg-1Mn-4Zn-0.5Na, polarized image at 500x (k) quenched Mg-1Mn-4Zn-0.5K, polarized image at 500x (l) quenched Mg-1Mn-4Zn-0.5Na-0.5K, polarized image at 500x .....	110
Figure 51: Charpy break energ of the alloying systems. ....	112
Figure 52: Charpy impact strength of the alloying systems.....	113
Figure 53: The fracture surface morphology of impact samples of pure magnesium at 6.5x (a) top view and (b) side view are for slowly cooled pure magnesium (Mg-LCR) (c) top view and (d) side view are for moderately cooled pure magnesium (Mg-MCR) (e) top view and (f) side view are for quenched pure magnesium (Mg-HCR). ....	114
Figure 54: The fracture surface morphology of impact samples at 6.5x (a) top view and (b) side view of quenched Mg-1Mn-2Zn (c) top view and (d) side view of quenched Mg-1Mn-4Zn. ....	115
Figure 55: The fracture surface morphology of impact samples at 6.5x (a) top view and (b) side view of quenched Mg-1Mn-4Zn-Na, (c) top view and (d) side view of quenched Mg-1Mn-4Zn-K, (e) top view and (f) side view are for quenched Mg-1Mn-4Zn-Na-K. ....	117

Figure 56: The MgMn4ZnNaK alloying system .....	119
Figure 57: Scale-H Rockwell Hardness.....	120
Figure 58: The stress-strain curves for pure manesium that were cooled by different solidification rates.....	122
Figure 59:The macrostructure of pure magnesium (a) cooled in the furnace (slow cooling rate) at 6.5x (b) cooled in the furnace with uninsulated-ends (moderate cooling) at 6.5x (c) and (d) quenched in liquid CO <sub>2</sub> at 500x.....	123
Figure 60: The tensile fracture morphology for pure manesium that were cooled by different solidification rates (a) LCR-Mg (b) MCR-Mg (c) HCR-Mg .....	124
Figure 61: The stress-strain curves for Mg-Mn-Zn alloying systems.....	125
Figure 62: The tensile fracture morphology for Mg-Mn-Zn alloying systems (a) Mg-1Mn-2Zn (b) Mg-1Mn-4Zn.....	125
Figure 63: The stress-strain curves for Mg-Mn-Zn-Na-K alloying systems.....	127
Figure 64: The tensile fracture morphology for Mg-Mn-Zn-Na-K alloying systems (a) Mg-1Mn-4Zn-0.5Na (b) Mg-1Mn-4Zn-0.5K (c) Mg-1Mn-2Zn-0.25Na-0.25K.....	128
Figure 65: Tensile properties chart for all alloying systems.....	129
Figure 66: The correlation between yield strength and dendrite spacing of Mg-1Mn-2Zn, Mg-1Mn-4Zn, Mg-1Mn-4Zn-0.5Na, Mg-1Mn-4Zn-0.5K, and Mg-1Mn-4Zn-0.25Na-0.25K alloying systems.....	130
Figure 67:The optical microstructure and SEM imaging of alloying systems (a) Mg-1Mn-2Zn at 50x, (b) Mg-1Mn-2Zn at 500x and 1 is the eutectic phase at of 10000x of the system, (c) Mg-1Mn-4Zn at 50x , (d) Mg-1Mn-4Zn at 500x and 1 is the eutectic phase at of 10000x of the system.....	131
Figure 68:The optical microstructure and SEM imaging of alloying systems (a) Mg-1Mn-4Zn-0.5Na at 50x, (b) Mg-1Mn-4Zn-0.5Na at 500x and 1 is the eutectic phase at of 10000x of the system, (c) Mg-1Mn-4Zn-0.5K at 50x , (d) Mg-1Mn-4Zn-0.5K at 500x and 1 is the eutectic phase at of 10000x of the system, (e) Mg-1Mn-4Zn-0.25Na-0.25K at 50x , (f) Mg-1Mn-4Zn-0.25Na-0.25K at 500x and 1 is the eutectic phase at of 10000x of the system.....	132
Figure 69: The correlation between ultimate tensile strength and dendrite spacing of Mg-1Mn-2Zn, Mg-1Mn-4Zn, Mg-1Mn-4Zn-0.5Na, Mg-1Mn-4Zn-0.5K, and Mg-1Mn-4Zn-0.25Na-0.25K alloying systems.....	134
Figure 70: The correlation between the ductility and dendrite spacing of Mg-1Mn-2Zn, Mg-1Mn-4Zn, Mg-1Mn-4Zn-0.5Na, Mg-1Mn-4Zn-0.5K, and Mg-1Mn-4Zn-0.25Na-0.25K alloying systems.....	134
Figure 71:SEM images of pure magnesium cooled in the furnace (slow cooling rate) at different magnifications (a) at 10000 x (b) at 20000 x.....	137
Figure 72:EDS elements map of pure magnesium cooled in the furnace (slow cooling rate) (a) area of intrest (b) Magnesium map (c) Oxygen map.....	137

Figure 73: The EDS spectrum images of pure magnesium cooled in the furnace (slow cooling rate).....	138
Figure 74: SEM images of pure magnesium cooled in the furnace with uninsulated-ends (moderate cooling) at different magnifications (a) at 1000 x (b) at 10000 x.....	139
Figure 75: EDS elements map of pure magnesium moderately cooled in the furnace with uninsulated-ends (a) area of interest (b) Magnesium map (c) Oxygen map.....	139
Figure 76: The sum EDS spectrum images of pure magnesium moderately cooled in the furnace with uninsulated-ends.....	140
Figure 77: SEM images of pure magnesium rapidly cooled in liquid CO <sub>2</sub> at different magnifications (a) at 1000 x (b) at 10000 x.....	141
Figure 78: EDS elements map of pure magnesium rapidly cooled in liquid CO <sub>2</sub> (a) area of interest (b) Magnesium map (c) Oxygen map.....	142
Figure 79: The point EDS spectrum images of pure magnesium rapidly cooled in liquid CO <sub>2</sub> .....	142
Figure 80: SEM images of Mg-1Mn-2Zn alloying system rapidly cooled in liquid CO <sub>2</sub> at different magnifications at 500 x (b) at 1000 x (c) at 2000 x (d) at 3000 x (e) at 5000 x (f) at 10000 x.....	144
Figure 81: SEM images of the eutectic phase of Mg-1Mn-2Zn alloying system rapidly cooled in liquid CO <sub>2</sub> at different magnifications (a) at 2000 x (b) at 3000 x (c) at 5000 x (d) at 10000 x.....	145
Figure 82: EDS elements map of Mg-1Mn-2Zn alloying system rapidly cooled in liquid CO <sub>2</sub> (a) area of interest (b) Magnesium map (c) Zinc map (d) Manganese map (e) Oxygen map.....	146
Figure 83: The sum EDS spectrum images of the primary and secondary phases Mg-1Mn-2Zn alloying system rapidly cooled in liquid CO <sub>2</sub> .....	147
Figure 84: SEM images of Mg-1Mn-4Zn alloying system rapidly cooled in liquid CO <sub>2</sub> at different magnifications (a) at 500 x (b) at 1000 x (c) at 2000 x (d) at 3000 x (e) at 5000 x (f) at 10000 x.....	149
Figure 85: EDS elements map of Mg-1Mn-4Zn alloying system rapidly cooled in liquid CO <sub>2</sub> (a) area of interest (b) Magnesium map (c) Zinc map (d) Manganese map (e) Oxygen map.....	150
Figure 86: The sum EDS spectrum images of Mg-1Mn-4Zn alloying system rapidly cooled in liquid CO <sub>2</sub> .....	151
Figure 87: SEM images of Mg-1Mn-4Zn-0.5Na alloying system rapidly cooled in liquid CO <sub>2</sub> at different magnifications (a) at 500 x (b) at 1000 x (c) at 2000 x (d) at 3000 x (e) at 5000 x (f) at 10000 x.....	153
Figure 88: The formed scattered-brittle-reactive secondary phase in Mg-1Mn-4Zn-0.5Na.....	154
Figure 89: EDS elements map of Mg-1Mn-4Zn-0.5Na alloying system rapidly cooled in liquid CO <sub>2</sub> (a) area of interest (b) Magnesium map (c) Zinc map (d) Manganese map (e) Sodium map (f) Oxygen map.....	156
Figure 90: The point EDS spectrum image for the matrix of Mg-1Mn-4Zn-0.5Na alloying system rapidly cooled in liquid CO <sub>2</sub> .....	157

Figure 91: The point EDS spectrum image for the secondary phase of Mg-1Mn-4Zn-0.5Na alloying system rapidly cooled in liquid CO <sub>2</sub> .	157
Figure 92: EDS elements map for the formed scattered-brittle-reactive secondary phase of Mg-1Mn-4Zn-0.5Na alloying system rapidly cooled in liquid CO <sub>2</sub> (a) area of interest (b) Magnesium map (c) Zinc map (d) Manganese map (e) Sodium map (f) Oxygen map.	158
Figure 93: The sum EDS spectrum image for the formed scattered-brittle-reactive secondary phase of Mg-1Mn-4Zn-0.5Na alloying system rapidly cooled in liquid CO <sub>2</sub> .	159
Figure 94: SEM images of Mg-1Mn-4Zn-0.5K alloying system rapidly cooled in liquid CO <sub>2</sub> at different magnifications (a) at 500 x (b) at 1000 x (c) at 2000 x (d) at 3000 x (e) at 5000 x (f) at 10000 x.	161
Figure 95: The EDS elements map of Mg-1Mn-4Zn-0.5K alloying system rapidly cooled in liquid CO <sub>2</sub> (a) area of interest (b) Magnesium map (c) Zinc map (d) Manganese map (e) Potassium map (f) Oxygen map. alloying system rapidly cooled in liquid CO <sub>2</sub> at different magnifications (a) at 500 x (b) at 1000 x (c) at 2000 x (d) at 3000 x (e) .	163
Figure 96: The point EDS spectrum image for the matrix of Mg-1Mn-4Zn-0.5Na alloying system rapidly cooled in liquid CO <sub>2</sub> .	164
Figure 97: The point EDS spectrum image for the main secondary phase of Mg-1Mn-4Zn-0.5K alloying system rapidly cooled in liquid CO <sub>2</sub> .	165
Figure 98: The point EDS spectrum image for the eutectic phase of Mg-1Mn-4Zn-0.5K alloying system rapidly cooled in liquid CO <sub>2</sub> .	165
Figure 99: SEM images of Mg-1Mn-4Zn-0.25Na-0.25K alloying system rapidly cooled in liquid CO <sub>2</sub> at different magnifications (a) at 500 x (b) at 1000 x (c) at 2000 x (d) at 3000 x (e) at 5000 x (f) at 10000 x.	167
Figure 100: SEM images for the formed scattered-brittle-reactive secondary phase of Mg-1Mn-4Zn-0.25Na-0.25K alloying system rapidly cooled in liquid CO <sub>2</sub> at 800x.	169
Figure 101: The EDS elements map of Mg-1Mn-4Zn-0.25Na-0.25K alloying system rapidly cooled in liquid CO <sub>2</sub> (a) area of interest (b) Magnesium map (c) Zinc map (d) Manganese map (e) Sodium (f) Potassium map (g) Oxygen map.	170
Figure 102: The point EDS spectrum image for the secondary phase of Mg-1Mn-4Zn-0.25Na-0.25K alloying system rapidly cooled in liquid CO <sub>2</sub> .	171
Figure 103: The point EDS spectrum image for the matrix of Mg-1Mn-4Zn-0.5Na-0.5K alloying system rapidly cooled in liquid CO <sub>2</sub> .	172
Figure 104: The EDS elements map for the formed scattered-brittle-reactive secondary phase of Mg-1Mn-4Zn-0.25Na-0.25K alloying system rapidly cooled in liquid CO <sub>2</sub> (a) area of interest (b) Magnesium map (c) Zinc map (d) Manganese map (e) Sodium map (f) Potassium map (g) Oxygen map.	173
Figure 105: The sum EDS spectrum image for the formed scattered-brittle-reactive secondary phase of Mg-1Mn-4Zn-0.25Na-0.25K alloying system rapidly cooled in liquid CO <sub>2</sub> .	174

Figure 106: The dendritic spacing of Mg-1Mn-2Zn, Mg-1Mn-4Zn, Mg-1Mn-4Zn-0.5Na, Mg-1Mn-4Zn-0.5K, Mg-1Mn-4Zn-0.25Na-0.25K alloying systems .....	175
Figure 107: The difference formation of the eutectic phases of Mg-1Mn-2Zn, Mg-1Mn-4Zn, Mg-1Mn-4Zn-0.5Na, Mg-1Mn-4Zn-0.5K, Mg-1Mn-4Zn-0.25Na-0.25K alloying systems. ....	178
Figure 108: The eutectic spacing of Mg-1Mn-2Zn, Mg-1Mn-4Zn, Mg-1Mn-4Zn-0.5Na, Mg-1Mn-4Zn-0.5K, Mg-1Mn-4Zn-0.25Na-0.25K alloying systems. ....	179
Figure 109: The XRD patterns of as cast pure magnesium that were cooled by different solidification rates. ....	180
Figure 110: The XRD patterns of Mg-Mn-Zn alloying systems. ....	182
Figure 111: The XRD patterns of Mg-Mn-Zn-Na-K alloying systems. ....	182
Figure 112: The surface characteristics of (a) pure magnesium cooled in the furnace (slow cooling rate) (b) pure magnesium-cooled in the furnace with uninsulated-ends (moderate cooling) (c) quenched pure magnesium (d) quenched Mg-1Mn-2Zn (e) quenched Mg-1Mn-4Zn. (f) quenched Mg-1Mn-4Zn-0.5Na (g) quenched Mg-1Mn-4Zn-0.5K (h) quenched Mg-1Mn-2Zn-0.25Na-0.25K. ....	185
Figure 113: The polarization curves of (a) pure magnesium cooled in the furnace (slow cooling rate) (b) pure magnesium-cooled in the furnace with uninsulated-ends (moderate cooling) (c) quenched pure magnesium. ....	187
Figure 114: Nyquist curves of (a) pure magnesium cooled in the furnace (slow cooling rate) (b) pure magnesium-cooled in the furnace with uninsulated-ends (moderate cooling) (c) quenched pure magnesium. ....	188
Figure 115: The polarization curves of (a) pure magnesium cooled in the furnace (b) quenched Mg-1Mn-2Zn (c) quenched Mg-1Mn-4Zn. ....	189
Figure 116: Nyquist curves of (a) pure magnesium cooled in the furnace (b) quenched Mg-1Mn-2Zn (c) quenched Mg-1Mn-4Zn. ....	190
Figure 117: The polarization curves of (a) quenched Mg-1Mn-4Zn (b) quenched Mg-1Mn-4Zn-0.5Na (g) quenched Mg-1Mn-4Zn-0.5K (c) quenched Mg-1Mn-2Zn-0.25Na-0.25K. ....	191
Figure 118: Nyquist curves of a) quenched Mg-1Mn-4Zn (b) quenched Mg-1Mn-4Zn-0.5Na (g) quenched Mg-1Mn-4Zn-0.5K (c) quenched Mg-1Mn-2Zn-0.25Na-0.25K. ....	191
Figure 119: Corrosion rate of the produced alloying systems over time period of 10 days in Hank's Balanced Salts Solution at temperature of 37 °C and 7.4 pH. ....	193
Figure 120: Optical images of exposed as-cast Magnesium alloying systems in Hank's Balanced Salts Solution at temperature of 37 °C and 7.4 pH. ....	198
Figure 121: Post-immersion SEM images of pure magnesium cooled in the furnace (slow cooling rate) at different magnifications (a) at 500 x (b) at 1000 x (c) at 3000 x. ....	200

Figure 122: Post-immersion EDS elements map of pure magnesium cooled in the furnace (slow cooling rate) (a) area of interest (b) Magnesium (c) Zinc (d) P (e) Calcium (f) Sodium (g) Cl. ....	201
Figure 123: Post-immersion EDS spectrum images of pure magnesium cooled in the furnace (slow cooling rate). ....	201
Figure 124: Post-immersion SEM images of pure magnesium cooled in the furnace with uninsulated-ends (moderate cooling) at different magnifications (a) at 20 x (b) at 500 x (c) at 2000 x (d) at 3000 x. ....	202
Figure 125: Post-immersion sum EDS spectrum images of pure magnesium moderately cooled in the furnace with uninsulated-ends. ....	203
Figure 126: Post-immersion SEM images of pure magnesium rapidly cooled in liquid CO <sub>2</sub> at different magnifications at (a) 100 x (b) 500 x. (c) 1000 x (d) 3000 x. ....	204
Figure 127: Post-immersion sum EDS spectrum images of pure magnesium rapidly cooled in liquid CO <sub>2</sub> . ....	205
Figure 128: Post-immersion SEM images of Mg-1Mn-2Zn alloying system rapidly cooled in liquid CO <sub>2</sub> at different magnifications at (a) at 200 x (b) at 500 x (c) at 3000 x (d) at 5000 x. ....	206
Figure 129: Post-immersion sum EDS spectrum images of the primary and secondary phases Mg-1Mn-2Zn alloying system rapidly cooled in liquid CO <sub>2</sub> . ....	207
Figure 130: Post-immersion SEM images of Mg-1Mn-4Zn alloying system rapidly cooled in liquid CO <sub>2</sub> at different magnifications (a) at 500 x (b) at 1000 x (c) at 2000 x (d) at 3000 x (e) at 5000 x (f) at 10000 x. ....	209
Figure 131: Post-immersion sum EDS spectrum images of Mg-1Mn-4Zn alloying system rapidly cooled in liquid CO <sub>2</sub> . ....	209
Figure 132: Post-immersion SEM images of Mg-1Mn-4Zn-0.5Na alloying system rapidly cooled in liquid CO <sub>2</sub> at different magnifications (a) at 50 x (b) at 500 x (c) at 1000 x (d) at 2000 x (e) at 3000 x (f) at 5000 x. ....	211
Figure 133: Post-immersion sum EDS spectrum image for the matrix of Mg-1Mn-4Zn-0.5Na alloying system rapidly cooled in liquid CO <sub>2</sub> . ....	211
Figure 134: Post-immersion SEM images of Mg-1Mn-4Zn-0.5K alloying system rapidly cooled in liquid CO <sub>2</sub> at different magnifications (a) at 200 x (b) at 500 x (c) at 1000 x (d) at 2000 x (e) at 3000 x (f) at 5000 x. ....	213
Figure 135: Post-immersion sum EDS spectrum image for the matrix of Mg-1Mn-4Zn-0.5Na alloying system rapidly cooled in liquid CO <sub>2</sub> . ....	214
Figure 136: Post-immersion SEM images of Mg-1Mn-4Zn-0.25Na-0.25K alloying system rapidly cooled in liquid CO <sub>2</sub> at different magnifications (a) at 50 x (b) at 100 x (c) at 500 x (d) at 1000 x (e) at 3000 x (f) at 5000 x. ....	215
Figure 137: Post-immersion sum EDS spectrum image for the secondary phase of Mg-1Mn-4Zn-0.25Na-0.25K alloying system rapidly cooled in liquid CO <sub>2</sub> . ....	216

Figure 138: The XRD patterns post-immersion of pure magnesium of different solidification rates. .... 217

Figure 139: The XRD patterns post-immersion of Mg-Mn-Zn alloying systems. .... 218

Figure 140: Figure 141: The XRD patterns post-immersion of Mg-Mn-Zn-Na-K alloying systems. .... 219

# LIST OF TABLES

Table 1: Examples of different alloying systems of Mg-based alloys.....	2
Table 2: Mechanical properties of different biomedical materials vs natural bone [72]. .....	11
Table 3: Corrosion rate of different alloying systems .....	29
Table 4: The generated amount of hydrogen gas for AlloyI (Mg-8.5Al- 0.2Mn—0.5Zn) and alloy II (Mg-8.5 Al- 0.2Mn—0.5Zn-2Na).....	62
Table 5: Examples of the Mechanical properties and grain size of Mg-based alloys.....	64
Table 6: The allowable daily intake [20, 22, 78, 103].....	72
Table 7: The standard reduction electrode at 7 pH and 25 °C.....	74
Table 8: Design of Experiment for studying the effect of solidification rates .....	81
Table 9: The properties of the alloying system .....	81
Table 10: Design of Experiment for studying the effect of alloying elements.....	83
Table 11: The impurity content in the purchased magnesium. ....	92
Table 12: The average grain size of pure magnesium under different cooling rates. ....	103
Table 13:Dendrite spacing of Mg alloying systems. ....	108
Table 14: The results summary for charpy impact testing .....	111
Table 15: The results summary for Rockwell hardness testing-scale H .....	118
Table 16: The results summary for tensile properties for all Mg alloying systems.....	121
Table 17: The correlation between laminal thickness of the eutectic phase and the tensile properties of Mg-1Mn-2Zn, Mg-1Mn-4Zn, Mg-1Mn-4Zn-0.5Na, Mg-1Mn-4Zn-0.5K, and Mg-1Mn-4Zn-0.25Na-0.25K alloying systems.....	134
Table 18: The phase constituion of the alloying systems. ....	183
Table 19: Corrosion rate of the produced alloying systems in Hank’s Balanced Salts Solution at temperature of 37 °C and 7.4 pH over a time of 240 hours. ....	196
Table 20: The phase constituion of the alloying systems post-immersion test .....	220

# LIST OF EQUATIONS

Oxidation reaction : $\text{Mg} \rightarrow \text{Mg}^{2+} + 2\text{e}^{-}$	(Eo = -2.363 V)----Equation 1..... 15
Reduction reaction : $2\text{H}_2\text{O} + 2\text{e}^{-} \rightarrow \text{H}_2(\text{g}) + 2(\text{OH})^{-}$	(Eo = +0.826 V) ----Equation 2 ..... 15
Product formation: $\text{Mg}^{2+} + 2\text{OH}^{-} \rightarrow \text{Mg}(\text{OH})_2$	----Equation 3 ..... 15
Overall reaction: $\text{Mg} + 2\text{H}_2\text{O} = \text{Mg}(\text{OH})_2 + \text{H}_2(\text{g})$	(Eo = -1.065 V)----Equation 4..... 15
$\text{Mg}^{2+} + \text{Ca}^{2+} + (\text{PO}_4)^{3-} = \text{Ca}_3\text{Mg}_3(\text{PO}_4)_4$	----Equation 5 ..... 18
$\text{Mg}^{2+} + (\text{CO}_3)^{2-} = \text{MgCO}_3$	----Equation 6 ..... 18
$Q = m \cdot c \cdot (k-1)$	----Equation 7 ..... 50
$\sigma = \sigma_0 + k d^{-1/2}$	----Equation 8..... 51

# ACKNOWLEDGEMENTS

I am thankful to Professor Hugo Lopez for his encouragement and support. I am grateful to Professor Benjamin Church for his continuous assistance and invaluable advice. Also, I would like to thank Dr. Benjamin Schultz and Robert Bauer for the tremendous support and guidance that they provided me during my study.

I would also like to thank the other committee members, Professor Wilkistar Otieno, Professor Habib Tabatabai, and Professor Xiaoli Ma for their time and priceless comments and suggestions. Also, I am grateful to Mr. Iftekharuddin Khan and Elisabeth Warras (Betty) for their unlimited support and kindness. My appreciation also goes to Avie Judes, Jane Martell, Professor Ethan Munson, and Steven Ohland for their help and efforts. Moreover, I would like to express my appreciation to the AOP-University of Wisconsin-Milwaukee, the H.H. Harris Foundation, the Minerals-Metals-Materials Society (TMS), the American Institute of Mining-Metallurgical-Petroleum Engineers (AIME), the Foundry Educational Foundation (FEF)-Northeastern Wisconsin- George J. Barker Memorial, the American Foundry Society (AFS), and the Association for Iron & Steel Technology (AIST) for honoring and supporting me with their awards.

# Chapter 1

## 1. Chapter Outline

This chapter gives introductory information about magnesium and its background, in addition to the research motivation.

### 1.1. Introduction

The bio-medical implants field made tremendous progress in using advanced techniques for fabricating and characterizing implantation devices. The recent development of bio medical alloying systems such as additive manufacturing and 3-D printing has attracted many researchers who focus on developing printing methods and materials. These can be used later as molds for metal-based alloys to make parts with complex shapes and details such as scaffolds and other orthopedic structures [1, 2, 3, 4, 5, 6, 7, 8, 9, 10]. Also, magnesium alloys have been studied to make cellular porous materials fabricated by different techniques [11, 12, 13]. Various metals such as titanium, stainless steel, cobalt, zinc, and magnesium alloys have been used in orthopedic applications [14, 15]. Moreover, magnesium and its alloys have been used in various industries such as automotive, aerospace, medical, electronic, non-structural, hydrogen storage, and sport [16, 17]. [Table 1](#) presents some Mg alloys that were used for different applications, which were classified based on the alloying elements [18, 19, 20, 21, 22, 23, 24, 25, 26, 27] [28, 29].

*Table 1: Examples of different alloying systems of Mg-based alloys.*

Examples	Alloying System	Composition
Commercial Mg-Al-based Alloys	AZ31	Mg-3Al-1Zn
	AZ31B	Mg-3Al-1Zn-0.5Mn
	AZ61	Mg-6Al-1Zn
	AZ91	Mg-9Al-1Zn
Mg-REE Based Alloys	AE21	Mg-2Al-1 REEs (Ce, Pr, Nd)
	ZK60	Mg-6Zn-0.6Zr
	Mg-Y	Mg-xY (x= 4, 8)
	Mg-Dy	Mg-xDy (x= 5, 10, 15, 20)
Mg-Nontoxic elements based Alloys	Mg-Zn	Mg-xZn (x= 1- 20)
	Mg-Si	Mg-xSi (x=0.3-2.3)
	Mg-Ca	Mg-xCa (x= 0.2-4)
	Mg-Ca-Zn	Mg-1Ca-xZn (x= 1-6)
	Mg-Mn-Zn	Mg-1Mn-xZn-0.2Al (x= 1-5)
	Mg-Ca-Mn-Zn	Mg-2Ca-0.5Mn-xZn (x= 1-6)

Throughout the development of biomedical implantation devices, several metal-based alloys were tested for their properties and compatibility. It was found that some metals such as iron have a poor biocompatibility. For example, iron stents that were implanted in rabbits it caused an inflammatory response and/or neointimal proliferation; however, it did not lead to systemic toxicity [30]. Other implantation devices made of different metals were limited due to the low recommended daily dosage. However, magnesium showed good compatibility with high allowable intake with no systemic toxicity. Additionally, the density and elastic modulus of Mg are close to the physical

properties of human bone [31, 32]. The results of using magnesium alloys as implants have been reported to be positive in animals and humans. For example, a stent was implanted in the left lung of a baby with a weight of 1.7 kg. The healing process post-implantation was reported to be successful [33].

Due to the physical properties and good biocompatibility of Mg alloys with the human body, magnesium (Mg) and its alloys have been used in several biomedical applications, such as stents, screws, pins, needles, and load-bearing for orthopedic applications, as shown in [Figure 1](#). The main advantages of using biodegradable implants is to avoid multiple surgeries and the biodegradation process occurs spontaneously due to the low thermodynamic stability of magnesium alloys. Furthermore, Mg can be absorbed as a vitamin by the body during the healing process. Also, it stimulates multiple enzyme systems and leads to increased formation of new bones; however, cast pure magnesium has poor mechanical properties and low corrosion resistance. In addition, many biomedical Mg alloys contain toxic elements that were added to improve the mechanical properties and reduce corrosion rate. The flammability and reactivity of magnesium increases the probability of inducing processing defects during the melting and solidification processes. These defects, such as gas porosity and impurity, also contribute in reducing the strength of Mg alloys and increase the tendency of the alloys to corrode faster [31, 34, 35, 36]. Therefore, special casting systems and procedures were developed for casting magnesium for this current study, as will be discussed in chapter 5, in addition to samples preparation section.

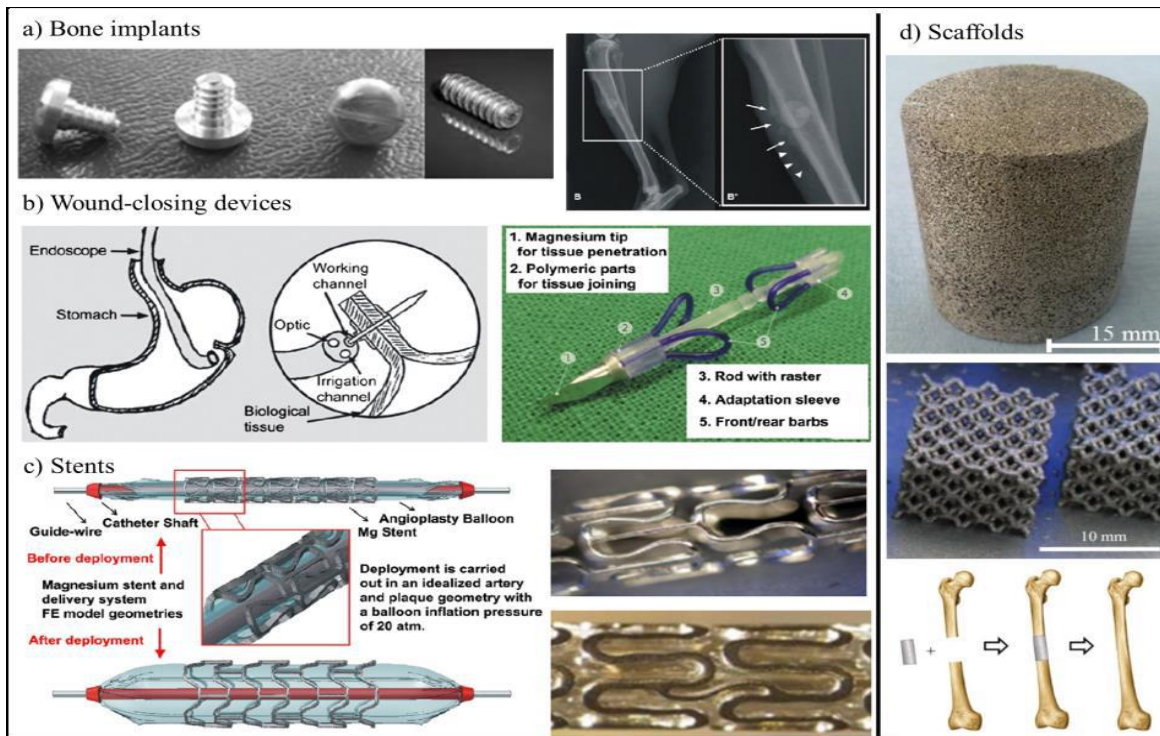


Figure 1: The use of magnesium in Biomedical applications (a) Screws (a) Orthopedic applications (b) Wound closing clips (c) Stents for artery revascularization (d) Structured scaffolds [36].

## 1.2. Background and Progress

Mg production was started at the beginning of the nineteenth century by Sir Humphry Davy and was further developed later by his assistant Michael Faraday. The first form of Mg was presented in wires and bands in 1862. The wires were used clinically later by Edward Huse. After that, the use of magnesium was enhanced strongly by the contribution of Dr. Payr from Austria. Moreover, the clinical trials were studied by Albin Lambotte and Jean Verbrugge between 1906 and 1937, where pure Mg, Mg–6Al–3Zn–0.2–Mn, and Mg–8Al were studied. Due to a developed process of a German scientist Robert Bunsen, Mg was commercially produced from electrolysis of fused  $\text{MgCl}_2$  in 1886. The process was further developed in 1896 by Chemische Fabrik Griesheim-Elektron. At the early stages of magnesium fabrication, Mg products were known to be brittle; therefore, different approaches were studied to improve the ductility of Mg such as processing methods and adding alloying elements like aluminum, zinc, cadmium, and manganese [37, 38].

The first reported production of extruded pure magnesium distilled in vacuum (99.99%) was by Seeling and the American Magnesium Corporation in 1924. Andrews used Mg to treat deep wounds, hemostasis in the brain, and intestinal anastomosis in 1917 in the form of wires, clips as ligature, and anastomosis. Then, Mg was made in the form of plates, bands, screws, and pegs by the Dow Chemical Corporation in the USA and Griesheim-Elektron in Germany in the period of 1933-1937 [30, 38, 39, 40].

Payr observed magnesium corrosion to be in the form of cavities and cracks in 1900, and the degradation rate for pure magnesium was 0.1 g for the period of three to four weeks. He also reported the uniform corrosion of high purity magnesium *in vivo*. The study included the effect of oxygen content in the blood on the oxidation process of magnesium and local hydrogen carbonic acid on the formation of magnesium carbonate layer. Similarly, a study done by Henschen et al found that a soluble layer of magnesium carbonate reduces the corrosion rate of the implanted magnesium for bone applications. Moreover, a different study concluded that the corrosion products of magnesium found to be nontoxic [38]. Recent clinical trials and studies of magnesium for biomedical applications revealed that no signs of systematic toxicity or allergic reactions occurred [31].

Lambotte studied the fast degradation rate and hydrogen accumulation when the magnesium and iron were used together for clinical application. He also found that the mechanical integrity of implanted magnesium in bones was good for four months after implantation. Furthermore, Lambotte found that the healing process and the pain management were better without infection during the observation time of nine to ten months after the implantation. However, the hydrogen evolution was a concern during the healing process [38].

Andrews and Seeling, in their individual studies, concluded that the surface area of the implanted magnesium directly affects the degradation rate. Also, it was found that the corrosion rate of magnesium depends on the type and location of the implanted medical

device. The difference in corrosion rate was found to be 23% for implanted magnesium devices in two different locations in dogs for the same period of time (two weeks). Similarly, the accumulation rate of corrosion gases depends on the type of tissues and location of implantation devices. Lispinasse investigated the hydrogen generation, and it was found that the generated hydrogen gas is  $1 \text{ cm}^3/\text{mg}$  at  $0 \text{ }^\circ\text{C}$ . Besides that, he assumed the accumulation of the generated hydrogen increases with increasing the temperature [38, 40]. In recent studies, it was approved that the temperature increase leads to accelerate the kinetics of the reaction and consequently increases the corrosion rate [27, 41, 42].

The major development of magnesium alloys started after the Second World War. Mg-based alloys have been used for the automobile industry, power, electronic, aerospace and defense applications due to their light weight and good castability [43, 44, 45]. The main manufacturing and recycling process for magnesium alloys is casting. A wide range of casting methods such as sand, permanent mold, and high-pressure die castings have been applied to make Mg parts.

The casting process of Mg has several restriction factors due to the high flammability and reactivity at high temperatures. Therefore, various approaches have evolved to overcome these challenges such as using flux, vacuum, and die casting. Even with using the mentioned techniques, the high evaporating rate of magnesium still is a problem for the casting process of magnesium. Additionally, there are disadvantages of using these modifications, like more inclusion traces resulting from using flux. Another

example is high decomposition rate that occurs under vacuum pressure [44, 46, 47, 48, 45]. Also, using cover gases could cause a negative environmental effect. Moreover, it was concluded that the deposition rate increases with increasing the time and temperature. On the other side, it was confirmed that the evaporation rate decreases with increasing the pressure. [Figure 2](#) shows the effect of temperature and time on the evaporation rate. The relation between the evaporation rate and pressure is presented in [Figure 3](#) [43, 44, 45].

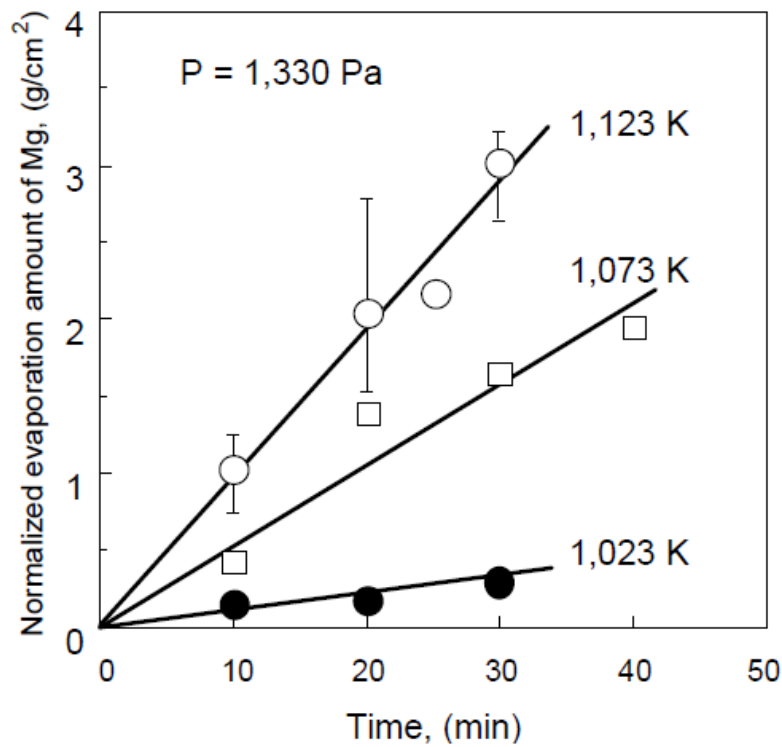


*Figure 2: The effect of melting temperature and time on the normalized evaporation rate [45].*

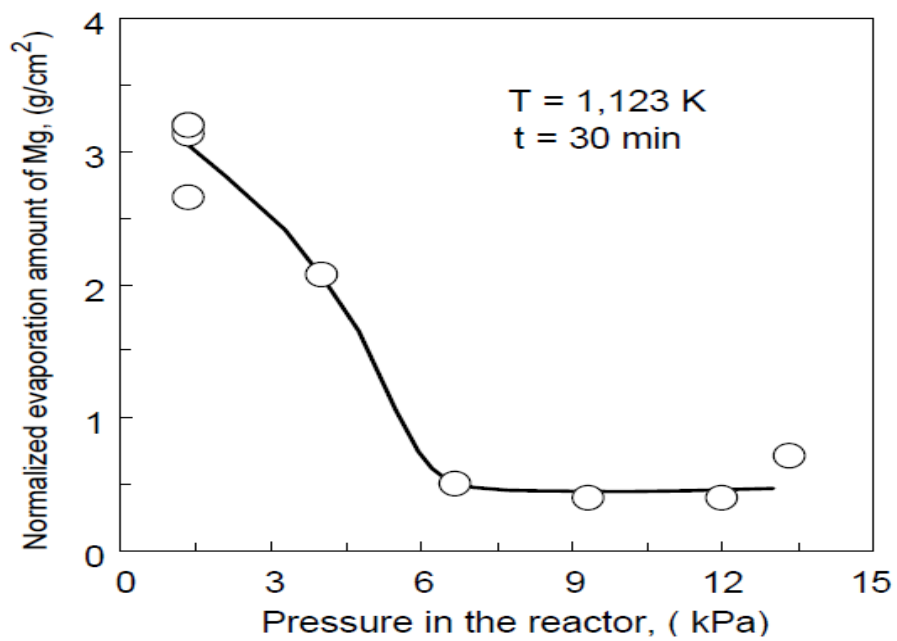


Figure 3: The effect of pressure on the normalized evaporation amount [45].

### 1.3. Research Motivation

Due to the increased demand for developing alloys that serve as implantation devices with outstanding properties, the performances of different biomedical Mg-based alloys have been investigated extensively for their properties. However, there are still major concerns in using magnesium alloys in such applications. These issues are the high corrosion rate, hydrogen generation, and maintaining the mechanical integrity for the designated healing time for the biomedical application. Toxicity can occur from adding alloying elements that are intended to improve the mechanical properties and corrosion resistance of Mg. Therefore, this work focuses on building an alloy that fits the medical triangle of biomedical-biodegradable-nontoxic with acceptable mechanical properties and corrosion rate to maintain the mechanical integrity during the designated healing time for the implantation device.

Additionally, Mg shows a great potential to be used for automotive, aerospace, and other industries due to its abundance and low density (37% less dense than Al). Mg drew researchers' attention toward developing a light weight alloy with optimum performance, which could potentially reduce the manufacturing cost and fuel consumption.

# Chapter 2

## 2. Literature Review

Magnesium shows good biocompatibility with a high allowable daily dosage (240-420 mg/day) with no systemic toxicity or infection, in addition to the density of magnesium and its alloys (1.73-1.85 g/cm<sup>3</sup>) that are close to the cortical bone density (1.75 g/cm<sup>3</sup>). Nevertheless, the elastic modulus of magnesium (41-45 GPa) is also close to natural bone (3–20 GPa) in comparison with other metals, which helps in reducing stress shielding of the bones in the human body [31, 32]. Biomedical applications have used different materials, which can be a specific type of metal or combination of metals as it was discussed in different studies [49, 50, 51, 52, 53, 54, 55, 56, 57, 58] [59, 60, 61, 62, 63, 64, 65, 66, 67, 68] [69, 70, 71, 72]. [Table 2](#) illustrates the mechanical properties of biomedical metals that are used as implantation devices in comparison to natural bone.

*Table 2: Mechanical properties of different biomedical materials vs natural bone [72].*

Properties	Natural Bone	Stainless Steel	Ti Alloy	Co-Cr Alloy	Magnesium
Density (g/cm <sup>3</sup> )	1.7–2.0	7.9–8.1	4.4–4.5	8.3–9.2	1.74–2.0
Elastic modulus (GPa)	3–20	189-205	110-117	230	41-45
Tensile strength (MPa)	80–150	480-620	930-1140	900-1540	170-270
Compressive yield strength (MPa)	130–180	170-310	758-1117	450-1000	65-100
Elongation at failure (%)	1-7	30-40	8-15	30-45	6-20

Fracture toughness (MPa m <sup>1/2</sup> )	3-6	50-200	55-115	100	15-40
---	-----	--------	--------	-----	-------

Figure 4 shows Young's modulus of different materials and alloys versus density, magnesium alloys included [73]. The chart indicates that magnesium and its alloys have demonstrate a good specific ratio. The crystal structure of magnesium is a Hexagonal Close-Packed (HCP) with a density of 1.738 g/cm<sup>3</sup> with electrochemical potential of -2.37 V. As-cast magnesium has poor mechanical properties and fast degradation rate of 2.89 mm/year in 0.9% NaCl solution [31, 32, 37]. The yield strength, the ultimate tensile strength, and elongation are 27.5 MPa, 97.5, and 7.31, respectively [74]. Moreover, it was stated that magnesium has multi-slip plans that affect the formability at ambient temperature due to the localized slip and built-up stresses at the grain boundaries [75].

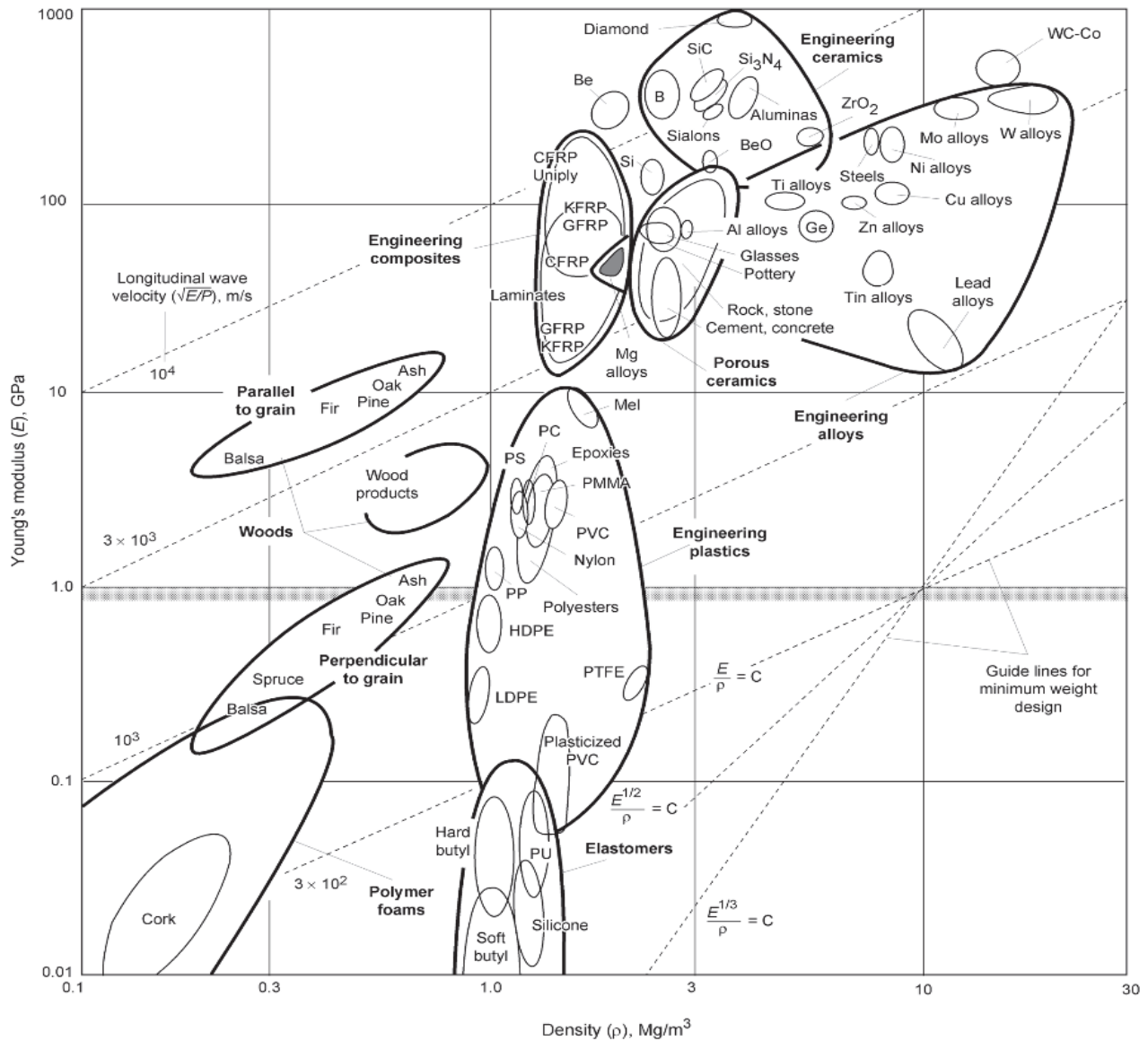


Figure 4: Ashby diagram of Young's modulus versus density for various materials and alloys [73].

Redha and Sreekanth [76] reviewed the use of magnesium alloys and composites in orthopedic implants. The work highlighted the close match of the physical and mechanical properties of Mg to bone besides the other benefits of using magnesium in orthopedic applications. The set of advantages can be summarized in the low density, high specific strength, high damping capacity, good biocompatibility, and reduced stress shielding effect.

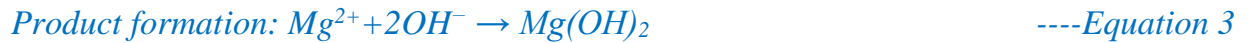
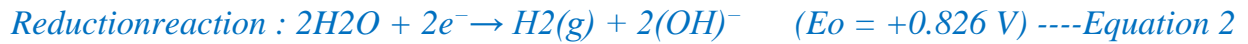
However, magnesium/ magnesium alloys need further work to improve the corrosion performance and increase the mechanical properties to overcome the main obstacles toward efficiently using Mg for orthopedic implants.

The selection process of the alloying system starts with studying the application, incubation environment, and needed characteristics for such implantation devices. The other steps are matching the requirements to an alloying system and verifying the designed alloying system by a series of tests [77].

## 2.1. Mg Corrosion

Corrosion plays a significant role in many applications such as automotive, aerospace, electronical, and structural applications. Numerous corrosion studies have been conducted on metals to monitor, test, and enhance the performance of this topic in several areas and sectors of the life [31, 18, 34, 78, 79, 80]. The corrosion process can be identified as the degradation of a metal by electrochemical reaction with the environment. Pure magnesium has a high corrosion rate which is attributed to the low Pilling-bedworth ratio ( $\sim 0.81$ ) of the formed film on the surface in the presence of moisture, and besides that, the lack of the regeneration of new film and the high electronegativity of this metal [75]. The oxidation reaction of magnesium and cathodic reaction of water lead to the generation of hydrogen gas. [Equations 1, 2, 3, and 4](#) show the anodic, cathodic, products formation, and the overall reactions of magnesium in water. The dissolution of magnesium occurs in the

anodic reaction (Equation 1), hydrogen evolution occurs in the cathodic reaction (Equation 2), and the formation of a surface layer (Equation 3) [27, 36, 41].



The degradation process of magnesium starts with a cathodic and anodic electrochemical reaction between the metal molecules at the interfacial surface with the surrounding. The produced electrons from the decayed metal are consumed by the reduction reaction with the aqueous solution. During the degradation process corrosion products are generated at the surface. These products could form a protective layer on the surface, the efficiency of that layer depends on several factors as it is discussed in this literature review [80]. Also, it was reported that the possibility of producing a dual protective layer of MgO and Mg (OH)<sub>2</sub> are contiguous with each other. The corrosion rate of Mg and its alloys, type of corrosion products, and formed film on the interfacial surface depend on several factors that are related to the compositions and conditions of the segment and its surrounding [81, 82, 83].

One other important matter to mention, the difference in the result of weight loss in the corrosion process between the calculated by faraday's law and measured value was

explained to be due to the exclusion of electron consumption by acidic corrosion from equation of computing the corrosion rate [84]. Figure 5 shows a schematic diagram of the corrosion process of magnesium due to the interaction with the solution.

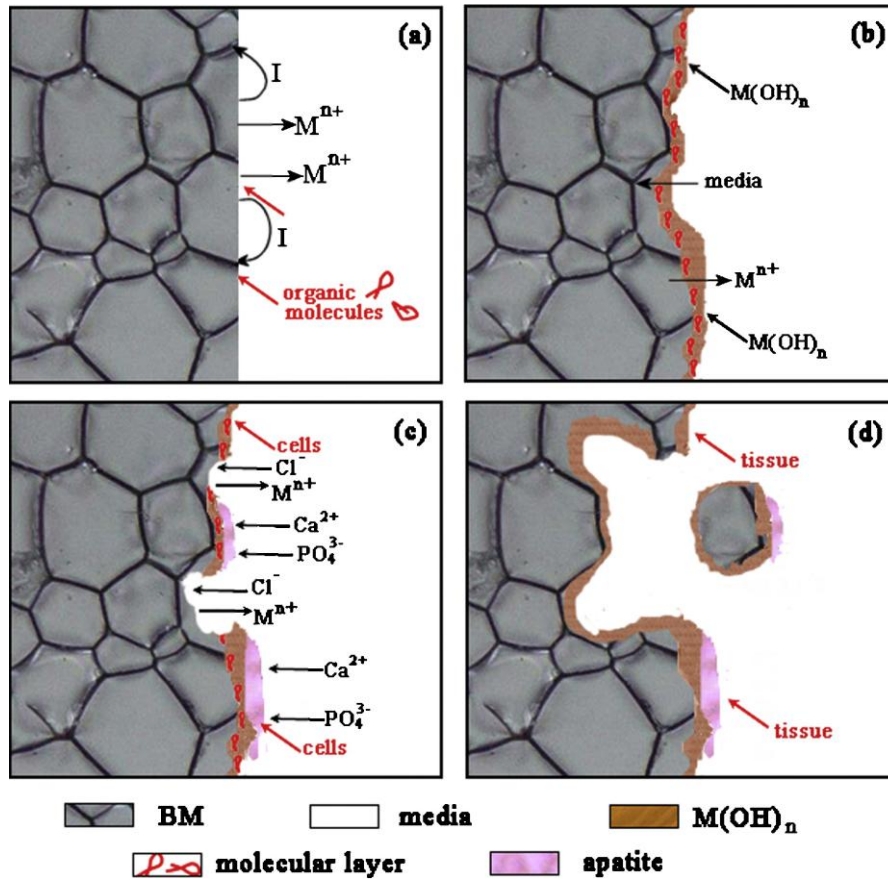


Figure 5: Schematic diagram of the biocorrosion process due to the interaction with the solution [80].

The corrosion studies can be classified based on three types. Vitro is a type corrosion test that is carried out in engineered and synthesized corrosion environments to mimic the actual biological environment of application to assess the performance of the system. Vivo usually is the next step test after vitro, where the corrosion performance of the specimen is

conducted in the body of a living animal model to track the interaction between the implantation devices and response of the host. Vitro testing is known to be more convenient and requires less time and cost than Vivo. Therefore, Vitro testing is considered an approval evaluation test to vivo and then in the human body. Thus, conducting a vitro test required a precise set up and high control of the variables to get accurate analyses and conclusion. The last phase is implanting the devices in human patients and analyzing the interaction of the implantation system and the human body [27, 85, 86, 87].

Kim et al [88] examined the influence of the surface area of commercially pure magnesium in Vitro and Vivo. Vitro test tracked the formation of the surface layer and weight loss of magnesium. The test was conducted in hank's solution at pH of 7.4 pH and 37 °C. And other part of the study, implantation devices were placed in L5-6 disc space posteriorly of twelve adults SD rats. The study concluded that increasing the surface area led to an increase in the precipitation of calcium phosphate, which led to a reduction in corrosion rate in both vitro and vivo studies. Nevertheless, the study reported the occurrence of different mechanisms caused the increase of the precipitation of calcium phosphate due to the surface increase. The calcium phosphate precipitation increases in vitro with increasing the surface area due to the increase in pH level of the solution. Whereas with in Vivo study, the increase in the local pH level led to elevate the concentration of phosphate and calcium from the homeostasis to balance the pH level, which led to the increase of the formation of a more stable layer of calcium phosphate.

### 2.1.1. Corrosion Products

The composition of the formed layer consists of magnesium oxide, magnesium carbonate, and hydroxyapatite (magnesium appetite), and the incubation time and environment type influence the composition of the formed layer. It was proposed that the formed layer is a result of magnesium ions and solution ions interacting with each other, where the biological incubation solutions such as Simulated Body Fluid and Hank's solution contain calcium, carbonate, and phosphate ions. The results can be clearly seen in the below reactions [33, 89]. It is worth mentioning that carbonate can promote the dissolution of magnesium but can also induce rapid surface passivation due to the precipitation of magnesium carbonate. Sulfate ions are more aggressive than chloride in the case of general corrosion [90].



Figure 6 illustrates the corrosion process of magnesium in SBF. The surface conditioning affects the electrochemical properties of metals and the formation of a surface film changes the overall potential of interfacial surface between the base metal and the electrolyte. Other factors like the microstructure of metals, geometric factors, and solution influence the corrosion behavior [72, 91, 92].

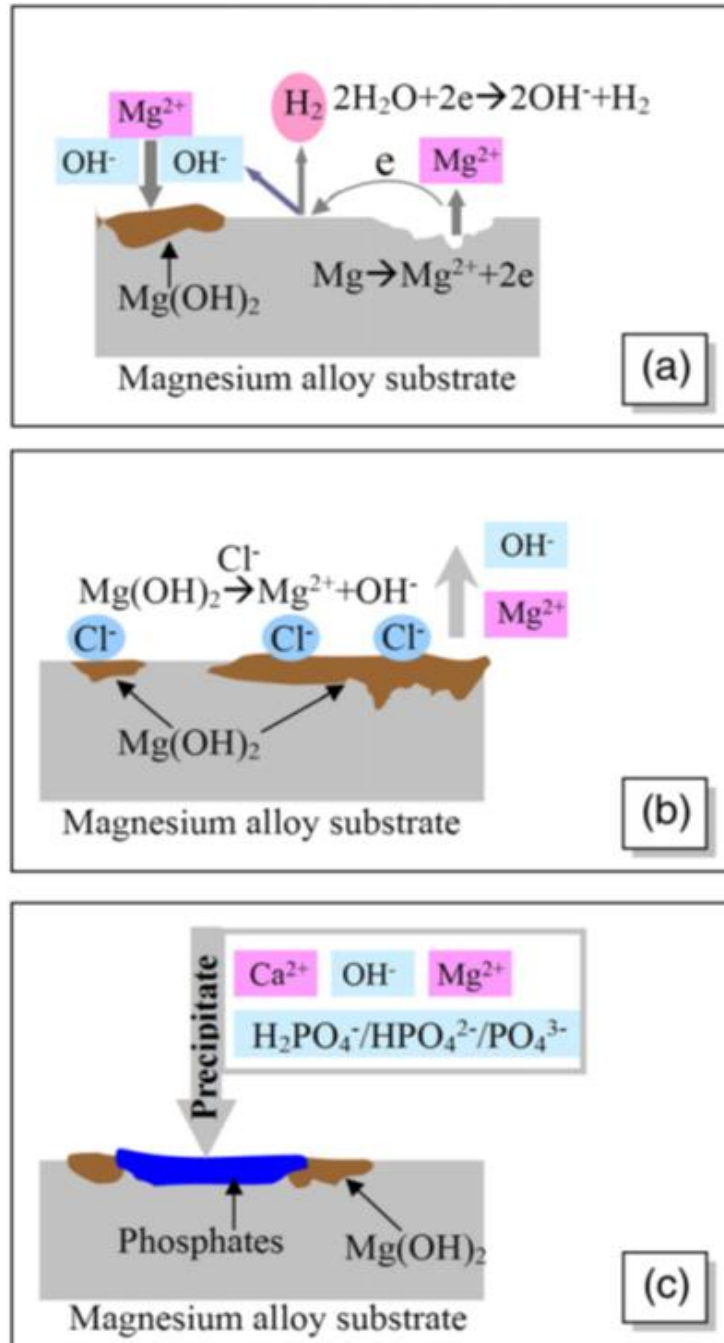


Figure 6: Schematic diagram of the interaction between Mg and SBF: (a) the degradation of Magnesium substrate surface with solution, (b) the dissolution of  $Mg(OH)_2$  layer, and (c) the formation and precipitate of phosphates [93].

Although the charge of the anodic reaction is equal to the cathodic reaction, the hydrogen gas generation does not represent the true corrosion rate. Part of the hydrogen is

dissolved into the biological/corrosion environment. On the other side of the reaction chain, not all of the magnesium dissolves and some species will form insoluble corrosion products. Therefore, different corrosion tests are preferred to evaluate the corrosion process because no individual corrosion test can give enough information about the corrosion behavior of magnesium. The biological environment can tolerate slow hydrogen gas generation, and the tolerance limit depends on the solubility and diffusivity of hydrogen gas in that biological environment. Hydrogen has high solubility in fat tissue and fast diffusivity through the skin [31, 27, 41].

The magnesium alloys suffer from stress-corrosion cracking and hydrogen embrittlement. The crack growth occurs in the form of intergranular stress corrosion cracking. The cracking is enhanced by a combination of a localized galvanic corrosion of the matrix ( $\alpha$ ) that is close to a second phase ( $\beta$ ) and the applied stress [33, 41].

### 2.1.2. The Effect of Impurities

The rate of the reaction for the anode and cathode is in balance and depends on the corrosion behavior of the alloy reaction in the environment. It was observed that magnesium tends to corrode non-uniformly due to the effect of impurities and second phases. The kinetic of the reaction increases with the presence of alloying/impurity traces of small overpotential elements such as iron and nickel and decreases with the presence of elements with large overpotential such as zinc. In the case of magnesium and its alloys, the common impurities are nobler, which act as a local cathode, while the base metal acts as

an anode. Therefore, exceeding the tolerance limit of impurities have very detrimental effects on the corrosion properties of magnesium and can increase significantly by 10-100 times. The corrosion rate, besides increasing the hydrogen evolution, are results of increasing the reaction rate of the anode and cathode. Figure 7 shows that increasing the impurities content led to a drastic evolution of hydrogen gas, especially with increasing the content of iron impurity from 45 ppm for high purity Mg to 280 ppm for low purity Mg and reducing the content of Aluminum [31, 33, 41, 94, 95].

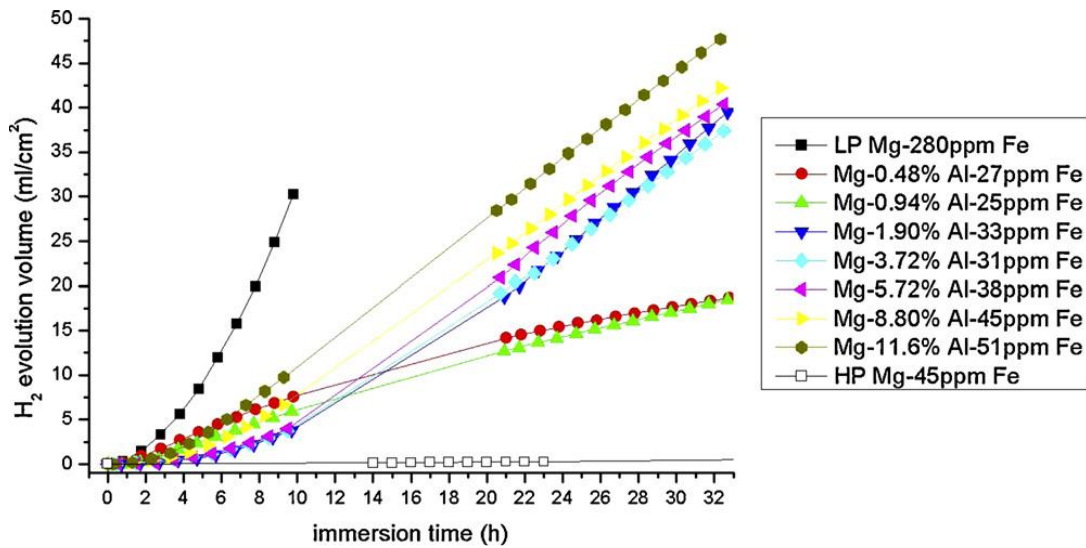


Figure 7: The effect of impurities on the corrosion behavior of Mg-based alloys in 3% NaCl solution [33].

It was found that the tolerance limit of impurities in Mg-based alloys must not exceed the range of 30-50 ppm for iron, 20-50 ppm for nickel, and 100-300 ppm for copper [96]. The tolerance limits of the impurities could be calculated using the thermodynamics of phase diagrams for Mg and the elements. It's worth mentioning that the presence of second phases could act as a micro-galvanic cathode when the size of the second phase is small. The second phase forms a corrosion cell with the matrix that acts as an anode due to

the difference in electro potential, where it is expected that a second phase ( $\beta$ ) is more stable than the primary phase ( $\alpha$ ). However, increasing the volume fraction of the second phase leads to balancing the effect of the cell and reducing the corrosion rate [33, 97].

Noviana et al [98] studied the hydrogen gas evolution in vivo post implantation. It was reported that hydrogen generation was rapid and accumulated in the form of cavities in the surrounding of porous commercially-pure magnesium implantation devices. The study examined with diameter of 13 mm and thickness of 2.5 mm in rats for a period of time up to 18 weeks. Overall, the implantation of the discs was not successful due to the high generation rate and buildup of hydrogen gas around the implantation site, which could be due to the porous structure that increases exposed surface area to the bioenvironment. Besides, the study did not take under consideration the tolerance limit of impurity and the size ratio of the implant to the femoral bone of the tested animal.

### 2.1.3. Corrosion Environments

The type of the biological corrosion fluid plays a significant role in the corrosion test of biomedical alloys for implantation devices. Several studies concluded that the corrosion rate depends on the type of the corrosion media and the time of the test. Different solutions have been used to test the corrosion behavior of magnesium and its alloys such as Hank's Balanced Salts Solution (HBSS), Simulated Body Fluid (SBF), Dulbecco's Modified Eagle Medium (D-MEM), Kokubo Solution, Phosphate Buffered Saline (PBS), Artificial Plasma (AP), Nor's Solution (NS) and NaCl solutions in different concentrations, as shown in [Figure 8](#) [31, 33, 41, 99]. [Figure 8](#) shows that testing the same type of alloy in different solutions and biological environments gives different degradation rates, for instance the corrosion rate of AZ31 (c) as cast was around 2 mm/year in Simulated Body Fluid and less than 0.7 mm/year in Vivo. It is worth mentioning, vivo environment is less aggressive than corrosion solutions [33, 90, 100].

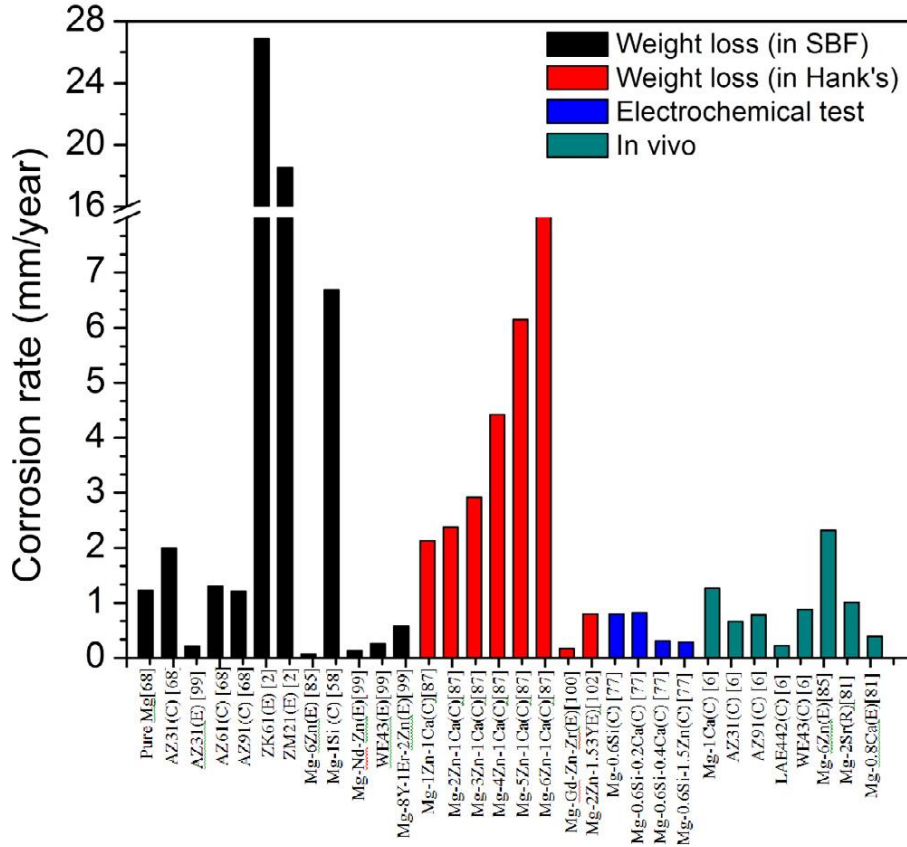


Figure 8: The corrosion of Mg-based alloys in different biological environments, the corrosion rate differs from one environment to another even for the same alloy [31].

Nevertheless, it was found that the additions of the biological factors to the solution affects the corrosion rate. The additions of the biological factors were found to be very important to mimic the physiological environment of the human body and to keep the corrosion media in balance. It is important to take these factors, such as proteins and buffers, into consideration when conducting a corrosion test. The effect of the biological additions varies from one factor to another. Whereas, it was found that the influence proteins such as Albumin and Serum depends on the concentration, type of the alloy, and period of time of the corrosion test. Moreover, the proteins could form a layer at the interfacial surface between the alloy surface and the biological environment, which leads

to the reduction of the corrosion rate. At the same time a local pH shift toward more alkalinity is expected to occur at interfacial contact between the layer and the alloy surface [31, 33, 29, 41, 90, 96].

Zeng et al [90] studied the influence of glucose on the corrosion rate of pure magnesium in Saline and Hank's solutions at 37 °C. It was stated that the effect of glucose depends on the type of corrosion media. The corrosion resistance and pH were reduced with increasing the glucose content in Saline due to the formation of gluconic acid from glucose, which attacks the oxide of the metal and attracts chloride ions to cluster on the interfacial surface between the metal and saline. It was also reported that chloride ions destabilize the surface layer and cause pitting corrosion. On the opposite side, the corrosion rate was decreased with the addition of glucose as a result of calcium phosphate compound formation.

Another important factor that can affect the corrosion behavior is pH change. During the corrosion process of magnesium, the pH tends to shift toward more alkalinity due to the generation of hydrogen that leads to increase the pH number. The shift in alkalization degree is due to the combined effect of anodic and cathodic reactions. The reaction of anodic products ( $Mg^{2+}$  ions) with water deposits  $H_2$  gas and hydroxyl ( $(OH)^-$ ) ions into the solution. On the other hand, the neutrality of products of the anodic reaction ( $Mg^{2+}$  cations) cannot counterbalance that shift. The shift in pH degree can be seen in [Figure 9](#), where the pH increased to more than 10 in non-buffered solutions (3% NaCl). The amount of that

shift depends on the type and presence of alloying elements. However, the increase of pH number at the interfacial surface between the alloy and the environment can enhance the formation of more stable and protective film. Generally, the formed layers consist of Mg(OH)<sub>2</sub> and CaP [18, 27, 41, 101]. The reduction in corrosion rate with increasing pH can be explained by studying pourbaix diagram for Mg, where increasing the pH induces the passivation of Mg and leads to increase the corrosion resistance, as shown in Figure 33.

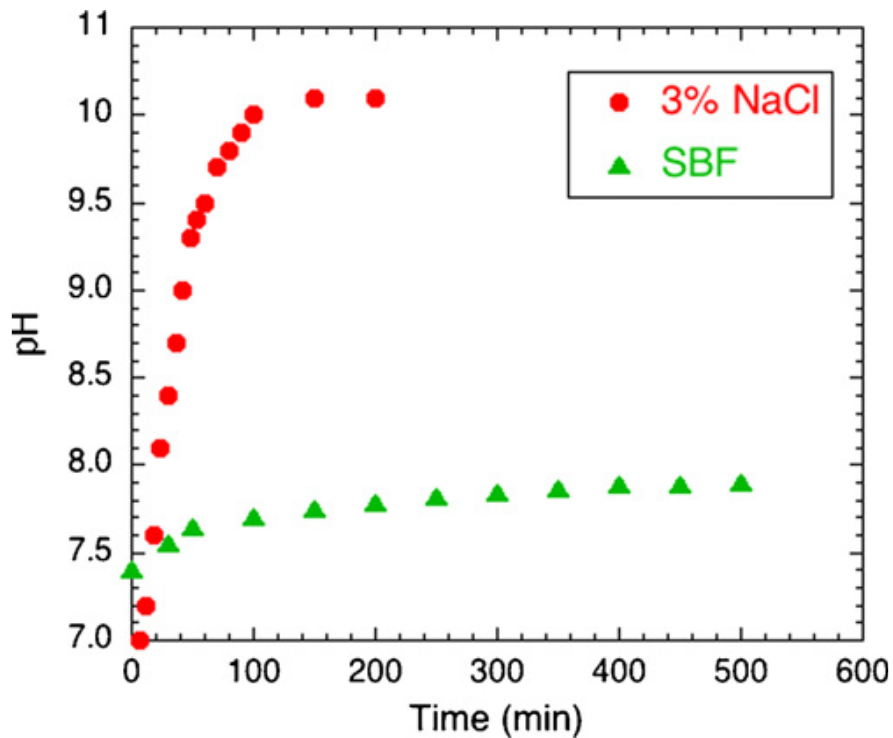


Figure 9: The pH change during the corrosion process in two different solutions, 3% NaCl and Simulated Body Fluid at 37 °C [41].

In recent studies, it was approved that the temperature increase leads to accelerate the kinetics of the reaction and consequently increase the corrosion rate [41]. Also, it was stated that the corrosion behavior highly depends on the temperature of corrosion media,

where the corrosion rate increased by 100% when increasing the temperature from 20 °C to 37 °C and by 50% with a further temperature rise to 40 °C [42]. Moreover, it was found that the change in temperature affects the solubility of gases in corrosion solution, where increasing the temperature increases the solubility of gases decreases [27].

Kirkland et al [27] reviewed the methodologies of corrosion tests for magnesium and its alloys. The study highlights the importance of considering vitro test variables and the setup of the test in interpreting the results. The study measured the mass loss in HBSS (at 37 °C and pH of 7.4) of pure magnesium, Mg-1Ca, and Mg-1Zn to be 9.1 mg/cm<sup>2</sup>, 8.3 mg/cm<sup>2</sup>, and 6.1 mg/cm<sup>2</sup>, respectively. It was found that the ratio of Hydrogen equivalent to the measured mass loss for the same systems to be 0.601, 0.651, and 0.540, respectively.

Theoretically, the generated hydrogen gas should match the mass loss. Whereas, it was reported that each degraded mole of magnesium (24.31 g) generates a mole of Hydrogen gas (22.4 L). Measuring the hydrogen evolution rate is a low-cost test that can be used to assess the shift in alkalization during the test. The change in pH could be calculated from the volume of the generated gas with assumption of one dissolved mole of Mg gives 2 mol of (OH)<sup>-</sup> [27]. However, experimentally the ratio of the generated amount of hydrogen gas to actual mass loss was reported to be widely varied between 0.22 and 1.31. This variation could be due to uncontrolled experimental variables and technical errors. Considering and controlling the experimental variables such as time, type of solution, temperature, degree of alkalization, influence of additives, and other justifications

play a significant role in getting accurate results as discussed earlier in this work. It was stated that Mg-1Zn had the lowest corrosion rate among other systems [27].

Yibin et al [28] analyzed the biodegradation behavior of pure magnesium in Hank's Balanced Salts Solution at 37 °C. It was concluded that the degradation rate and the hydrogen evolution of Pure Mg with pH of 7.4 were 0.2 mm/year and 0.15 ml/cm<sup>2</sup>, respectively. At the same time, the values in uncontrolled pH solution decreased to 0.02 mm/year and 0.1 ml/cm<sup>2</sup>, respectively. This was due to the increase in the pH of the solution. Moreover, the formation of surface layer that consists of Ca-P, was similar to the bone tissue.

In general, the alloying elements tend to blend with the  $\alpha$ -matrix of Mg alloying systems when the mixed amount is less than the solubility limit of that element in magnesium, which leads to hinder the anodic kinetics. However, increasing the added amount of alloying elements prompts increasing the formation and the volume fraction of secondary phases, subsequently increasing the corrosion. Therefore, the content of alloying elements in Mg-alloying systems is preferred to be less than the solubility limit [42].

The best corrosion resistance was reported for magnesium-manganese-based alloy with a corrosion rate of 2 mg/day for subcutaneous implantation in dogs [38, 102, 103]. Also, Mg-Mn-based alloy showed good biocompatibility and a very low corrosion rate with weight loss of 0.09g and 0.1g for implantation time of 50 day and 70 day, respectively. It was recorded that Mn has been added to magnesium alloys to increase the corrosion

resistance [102]. Table 3 summarizes the corrosion rates for different alloying systems of Mg.

Table 3: Corrosion rate of different alloying systems

Alloy	Solution		
	Hank's solution mm/year	C-SBF	Reference
Mg-1Mn-1Zn	0.003–0.010	-----	[104]
Pure Mg	2.08 ±0.2	-----	[20]
Mg-1Ca	3.16±0.5	-----	[20]
Mg-1Ca-1Zn	2.13±0.2	-----	[20]
Mg-1Ca-2Zn	2.38±0.3	-----	[20]
Mg-1Ca-3Zn	2.92±0.5	-----	[20]
Mg-1Ca-4Zn	4.42±1.0	-----	[20]
Mg-1Ca-5Zn	6.15±1.5	-----	[20]
Mg-1Ca-6Zn	9.21±1.5	-----	[20]
Pure Mg	-----	2.13 (V)	[102]
As-cast Mg–4.0Zn–0.2Ca	-----	2.05 (V)	[102]
Pure Mg	9.1 (mg/cm <sup>2</sup> )	-----	[27]
Mg–1 Ca	8.3 (mg/cm <sup>2</sup> )	-----	[27]
Mg–1 Zn	6.2 (mg/cm <sup>2</sup> )	-----	[27]
Pure Mg	0.2 at 37 and 7.5	-----	[28]
Pure Mg	0.02 at 37 and uncontrolled pH	-----	[28] [101]

The corrosion resistance can be enhanced by using different approaches such as reducing the chemical potential difference with other elements and using high cooling rates to solidify magnesium. Whereas, using elements that do not have a negative effect such as manganese and Sodium helps in improving the performance of magnesium alloys. In addition to that, using rapid solidification produces small grains and supersaturated phases to improve the mechanical properties and reduce the aggressivity of corrosion [75, 105].

## 2.2. Mg Alloying Systems

Different mechanisms have been investigated to enhance the mechanical and corrosion properties, these methods can be classified into five main techniques. These methods are adding alloying elements, processing methods, coating, solidification and heat treatments [31, 18, 37, 38, 104, 106, 107]. Adding alloying elements can be divided into four categories of magnesium alloys: commercial Mg alloys, Mg alloys containing rare earth elements (REE), Mg alloys with nontoxic elements, and Mg alloys containing a mix different alloying systems [29, 41, 100]. [Table 1](#) shows some examples of Mg alloying systems. The preferred atomic size of alloying elements is in the range of  $\pm 15\%$  of the atomic diameter of magnesium (0.320 nm) [31]. [Figure 10](#) shows the range of the preferred atomic size of alloying elements in comparison to Mg.

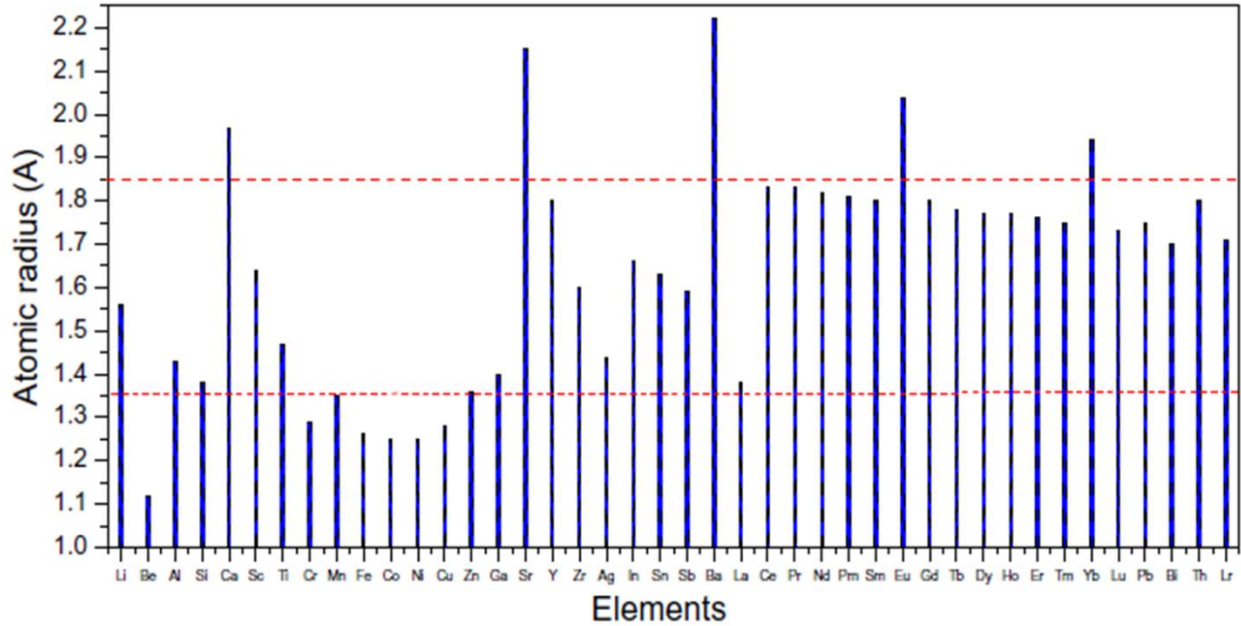


Figure 10: The atomic radius of different alloying elements [31].

Witte et al [100, 108] studied the biological inflammatory response of a magnesium alloy (AZ91D), the hydrogen gas generation, and corrosion process for six months after the devices were implanted into the distal femur condyle of rabbits. It was found that no significant inflammation was observed, and the initial inflammatory response was considered to be normal due to the immune system reaction of the host. The study stated that the formed gas cavities during the first two weeks were dissipated during the third week. Similar results were found in another study [33].

It also was found that the magnesium alloy stimulated the formation of and increased the density of new bone. However, traces of Aluminum were found in the blood, kidneys, liver, and other organisms. Moreover, Aluminum species were spotted with residual insoluble corrosion byproducts [33]. Overall, although Mg-Al-based and Mg-

REE-based alloys have good mechanical properties and corrosion resistances, they have very poor biocompatibility and hepatotoxicity [32, 103].

Fan et al [109] examined the effect of adding 1.35 wt.% Cerium (Ce) to Mg-2Zn-0.5Mn-1Ca. It was assessed to have a negative influence on the corrosion resistance of the alloy, although the grain size was reduced from 125  $\mu\text{m}$  to 65  $\mu\text{m}$ . However, adding Ce led to disturbing the formation of  $\text{Ca}_2\text{Mg}_6\text{Zn}_3$  and formed two disconnected phases of  $\text{Mg}_2\text{Ca}$  and  $\text{Mg}_{12}\text{CeZn}$ .

Yang et al [19] studied the effect of adding different amounts of a rare earth element Dy (Dysprosium) to magnesium on the microstructure, mechanical properties, and corrosion rate. Four alloys of Mg-Dy in concentration of Mg-5, 10, 15, 20 wt.% of Dy were made. He also examined the effect of heat treatment on the properties of the alloys, where the samples were heated under 520°C for 24h and then quenched in water. The study concluded that increasing the content of Dy led to an increase in the tensile yield strength and ultimate tensile strength (UTS).

The addition of 10% Dy led to a noticeable improvement in UTS from 77 MPa to 130 MPa. Further addition of Dy did show a slight increase in the UTS of the alloys. However, the ductility increased slightly from 4.5% to 5.5% with addition of up to 5% Dy and then decreased with increasing the content of Dy to 15% and 20%. The best corrosion resistance was reported for 10% Dy alloy to be 3 mm/year in 0.9% NaCl solution. The corrosion morphology of as-cast alloys can be seen in [Figure 11](#). On the other hand, the

heat treatment reduced the mechanical properties and improved the corrosion resistant significantly. The distribution of Dy became homogeneous, which enhanced the formation of filiform over pitting corrosion. It was noticed that the overall impurity of the alloys exceeded the tolerance limit in this study [19].

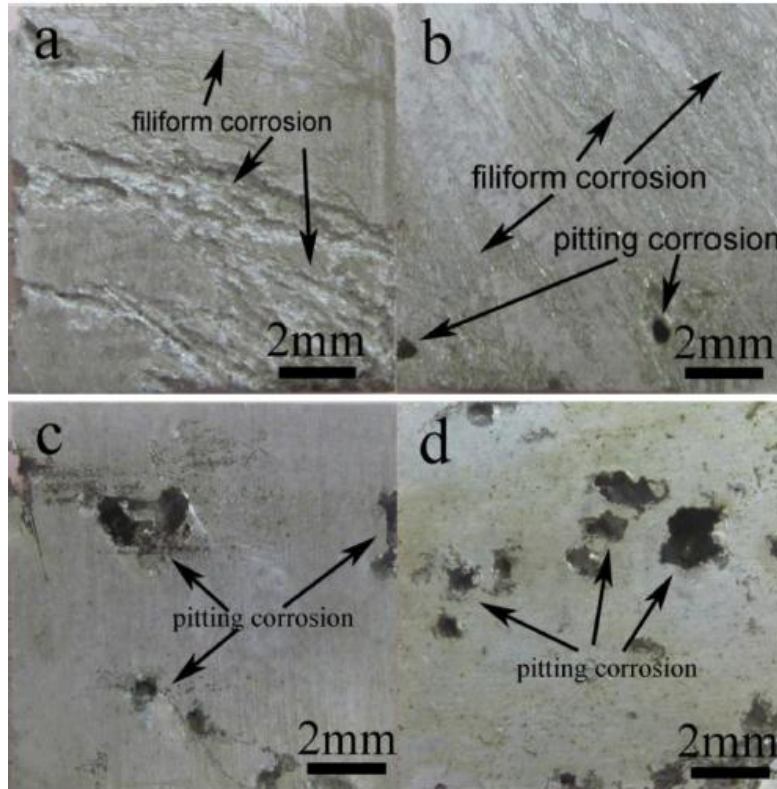


*Figure 11: The corrosion morphology of Mg-Dy alloying system after immersion test in 0.9% NaCl solution for 72 hrs (a) 5% Dy (b) 10% Dy (c) 15% Dy (d) 20% Dy [19].*

Gu et al [110] characterized the effect of adding different contents of Strontium (1-4 wt.%) on the strength, cytotoxicity, and corrosion resistance (in vivo and vitro). The study found that the yield strength, UTS, and degradation rate were increased with increasing the content of Sr up to 2 wt%, in spite of the continuous reduction in ductility with the addition

of Sr. Overall, the Mg-Sr alloying system showed very poor biocompatibility with high toxicity.

Bornapour et al [111] studied the cytotoxicity and corrosion process (in Hank's solution and in vivo) of Mg-xSr ( $x=0.3-2.5$  wt.%) alloys. The alloys were used as stents and implanted in dogs' femoral arteries. The record showed that Mg-0.5Sr showed the lowest degradation rate and no indicated toxicity. However, pitting corrosion was observed on the surface of Mg-0.5Sr with high hydrogen gas evolution at the early stages.

Calcium has a solubility of 1.34 wt.% in Mg and it's a non-toxic element with high allowable daily intake [32]. Different percentages of Ca content were tested for their properties. Zijian Li et al [101] investigated the effect of adding different amounts of Ca (1-3 wt.%) to commercially pure magnesium on the mechanical properties and corrosion rates of the alloying system. The study prepared as-cast, hot-rolled, and hot-extruded samples for both the mechanical and corrosion tests. The corrosion test was done in vitro in Simulated Body Fluid for 250 hours and in vivo for three months, where Mg-Ca pins were implanted in femoral and cortical bones of eighteen adult rabbits. It was concluded that increasing Ca content led to decreasing the yield strength, ultimate tensile strength, and ductility (as shown in [Table 5](#)), and led to increasing the corrosion rate and the presence of corrosion byproducts.

Also, a layer was formed on the top of the surface that did not show a good coherency. The layer contained high concentrations of carbon, oxygen, magnesium,

phosphorus, and chloride. Moreover, the mechanical properties and corrosion resistance were improved significantly with hot-extrusion and hot-rolling. Overall, Mg-1Ca showed the best mechanical properties, corrosion resistance ( $2.28 \text{ mg/mm}^2/\text{year}$ ), and compatibility among other alloys [101]. It was reported that Mg-Ca-based alloys with high content of Ca tend to form insoluble massive corrosion byproducts after immersing the samples in SBF solution at  $37 \text{ }^\circ\text{C}$ , as shown in Figure 12 [42].

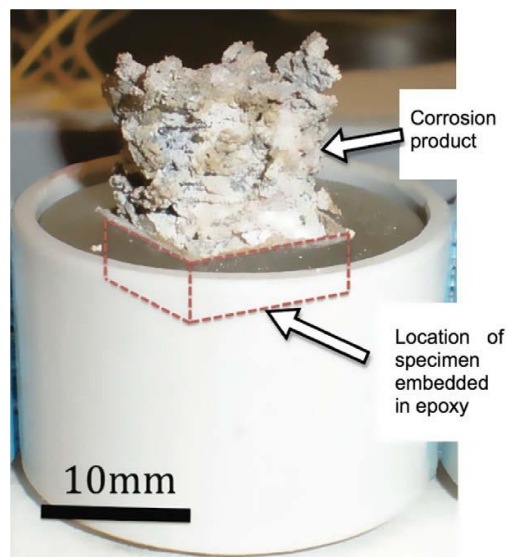


*Figure 12: The formation of massive corrosion byproducts on the top of Mg-Ca alloy with high content of Ca [42].*

The alloying system of Mg-Si-based alloys was found to consist of the matrix ( $\alpha$ -Mg) and intermetallic compound of Chinese script ( $\text{Mg}_2\text{Si}$ ) due to the low solubility (0.003 wt.%) of Si in Mg. The maximum mechanical properties can be achieved with the addition of 0.8 wt.% Si. YS, UTS, and ductility reached 52 MPa, 152 MPa, and 9.5%, respectively. However, the formed intermetallic compound ( $\text{Mg}_2\text{Si}$ ) is brittle and has a detrimental effect when it's formed in coarse size [31].

Chen et al [31] review the recent developments of magnesium alloys for biomedical implantation devices. The study highlighted the different biomedical applications of magnesium and the importance of considering the required healing time for each medical application. Recently, the magnesium alloys have been fabricated in the forms of Stents, Screws, Pins, and devices for orthopedic applications. The required time to maintain the mechanical stability is estimated to be 12-18 weeks for bone implantations, 6-12 months for stents, and 12-24 months for vessels.

Gu et al [112] examined the mechanical properties, corrosion performance in vitro, and biocompatibility of several binary alloying systems of magnesium with addition of 1 wt. % of each alloying element (Zn, Mn, AL, Ag, In, Si, Sn, Y, and Zr) in addition to pure Mg. The as-cast Mg binary systems of Zn, Si, Al, Sn, and Zr showed better mechanical properties in comparison to pure Mg. The corrosion performance of Mg was reduced with adding Zn, Mn, Al, In, and Zr. Additionally, the hydrogen evolution was reduced significantly with the addition of Zn. The Mg-Zn system exhibited acceptable biocompatibility of cell viability to fibroblasts, toxicity to osteoblasts, and blood vessel viabilities.

Another study reviewed a wide range of magnesium-based alloys and the effect of adding different alloying elements on the mechanical properties. It was found that the highest yield strength and ductility can be achieved by using Mg-REE-based and Mg-Zn-

based alloys among other Mg-Al-based, Mg-Si-based, and Mg-Zr-based alloys, as shown in [Figure 13](#) [31].

The effect of adding low manganese concentration boosts the grain refinement of Mg-Al system besides hindering the influence of impurity by forming harmless phases, which enhance the corrosion resistance of Mg systems. Additionally, adding manganese leads to increase the yield strength moderately and decrease the ultimate strength and elongation. [29, 49, 51, 62, 63, 64, 65, 66, 68] [113, 114]. The addition of zinc increases the mechanical, corrosion performance of magnesium with reducing the hydrogen evolution. However, the high concentration rate ( $\geq 5\%$ ) of zinc decreases the corrosion resistance and mechanical properties and reduces the biocompatibility [52, 53, 54, 55, 56, 57, 58, 59, 60, 61] [69, 93, 113, 115].

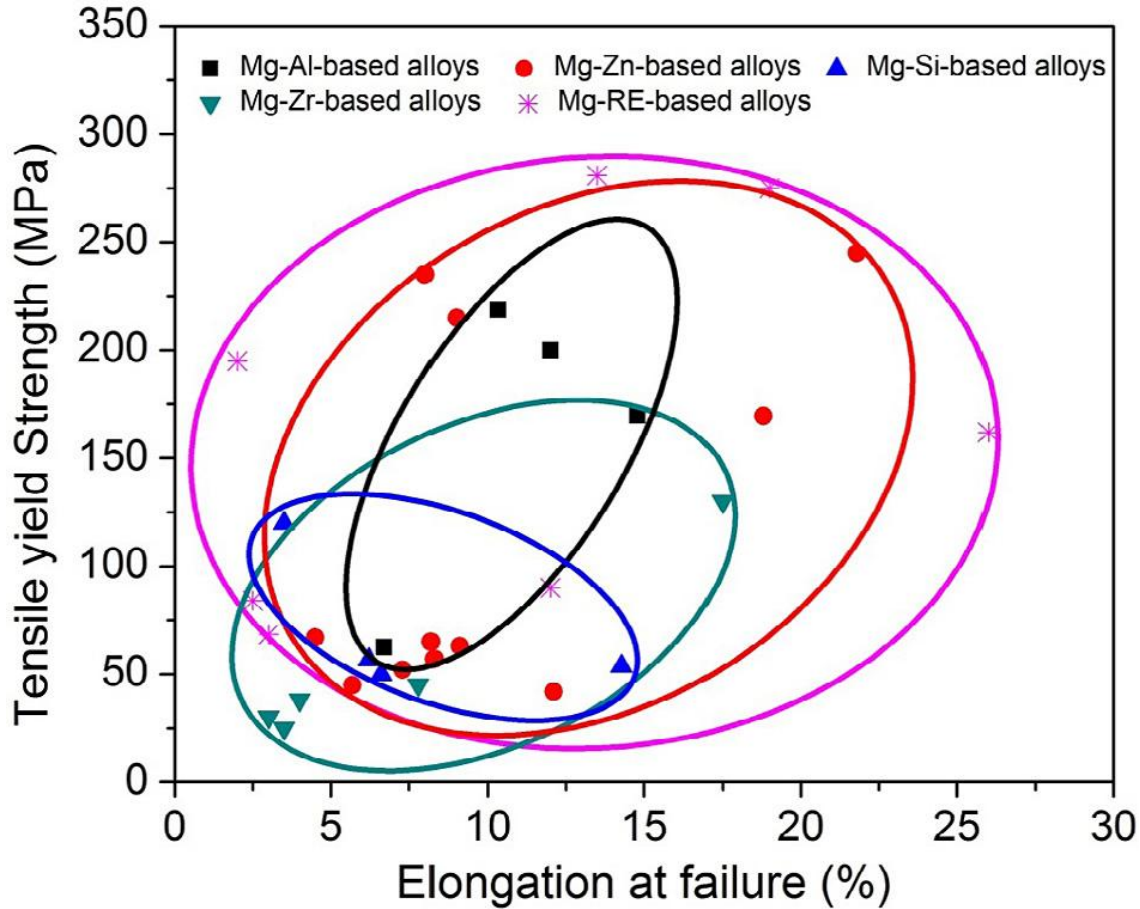


Figure 13: The tensile strength versus the elongation of different alloying systems of Mg [31].

Yuen et al [116] studied the theoretical limits of using magnesium alloys as biodegradable materials for biomedical applications. It was concluded that aluminum as alloying element in Mg-based alloy has the lowest tolerance limit with amount of  $\leq 1$  g per year whereas the tolerance limit for other elements exceeded 10 g per year. It is worth mentioning that the study excluded some elements such as rare earth elements and zirconium due to the inadequate data and information on these elements. Zinc (Zn) has a good solubility (6.2 wt.%) in Mg and has been added to increase the mechanical properties.

Zn is a nontoxic element with a recommended daily dosage (8-11 mg/day for adults) [31, 32, 34].

Mg-Zn-based alloys showed good mechanical and corrosion properties. The alloy consists of  $\alpha$ -Mg matrix and  $\gamma$ -MgZn phase. The characterization of this type of alloying system showed that the highest ultimate tensile strength (216.8 MPa) and ductility (15.8%) can be obtained by adding 4 wt.% of zinc. The addition of other alloying elements such as manganese (Mn), silicon (Si), calcium (Ca), and rare earth elements (REE) has been investigated. It was found that adding Ca up to 0.5% improved the mechanical properties slightly; however, further addition of Ca had a negative effect on the properties of the alloy [31].

The addition of manganese to the alloying system of Mg-Zn-based alloys led to increase the corrosion resistance due to the ability to encounter the detrimental effect of impurities, such as iron, nickel, and copper, by transferring them into non-active intermetallic compounds. The corrosion rate of Mg-2Zn-0.2Mn alloy in Hank's solution was reported to be 0.03 mm/year, and a protective layer was formed on the surface of the alloy. Moreover, Mn stimulates multiple enzyme systems [32, 33, 18].

Cha et al [117] characterized the impact of adding calcium and zinc on corrosion behavior of casted and extruded magnesium. It was found that adding zinc in an amount of more than 1% to Mg-Ca alloying system refined the microstructure, improved the corrosion resistance, and reduced the galvanic effect. The further increase of Zn content to 3%

showed the best corrosion performance. Additionally, the study concluded that refining the microstructure by using extrusion process reduced the hydrogen generation of the studied alloys in vivo studies.

Zhang et al [20] tested the effect of adding various content (1-6 wt%) of zinc on the strength, corrosion behavior, microstructure, and cytotoxicity of Mg-1Ca alloying system. The addition of zinc was found to reduce the grain size and improve all of the mechanical properties upto 4 wt%, with values for yield strength, UTS, and ductility of 63MPa, 185 MPa, and 9.1%, respectively. However, the change in young Modulus was slight ( $45 \pm 1$  GPa). Nevertheless, the study conducted the vitro corrosion test in Hank's solution at  $37^\circ\text{C} \pm 0.5$  with pH of (7.2-7.4). It was reported that Mg-1Ca-xZn alloys with zinc content upto 3wt.% showed lower corrosion rate than Mg-1Ca alloy, but higher than pure magnesium. Also, the addition of zinc up to 3wt% did not cause toxicity. [Table 5](#) summarizes the mechanical properties for the alloying system.

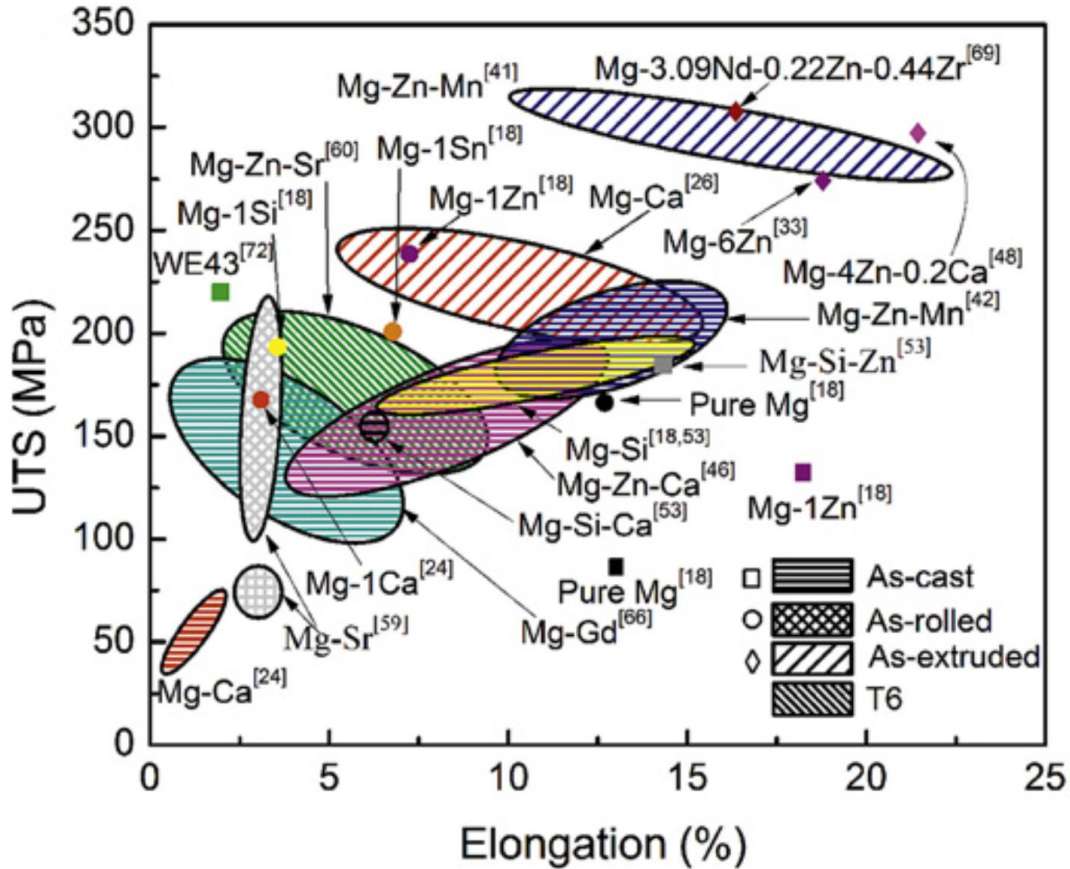
Ibrahim et al [118] analyzed the impact of heat treatment on the mechanical, microstructure, and corrosion resistance of Mg-1.2Zn-0.5Ca. As-cast alloy consists of  $\alpha$ -Mg matrix with small spherical eutectic secondary phases, embedded in the matrix, and lamellar eutectoids along the grain boundaries. Although the grain size was enlarged slightly, the heat treatment improved the mechanical and corrosion properties considerably by diffusing the secondary phases, high content of Zn and Ca, into the matrix and

consequently reducing the micro-galvanic effect that can boost the degradation rate. Thus, reducing volume fraction of secondary phases enhances the performance of the alloy.

Li et al [32] have analyzed Mg-Zn-based alloys and the performance of the alloying system after adding different alloying elements and concentrations. It was found that the yield strength and the ultimate tensile strength increased by 64% and 33% with increasing the content of Zn from 1 wt.% to 6 wt.% , while the elongation was decreased slightly by 11%. It was concluded that the addition of manganese enhanced the corrosion resistance by eliminating the harmful effect of impurities. Similarly, adding 4 wt% Zn to Mg-0.2 Ca led to high mechanical properties and corrosion resistance. In the case of Mg-Si- based alloys, adding 1.6 wt.% Zn to Mg-0.6Si refined the brittle phase of coarse Chinese Scripts and boosted the mechanical properties and reduced the corrosion rate. The study also reviewed adding other alloying elements (Zr and Y) to the system.

It was concluded that the corrosion rate of Mg-5.4Zn-0.55Zr was higher than Mg-5.6Zn-0.55Zr-0.9Y, and both rates were higher than the rate for pure magnesium although the alloying elements improved the mechanical properties. The study concluded that increasing the number and volume fraction of different secondary phases could lead to deteriorated performance of Mg alloys. Furthermore, the study summarized the mechanical properties of different alloying systems that were fabricated by various processing methods. As-cast Mg-Mn-Zn alloying system exhibited favorable UTS and ductility around 200 MPa and 15%, respectively. Meanwhile, Mg-Ca, Mg-Si, Mg-Sr, Mg-Ca-Si,

Mg-Zn-Ca demonstrated lower mechanical properties, as shown in Figure 14 [32]. Other studies suggested that the required properties for bone applications should be with a range of 200 MPa UTS, 10% ductility, and corrosion rate of less than 0.5mm/year [31, 119].



of zinc improves the corrosion resistance and reduces the volume fraction of the secondary phase better than Sr.

Sun et al [120] tested the mechanical properties and corrosion resistance (in C-SBF) of Mg–4.0Zn–0.2Ca alloy as-casted and as-extruded. Adding Zn and Ca led to improved mechanical properties and corrosion behavior significantly; in addition, the alloying system showed good biocompatibility. The very good properties of as-cast alloy were further increased by the extrusion process. The extrusion process refined and homogenized the micro structure ( $\alpha$ -Mg,  $\text{Ca}_2\text{Mg}_6\text{Zn}_3$  and  $\text{Ca}_2\text{Mg}_5\text{Zn}_{13}$ ). Generally, reducing the grain size and homogenizing the alloying systems improve the corrosion resistance and mechanical properties [121, 122].

Xu et al [24] studied the effect of the cooling rate on the microstructure, hardness, and corrosion of Mg-Zn-Ca alloying system. Three alloys (Mg–10Zn–1Ca, Mg–20Zn–1Ca, and Mg–6Zn–1Ca) were made, and a combination of powder and granules were mixed and pressed to make studs. The studs were melted in a mild steel crucible under a controlled environment, then poured into graphite molds and solidified by applying three different cooling rates. The alloys were cooled with insulated environment ( $\sim 40$  °C/min), air ( $\sim 100$  °C/min), and liquid nitrogen ( $\sim 3000$  °C/min). It was found that alloys cooled with rapid solidification showed higher micro-hardness and corrosion resistance in Phosphate Buffered Saline (PBS) than slowly cooled alloys. Nevertheless, rapidly cooled

alloys formed a smaller grain size and connected network of a secondary phase that was supersaturated with alloying elements around the grains (mainly  $\alpha$ -Mg).

The study claimed that a well distributed network of a supersaturated secondary phase can work as coating and inhibit the corrosion propagation and protect the matrix. Meanwhile, the low cooling rate produced alloys that had a larger grain size, wider precipitates of secondary phases, and impurities segregation. Moreover, corrosion resistance for quenched alloys with low content Zn (6%) was higher than quenched alloys with higher Zn content. [Table 5](#) summarizes the mechanical properties for the alloying system [24].

Lisitsyn et al [21, 23] and Ben-Hamu [22] studied the role of adding 0.2-0.4 wt.% Ca and/or 0.5-2 wt.% Si on the corrosion rate (in 3.5% NaCl solution saturated with  $\text{Mg}(\text{OH})_2$ ) and microstructure of Mg-0.5Mn-6Zn alloying system, which was made by an extrusion process. The addition of Si refined the grain size and produced Chinese Script intermetallic. The Chinese Scripts were reduced to a polygonal shape with addition of Ca or 1% Si content or more. The corrosion rate increased with addition of (0.5 and 1%) Si and then reduced slightly with 2% Si content in comparison to Mg-0.5Mn-6Zn. However, the corrosion resistance was improved with refining the Chinese script by adding 1% and 2% Si content or Ca in case of 0.5% Si addition. Nevertheless, four secondary inter metallic phases ( $\text{MgZn}_2$ ,  $\text{Mn}_5\text{Si}_3$ ,  $\text{Mg}_2\text{Si}$  and  $\text{CaMgSi}$ ) were observed in the alloying system.

Zhang et al [123] characterized the microstructure, mechanical properties, and corrosion behavior of Mg–Zn–Mn–Ca. Three as-cast alloys were prepared with composition of Mg–1.8Zn–1.1Mn–0.3Ca, Mg–2Zn–1.2Mn–0.5Ca, and Mg–1.5Zn–1.1Mn–1Ca. The grain size of Mg–1.8Zn–1.1Mn–0.3Ca alloy was considerably reduced from 175  $\mu\text{m}$  to 63  $\mu\text{m}$  with increasing the content of Zn and Ca by 0.2%, and Mg primary phase with secondary eutectic ( $\alpha\text{-Mg} + \text{Ca}_2\text{Mg}_6\text{Zn}_3$ ) were observed. The addition increased yield strength, UTS, and elongation by 20%, 16%, and 20%, respectively. However, increasing the Ca content further to 1% and decreasing Zn content to 1.5% significantly decreased the strength and ductility due to the formation of an additional secondary brittle phase ( $\text{Mg}_2\text{Ca}$ ). Overall, the best mechanical and corrosion performance (in Hank's solution at 37 °C) reported for Mg–2Zn–1.2Mn–0.5Ca. [Table 5](#) summarizes the mechanical properties for the alloying system.

Bakhsheshi-Rad et al [74] studied the binary and quaternary alloying systems of Mg–xCa ( $x= 2$  and 4 wt.%) and Mg–2Ca–0.5Mn–xZn ( $x=2, 4,$  and 7 wt.%) , respectively. The study tested the mechanical properties, microstructure, and corrosion resistance in Kokubo Simulated Body Fluid for 240 hours for both alloying systems. It was found that adding 2wt. % of Ca to pure magnesium reduced the grain size to 92  $\mu\text{m}$  and ductility by 58% and increased the yield strength, ultimate tensile strength, compression strength, and hardness by 72%, 18%, 27% and 49%, respectively.

Although the corrosion rate in cell culture media magnesium was reduced with adding 2% Ca from 8.47 to 6.89 mm/year, further addition of Ca increased the volume fraction of the secondary phase ( $\text{Mg}_2\text{Ca}$ ) in grain boundaries and deteriorated both of the mechanical properties and corrosion resistance. On the other hand, Mg-2Ca-0.5Mn-4Zn had the highest mechanical properties among all examined alloys due to the small grain size of 59  $\mu\text{m}$  and solution strengthening, and the presence of secondary phases  $\text{Mg}_2\text{Ca}$  and  $\text{Ca}_2\text{Mg}_6\text{Zn}_3$  was detected. YS, UTS, ductility, compression strength, and hardness increased significantly in comparison to the pure magnesium by 202%, 94%, 20%, 85%, and 139%, respectively [74].

Figure 15 shows the microstructures of Mg-Ca and Mg-Ca-Mn-Zn alloying systems. Mg-2Ca-0.5Mn-4Zn alloy showed the second lowest corrosion rate and hydrogen generation after Mg-2Ca-0.5Mn-2Zn, as shown in Figure 16. The degradation rates Mg-2Ca-0.5Mn-4Zn and Mg-2Ca-0.5Mn-2Zn were reduced to 2.27 and 1.78 mm/year, respectively. The formation of lamellar eutectic structure of ( $\alpha\text{-Mg} + \text{Ca}_2\text{Mg}_6\text{Zn}_3 + \text{Mg}_2\text{Ca}$ ) at the grain boundaries was observed in SEM images, as shown in Figure 17 [74].

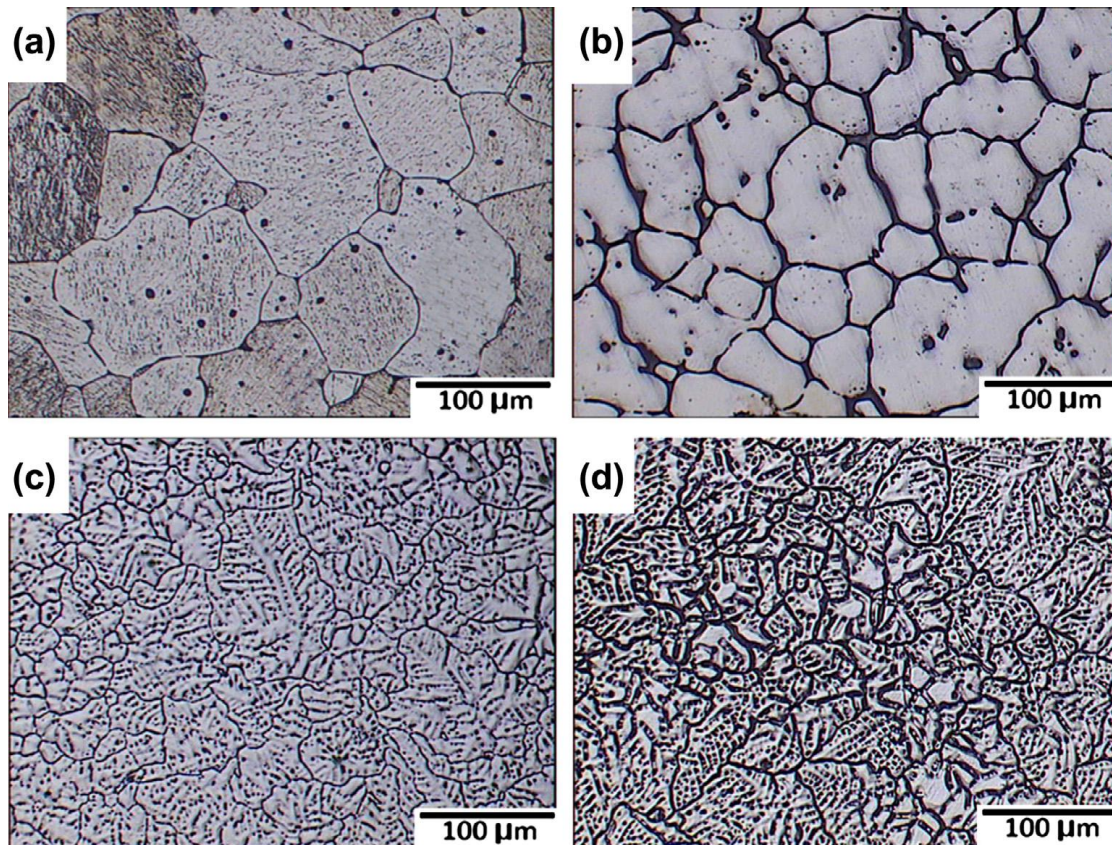


Figure 15: The microstructure images of Mg-Ca and Mg-Ca-Mn-Zn alloying systems (a) Mg-2Ca, (b) Mg-4Ca, (c) Mg-0.5Ca-0.5Mn-2Zn (c) Mg-0.5Ca-0.5Mn-4Zn [74].

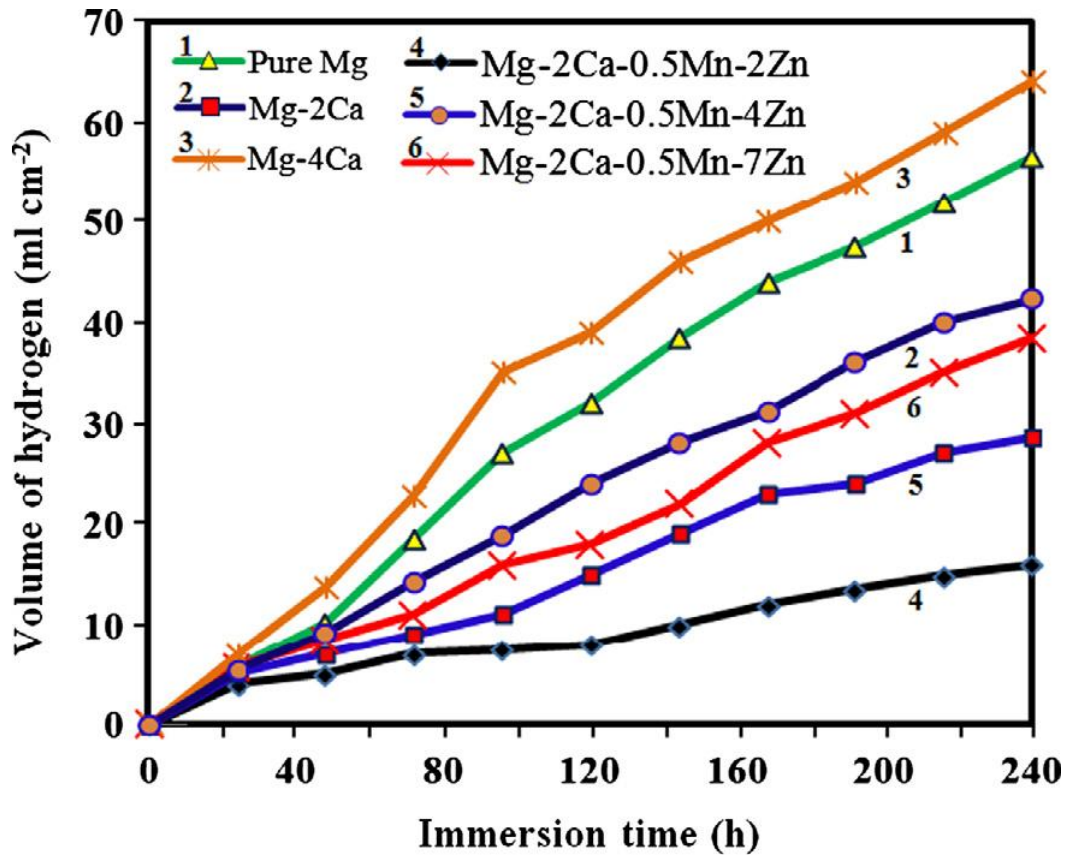


Figure 16: The hydrogen gas evolution rate of Mg-Ca and Mg-Ca-Mn-Zn alloying systems in Kokubo solution for duration of 240 hours [74].

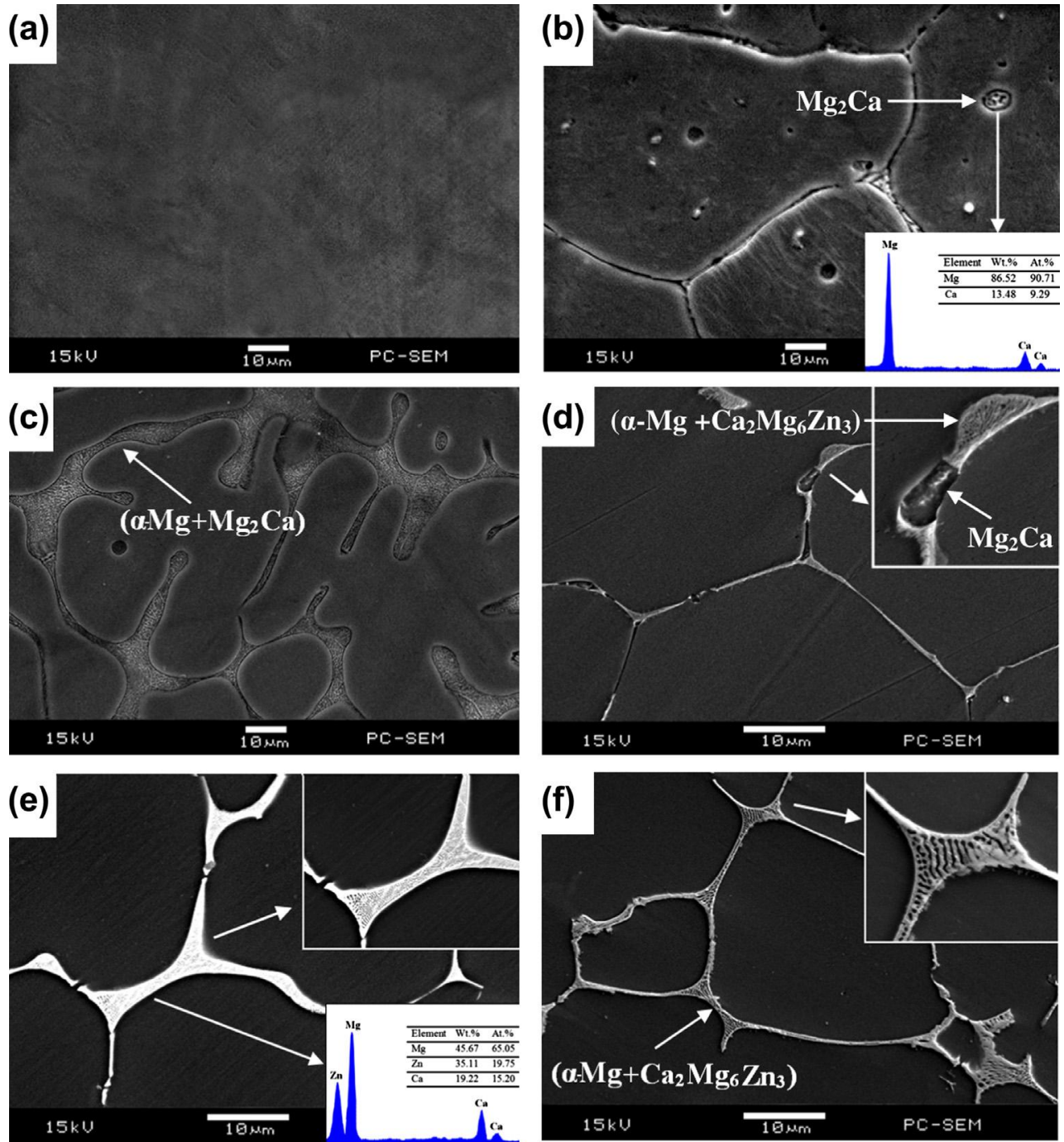


Figure 17: SEM images of Mg-Ca and Mg-Ca-Mn-Zn alloying systems (a) pure Mg (b) Mg-2Ca, (c) Mg-4Ca, (d) Mg-0.5Ca-0.5Mn-2Zn (e) Mg-0.5Ca-0.5Mn-4Zn (f) Mg-0.5Ca-0.5Mn-7Zn [74].

The study concluded that zinc has maximum solubility of 1.6 wt.% in Mg–Zn alloys at ambient temperature at equilibrium, and it is a more effective refinement alloying element than calcium, since Zn has a higher growth restricted factor (Q) according to Equation 7. Moreover, the liquidus line of Mg-Zn alloying system has a higher slope ( $m=6.04\text{ }^{\circ}\text{C}/\text{wt.}\%$ ) than Mg-Ca alloying system ( $m=2.12\text{ }^{\circ}\text{C}/\text{wt.}\%$ ) [74].

$$Q = m c_0 (k-1)$$

----Equation 7

Where (Q) is the growth restricted factor, m is the gradient of the liquidus line of a binary alloy,  $c_0$  is the bulk concentration of the solute, and k is the equilibrium partition coefficient of the solute [74].

The solubility limits of zinc and manganese are 6.2 wt.% and 2.2 wt.%, respectively. In metals, the main purpose of adding alloying elements is to improve the mechanical properties and enhance the corrosion resistance. There are a number of mechanisms to strengthening matrixes with alloying elements. These mechanisms are grain refinement, solid solutions, and precipitation hardening. The impact of improving the properties depends on the size, shape, structure, and formed phases in alloys. In the case of grain refinement, this effective mechanism can improve the mechanical properties and corrosion behavior. The effectiveness of the grain refinement is governed by the Hall–Petch (Equation 7), where high strengthening coefficient of Mg alloys ( $280\text{--}320\text{ MPa } \mu\text{m}^{1/2}$ )

indicates the high potential of using this mechanism to improve the alloying system [31, 124, 125].

$$\sigma = \sigma_0 + kd^{-1/2} \quad \text{---Equation 8}$$

Where  $\sigma$  is the Yield Stress (YS),  $\sigma_0$  is the contribution from other strengthening mechanisms material constant,  $d$  is the average grain diameter, and  $k$  is the strengthening coefficient.

Figure 18 and Figure 19 show the binary phase diagram of Mg-Zn and Mg-Mn alloying systems with the expected formation of phases. Also, the thermodynamic analysis of the binary system confirmed the formation of five intermetallic compounds:  $Mg_{51}Zn_{20}$ ,  $Mg_{21}Zn_{25}$ ,  $Mg_4Zn_7$ ,  $MgZn_2$ , and  $Mg_2Zn_{11}$  [126].

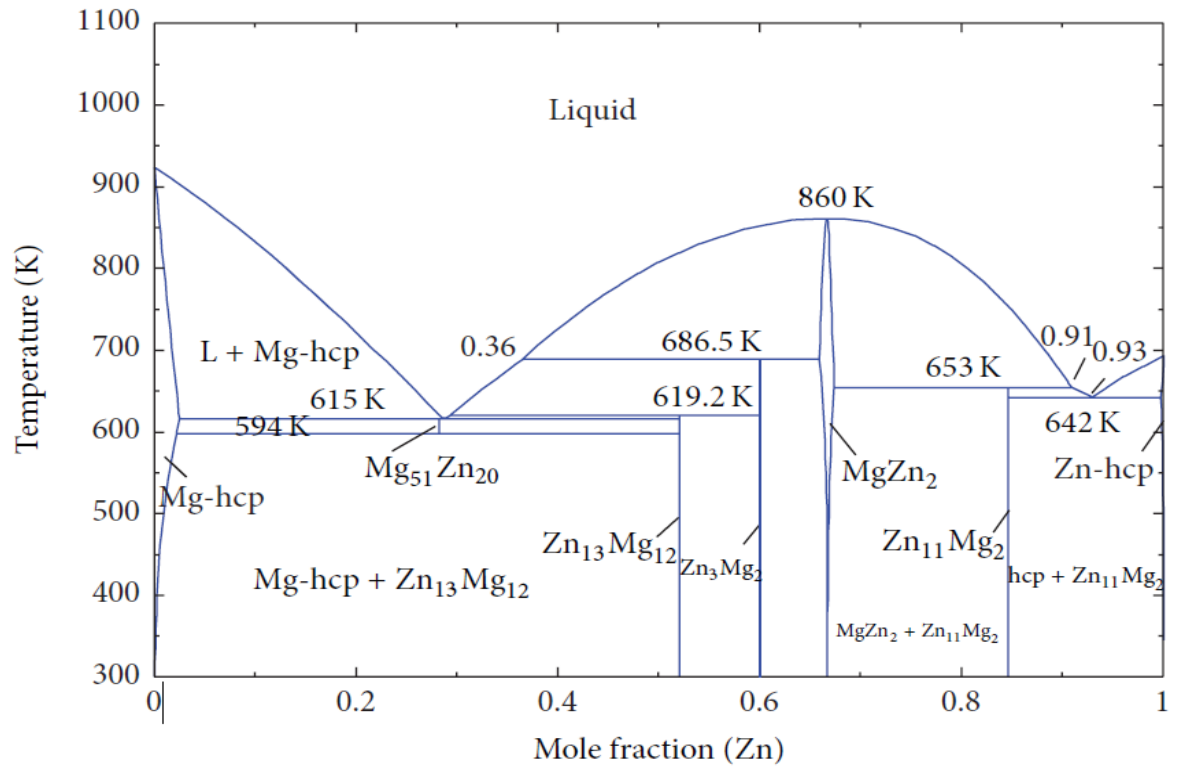


Figure 18: The binary phase diagram of Mg-Zn [126].

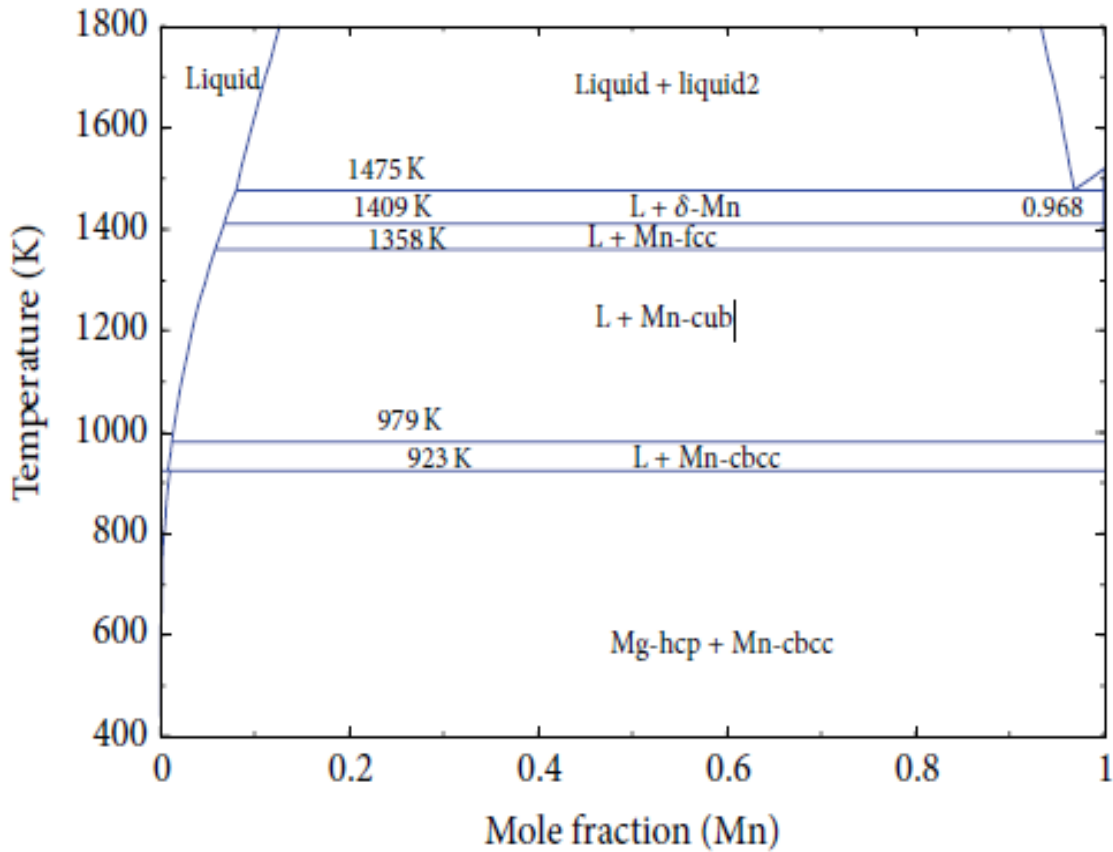


Figure 19: The binary phase diagram of Mg-Mn [126].

Agarwal et al [127] analyzed the previous studies on magnesium alloys and the corrosion performance, biocompatibility, and surface modification. The review concluded that the presents of Zn and Mn increased the corrosion resistance. Furthermore, using polymeric coatings was proved to enhance the corrosion performance of Mg [127, 128]. Yin et al [104] examined adding 1wt. % of manganese to pure magnesium with various amounts of zinc (1-3 wt.%). The grain size of the extruded Mg-1Mn was reduced from 12  $\mu\text{m}$  to 4  $\mu\text{m}$  with an addition of 3 wt.% Zn. However, the alloying system of Mg-1Mn-1Zn showed the best corrosion behavior. In addition, other studies confirmed that using heat

treatments and other processing methods such as extrusion process improves the mechanical properties, corrosion resistance, and prompts more homogeneous structure [26, 104, 129, 130].

The degradation of Mg-Zn-Mn alloying system was further examined and monitored in vivo studies over different post-implantation time periods. Mg-1.0 Zn-0.8 Mn alloy devices were implanted into the femora of lab rats. The degradation rate of the alloy was found to be more in the zone of the marrow channel than in the cortical bone. The formation of new bone tissue was observed around the implant (the degradation zone) after six weeks, and no fibrous capsule was noticed. The magnesium calcium phosphate was detected on the interfacial surface, and two layers were formed with many fibroblasts on the side of the new bone tissue. The formed tissues were connected firmly through the layers to the implantation device. The formation of the new bone and interfacial layer and membrane were found to be continued after 10 and 26 week with no increase in the membrane thickness of 10-30  $\mu\text{m}$ , as shown in [Figure 20](#) [131, 132].

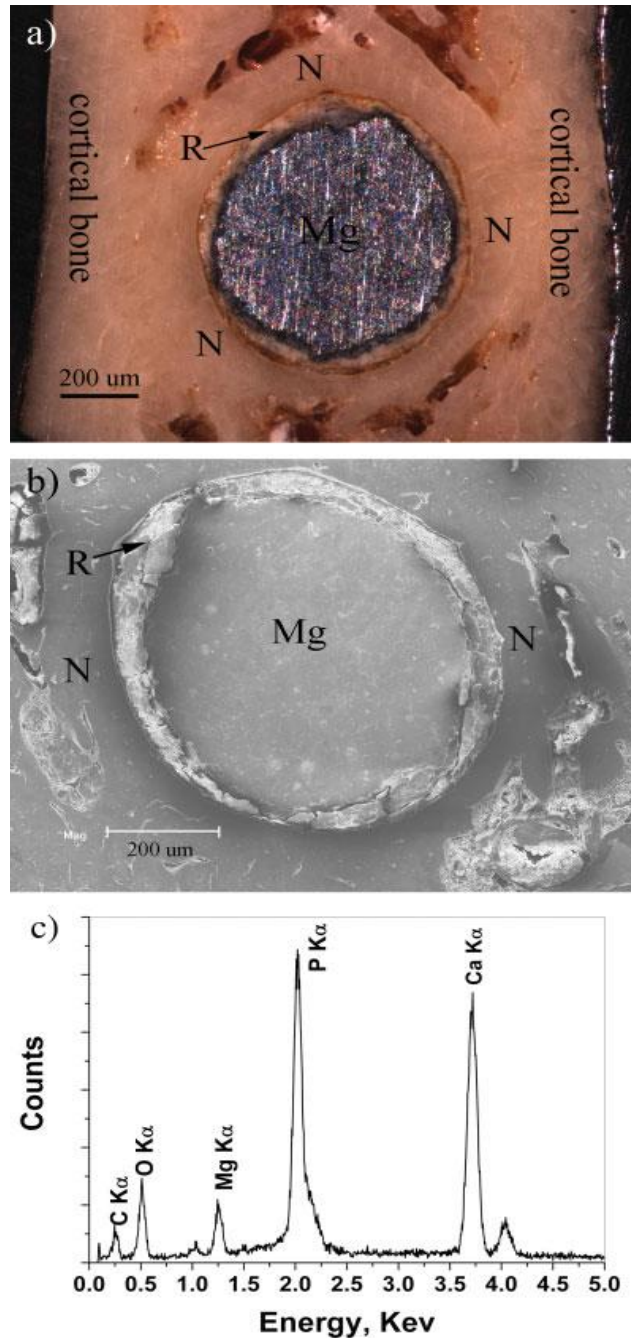


Figure 20: The microstructure of Vivo interaction of Mg-Mn-Zn alloying system as implants with the host after 10 weeks of the implantation. The tagged area “N” represents the new bone tissue and “R” is the interaction layer between the implant and the biological surrounding (a) Optical microstructure of the implant and the biological surrounding (b) SEM microstructure of the implant and the biological surrounding, and (c) EDS analysis on the interface phase. [131].

Figure 21 illustrates the microstructure of Vivo interaction of Mg-Mn-Zn alloying system as implants with the host after 9 weeks and 18 weeks of the implantation. There was no detected disorder in the liver or kidneys, however, a minor change in the blood composition was found. Other composition of Mg-1.2Mn-1.0Zn was studied using the same parameters, and the study investigated the post-implantation stage of over 9, 15, and 18 week. The histology test showed there in no difference in the microstructure between the newly formed bone and the cortical bone. The degradation zone was found to consist a high concentration rate of Ca in addition to P, O, and Mg after 9 weeks, and 10-17% of Mg was degraded with no inflammation. After 15 weeks, no change in serum magnesium or kidney disorder was detected. 54% of the implant was degraded after 18 weeks and homogeneous distribution of the degraded alloying elements in the area of interest which indicates the sufficient absorption of the element during the healing process [131, 132].

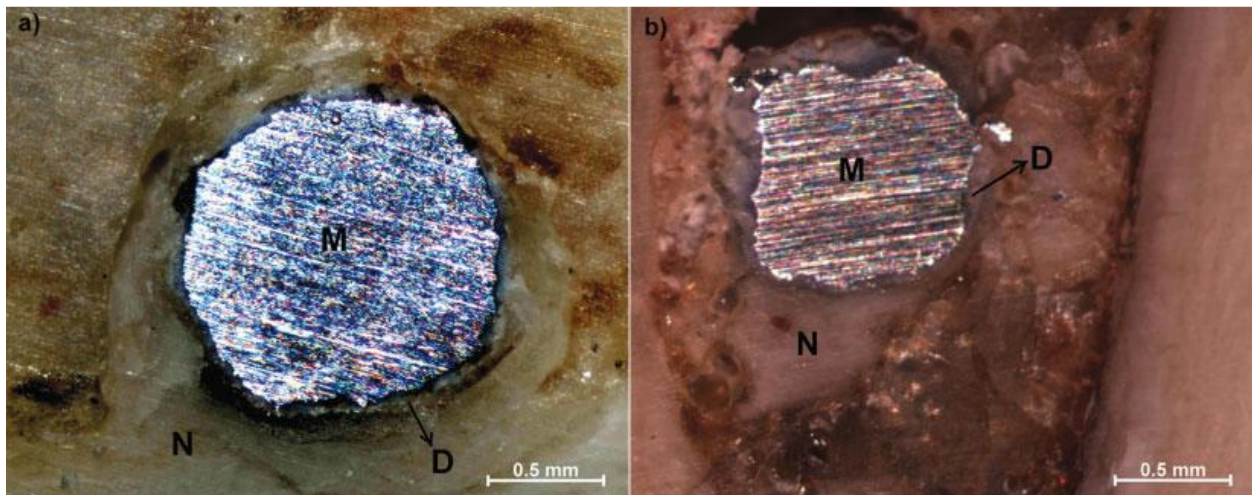


Figure 21: The microstructure of Vivo interaction of Mg-Mn-Zn alloying system as implants with the host. The tagged area 'N' represents the new bone tissue, 'D' is the degradation area due to the interaction between the implant and the biological surrounding, and 'M' is the implantation devise Optical images

*of the cross-sections of Mg-Mn-Zn implants and bones. (a) after 9 weeks of the implantation (b) after 18 weeks of the implantation [132].*

Huang et al [133] investigated the phase equilibria of the Mg-Mn-Zn system at 320 °C by using X-Ray Diffraction (XRD) and Electron Probe Microanalyses (EPMA). It was stated that adding manganese reduces the grain size and corrosion rate. Meanwhile, the addition of zinc significantly increased the creep strength and castability. It was reported for Mg-1Mn-6Zn alloy the formation of  $Mg_{21}Zn_{25}$  phase with phase composition of 0.0% Mn and 48.8% Zn, and the formation of  $MgZn_2$  phase with phase composition of 6.8% Mn and 52.7% Zn. [Figure 22](#) shows an isothermal section for the ternary system of Mg-Mn-Zn at 320 °C.

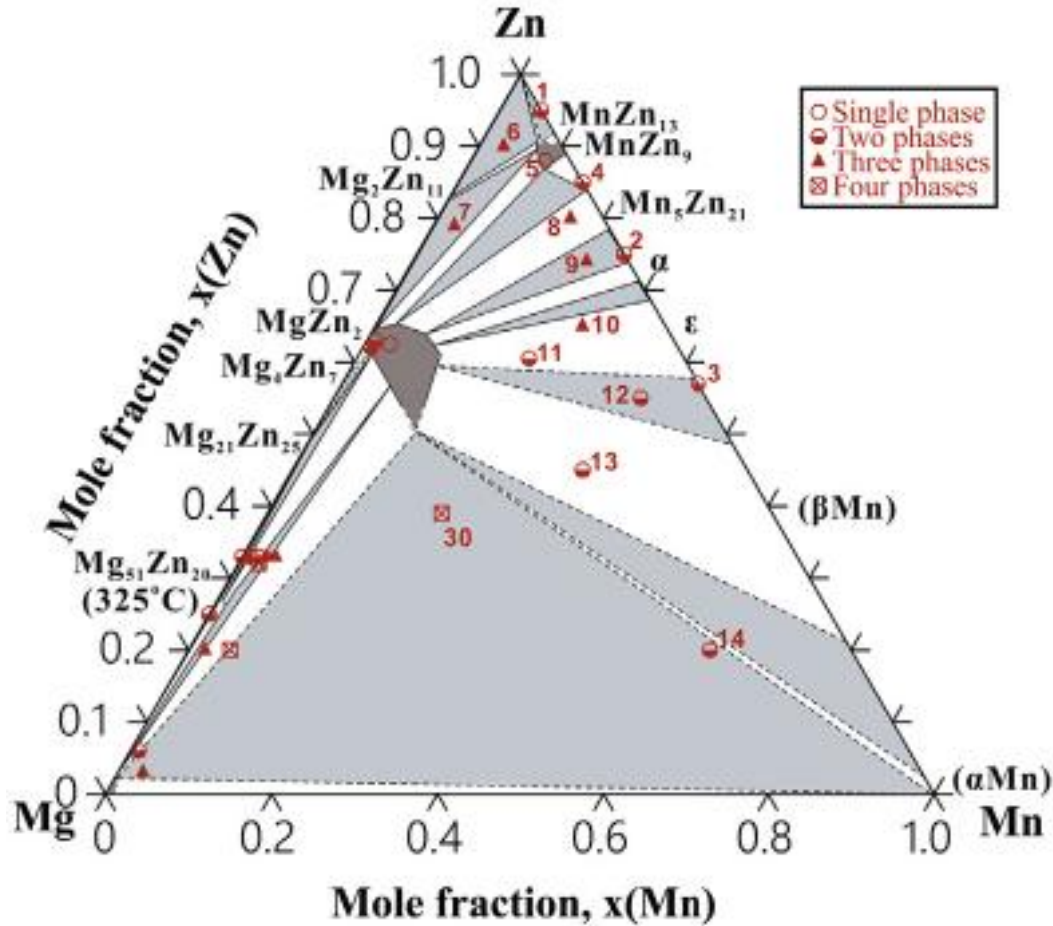
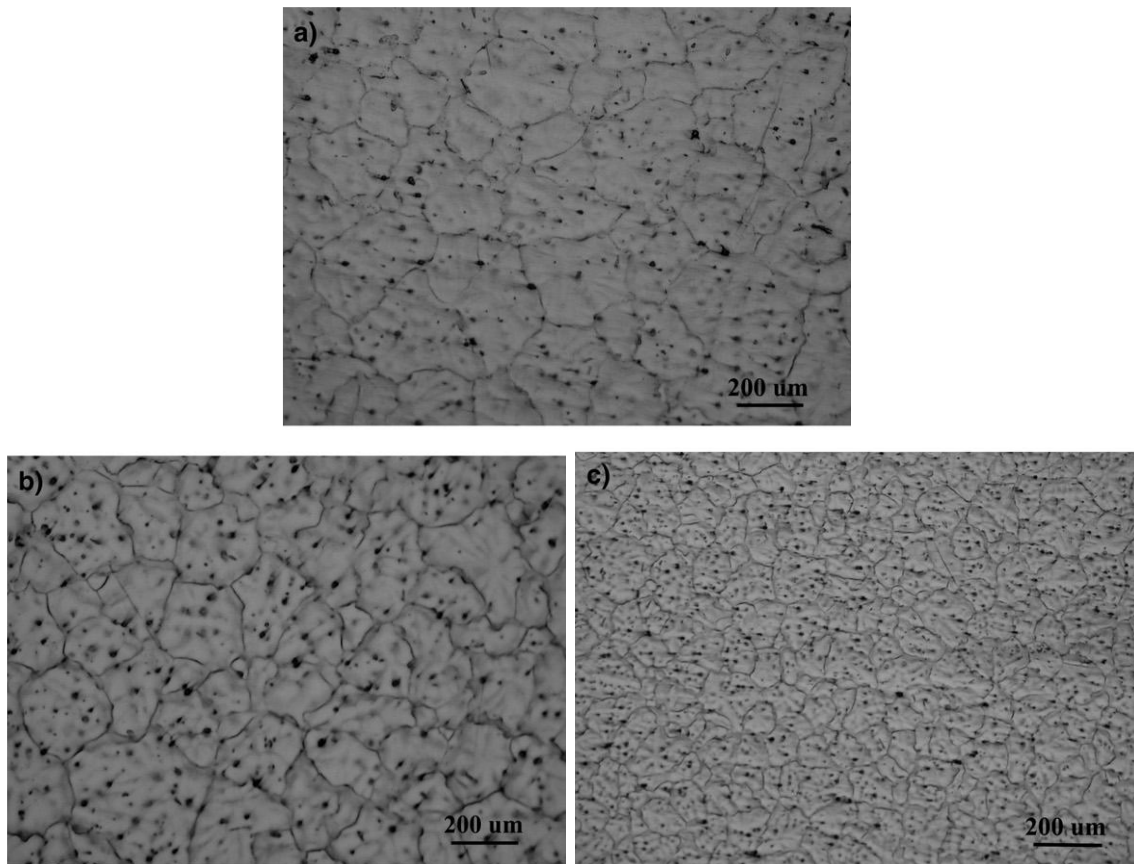


Figure 22: Isothermal section for the ternary system of Mg-Mn-Zn at 320 °C [133].

Zhang et al [25] tested the effect of adding different amounts of zinc (1, 2, 3 wt.%) on the microstructure, mechanical properties, corrosion resistance, and biocompatibility of Mg-1Mn alloying system with a small amount of Aluminum (<0.3wt.%) for as-casted and as-extruded samples. It was stated that increasing Zn content in as-cast alloys from 1 wt.% to 3wt.% reduced the grain size from 200-400  $\mu\text{m}$  to 50-80  $\mu\text{m}$  and increased yield strength, UTS, and ductility by 54%, 25%, 29%, respectively. The microstructure of the alloys can be seen in Figure 23.

Besides, the cell culture test (L-929) indicated good biocompatibility and no toxicity. However, hemolysis test showed a negative effect when the tested sample was put in contact with blood. On the other hand, the highest corrosion resistance (in SBF at  $37\text{ }^{\circ}\text{C} \pm 1$ ) was reported for Mg-1Mn-1Zn- $<0.3\text{Al}$  alloy; although the longest passivation was noted for Mg-1Mn-3Zn- $<0.3\text{Al}$ , it was claimed that Zn stimulates the formation of a protective film.



*Figure 23: Microstructure of as-cast Mg-Zn-Mn alloying system. (a) Mg-1Mn-1Zn, (b) Mg-1Mn-2Zn (c) Mg-1Mn-3Zn [25].*

Dongsong et al [26] examined the microstructure, mechanical properties, and fracture mechanism of Mg-0.9Mn-xZn (x= 0, 1, 2, 3, 4, and 5 wt.%) with high impurity content of Aluminum (0.2 wt.%). It was found that the grain size was reduced considerably to 50-80  $\mu\text{m}$  with 3% content of Zn in comparison 0% Zn (700-900  $\mu\text{m}$ ). However, further addition did not show noticeable grain size reduction. The microstructure of the alloys can be observed in [Figure 24](#). [Table 5](#) shows that yield strength, ultimate tensile strength, and elongation significantly increased with increasing the Zn content up to 3wt.%, and then decreased slightly with the additions of 4% and 5% Zn, which could be due to the formation of thin (Mg, Zn)-containing phases at the grain boundaries. It was claimed that the formation of these phases promotes the occurrence of a tearing mechanism at the fracture and widens the grain boundaries. Also, (Mg, Zn) and (Mg, Mn, Al)-containing secondary phases were observed to be embedded in the matrix.

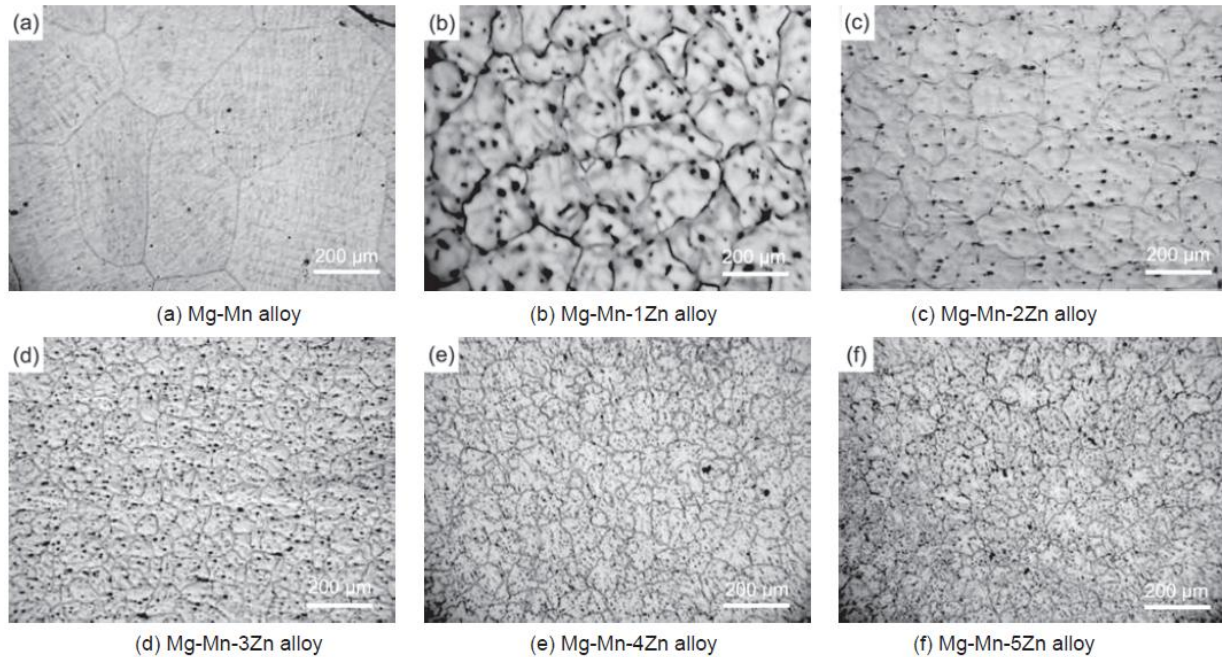


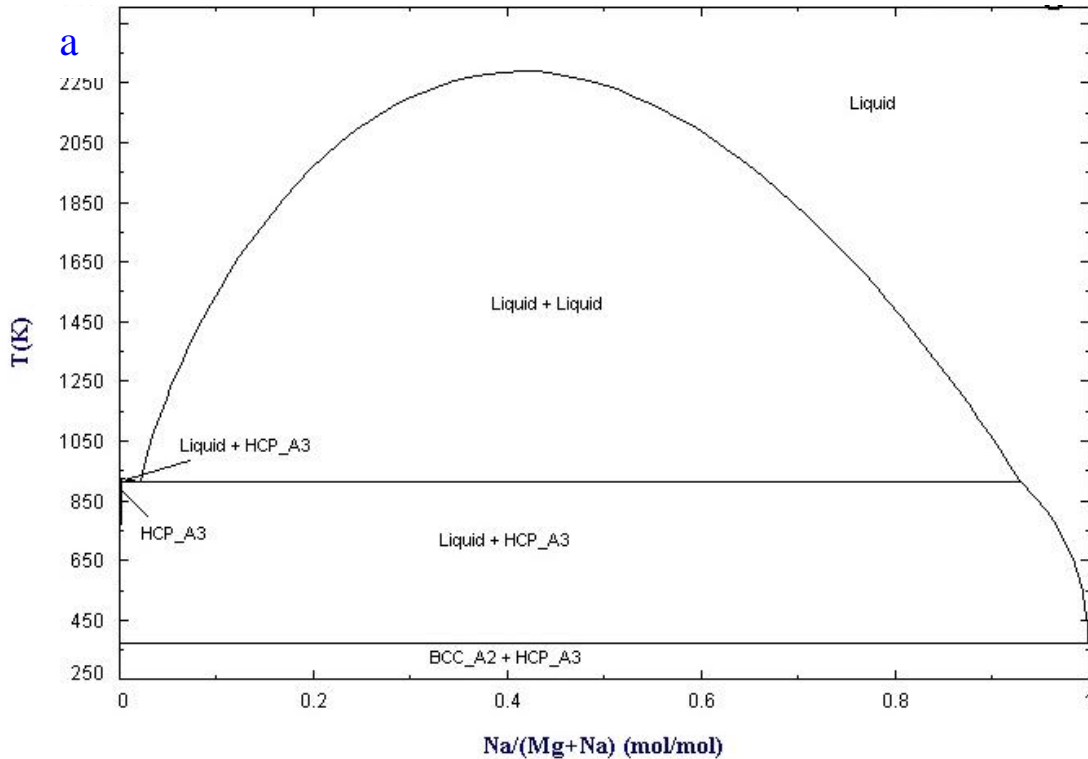
*Figure 24: The microstructure of Mg-Mn-Zn alloying system [26].*

Burkhardi et al [105] worked on analyzing the effect of adding Sodium (Na) and/or Potassium (K) on the corrosion rate and machinability of Mg-Al-Mn-Zn alloying system. Different amounts of each element were added to Mg; the content ranges of Al, Mn, and Zn were (6.5%-11%), (0.2%-0.5%), and (0.5%-1%), respectively. Moreover, the addition of Na and K ranged from 0.5% to 5% separately or simultaneously. It was found that adding Na and/or K formed a protective thin layer, increased the corrosion resistance, and reduced hydrogen evolution significantly. [Table 4](#) presents the generated amounts of hydrogen gas after immersing Mg-8.5Al-0.2Mn-0.5Zn alloy without Na (Alloy I) and with 2% Na (Alloy II) in 100 cm<sup>3</sup> solution of 3% Sodium Chloride, 1% Hydrogen Peroxide, and 0.01 cm<sup>3</sup> Hydrochloric acid. It was concluded that the preferred amount of Na and K was found to be 2%, when added together which can be divided equally. Also, it was stated in the study

that individual additions preferred to be 3% Na or 5% K. Figure 25 lays out the binary phase diagrams of magnesium-sodium, potassium-magnesium, sodium-zinc, potassium-zinc, and potassium-sodium.

Table 4: The generated amount of hydrogen gas for Alloy I (Mg-8.5Al- 0.2Mn—0.5Zn) and alloy II (Mg-8.5 Al- 0.2Mn—0.5Zn-2Na).

Time (min)	Gas Generation (cm <sup>3</sup> )	
	Alloy I	Alloy II
30	12	0.3
60	22	0.4
90	49	0.7



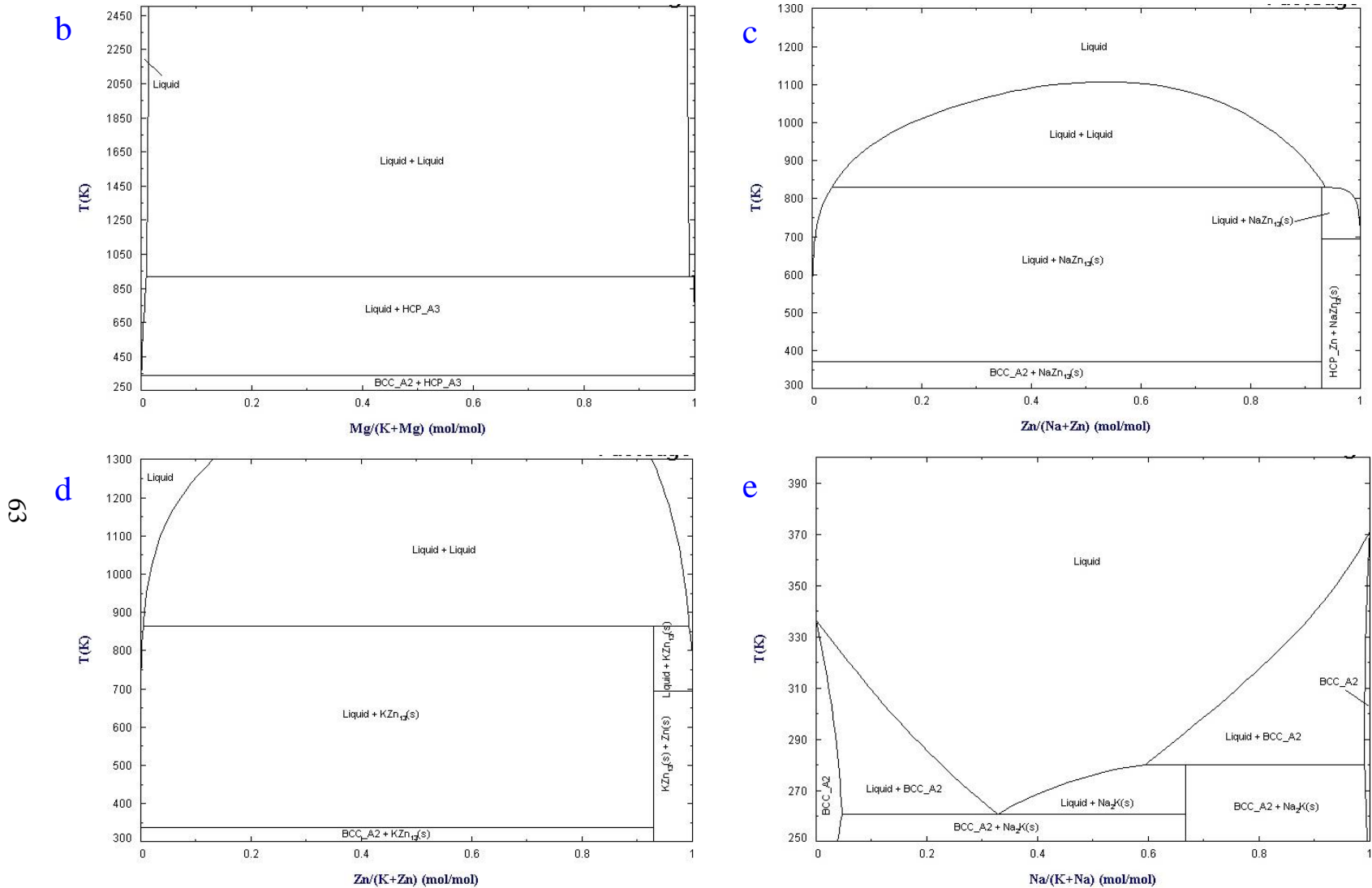


Figure 25: The binary phase diagrams of (a) magnesium-sodium, (b) potassium-magnesium, (c) sodium-zinc, (d) potassium-zinc, and (e) potassium-sodium.

Table 5: Examples of the Mechanical properties and grain size of Mg-based alloys.

Composition	Y S (MPa)	UTS (MPa)	Ductility (%)	Grain Size ( $\mu\text{m}$ )	Reference
Cortical Bone	104.9–114.3	35–283	1.07–2.10	-----	[103]
Pure Mg	20.9 $\pm$ 2.3	86.8 $\pm$ 2.5	13 $\pm$ 1.4	-----	[20]
Mg–1Ca	40	73	1.87	-----	[101]
Mg–2Ca	37	50	1.55	-----	[101]
Mg–3Ca	15	40	0.6	-----	[101]
Mg–1Zn	25	140	18	-----	[32]
Mg–6Zn	70	210	16	-----	[32]
Pure Mg	27.5	97.5	7.31	-----	[74]
Mg–2Ca	47.3	115.2	3.05	-----	[74]
Mg–4Ca	34.5	77.4	2.10	-----	[74]
Mg–2Ca–0.5Mn–2Zn	78.3	168.5	7.84	-----	[74]
Mg–2Ca–0.5Mn–4Zn	83.1	189.2	8.71	-----	[74]
Mg–2Ca–0.5Mn–7Zn	45.4	140.7	4.15	-----	[74]
Pure Mg	20.9 $\pm$ 2.3	86.8 $\pm$ 2.5	13 $\pm$ 1.4	-----	[20]
Mg–1Ca	39	105 $\pm$ 4	4.1 $\pm$ 0.5	-----	[20]
Mg–1Ca–1Zn	45	125 $\pm$ 5	5.7 $\pm$ 1.0	-----	[20]
Mg–1Ca–2Zn	52	143 $\pm$ 5	7.3 $\pm$ 1.5	-----	[20]
Mg–1Ca–3Zn	57	160 $\pm$ 10	8.3 $\pm$ 1.0	-----	[20]
Mg–1Ca–4Zn	63	182 $\pm$ 5	9.1 $\pm$ 2.5	-----	[20]
Mg–1Ca–5Zn	65	173 $\pm$ 5	8.2 $\pm$ 0.5	-----	[20]
Mg–1Ca–6Zn	67	145 $\pm$ 5	4.5 $\pm$ 0.5	-----	[20]
Mg–1.2Zn–0.5Ca	60 $\pm$ 3.1	121.3 $\pm$ 5.2	3.2 $\pm$ 0.13	-----	[118]
Mg–1.8Zn–1.1Mn–0.3Ca	60	162	7.5	175 $\pm$ 15	[123]
Mg–2Zn–1.2Mn–0.5Ca	72	188	9	63 $\pm$ 7	[123]
Mg–1.5Zn–1.1Mn–1Ca	80	138	2.8	51 $\pm$ 5	[123]
Mg–4.0Zn–0.2Ca	60 $\pm$ 1.5	185 $\pm$ 15	12.5 $\pm$ 1.5	100–130	[120]
Mg–1Mn–1Zn–0.3Al	44	174	~12	200–400	[25]
Mg–1Mn–2Zn–<0.3Al	~59	~185	~11	-----	[25]

Mg-1Mn-3Zn-<0.3Al	~68	~216	~15.5	50-80	[25]
Mg-0.9Mn-0.2Al	23.0 ± 4.3	89.2 ± 7.6	6.7 ± 1.0	700-900	[26]
Mg-0.9Mn-1Zn-0.2Al	43.6 ± 5.4	174.5 ± 1.5	12.1 ± 1.1	-----	[26]
Mg-0.9Mn-2Zn-0.2Al	58.6 ± 5.7	182.4 ± 6.8	11.0 ± 1.0	-----	[26]
Mg-0.9Mn-3Zn-0.2Al	65.6 ± 0.7	218.0 ± 6.0	15.5 ± 2.0	50-80	[26]
Mg-0.9Mn-4Zn-0.2Al	65.3 ± 2.1	199.6 ± 8.3	11.5 ± 1.8	-----	[26]
Mg-0.9Mn-5Zn-0.2Al	62.2 ± 1.3	194.6 ± 7.5	10.5 ± 1.6	-----	[26]

### 2.3. The Effect of Solidification Rate on Mg Properties

Pang et al [134] investigated the relationship between the cooling rates and the performance of Mg-REE-based alloys. The work tested the influence of low cooling rates (0.7–3.6 °C/sec) on the mechanical properties and microstructure of Mg–10Gd–3Y–0.5Zr. The mold was designed with a gradual tapered shape in various thicknesses to meet the goal of having multiple zones with different cooling rates. A sand casting process was used in this study. Although the difference in cooling rates was not significant, a change in grain size was observed to be from 59 μm to 39 μm with increasing the cooling rate. Subsequently, the strength and hardness were improved due to the effect of refining the microstructure.

Candan et al [135] examined the effect of the cooling rate on the corrosion behavior of AZ91 and AZ91-0.5Ti. Four steps cast iron crucible was used to achieve four zones with different cooling rates of 1.4, 2, 4, and 8 °C/sec for both alloys. Generally, the structure magnesium alloys consists of primary phase and secondary phase or phases, the secondary

phase tends to form a network around ( $\alpha$ -Mg). The secondary phase usually contains nobler elements than the matrix which creates a micro galvanic effect that leads to increase the degradation rate. It was concluded that using a higher cooling rate increases the nucleation rate, reduces the grain size, and disrupts the network of the secondary phase; these modifications cause a better corrosion resistance. Reducing the grain size by adding Ti to create more nucleation sites was more effective than using the selected cooling rates above. Therefore, the corrosion rate was less for the alloys with Ti at same cooling rate. Nevertheless, AZ91-0.5Ti alloy showed slight corrosion improvement at a higher cooling rate.

Izumi et al [136] carried out a study to analyze the effect of various cooling rates on the microstructure and the corrosion resistance of Mg-0.7Zn-2Y alloying system. The study examined five alloys (GC, IC, MS10, MS20, MS40) that were solidified at different cooling rates of  $10^1$ ,  $5.5 \times 10^2$ ,  $1.8 \times 10^4$ ,  $3.5 \times 10^4$ , and  $1.4 \times 10^5$  K/S, respectively. The immersion test was conducted in 0.17 NaCl aqueous solution (pH 6.8) at 298 K to assess the corrosion behavior. [Figure 26](#) shows that the corrosion rate of the alloys was reduced from 34 mm/year for cooling rate of  $10^1$  K/S to 1 mm/year for cooling rate of  $1.4 \times 10^5$  K/S, which is due to reducing the grain size and the formation of a supersaturated single phase of a solid solution. In addition, the slope of corrosion depth was decreased with increasing the cooling rate toward rapid solidification (more than  $3 \times 10^4$  K/S), as shown in [Figure 27](#). It was concluded that the corrosion rate and depth decrease significantly by increasing the

cooling rate due to the reduction in the grain size and the formation of a supersaturated phase.

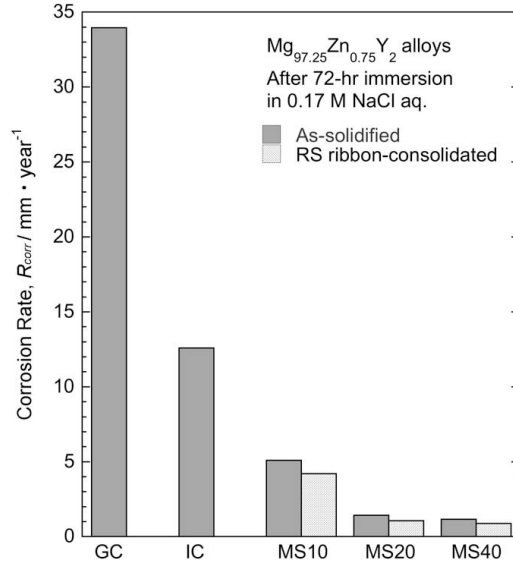


Figure 26: The effect of various cooling rates on the corrosion rates of Mg-0.7Zn-2Y for as-solidified and RS ribbons in 17% NaCl solution with a pH of 6.8 [136].

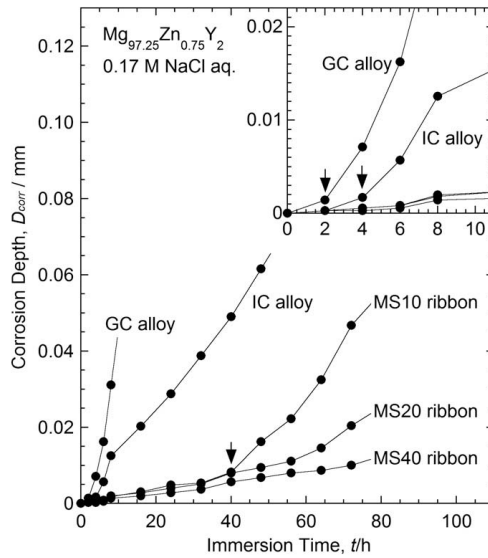
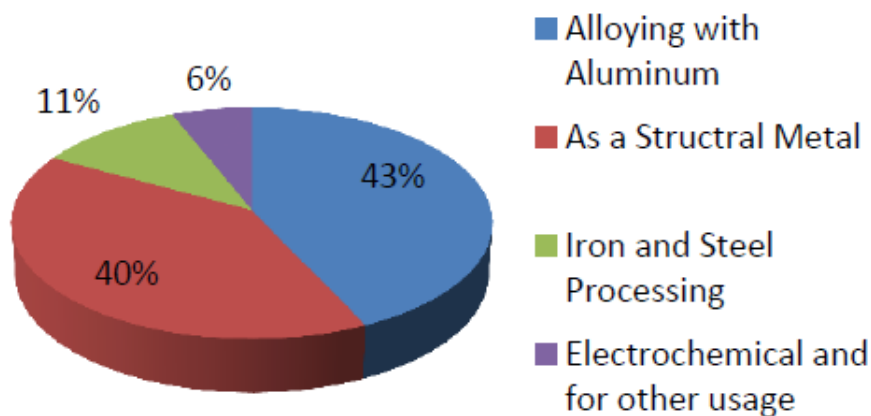


Figure 27: The effect of various cooling rates on the corrosion depth of Mg-0.7Zn-2Y in 17% NaCl solution with a pH of 6.8 [136].

## 2.4. The Economic Impact

The high compatibility and physical properties of magnesium brought the attention of scientist toward using magnesium in biomedical applications. [Figure 28](#) illustrates the usage of magnesium classified by the applications. On a wide scope, Mg has been used widely in industrial applications due to the light weight and abundance of Mg, especially in automotive applications. Reducing the weight of vehicles by using magnesium led to reduce the fuel consumption and consequently the CO<sub>2</sub> emission. Magnesium has 75% and 33% lighter density than steel and aluminum, respectively. [Figure 29](#) lays out the density of Magnesium in comparison with other metals. The annual growth rate of Magnesium between 2002 and 2014 was 6% with demand of 7% widely used in industrial applications such as alloys, fertilizer, refractories, flame retardants, and water purification [137, 138].



*Figure 28: The usage of magnesium in different applications [139].*

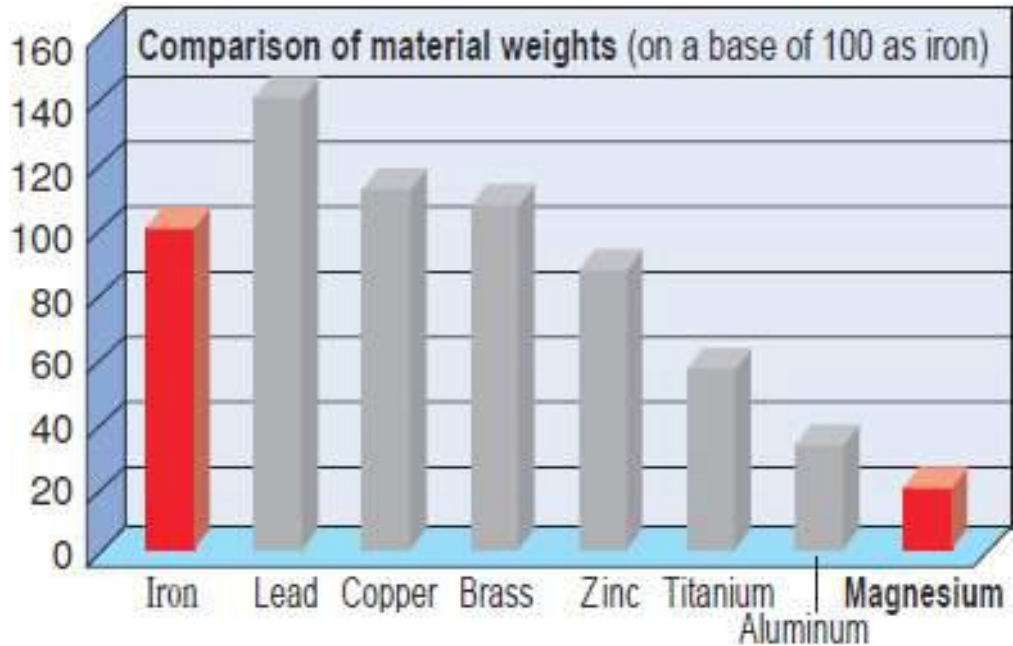


Figure 29: The density of Magnesium in comparison with other metals, based on 100 iron. [137].

Besides the low density, magnesium has a lower cost than aluminum, as shown in Figure 30 [139]. The estimated world market production by USGS of magnesium compounds and metal for 2018 are 29000 and 970 thousand metric tons, respectively. Figure 31 shows the world production of magnesium classified by the producing country [140, 141].



Figure 30: Comparison graph between Mg and Al price [139].

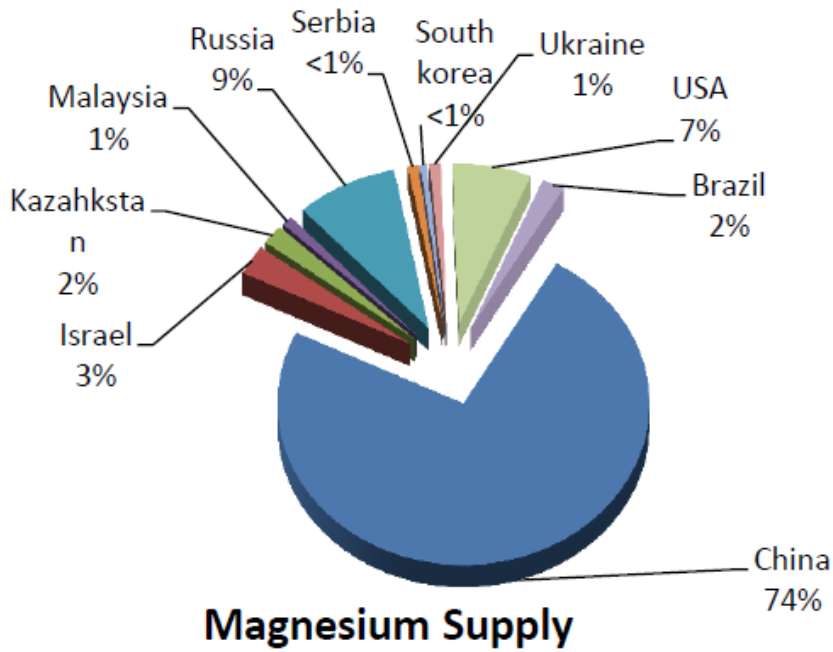


Figure 31: The production of Magnesium [16, 139].

# Chapter 3

## 3. Research

This chapter lays out the research selection process and reasoning, goals and objectives, and the outline of the dissertation.

### 3.1. Research Selection Process and Expectations

Although many Mg alloying systems have been studied, Mg alloys need more work to improve the performance of Mg-based alloys. The current research works on combining effective factors (casting process, alloying systems, and rapid solidification) to promote fabricating an alloy with outstanding properties, a novel alloying system, and processing procedures will be developed for this work.

The selection of alloying elements was based on three screening stages to fulfill the goal of this study of designing a biomedical-biodegradable-nontoxic alloying system with optimum performance. The first stage is selecting elements with good biocompatibility which depends on the toxicity and allowable daily dosage, [Table 6](#) shows the average daily intake of the different alloying elements. The following stages review the effect of alloying elements on the mechanical properties and corrosion behavior, as shown in [Figure 32](#).

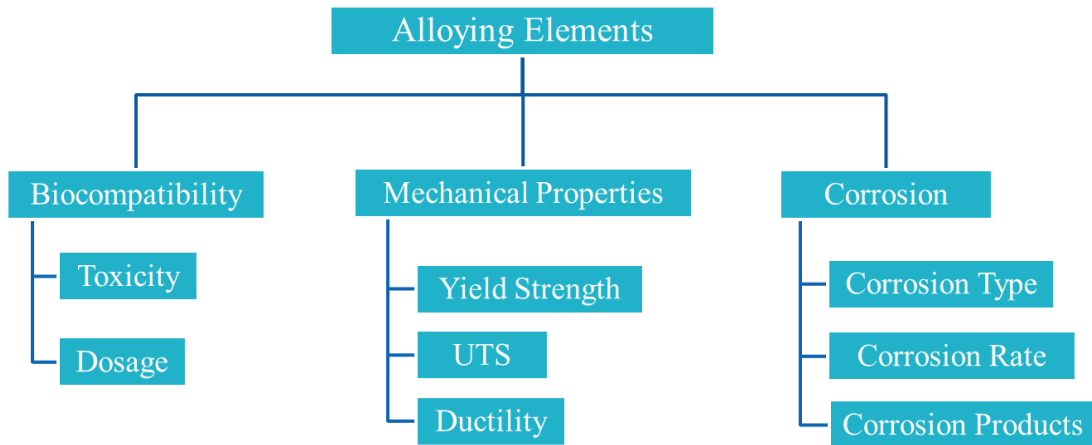


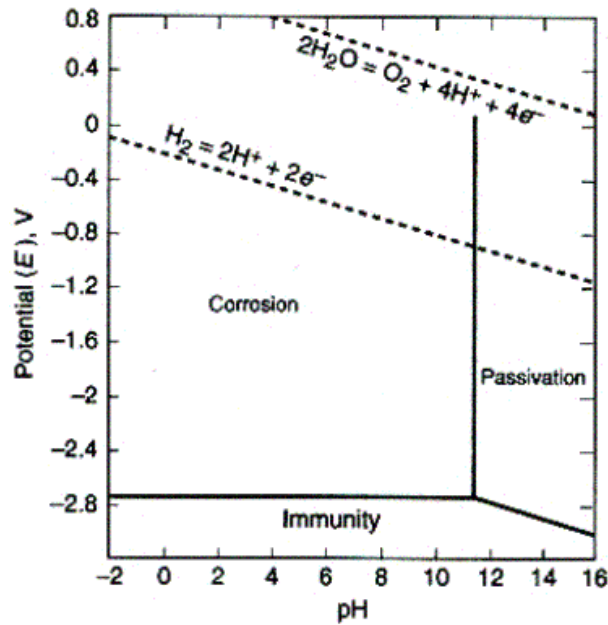
Figure 32: The selection process of alloying elements for designing the alloying systems

Table 6: The allowable daily intake [32, 18, 78, 103].

Element	Daily Allowance (mg)
Ca	800
Mg	240-400
Zn	15
Mn	1.9-4
Na	1200-1500
K	4500-5100
Si	20-50

In this work, two mechanisms are proposed. The first one is adding alloying elements that are not toxic with good biocompatibility and improve the mechanical and corrosion properties. One of these alloying elements is zinc (Zn) that was chosen as a nontoxic element with recommended daily dosage of 8-15 mg/day for adults to be added

to increase the mechanical properties [31, 34, 35, 103]. Another nontoxic element is manganese (Mn) with recommended daily intake average of 1.9-4 mg/day that was picked to improve the corrosion resistance of the alloys by reducing the detrimental effect of impurities, in addition to improving the mechanical properties slightly [5, 18, 78]. Furthermore, sodium (Na) and potassium (K) were selected for this alloying system to improve the corrosion resistance and reduce the hydrogen evolution by producing a protective film on the surface [75, 105]. Although the previous studies did not give any explanation about why adding Na and/or K reduces the corrosion, it is expected that this effect is due to reducing the overall chemical potential of the alloy. The chemical potentials of Na (-2.71) and K (-2.931) are more negative than Mg (-2.372), which drives the alloy toward the immunity zone according to the pourbaix diagram of Mg, as shown in [Figure 33](#). [Table 7](#) illustrates the chemical potentials for the proposed alloying system.



*Figure 33: Pourbaix diagram for Mg and water at 25°C [18].*

Table 7: The standard reduction electrode at 7 pH and 25 °C.

Oxidant/Reactant	Electrode Reaction	$\mathcal{E}^\circ$ (V)
K <sup>+</sup> /K	$\text{K}^+ + \text{e}^- \rightarrow \text{K}$	-2.931
Na <sup>+</sup> /Na	$\text{Na}^+ + \text{e}^- \rightarrow \text{Na}$	-2.713
Mg <sup>2+</sup> /Mg	$\text{Mg}^{2+} + 2\text{e}^- \rightarrow \text{Mg}$	-2.372
Mn <sup>2+</sup> /Mn	$\text{Mn}^{2+} + 2\text{e}^- \rightarrow \text{Mn}$	-1.185
Zn <sup>2+</sup> /Zn	$\text{Zn}^{2+} + 2\text{e}^- \rightarrow \text{Zn}$	-0.7618

The other mechanism of this work is to improve the processing side of making the alloys by reducing the casting defects and using rapid cooling rate to refine the grain size and reduce the segregation, consequently increasing the mechanical properties and reducing the corrosion rate [31, 134, 135, 136]. Besides, using farmable-reactive elements increases the risk factor and jeopardizes the personal safety in addition to reducing the performance and increasing the manufacturing cost of magnesium. Therefore, special

melting, cooling, and preparation processes were designed and built at the University of Wisconsin-Milwaukee to achieve these goals, as shown in [Figure 43](#) and [Figure 44](#).

## 3.2. Goal and Objectives

The goal is developing a novel magnesium alloying system with an appropriate mechanical integrity and acceptable corrosion behavior, in addition to satisfying the biocompatibility aspect that is essential for biomedical-biodegradable applications to avoid potential toxicity. The objectives for this research are as follows:

- 1- Selecting nontoxic alloying elements with suitable intake dosage to reduce the toxicity and infection and enhance the biocompatibility.
- 2- Eliminating the processing defects such as porosities and inclusions that can occur during casting process by developing a new closed-system and procedure for casting.
- 3- Reducing the micro segregation by using rapid solidification.
- 4- Studying the effect of the cooling rates and the alloying elements on the corrosion rate and the mechanical properties.
- 5- Studying the combined effect of cooling rate and alloying elements on the corrosion rate and the mechanical properties.
- 6- Studying the effectiveness of shifting the overall chemical potential of the alloy to enhance the interaction with the environment by using elements that have a higher electronegative.
- 7- Studying the correlation between the microstructure of each composition and the performance to assess the dominant factors.
- 8- Studying the interaction between the alloying elements to assess the overall performance of each alloying system.

### 3.3. Outline of the Dissertation

The background of magnesium and the motivation of this research are mentioned in the first chapter, along with the introduction and the use of magnesium in different applications. The literature review on magnesium alloying systems and biomedical applications is covered in chapter 2. The literature review is divided into four main sections: Mg corrosion, Mg alloying systems, the effect of solidification rate on Mg properties, and the economic impact. The section of Mg corrosion is subdivided into the subsections: corrosion products, the effect of impurities, and the corrosion environments. Chapter 3 includes the research selection process and expectation, goal and objectives, and outline of the proposal. Meanwhile, the research methodology is illustrated in chapter 4, in addition to the design of experiments and various characterization methods to evaluate the microstructure, the composition analysis, mechanical properties, and corrosion behavior.

The materials and samples preparation are illustrated in chapter 5. The first section of chapter 5 discusses the alloys, developed casting system and its procedure, along with the grinding and polishing procedures. The effect of solidification rates and adding the selected alloying elements at different concentrations on the performance of the systems are investigated in that chapter. The second section covers the results and discussion where different types of properties are analyzed thoroughly. These examined properties are: microstructure, impact and fracture mechanism, hardness, tensile and fracture mechanism,

microstructural topography and composition, and corrosion. Chapter 6 covers the conclusion of the research and future work.

# Chapter 4

## 4. Research Methodology

Figure 34 illustrates the layout of the research methodology that was developed for this work. After the selection process of alloying systems, two sets of experiments were designed to study the effect of various factors. Then, the fabrication of the alloys will be followed by four main characterization methods to determine the mechanical properties, corrosion performance, microstructure, and composition of the alloying systems.

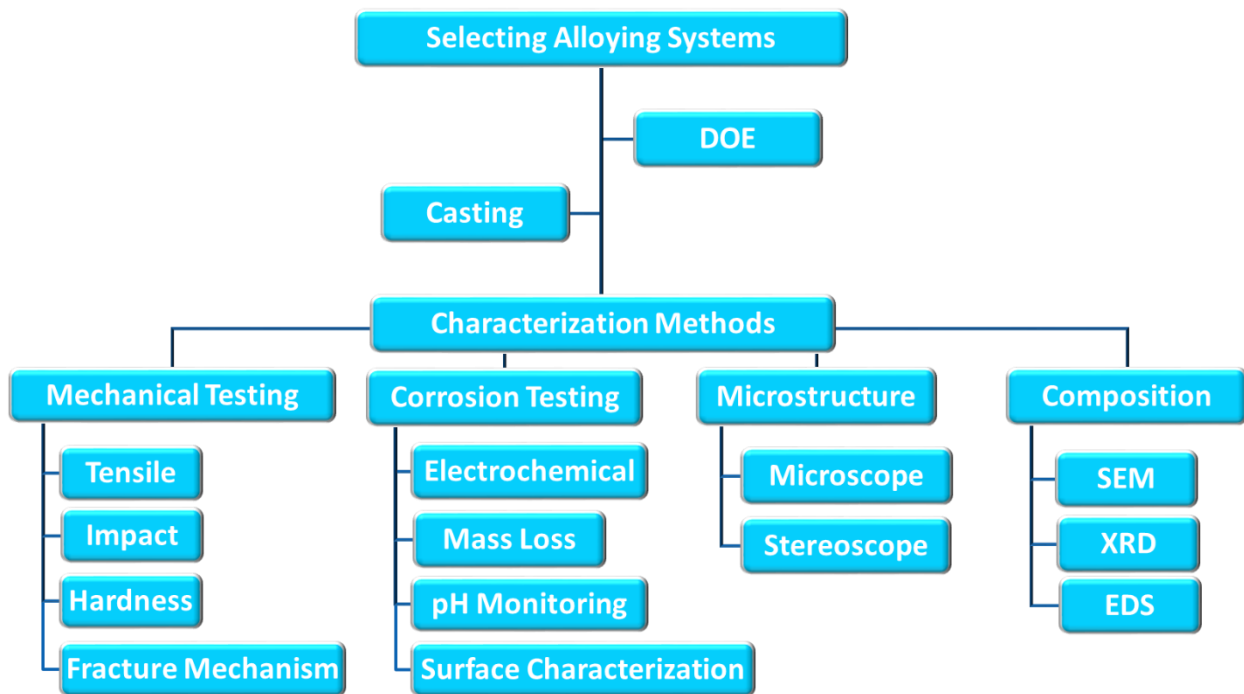
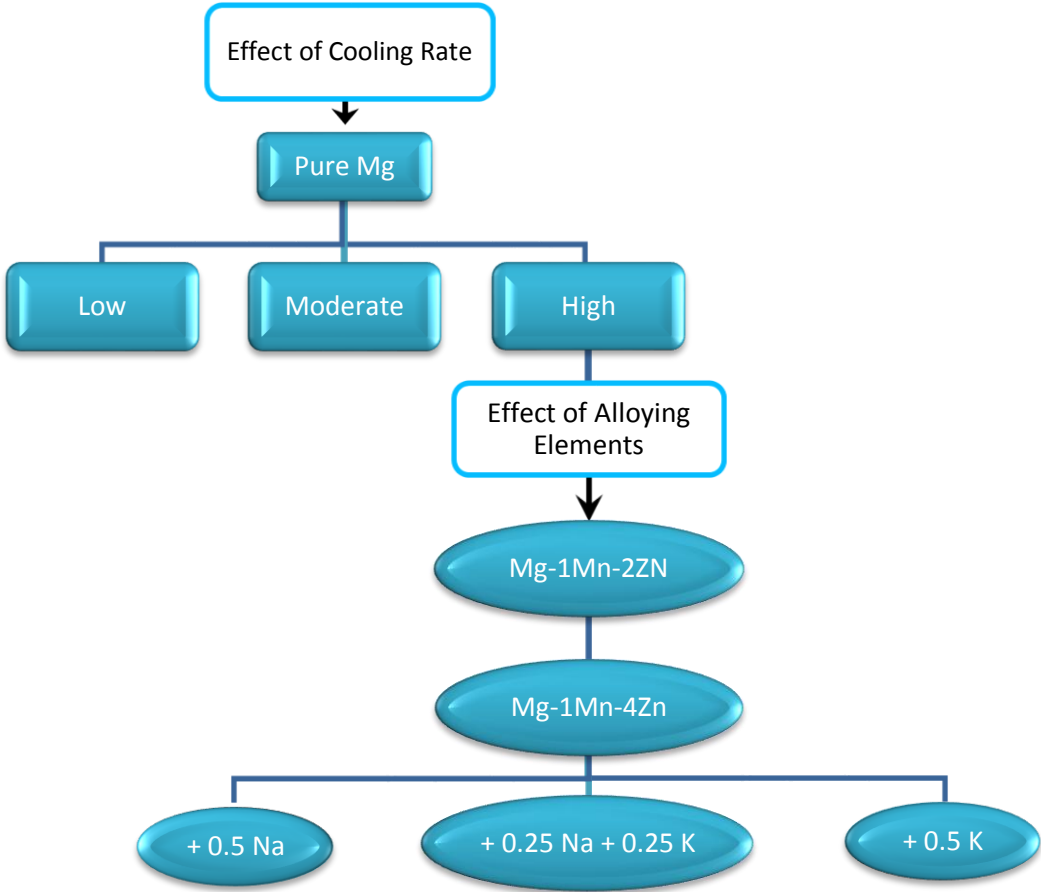


Figure 34: Research methodology chart.

### 4.1. Design of Experiment

The study is designed to analyze the effect of two main factors: the effect of cooling rates and alloying elements. The alloying element are also divided into two parts. In order to examine these parameters, different variables for each factor were selected based on the literature review. [Figure 35](#) illustrates the Design of Experiment for the research.



*Figure 35: Design of Experiment Chart.*

The purpose of the first set of experiments is to examine the influence of solidification rate on the microstructure, mechanical properties, and corrosion behavior of pure magnesium. Various cooling rates were chosen to examine the effectiveness of the variables on pure magnesium. [Table 8](#) shows three cooling rates: low cooling rate of 0.035°C/sec that was done in a closed-insulated furnace; the medium cooling rate of 0.074 °C/sec was carried out in a tube furnace with uninsulated-ends (moderate cooling); and a rapid solidification by liquid CO<sub>2</sub> with cooling rate of 13.5 °C/sec.

*Table 8: Design of Experiment for studying the effect of solidification rates*

	Cooling Rate (°C/Sec)		
Pure Magnesium	Low	Moderate	High
	0.035	0.074	13.5

After reviewing the influence of alloying elements on the performance of Mg-based alloys, as it was discussed in the literature review, a set of alloying elements were chosen to be investigated. The proposed alloying elements are expected to promote the mechanical and corrosion characteristics, where each element is assigned to contribute to a segment of the overall enhancement of the properties. The chosen alloying elements are presented in [Table 9](#).

*Table 9: The properties of the alloying system*

Element	Crystal Structure	Atomic Radius (A)	Melting Temperature (°C)	Boiling Temperature (°C)	Density(S) (g/cm <sup>3</sup> )	Density(L) (g/cm <sup>3</sup> )
Magnesium Mg	HCP	1.6	650	1091	1.738	1.584
Manganese Mn	BCC	1.27	1246	2061	7.21	5.95
Zinc Zn	HCP	1.34	419	907	7.14	6.57
Sodium Na	BCC	1.86	97 °C	882	0.968	0.927
Potassium K	BCC	2.27	63 °C	759	0.862	0.828

The experiments were designed to examine the effect of two groups of alloying elements. The first phase is adding manganese and zinc, with 1% Mn and different amounts of Zn (2% and 4%). The main purpose of adding Zn is to increase the mechanical properties of the alloy in addition to the minor positive effect on the corrosion behavior. Since the improvement in mechanical properties can be obtained with maximum content of 4% zinc, the DOE was designed to confirm zinc content range of 2% to 4%. Additionally, the study considers the influence of rapid solidification on the alloys' performance. The second phase is adding 0.5% of sodium and potassium separately and simultaneously to the first group of elements to examine their effect on the corrosion behavior of Mg alloys. [Table 10](#) illustrates the proposed alloying systems. It is worth mentioning that an alloying system of Mg-1Mn-4Zn-4Na was found to be highly reactive and fragile, as shown in [Figure 36](#).



Figure 36: The Mg-1Mn-4Zn-4Na-as cast alloying system.

Table 10: Design of Experiment for studying the effect of alloying elements.

Alloying System	Alloying Element %			
	Manganese (Mn)	Zinc (Zn)	Sodium (Na)	Potassium (K)
Mg-1Mn-2Zn	1	2	—	—
Mg-1Mn-4Zn	1	4	—	—
Mg-1Mn-4Zn-0.5Na	1	4	0.5	—
Mg-1Mn-4Zn-0.5K	1	4	—	0.5
Mg-1Mn-4Zn-0.25Na-0.25K	1	4	0.25	0.25

## 4.2. Characterization Methods

In order to study the effect of adding alloying elements and the cooling rate on the microstructure, mechanical Properties, and corrosion behavior of the alloys, several types of samples were made to be analyzed by various testing methods. The tests were run on

the samples by using the facilities of UW-Milwaukee at the College of Engineering and Applied Sciences. These tests are as follows:

#### 4.2.1. Macrographic and Micrographic Characterization

This type of characterization methods were used to observe the surface features and microstructure and analyze failure mechanisms of the samples. These testing methods are as below:

##### 4.2.1.1. Stereoscope

Stemi 2000-C stereoscope from Zeiss equipped with Axiocam ERc 5s microscope camera equipped with acquired flexibility and 5 megapixel color imaging capability, located in EMS W308. This instrument was used to analyze the fracture mechanism for impact, tensile, and monitor the corrosion samples pre-testing and post-testing. Also, a digital camera was used for imaging and recording the casting and solidification processes.

##### 4.2.1.2. Optical Microscope

Axio vert A1 from Zeiss is equipped with a Axiocam MRc5 with 12 different acquisition modes and 5 megapixels resolution for images, the microscope is located in EMS W308. The instrument was used to measure the grain size and observe the microstructure of the alloying systems, with range of magnification between 50x to 500x with/without polarization. The samples were taken from different locations of each casting. The grain size was determined according to ASTM standard E112-G6.

## 4.2.2. Structure and Composition Characterizations

In order to investigate the properties and understand the behavior of the alloys, the samples were analyzed by using more advanced techniques. This series of tests was designated to pinpoint the composition and distribution of the phases and surface morphology. These techniques are as below:

### 4.2.2.1. SEM and EDS

JEOL JSM-6460 LV Scanning Electron Microscope (SEM) with Energy Dispersive X-ray Spectrometer (EDS) is located in the AAF EMS 1262. The tool has a high magnification ability up to 50000x and was used to identify the phases and quantify the compositions for the alloys before and after the corrosion tests.

### 4.2.2.2. XRD

The compositions analysis was conducted in X-ray Diffractometer D8 Discovery with Linxeye XE detector from Buker, placed in the AAF EMS 1262. Also, this instrument was used to identify the composition of samples and corrosion byproducts.

## 4.2.3. Mechanical Properties

### 4.2.3.1. Tensile Testing

Tensile properties like yield strength (YS), Ultimate Tensile Strength (UTS), and extension at the break were measured using Instron Bluehill 3365 universal testing

machine, located in the Structural Lab. Four tensile samples were taken from different locations of each casted alloy. The samples were made according to ASTM B557-subsize with a total length of 120mm, thickness of 6mm, grip length (b) of 40 mm, reduced section (G) of 32mm in length, and reduced section of 6mm in thickness, as shown in [Figure 37](#).

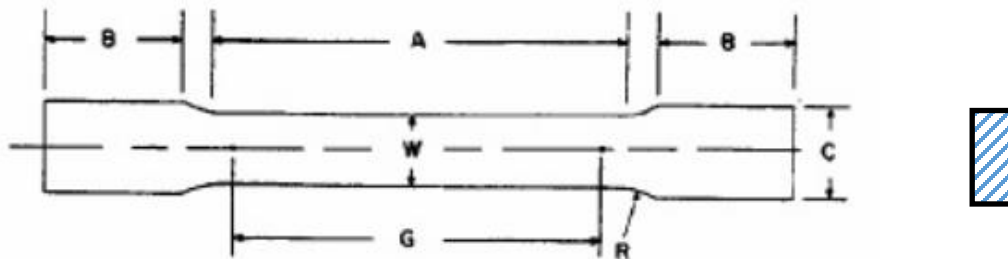


*Figure 37: Tensile specimen geometry*

#### 4.2.3.2. Impact testing

Charpy impact properties were determined using Tinus Olsen impact testing machine (model IT 504), located in EMS B80. The instrument was calibrated with respect to the installed 15 Joule -heavy hammer. Four samples from different locations were machined out and tested for each alloy according to ASTM E23-16b. The dimensions of the samples were 10\*10\*55 mm, and a 45°-V-shape notch was made in the middle of the sample with 2 mm depth, as shown in [Figure 38](#).

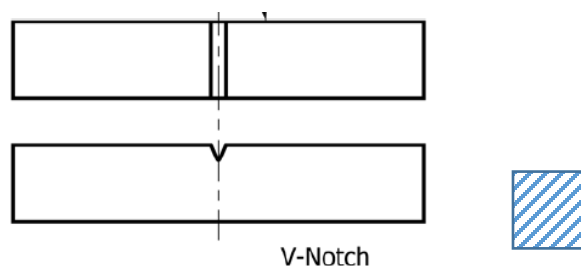


*Figure 38: Charpy impact specimen geometry*

#### 4.2.3.3. Hardness

The hardness of the alloys was measured using Rockwell Hardness tester, digital model Macromet II Twin from Bueler. The test was done depending on the ASTM E-18 standard, where a scale H with 1/8” Ball indenter made of tungsten carbide was used. The load weight was 60 Kg and the speed control had 5 and 10 sec load time. For assessing the hardness properties, a minimum of 30 readings from different regions of each alloy were recorded.

#### 4.2.4. Corrosion Performance

For better understanding the corrosion behavior of different alloying systems, various types of tests were conducted. These techniques were run with respect to the biological environment of the human body, especially the solution that is often used for orthopedic implantation applications. Hank’s Balanced Salts Solution was used for all the tests, at temperature of 37 °C, with estimated  $\pm 0.1$  and 7.4 pH. The tests are as follows:

##### 4.2.4.1. Mass loss

The degradation rates of the alloys were measured by using the corrosion setup that was specifically developed for this project at UWM. [Figure 39](#) shows the corrosion setup for mass loss test. The setup consists of thermocouples and low rate air supply of 5 cc/min, the sample was submerged in HBSS at 37 °C and 7.4 pH. Additionally, the internal beaker

was equipped with a magnetic stirrer to maintain a homogenous environment and minimize the temperature gradient. The components were assembled in jacketed glass beakers, which were filled with running fluid from a chiller. A highly controlled circulator (polyscience chiller) with temperature stability of  $\pm 0.005^{\circ}\text{C}$  was used to feed the jacketed beakers with circulated fluid in sequence. The temperature of the setup was adjusted tightly through the control probe of the chiller. The samples were shaped in a small disk ( $1\text{cm}^2$  area x 8mm thickness) and only the top face was exposed to the solution by isolating the perimeter and bottom face during the immersion process.

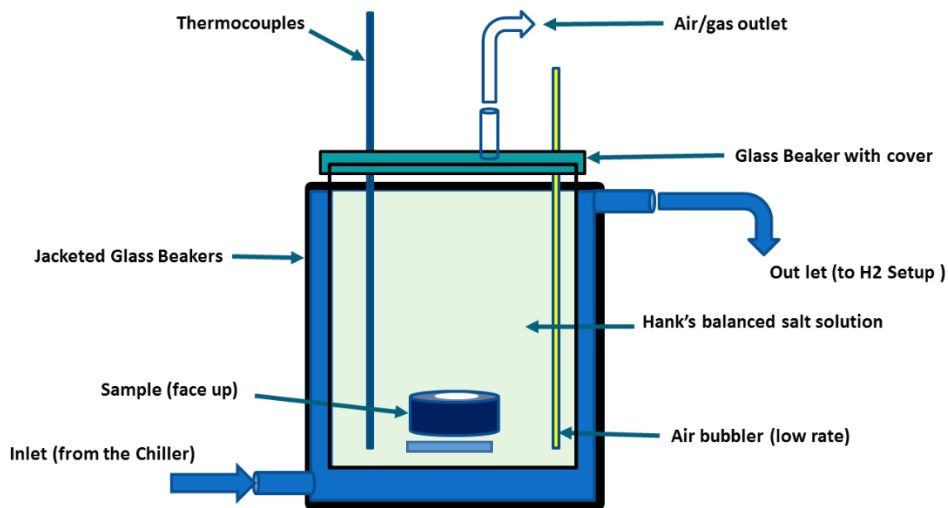


*Figure 39: Corrosion setup for mass loss testing*

#### 4.2.4.2. pH Monitoring

The change in the pH level occurs during the corrosion process of magnesium, which increases with time and pushes the solution toward more basic surroundings. Controlling this variable is important to mimic the bio-environment and lead to accurate data and better understanding of the results. Therefore, adjusting the pH level is needed to maintain the 7.4 pH level by adding CO<sub>2</sub> gas or 1 N HCl solution. Also, it is necessary to provide a continuous circulation of the solution to reserve the homogeneity across the solution.

#### 4.2.4.3. Electrochemical Cell

In order to assess the electrochemical properties of the alloying systems, electrochemical cell testing was conducted. This test can provide important information in regard to the resistance, electrochemical potential, degradation intervals, and corrosion curve shape. The test was conducted on the samples using a SP-300 potentiostat instrument from Biologic with a range of 500 mA to 10 A and built-in EIS.

The samples were machined to small disks with dimensions of 1cm<sup>2</sup> area x 8mm thickness. Additionally, a small hole was drilled on the back of each sample to insert the copper wire, which has the same diameter of the hole. The inserted wire was bent and taped to the back of the sample using a conductive tape. After mounting the samples using waterproof urethane resin (D-85), the resistance of the sample was measured to validate

the conductivity. On the other side, a jacketed electrochemical cell filled with Hank's Balanced Salts Solution was used to run the test. The cell was connected to a circulator chiller to control the temperature, as described above. The setup was designed to have six ports for the reference electrode (Ag/AgCl), thermocouple, pH probe, graphite rod, and air supply (5 cc/min), as shown in

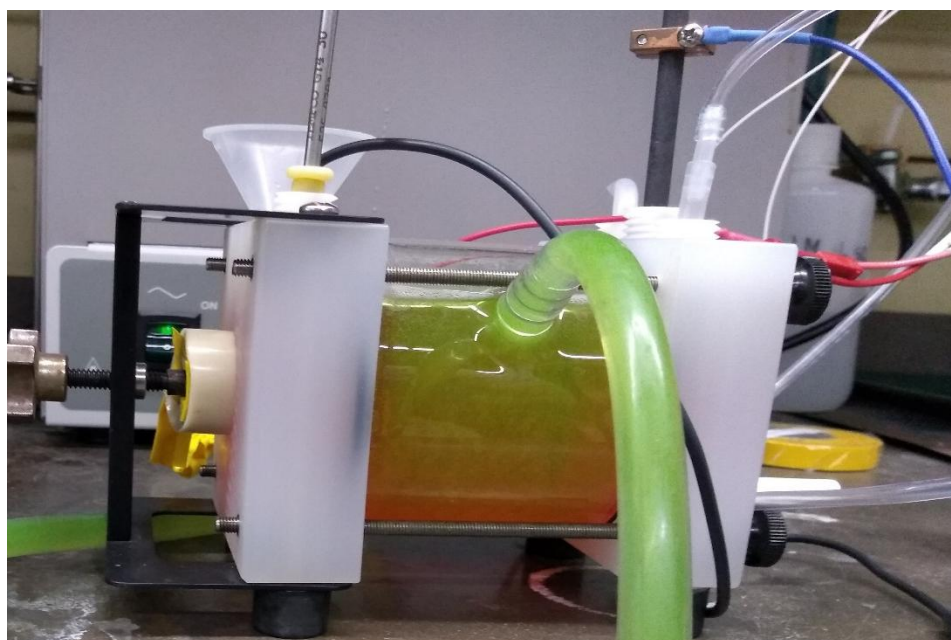
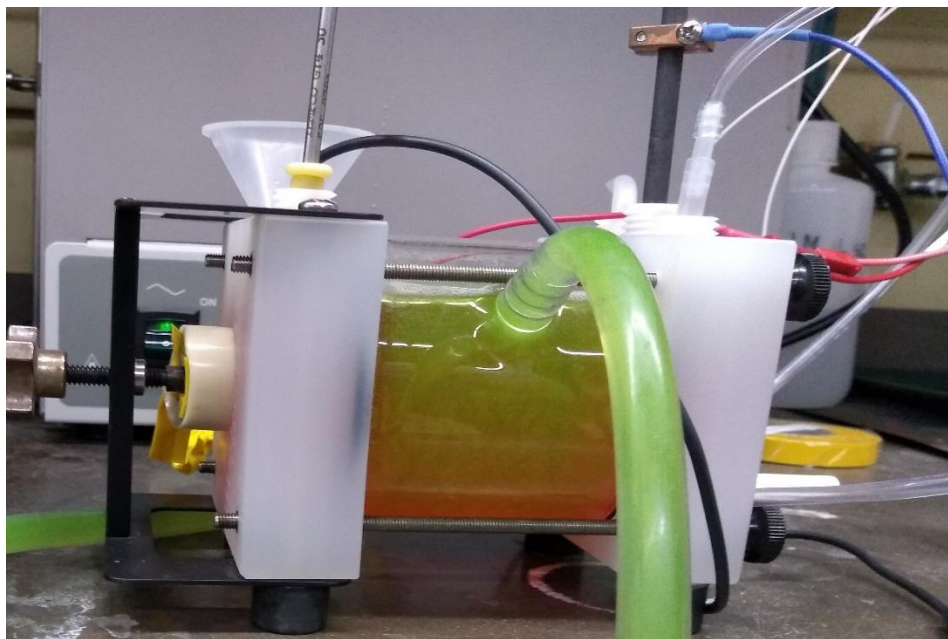


Figure 40.



*Figure 40: The electrochemical cell set up for the potentiostat test.*

# Chapter 5

## 5. Experimental Work

The first section of chapter 5 discusses the alloys, developed casting system and its procedure, along with the grinding and polishing procedures. The effect of solidification rates and adding the selected alloying elements at different concentrations on the performance of the systems are also investigated in that chapter. The second section covers the results and discussion where different types of properties are analyzed thoroughly. These examined properties are: microstructure, impact and fracture mechanism, hardness, tensile and fracture mechanism, microstructural topography and composition, and corrosion.

### 5.1. Materials and Processes

The fabrication process of the alloys was started from raw materials, and several pieces of equipment were used to make the final samples that were needed for the tests. This section also includes information about the materials, manufacturing process, and samples preparation.

## 5.1.1. Materials

### 5.1.1.1. Magnesium

Pure magnesium (99.8%) in the form of rods (1.3”x12”) was purchased from Alfa Aesar and the certificate of analysis was obtained to confirm the impurities contents. The rods were cleaned thoroughly from inclusions and oil traces. [Table 11](#) shows the impurities contents, which were found to be below the tolerance limits according to the literature review.

*Table 11: The impurity content in the purchased magnesium.*

Elements	Content Percentage
Manganese	<0.05
Silicon	<0.05
Cobalt	<0.01
Aluminum	<0.005
Copper	<0.005
Iron	<0.001
Lead	<0.001
Nickel	<0.001
Zinc	<0.001

#### 5.1.1.2. Zinc

Zinc is the main alloying element that was added to Mg alloying systems. Pure zinc rods (99.99%) were purchased from Alfa Aesar. The same cleaning process above was done for this element.

#### 5.1.1.3. Manganese

Due to the positive influence of manganese on the corrosion performance, pure manganese (99.98%) was added to all of the alloys, also purchased from Alfa Aesar. The manganese flakes were washed by isopropyl alcohol.

#### 5.1.1.4. Sodium

Pure sodium metal (99.8%) was purchased from Ward's Science to be added to Mg-based alloys, as planned in the DOE. The pure element was stored in a sealed container filled with oil. Prior to the casting process, sodium element was cleaned of oxides in hot oil bath and then washed by a hexane solution.

#### 5.1.1.5. Potassium

The high purity element was purchased from Alfa Aesar. The element was stored in a sealed container filled with oil. Prior to the casting process, sodium element was cleaned of oxides in hot oil bath and then washed by a hexane solution.

### 5.1.1.6. Hank's Balanced Salt Solution

Sine HBSS is widely used in vitro testing to simulate the environment of living organisms, which was selected for this work. The solution was obtained from Fisher Scientific. The concentration of the solution was 10X and with additives calcium, magnesium, sodium bicarbonate, phenol red, and sodium pyruvate. The solution formulation was consisted of D-Glucose (Dextrose), Potassium Chloride (KCl), Potassium Phosphate monobasic (KH<sub>2</sub>PO<sub>4</sub>), Sodium Chloride (NaCl), and Sodium Phosphate dibasic (Na<sub>2</sub>HPO<sub>4</sub>-7H<sub>2</sub>O). A 1X diluted solution was prepared from HBSS concentrate, in addition to adjusting the pH to 7.4 by adding Sodium Bicarbonate. The dilution process was carried out with respect to the provided protocol from Gibco. [Figure 41](#) illustrates the flow chart of the dilution process of the 10X HBSS to 1X with pH number of 7.4 [142].

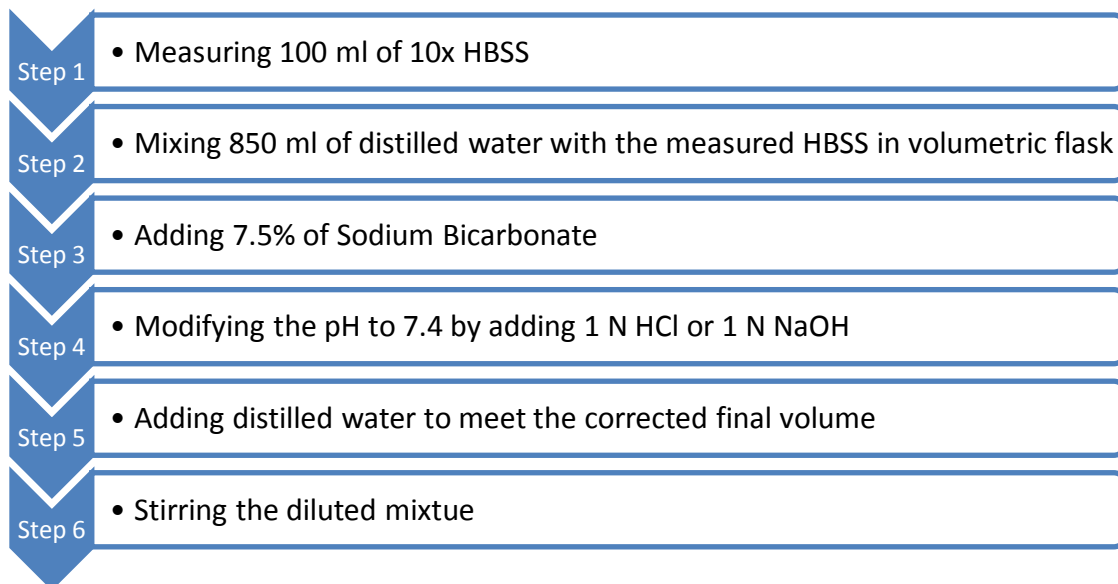


*Figure 41: Preparation chart of 1X Hank's Balanced Salt Solution from 10X.*

## 5.1.2. Samples Preparation

Various fabrication processes were conducted to make the final samples from raw materials. Due to the high sensitivity of magnesium, the developed systems and methods were specifically created to produce quality samples. Therefore, special procedures were developed for this research by using the facilities at the UW-Milwaukee at the College of Engineering and Applied Sciences. This section describes the molding, casting, solidification, grinding, and polishing processes, as below:

### 5.1.2.1. Casting

Due to the high flammability-reactivity and evaporation of magnesium at high temperatures, different methods were applied to control the casting process of magnesium alloys. Mg has a high decomposition rate and this rate increases with increasing temperature in addition to the oxidation that occurs during the process. [Figure 2](#) shows the relationship between the evaporation rate and temperature. Also, the evaporation increases with decreasing the pressure, as shown in [Figure 3](#). Not to mention, other process defects can occur in the castings. Therefore, different casting accommodations have been applied to reduce the oxidation and decomposition of Mg such as casting with flux and under vacuum. However, there are disadvantages for these modifications, like more inclusion traces resulting from using flux and high decomposition rates that occur under vacuum pressure. Additionally, using cover gases could cause negative environmental effects. On

the other side, using traditional methods to achieve rapid solidification compromises the safety due to the high flammability-reactivity of magnesium [44, 45, 46, 47, 48, 143, 144].

In this study, an optimum casting procedure was developed to enhance the fabrication process. The process consists of two parts: melting and solidification. The melting and quenching parts were designed and built by the research group at UWM. The designed system uses a combination of negative and positive pressures both static and dynamic, which can be used for different types of alloying systems, especially flammable-reactive metals with high decomposition rates. The designed system set to achieve four goals, as below.

- 1- Producing a safe and efficient system.
- 2- Reducing the processing defects to attain alloys with optimum properties.
- 3- Reducing the manufacturing cost.
- 4- Improving the environmental efficiency.

These goals can be reached by implementing the following objectives:

- 1- Reducing the interaction with the environment by using a closed system.
- 2- Reducing the oxidation by using inert gas.
- 3- Reducing the decomposition rate by using positive pressure.
- 4- Reducing the inclusions and micro segregation and increasing the mechanical properties by using rapid solidification.

Figure 43 and Figure 44 show the melting and quenching designs that were used for the casting process. The crucibles were made of a low carbon steel (16 " L x 1.75" OD x 1.584" ID x .083" Wall) that were welded (sealed) from one end and plugged from the other (not sealed). Holes were drilled into the plug to hang the crucible to the top of the melting setup. Nevertheless, another crucible was made of pure Mg to contain the alloying elements and to be inserted inside the other big-permanent crucible. The purpose of making the sacrificial crucible (made of pure Mg) was to contain and protect the alloying elements during the first stages of the melting process; at the same time, it was part of the composition, as shown in Figure 42-b.

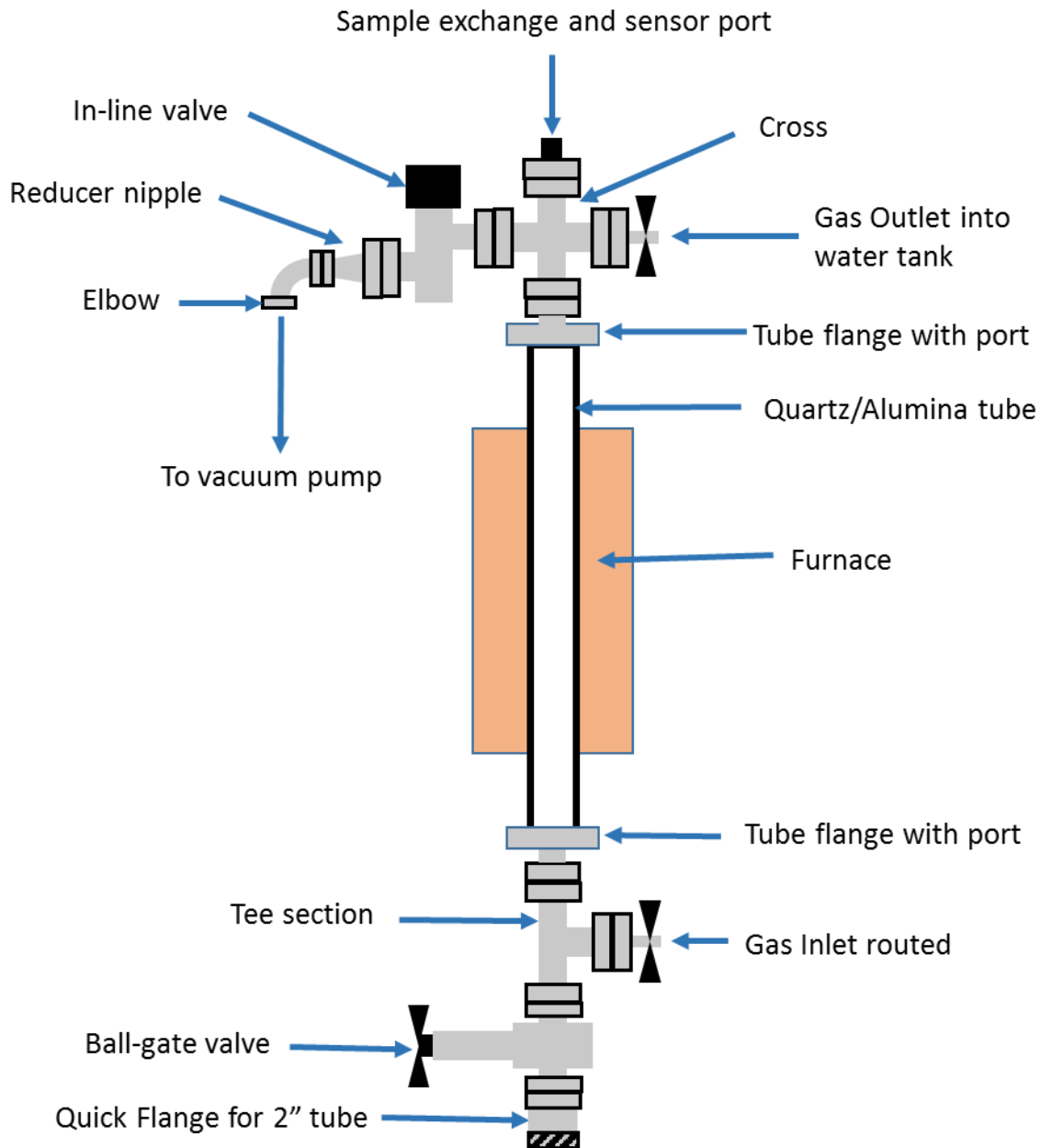


Figure 42: Crucibles that was used to melt Mg (a) low carbon steel permanent crucible(b) Mg sacrificial crucible.

After cold (at room temperature) and hot (at 600 °C) cleanings for the permanent crucibles, the crucibles were also used as molds and were coated with super enhanced Graphite (SEG AEROSOL) and heated in a drying furnace. The process began with sliding the crucible component inside the closed-melting system. The procedure was a combination of applying positive and negative pressures. The first phase was applying vacuum pressure (-0.1 MPa) from room temperature up to 500 °C; during this phase, the

closed-system was flushed with argon gas and vacuumed a couple of times to ensure the purification of the melting process.

This was followed by the second phase, where a positive pressure (0.05 MPa) of ultra-pure argon gas was applied all the way to the set-melting temperature (710 °C). Putting the system under a constant positive pressure serves two goals. The first one is to reduce the evaporation rate and inhibit the reactivity and flammability under the inert gas. The second goal is to enhance the environmental efficiency and lower the operation cost by feeding the system with the inert gas and maintaining the closed system under a positive static pressure. The argon was maintained at that pressure to the end of the melting process. It can be concluded that the system and followed procedure eliminated the oxidation and significantly minimized the decomposition of magnesium during the melting process. Meanwhile, the decomposed amount was found to be significant in the case of subjecting the system to vacuum pressure and high under atmosphere pressure in comparison to the developed procedure.



*Figure 43: The developed closed melting system*

The solidification process was done at three different cooling rates (low, moderate, and high). The low cooling ( $0.035^{\circ}\text{C/s}$ ) was carried out in a closed-insulated furnace, while the moderate rate ( $0.074^{\circ}\text{C/s}$ ) was conducted under argon pressure in the setup above with

uninsulated-ends. The rapid solidification ( $13.5\text{ }^{\circ}\text{C/s}$ ) was achieved by liquid  $\text{CO}_2$  quenching after dropping the crucible down into the developed quenching design that was stationed right under the melting setup. [Figure 44](#) shows the quenching design.

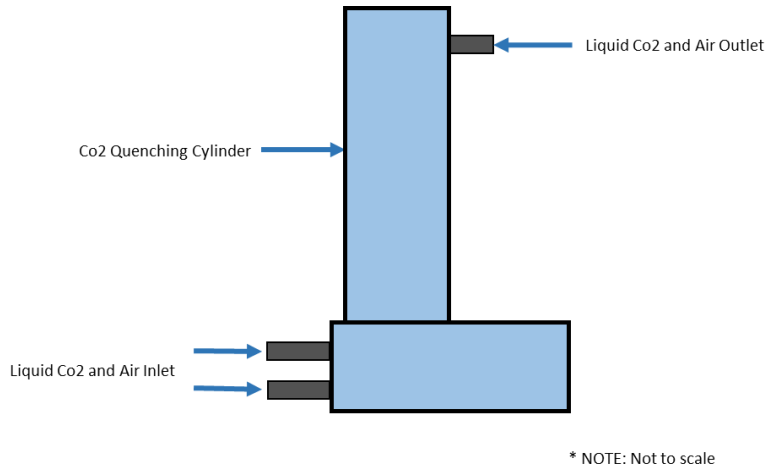


*Figure 44: The developed quenching system*

The developed procedure led to an optimal final casting and eliminated the Mg evaporation and porosity. Also, a homogenous shrinkage pipe was formed at the top of the casting, as shown in [Figure 45](#). Moreover, the established procedure reduced the fabrication cost and risk factor of casting magnesium since Mg has high flammability and oxidation at high temperatures.



*Figure 45: Quenched magnesium casting (a) side-image of Mg casting (1.5" D x 10" L) (b) Shrinkage pipe at the top of mg casting.*

### 5.1.2.2. Grinding and Polishing

The first step in samples preparation was machining various types of specimens with high surface finishing for microstructure, mechanical, and corrosion characterizations. The samples for microstructure, composition, and corrosion analysis needed further preparations including mounting, grinding and polishing. The mounting for microstructure and composition analysis specimens was done in SimpliMet 1000, an automatic mounting press from Buehler. Two types of compounds were used for press mounting: Phenolic powder from ACETechnologies and KonductoMet conductive filled mounting compound. Additionally, a number of samples were mounted manually using water proof urethane (D-85) for corrosion tests.

Since magnesium is very soft physically and highly reactive in water, the samples were briefly exposed to water during the grinding process with different grades of SiC paper including 400, 600, 800, and 1200. The grinding process was followed by a polishing stage with a mix of 1  $\mu\text{m}$  Alumina powder and water for a very short time due to the fast degradation of Mg. However, the samples required more surface finishing and further polishing in a vibratory polisher (ViboMet 2 from Buehler). Using Alumina/Colloidal Silica slurries caused severe surface damage and deep corrosion on the surface. Therefore, a recipe was developed for the vibratory polishing stage, which consists of 200 ml polishing

oil and 0.5g of Al<sub>2</sub>O<sub>3</sub> powder (0.05 μm). The developed mixture produced a clear polished surface and no degradation signs at all even after polishing for a long time.

## 5.2. Results and Discussion

### 5.2.1. Microstructure

The microstructure imaging was conducted after etching the polished samples with a modified etchant solution with a composition of 24ml of distilled water, 75ml ethylene glycol, and 2ml of nitric acid for 1 minute [145]. The microstructure of pure magnesium and the alloying systems were analyzed in order to measure the grain size, observe the structure of phases, and determine the effect of different cooling rates and the alloying systems.

The average grain size of pure magnesium that was slowly cooled in a completely insulated furnace (0.035 °C/Sec) was found to be 4235 μm, as shown in [Figure 46 \(a\)](#). The moderate cooling rate (0.074 °C/Sec) was achieved by cooling the casting in an uninsulated-ends furnace and was found to be 2257 μm, as shown in [Figure 46 \(b\)](#). The grain size of quenched pure magnesium in liquid CO<sub>2</sub> was decreased significantly to an average range of 6 μm to 12 μm, as shown in [Table 12](#). [Figure 47](#) shows the microstructure of pure magnesium rapidly cooled. The influence of the cooling rate on the grain size of pure magnesium is illustrated in [Figure 48](#).

Table 12: The average grain size of pure magnesium under different cooling rates.

Pure Mg	~ Grain Size ( $\mu\text{m}$ )
LCR-Mg	4235
MCR-Mg	2252
HCR-Mg	6 to 12

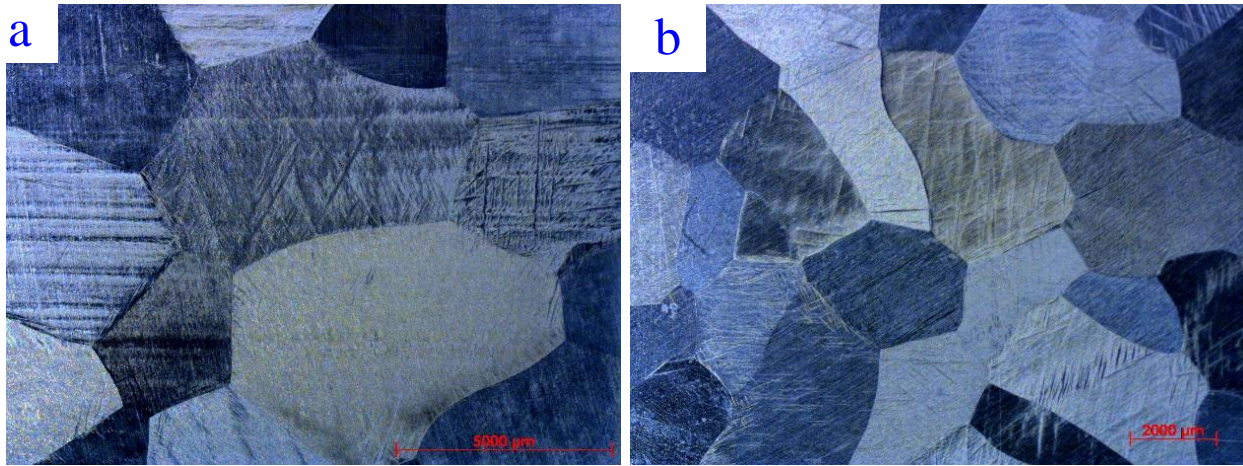


Figure 46: The macrostructure of pure magnesium at 6.5x (a) cooled in the furnace (slow cooling rate) (b) cooled in the furnace with uninsulated-ends (moderate cooling)

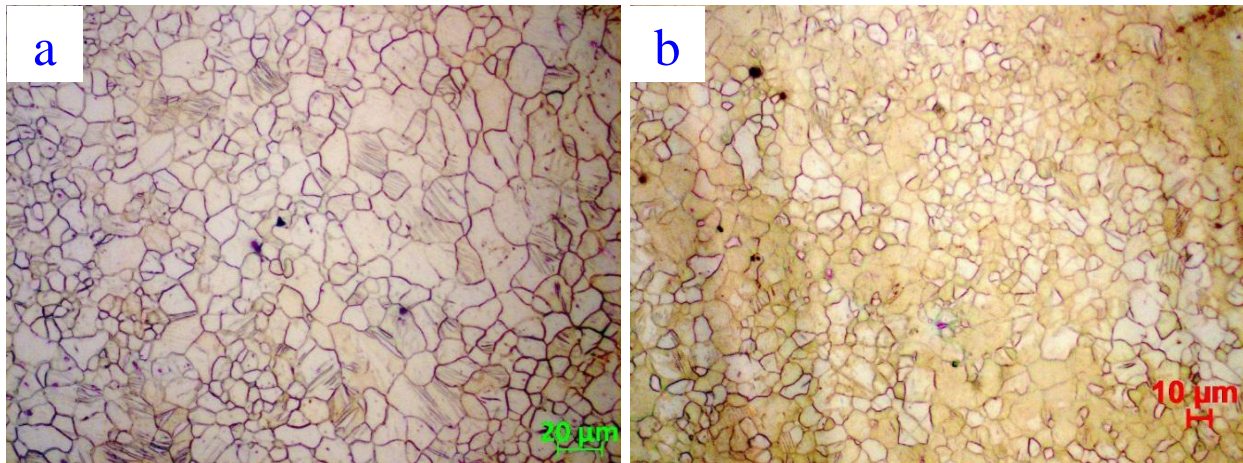
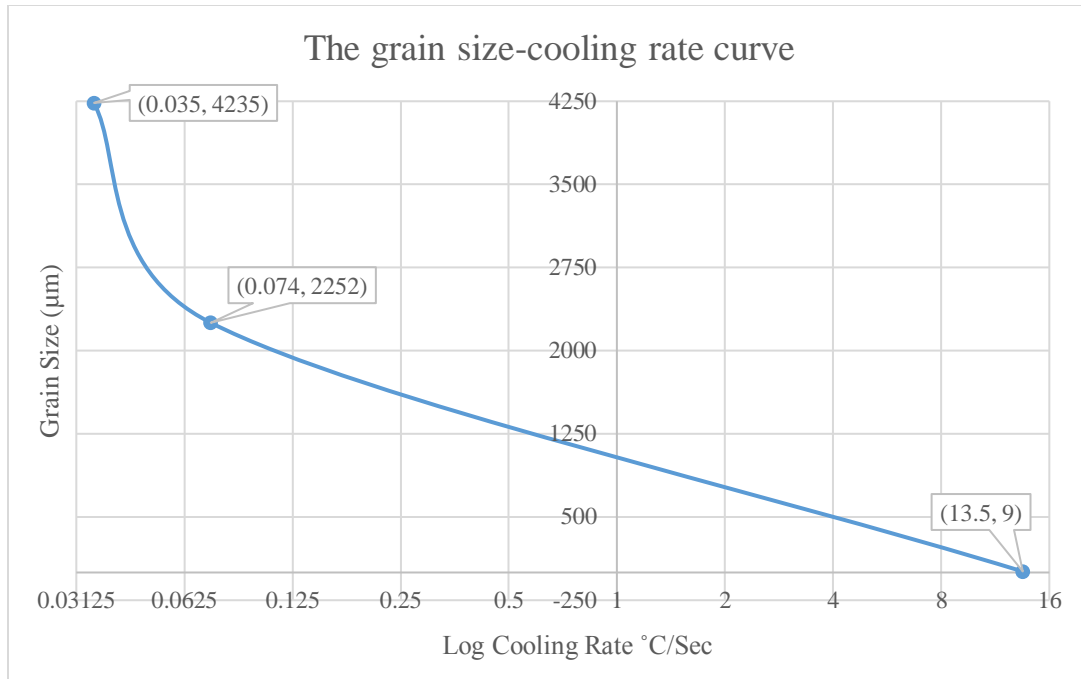


Figure 47: The microstructure of pure magnesium quenched in liquid  $\text{CO}_2$  at 500x.

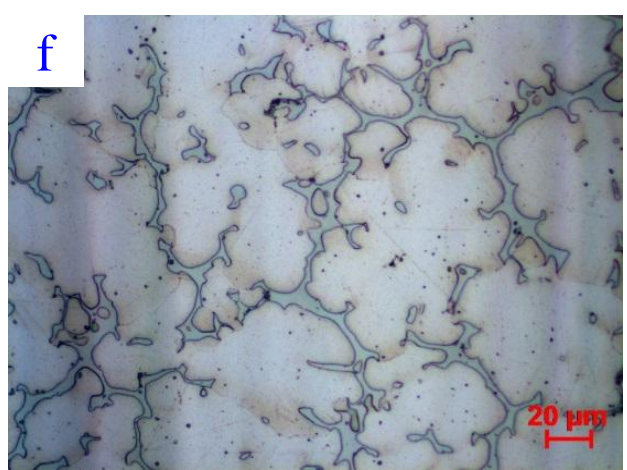
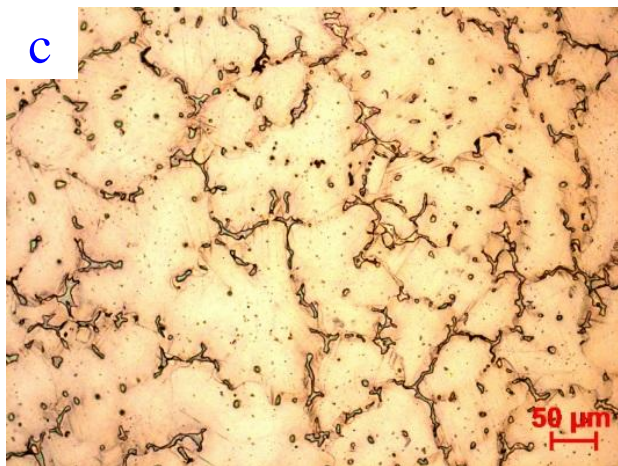
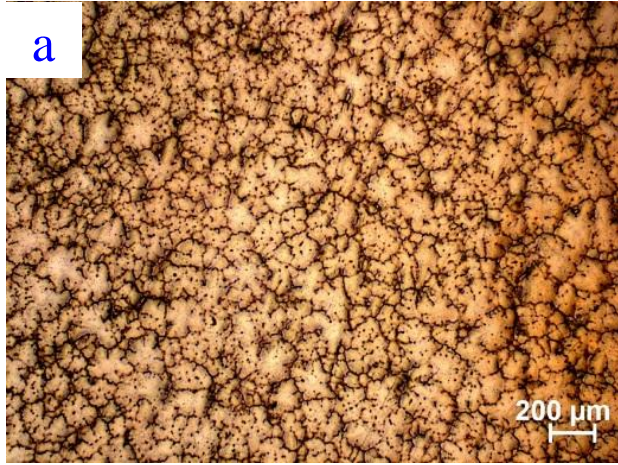


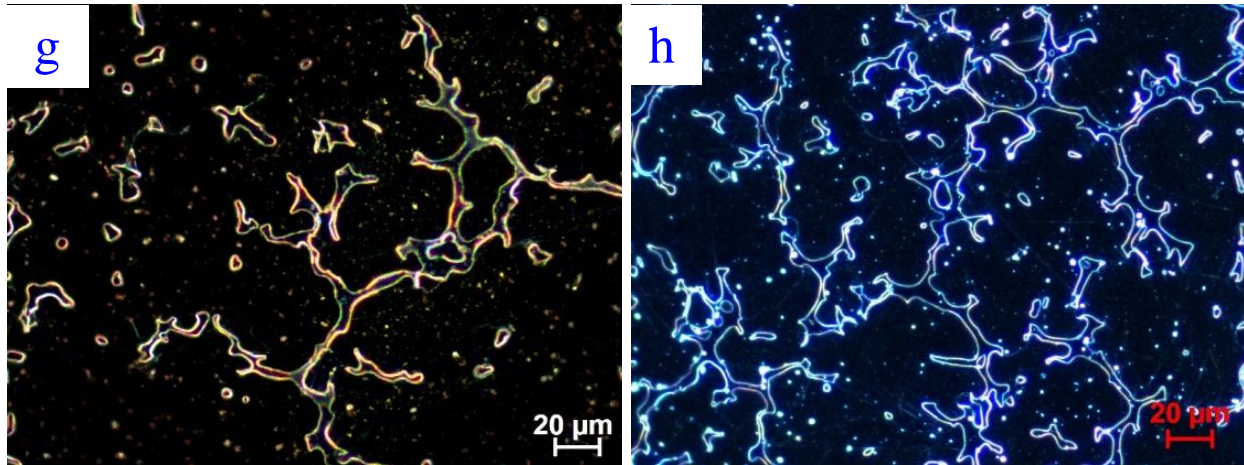
*Figure 48: The grain size-cooling rate curve.*

The combined effects of alloying elements (Mn and Zn) and rapid quenching were observed at various magnifications, as shown in Figure 49. In Figure 49 (a and b), it can be seen clearly that the microstructure consists of the secondary phases (Mg-Mn-Zn-containing phases) in the forms of a longitudinal structure and scattered nodules across the matrix ( $\alpha$ -Mg). The spacing of the Mg-1Mn-2Zn alloy was measured to be within the average of 100  $\mu\text{m}$  with a limited sub-branching ability from the main arm, which limits the influence of the secondary phase and dominates a ductile behavior in the alloy.

The quenched Mg-1Mn-4Zn alloy was found to have a dendrite spacing average of 68.75  $\mu\text{m}$  and a much higher arming density than quenched Mg-1Mn-2Zn, which was also smaller than the unquenched Mg-0.9Mn-4Zn-0.2Al [26]. Moreover, adding 4% Zn

promoted the formation of a continuous network of the main secondary phase that feeds the sub-branches, as shown in [Figure 49 \(c and d\)](#). The thin phases of (Mg, Zn) and (Mg, Mn)-containing at the boundaries became thicker with increasing the content of Zn. Additionally, the scattered nodules of secondary phases were found to be embedded in the matrix ( $\alpha$ -Mg), as shown in [Figure 49 \(e-h\)](#). The merged impact of promoting a continuum network and sub-branches of the secondary phase hinder the ductility of the alloy and dictate a brittle behavior. [Table 13](#) lays out the dendrite spacing of Mg alloying systems.





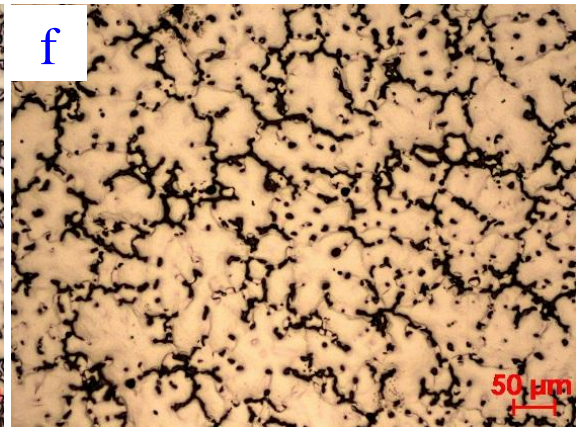
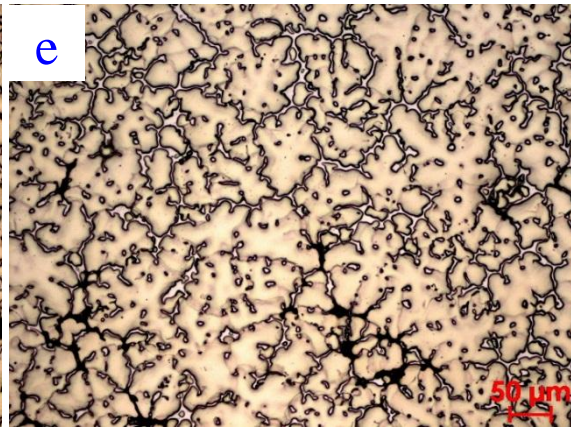
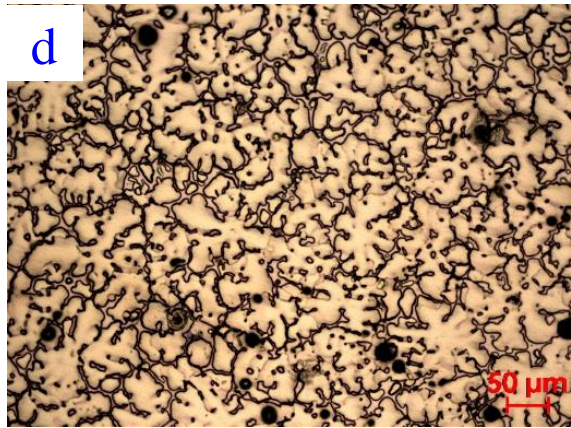
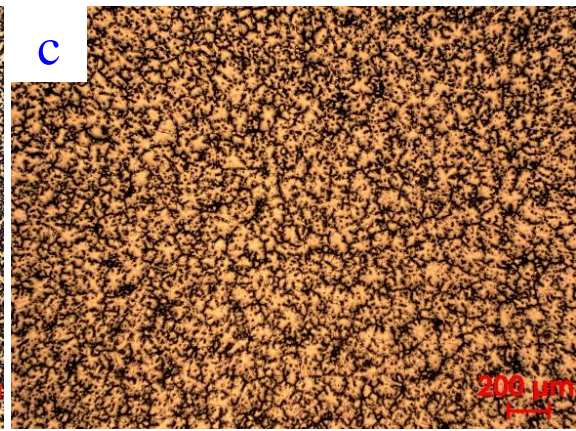
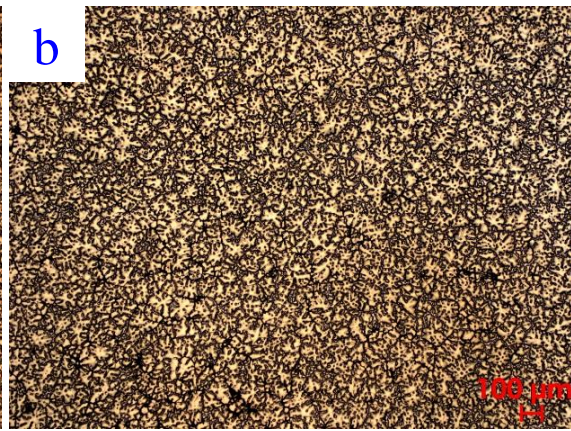
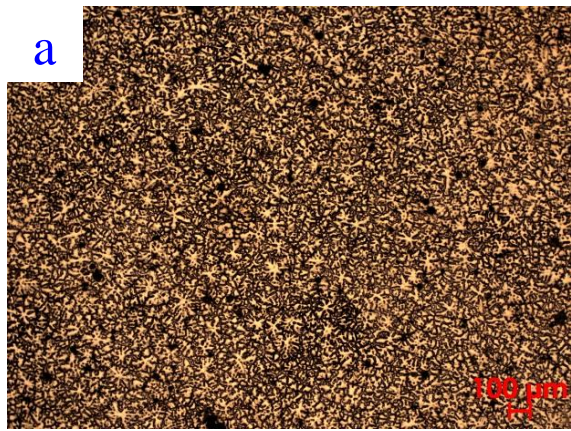
*Figure 49: The microstructure of the alloying systems (a) quenched Mg-1Mn-2Zn at 50x (b) quenched Mg-1Mn-4Zn at 50x (c) quenched Mg-1Mn-2Zn at 200x (d) quenched Mg-1Mn-4Zn at 200x (e) quenched Mg-1Mn-2Zn at 500x (f) quenched Mg-1Mn-4Zn at 500x (g) quenched Mg-1Mn-4Zn, polarized image at 500x (h) quenched Mg-1Mn-4Zn, polarized image at 500x.*

Figure 50 (a-l) shows the effect on the microstructure of adding sodium and potassium individually and simultaneously to the system at different magnifications from 50x to 500x. Adding 0.5% Na and 0.5% K to the quenched alloying system of Mg-1Mn-4Zn reduced the grain size further than adding just manganese and zinc in addition to causing the formation of a continuous network of a secondary phase. However, the effect of adding sodium individually to the alloying system produced a smaller spacing size than adding potassium individually or simultaneously with Na (0.25% of each element) to the system. The formed structure of Mg-1Mn-4Zn-0.5Na was found to be the smallest, with an average spacing of 41.3  $\mu\text{m}$ . Nevertheless, it is produced the highest density of sub-branches among all of the other alloying systems. Table 13 lays out the dendrite spacing of Mg alloying systems.

On the other side, adding potassium interrupted the formation of a connected secondary phase and reduced the number of sub-branches. This alloying system formed a dendrite spacing of 59.67 $\mu\text{m}$ . The effect of the alloying elements on the spacing was hindered by adding sodium and potassium simultaneously producing a spacing of 75  $\mu\text{m}$ . This could be due to the formation of brittle secondary phases that locally absorbed more alloying elements. The secondary phases showed the same behavioral microstructure distribution as a semi connected secondary phase at the grain boundaries with scattered nodules embedded in the matrix ( $\alpha\text{-Mg}$ ). It's worth mentioning that the alloying systems of MgMn4ZnNa and MgMn4ZnNaK formed a reactive-brittle phase scattered around the structure. Moreover, it was noticed that the color of the area close and around the secondary phases tends to turn into a black color, which indicates that these areas are more chemically reactive.

*Table 13: Dendrite spacing of Mg alloying systems.*

<b>Mg Systems</b>	<b>Spacing <math>\mu\text{m}</math></b>
<b>MgMn2Zn</b>	100
<b>MgMn4Zn</b>	68.75
<b>MgMn4ZnNa</b>	41.3
<b>MgMn4ZnK</b>	59.67
<b>MgMn4ZnNaK</b>	75



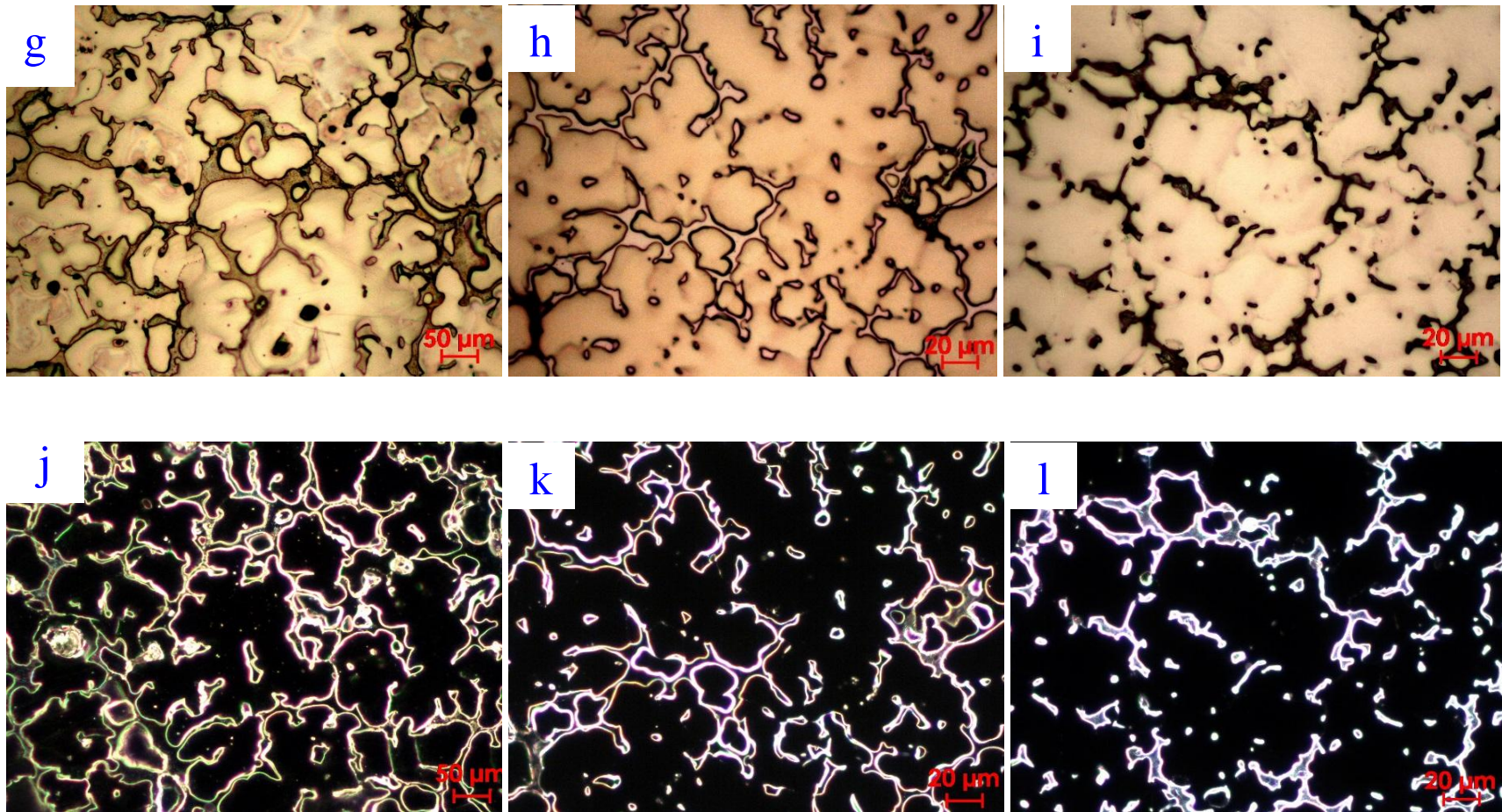


Figure 50: The microstructure of the alloying systems (a) quenched Mg-1Mn-4Zn-0.5Na at 50x (b) quenched Mg-1Mn-4Zn-K at 50x (c) quenched Mg-1Mn-4Zn-0.5Na-0.5K at 50x (d) quenched Mg-1Mn-4Zn-0.5Na at 200x (e) quenched Mg-1Mn-4Zn-K at 200x (f) quenched Mg-1Mn-4Zn-0.5Na-0.5K at 200x (g) quenched Mg-1Mn-4Zn-0.5Na at 500x (h) quenched Mg-1Mn-4Zn-K at 500x (i) quenched Mg-1Mn-4Zn-0.5Na-0.5K at 500x (j) quenched Mg-1Mn-4Zn-0.5Na, polarized image at 500x (k) quenched Mg-1Mn-4Zn-0.5K, polarized image at 500x (l) quenched Mg-1Mn-4Zn-0.5Na-0.5K, polarized image at 500x

## 5.2.2. Impact and Fracture Mechanism

Four samples for each type were tested by using the Charpy impact tester. Table 14 illustrates the summary of the results for all alloying systems. The impact strength of the slowly cooled pure magnesium in a completely insulated furnace (LCR-Mg) and moderately cooled pure magnesium Mg-cooled in a tube furnace with uninsulated ends (MCR-Mg) exhibited the highest values of 660 and 654.29 j/m among the other types, respectively. The total absorbed energy was consumed by two mechanisms: the energy needed for fracture propagation and the ductile deformation. The high deformation and long fracture path, in Figure 53 (a-d), justifies the increase in the absorbed energy.

*Table 14: The results summary for charpy impact testing*

Mg Systems	Break Energy (j)	Strength (j/m)
LCR-Mg	6.6	660
MCR-Mg	6.54	654.2
HCR-Mg	5.49	549.2
MgMn2Zn	5.92	592.1
MgMn4Zn	5.66	566.4
MgMn4ZnNa	0.92	94.7
MgMn4ZnK	4.39	439.12
MgMn4ZnNaK	1.01	101.89

Generally, pure magnesium has low mechanical properties. However, the high deformation indicates high ductility that was due to the large grain size of LCR-Mg (4235

$\mu\text{m}$ ) and MCR-Mg (2252  $\mu\text{m}$ ). The impact strength was decreased to 549.19  $\text{J/m}$  for quenched pure Mg (HCR-Mg), which was due to the reduction in the ductility of pure Mg. As it was discussed in the previous section, quenched pure Mg has an average grain size of 6-12  $\mu\text{m}$ , which is smaller than unquenched Mg and reduces the ductility of the sample.

Figure 53 (e and f) shows the fracture of quenched pure Mg.

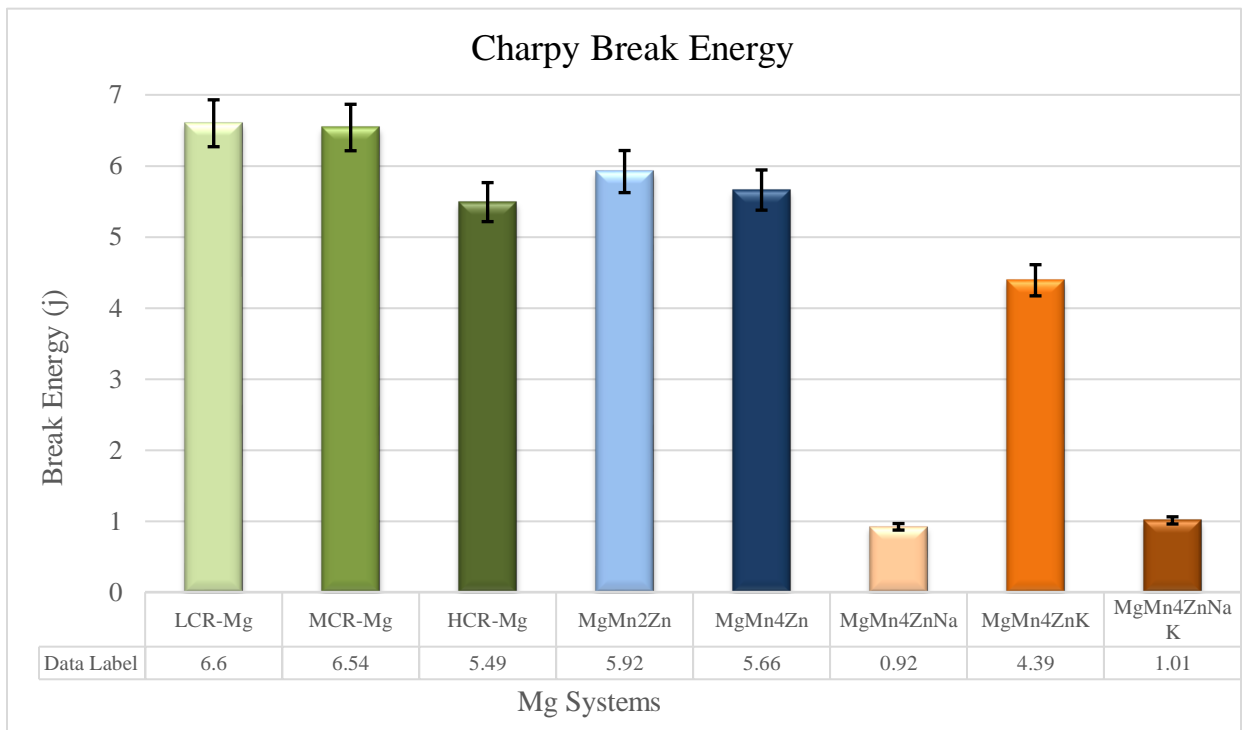
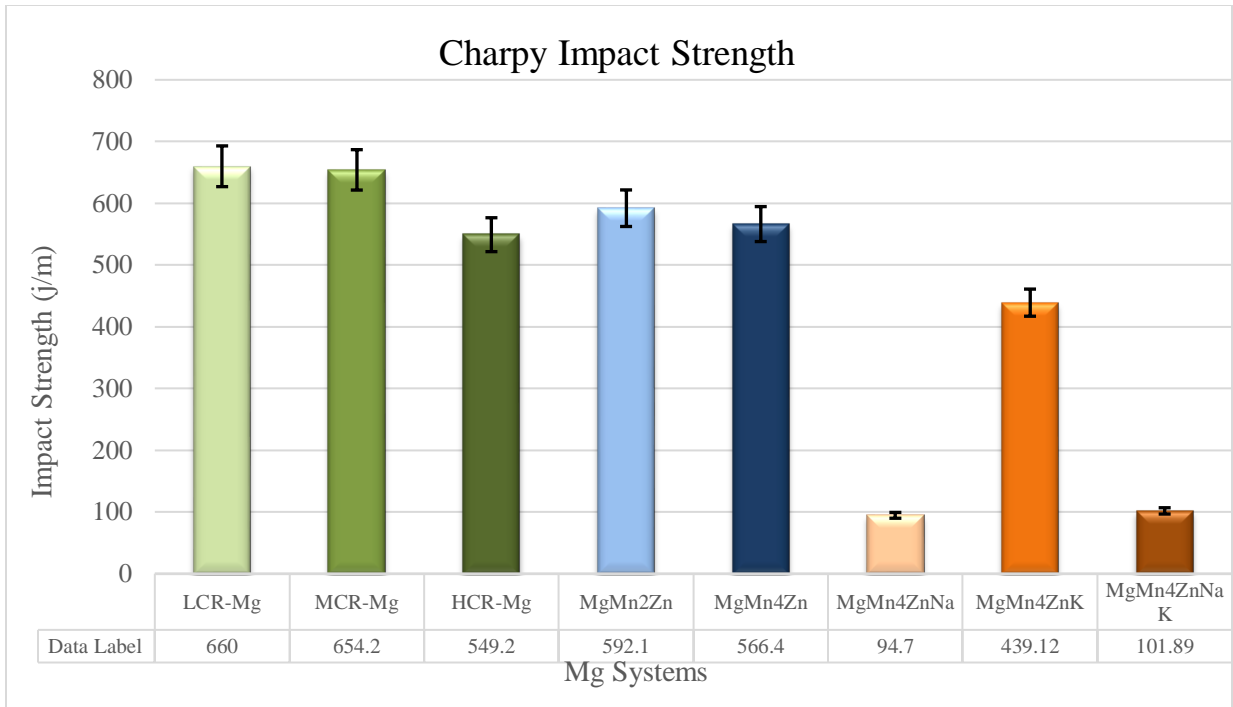
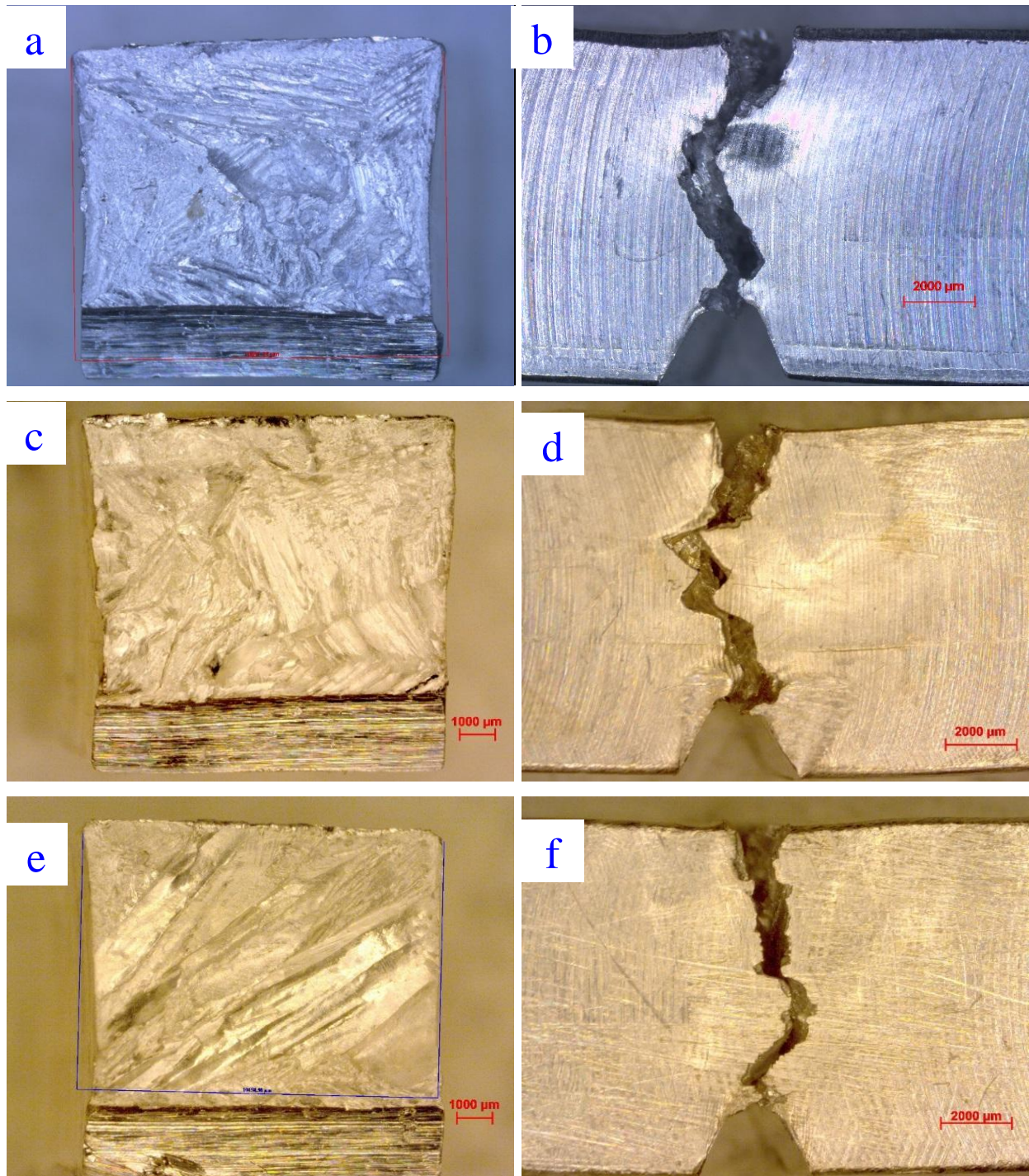


Figure 51: Charpy break energ of the alloying systems.



*Figure 52: Charpy impact strength of the alloying systems.*



*Figure 53: The fracture surface morphology of impact samples of pure magnesium at 6.5x (a) top view and (b) side view are for slowly cooled pure magnesium (Mg-LCR) (c) top view and (d) side view are for moderately cooled pure magnesium (Mg-MCR) (e) top view and (f) side view are for quenched pure magnesium (Mg-HCR).*

The Charpy impact strength of quenched Mg increased to 592.18 j/m with the addition of 1% Mn and 2% Zn. It was noticed that the surface of the fracture has a clear cut with a minor deformation and semi straight fracture path, which indicates that most of the energy was absorbed by the fracture propagation mechanism. However, the strength was decreased slightly to 566.412 j/m and the sample exhibited very minor deformation with increasing Zn content to 4%. This is due to the formation of a continuous network of a secondary phase that feeds sub-branches. [Figure 54](#) illustrates the fracture morphology of Mg-1Mn-2Zn and Mg-1Mn-4Zn.

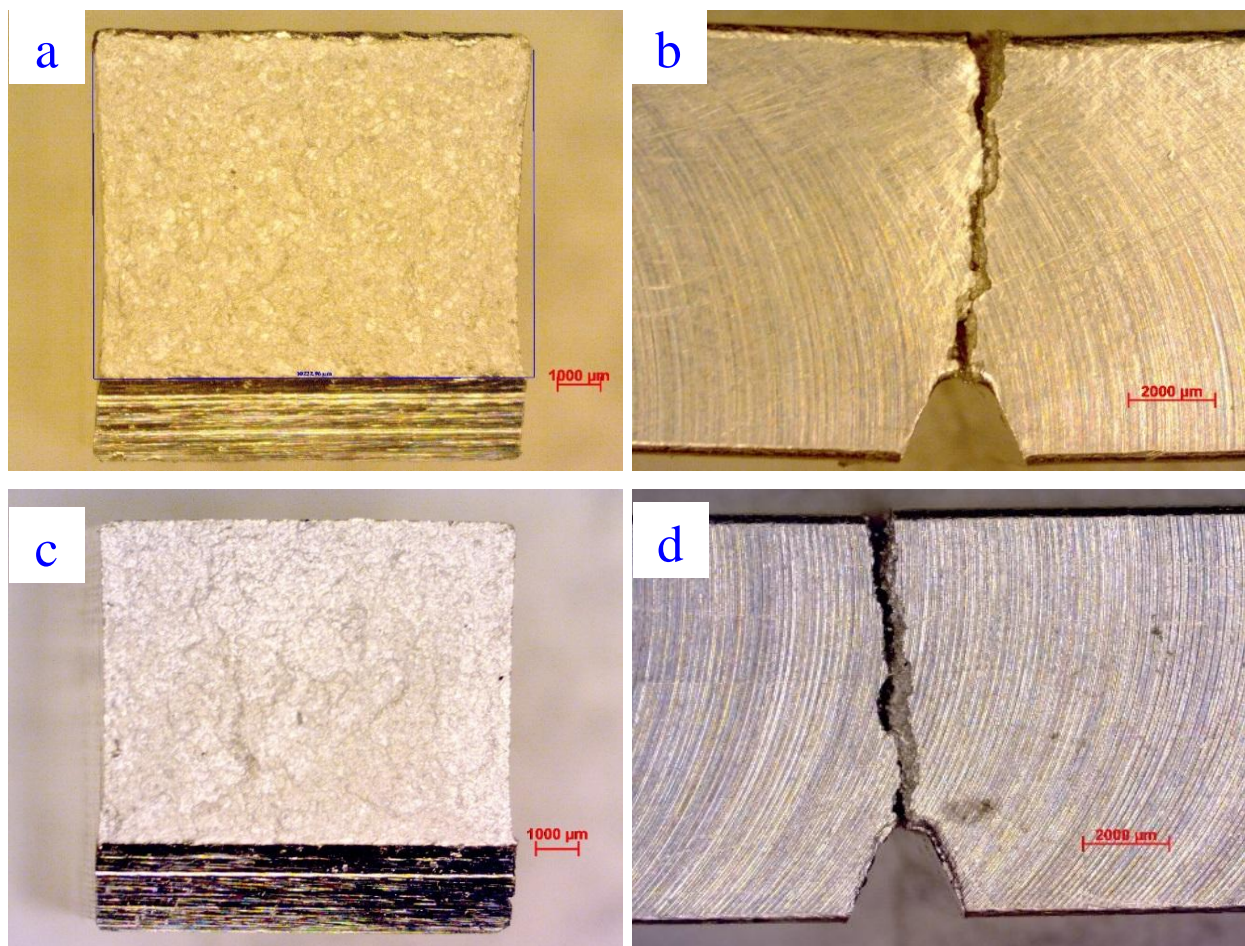


*Figure 54: The fracture surface morphology of impact samples at 6.5x (a) top view and (b) side view of quenched Mg-1Mn-2Zn (c) top view and (d) side view of quenched Mg-1Mn-4Zn.*

The impact strength of Mg-1Mn-4Zn alloy was reduced considerably by 83% with the addition of 0.5% Na. The fracture morphology followed a straight path with no noticeable deformation, which indicates a brittle fracture behavior. This deterioration in the strength of the system is due to the production of a connected main-secondary phase and other brittle secondary phases, in addition to the further reduction of the spacing and the presence of the eutectic, as shown in [Figure 55 \(a and b\)](#). The impact strength was increased significantly by 363.6% with the addition of 0.5% K in comparison with Mg-1Mn-4Zn-0.5Na. Moreover, the fracture surface showed more deformation and a longer fracture path, as shown in [Figure 55 \(c and d\)](#).

The strength of Mg-1Mn-4Zn reduced tremendously to 101.89 j/m with the simultaneous addition of sodium and potassium (0.25% Na+0.25% K). This reduction is a direct cause of forming brittle-reactive secondary phases as can be characterized thoroughly by using the microstructural and compositional analyses. The fracture analyses for the system was observed to adopt the same fracture mechanism of Mg-1Mn-4Zn-0.5Na alloying system, as shown in [Figure 55 \(e and f\)](#). It's worth mentioning that the addition of alloying elements demonstrated more effectiveness than increasing the solidification rates.

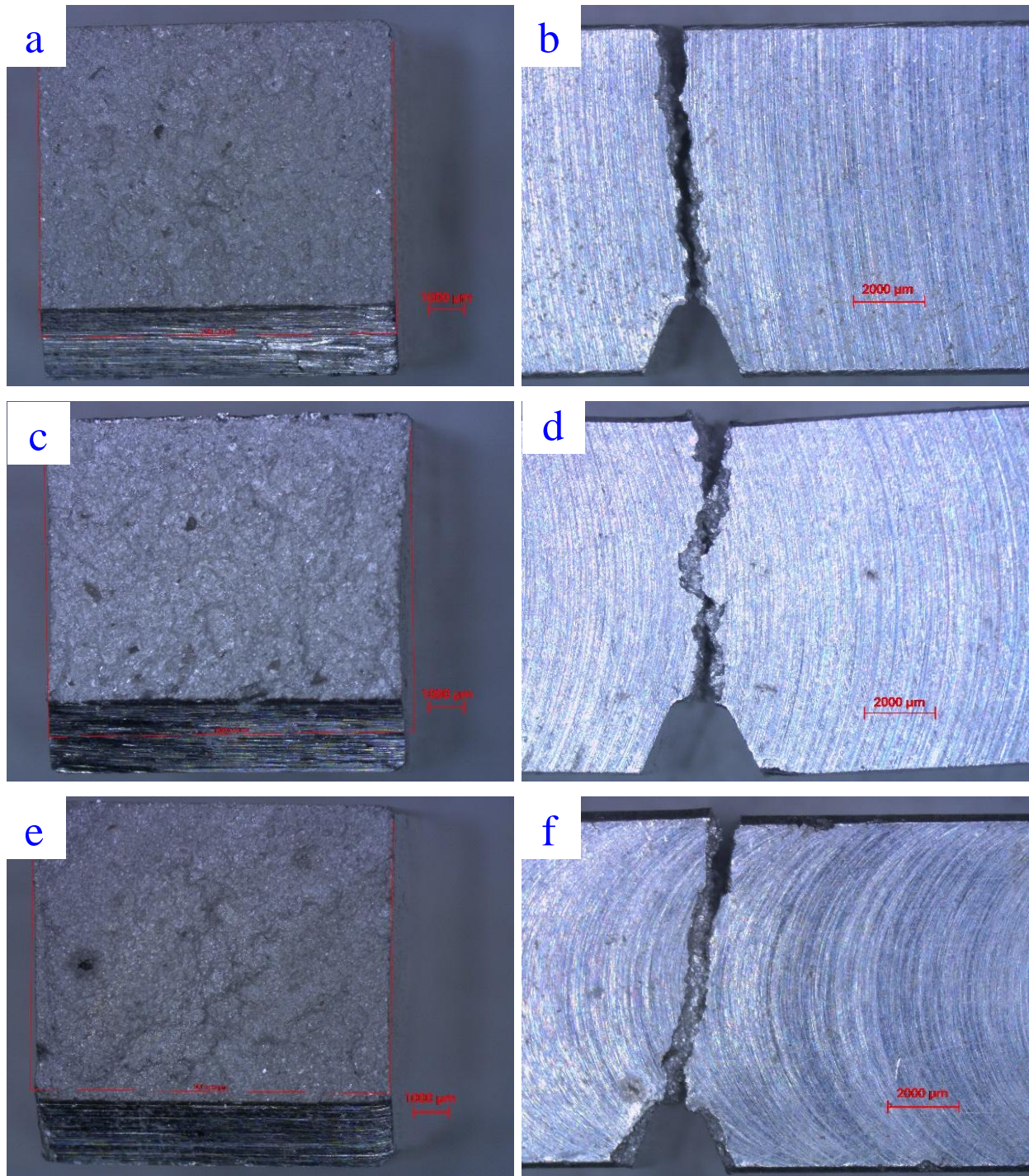


Figure 55: The fracture surface morphology of impact samples at 6.5x (a) top view and (b) side view of quenched Mg-1Mn-4Zn-Na, (c) top view and (d) side view of quenched Mg-1Mn-4Zn-K, (e) top view and (f) side view are for quenched Mg-1Mn-4Zn-Na-K.

### 5.2.3. Hardness

A minimum of 30 readings were obtained from each sample by using scale H-Rockwell Hardness RHH. [Table 15](#) summarizes the results of the hardness test. The hardness of pure Mg was increased with increasing the cooling rate. MCR-Mg hardness was improved slightly by 11% in comparison to the slowly cooled Mg while the hardness for the rapidly cooled pure magnesium (HCR-Mg) was significantly increased to 57% and 40% in comparison to LCR-Mg and MCR-Mg, respectively. The hardness was further improved with adding alloying elements (1%Mn and 2%Zn) by 123%, 100% and 41% in comparison to LCR-Mg, MCR-Mg, and HCR-Mg, respectively. Increasing the Zn content to 4% increased the hardness by 160%, 132%, 65%, and 16% in proportion to slowly cooled pure Mg, moderately cooled pure Mg, quenched pure Mg, and quenched Mg-1Mn-2Zn, respectively, as shown in [Figure 57](#).

*Table 15: The results summary for Rockwell hardness testing-scale H*

Mg Systems	Hardness
LCR-Mg	30.75
MCR-Mg	34.43
HCR-Mg	48.53
MgMn2Zn	68.82
MgMn4Zn	80.09
MgMn4ZnNa	90.27
MgMn4ZnK	78.22
MgMn4ZnNaK	81.44

The hardness of Mg-1Mn-4Zn was increased by 12% to 90.2 RHH with adding sodium (0.5%), which reflects the combined effect of forming brittle secondary phases and fine grain size structure. The effect of adding 0.5% of potassium showed unnoticeable change to 78.2 RHH in comparison to Mg-1Mn-4Zn alloying system, which demonstrates more ductility than the alloying system in the case of sodium addition. The final addition of both sodium and potassium did not show appreciable change in the hardness. MgMn4ZnNaK alloying system exhibited poor machinability and surface finishing due to the high brittleness of the system, as shown in [Figure 56](#).

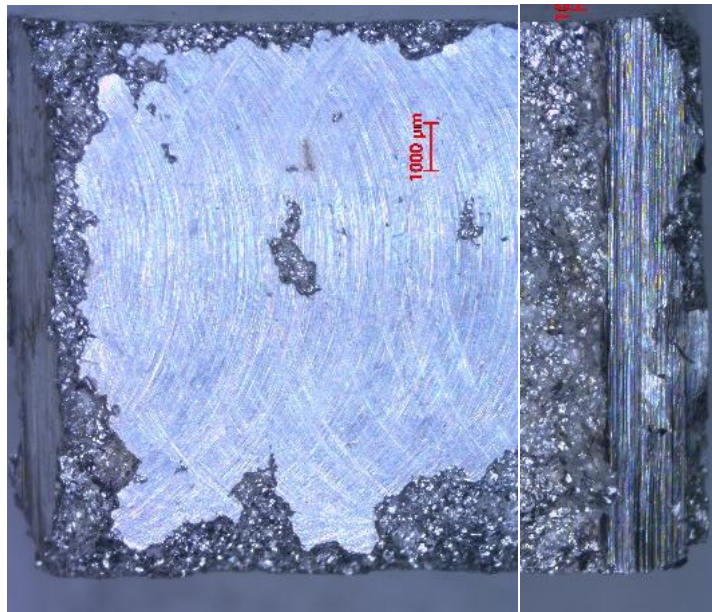


*Figure 56: The MgMn4ZnNaK alloying system.*

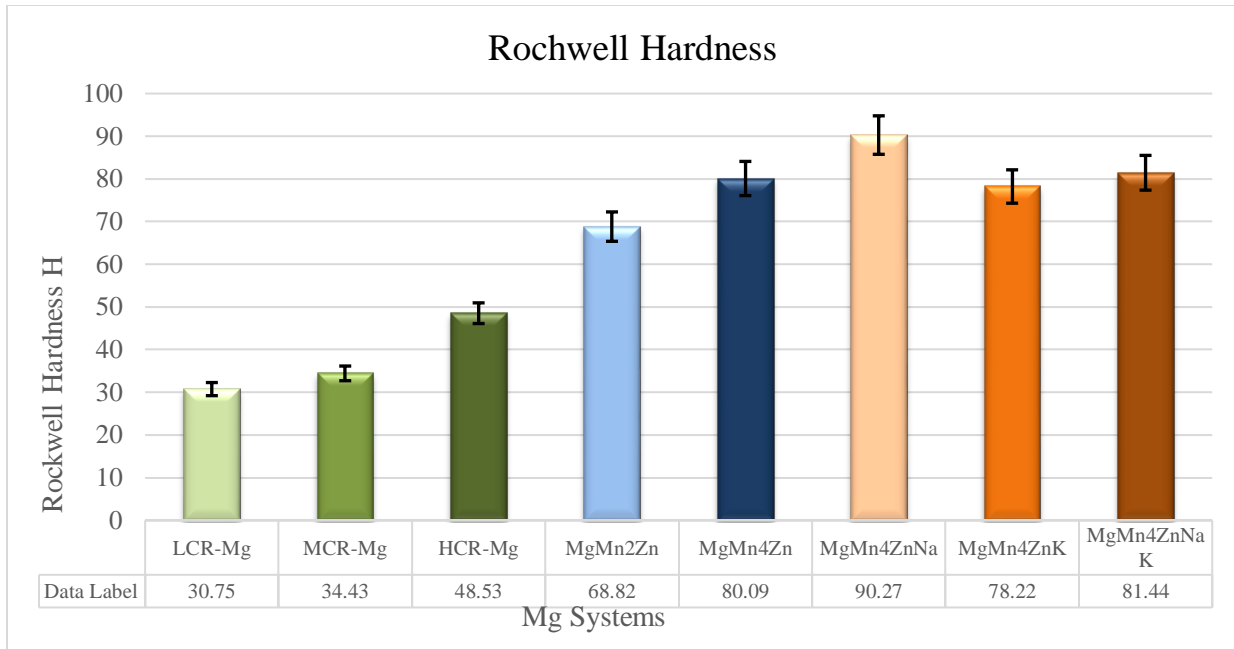


*Figure 57: Scale-H Rockwell Hardness.*

#### 5.2.4. Tensile and Fracture Mechanism

The tensile properties of the alloying systems were collected to study the effect of the solidification rates and alloying elements. Four samples were tested for each alloying system. The test was done by using INSTRON universal testing machine with a strain rate of 1 mm/min. Table 16 summarizes the tensile properties of mg alloying systems. The first set of testing was conducted on pure magnesium samples to study the effect of solidification rates.

The slowly cooled pure magnesium showed low yield strength and ultimate tensile strength of 15.4 MPa and 48.9 MPa, respectively. However, the LCR-Mg exhibited a good ductility of 10.3%. Increasing the solidification rate to 0.074 °C/Sec improved the yield

and ultimate tensile strengths considerably. The YS and UTS of MCR-Mg increased in comparison with LCR-Mg by 57% and 37%, respectively. On the other side, the ultimate tensile strength of the quenched pure magnesium increased by 78% and 29% in respect to LCR-Mg and MCR-Mg, respectively. However, the effect of the solidification rate on the ductility was found to be insignificant, as shown in [Figure 58](#).

*Table 16: The results summary for tensile properties for all Mg alloying systems*

Alloying Systems	E (GPa)	YS (Mpa)	UTS (Mpa)	Ductility (%)
Mg-LCR	4.6	15.40	48.97	10.30
Mg-MCR	2.6	24.19	67.4	10.29
Mg-HCR	7.7	24.34	87.18	9.50
MgMn2Zn	7.8	30.43	126.44	13.03
MgMn4Zn	7.9	36.29	38.1	0.92
MgMn4ZnNa	7.9	39.7	40.8	0.82
MgMn4ZnK	6.2	39.57	57.1	2.20
MgMn4ZnNaK	8.5	13.79	13.79	0.20

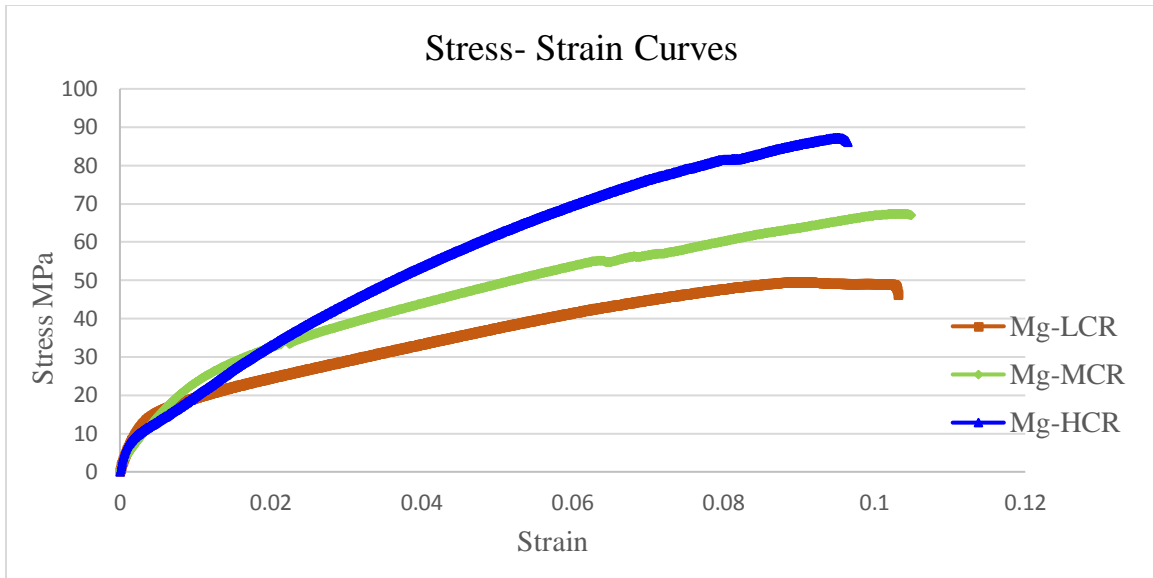


Figure 58: The stress-strain curves for pure magnesium that were cooled by different solidification rates.

Figure 59 shows the microstructure of pure magnesium at different magnifications of 6.5 x for slowly and moderately cooled pure Mg and 500 x for quenched Mg. The fracture morphology of all pure magnesium samples is presented in Figure 60. LCR-Mg showed enormous deformation (twisted around shape), which is due to the large grain size (4235  $\mu\text{m}$  for cooling rate of 0.035  $^{\circ}\text{C}/\text{Sec}$ ). The deformation of the samples was decreased and became more uniform with increasing the solidification rates since the grain size was decreased to 2252  $\mu\text{m}$  for cooling rate of 0.074  $^{\circ}\text{C}/\text{Sec}$  and 6-12  $\mu\text{m}$  for cooling rate of 13.5  $^{\circ}\text{C}/\text{Sec}$ .

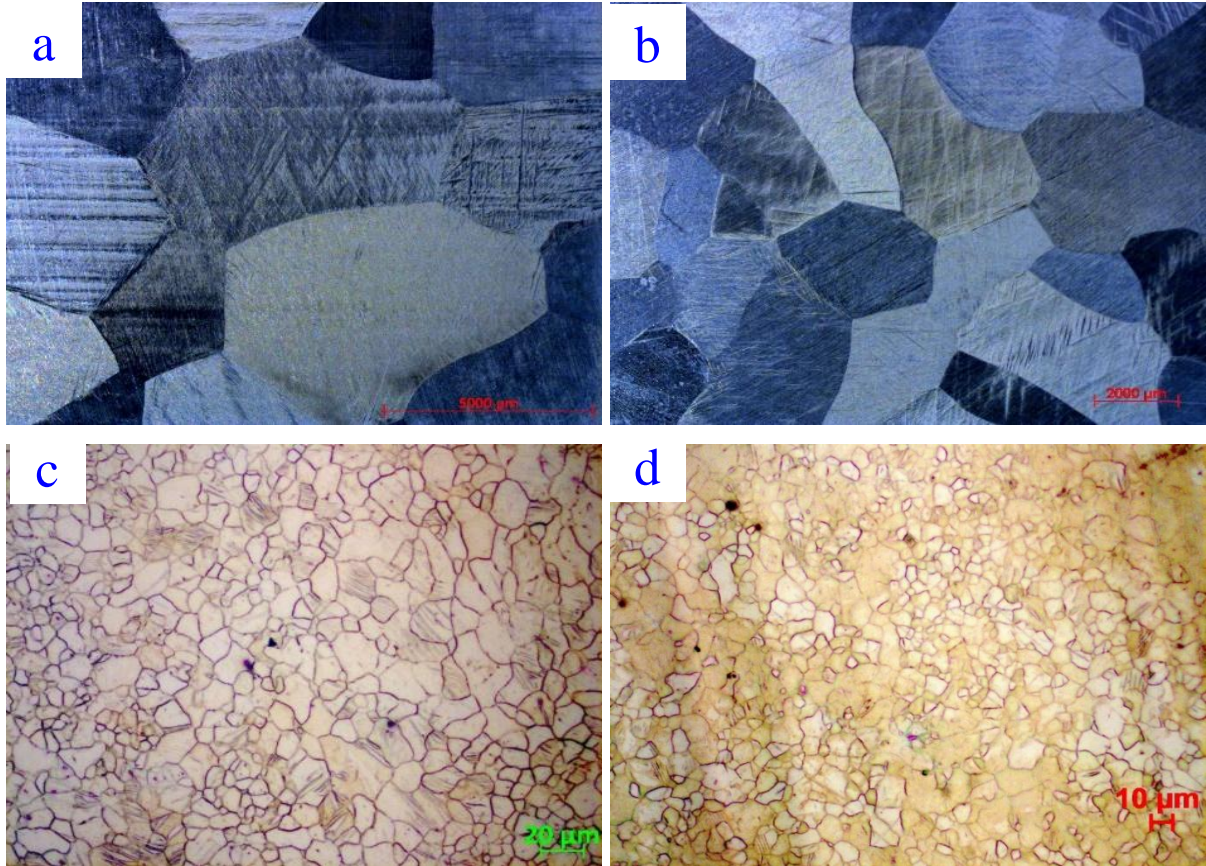
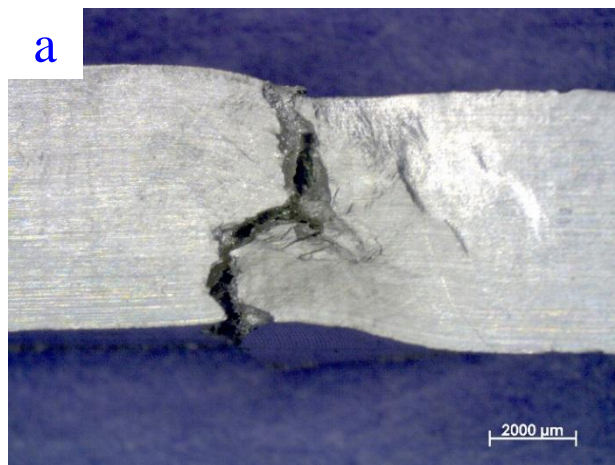
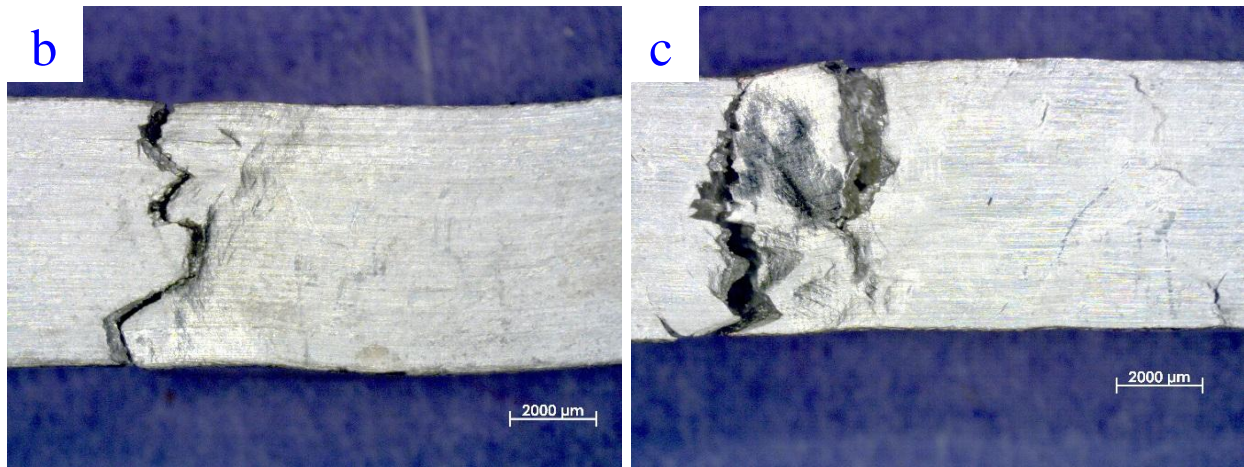


Figure 59: The macrostructure of pure magnesium (a) cooled in the furnace (slow cooling rate) at 6.5x (b) cooled in the furnace with uninsulated-ends (moderate cooling) at 6.5x (c) and (d) quenched in liquid  $CO_2$  at 500x.





*Figure 60: The tensile fracture morphology for pure magnesium that were cooled by different solidification rates (a) LCR-Mg (b) MCR-Mg (c) HCR-Mg .*

The combined effect of the rapid solidification (13.5 °C/Sec) and the alloying elements (manganese and zinc) on the tensile properties were analyzed, and the summary of the results is included in [Table 16](#). The yield strength and the ultimate tensile strength were increased significantly with the addition of 1% Mn and 2% Zn to the system by 25% and 45% in proportion to the quenched pure magnesium, respectively. This alloying system exhibited the highest tensile strength in addition to the ductility, where the ductility was increased to 13%. Nevertheless, the deformation of the tensile sample was more uniform and showed a ductile fracture behavior, as shown in [Figure 62 \(a\)](#).

On the other side, increasing the zinc content to 4% deteriorated the UTS and the ductility greatly to 38 MPa and 0.9% with respect to 2% Zn. The decline in the mechanical properties could be due to the increase in the presence of the sub-branches and the formation of a continuous network of secondary phase, as shown in [Figure 49](#). Besides, the decrease in the presence of the eutectic phase hindered the mobility within the secondary

phase and consequently led to a more dominant brittle structure. Also, the deformation of this alloying system was unnoticeable with semi straight fracture, as shown in Figure 62 (b). Figure 61 illustrates the stress-strain curves for quenched Mg-1Mn-2Zn and Mg-1Mn-4Zn alloying systems in comparison to quenched pure magnesium.

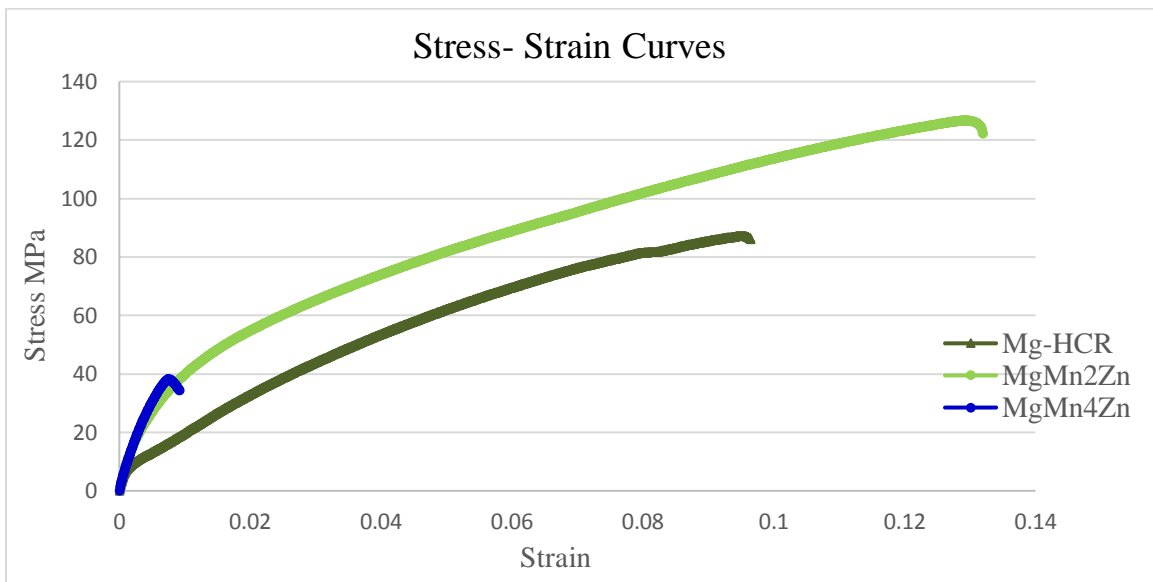


Figure 61: The stress-strain curves for Mg-Mn-Zn alloying systems.

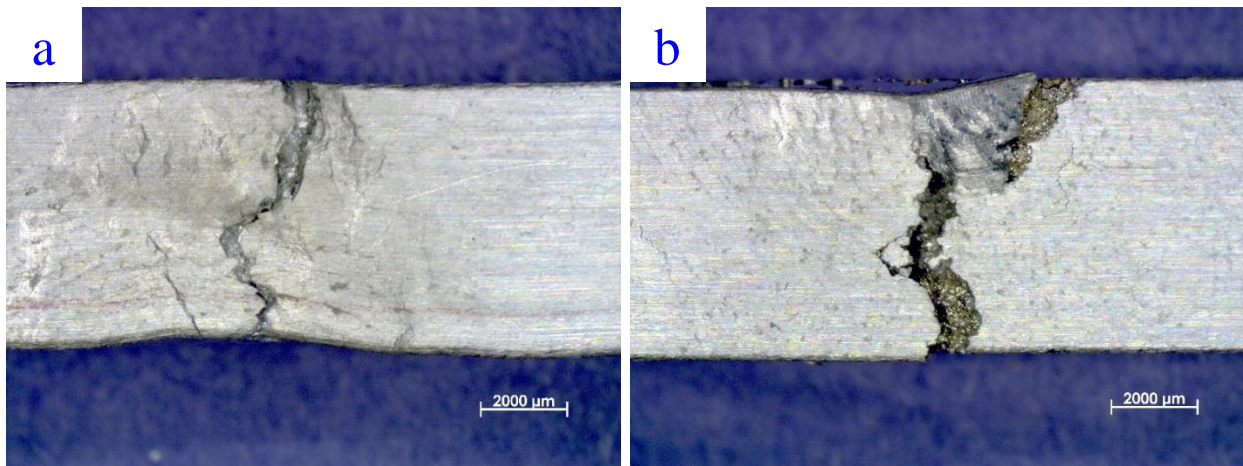


Figure 62: The tensile fracture morphology for Mg-Mn-Zn alloying systems (a) Mg-1Mn-2Zn (b) Mg-

### *1Mn-4Zn.*

As it is mentioned above, the addition of 4% Zn led to undesirable mechanical properties due to the broadening of the secondary phases. This work examined the response of adding 0.5 Na and 0.5K to the quenched alloying system (Mg-1Mn-4Zn) individually or simultaneously with Na and K (0.25% of each element). The addition of sodium individually showed inconsiderable change in the tensile properties and demonstrated the same failure structure, as shown in [Figure 63](#) and [Figure 64 \(a\)](#). This change is a result of combined influences of several factors related to the continuity of the main-secondary phase, dendrite spacing, eutectic phase, and formation of other secondary phases.

On the other hand, using the same percentage of potassium to replace sodium enhanced the ultimate tensile strength and ductility significantly by 49% and 139% in comparison to Mg-1Mn-4Zn, respectively. The improvement of the tensile properties could be due to the impact of adding potassium on the microstructure. The addition of potassium interrupted the continuum of the main-secondary phase. The formation of a less connected secondary phase network hindered the brittle effect of the phase, as shown in [Figure 50](#).

It is believed that the induced increase in the thickness of the secondary phase and the laminal thickness ( $\beta$ ) of the formed eutectic consumed more alloying elements and thus the interruption in the structure was provoked. However, adding with 0.25% Na and 0.25% K simultaneously reduced the UTS dramatically to 13.7 MPa and showed very poor

mechanical properties and high brittleness, which could be due to the formation of brittle secondary phases that locally absorbed more alloying elements. Figure 63 presents the stress-strain curves of Mg-1Mn-4Zn, Mg-1Mn-4Zn-0.5Na, Mg-1Mn-4Zn-0.5K, and Mg-1Mn-4Zn-0.25Na-0.25K alloying systems. The failure morphology of the systems can be seen in Figure 64. Moreover, the mechanical properties of the natural human bone vary depending on the several factors such as age and the type of bone. It was reported that the tensile properties of bones range for UTS 35-283 MPa, E 3-20 GPa, ductility 1.07-2.1%, respectively [103, 146, 147, 148].

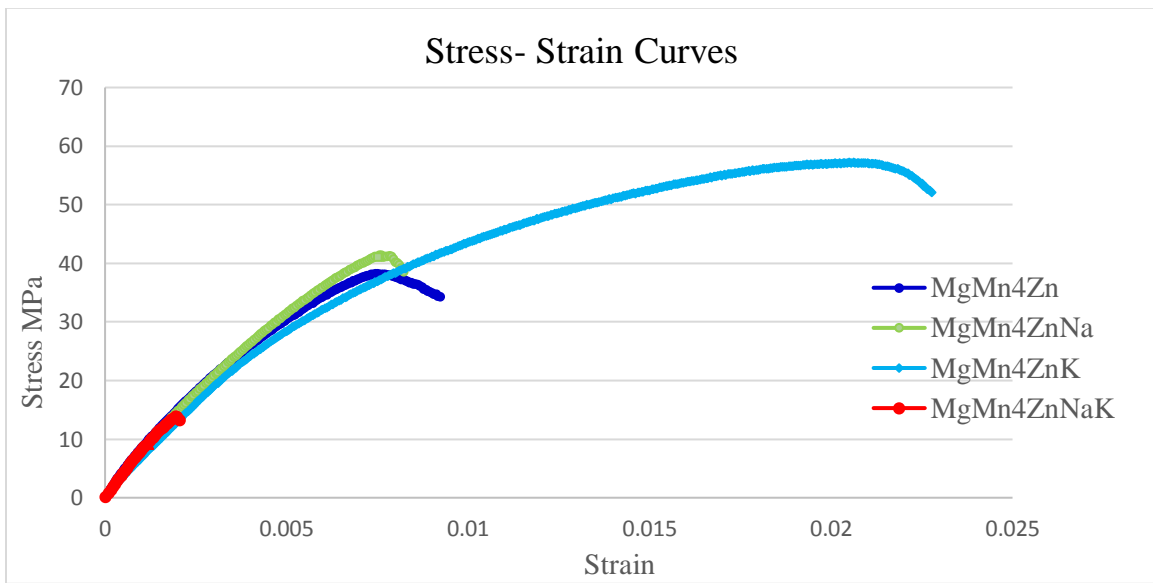


Figure 63: The stress-strain curves for Mg-Mn-Zn-Na-K alloying systems.

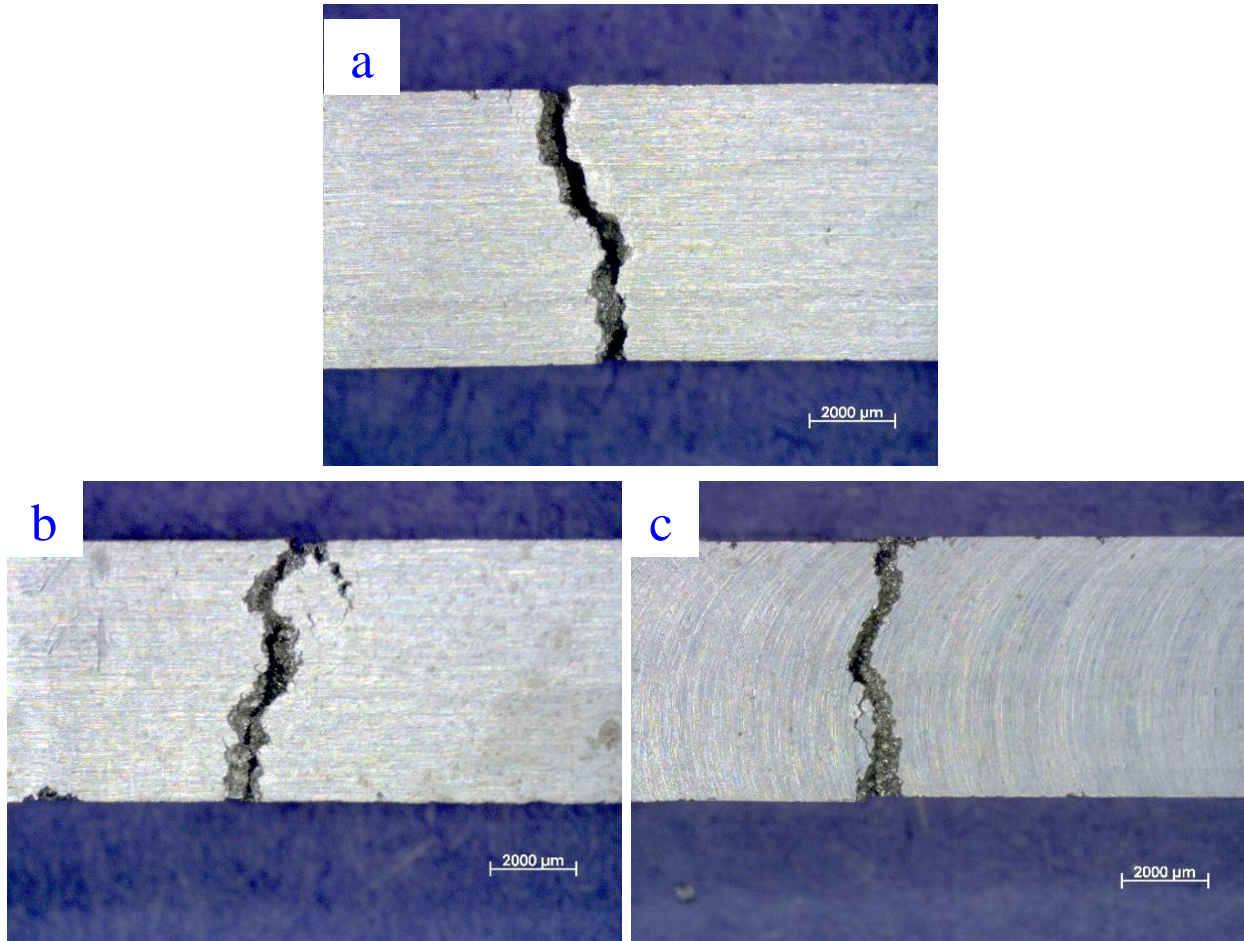


Figure 64: The tensile fracture morphology for Mg-Mn-Zn-Na-K alloying systems (a) Mg-1Mn-4Zn-0.5Na (b) Mg-1Mn-4Zn-0.5K (c) Mg-1Mn-2Zn-0.25Na-0.25K.

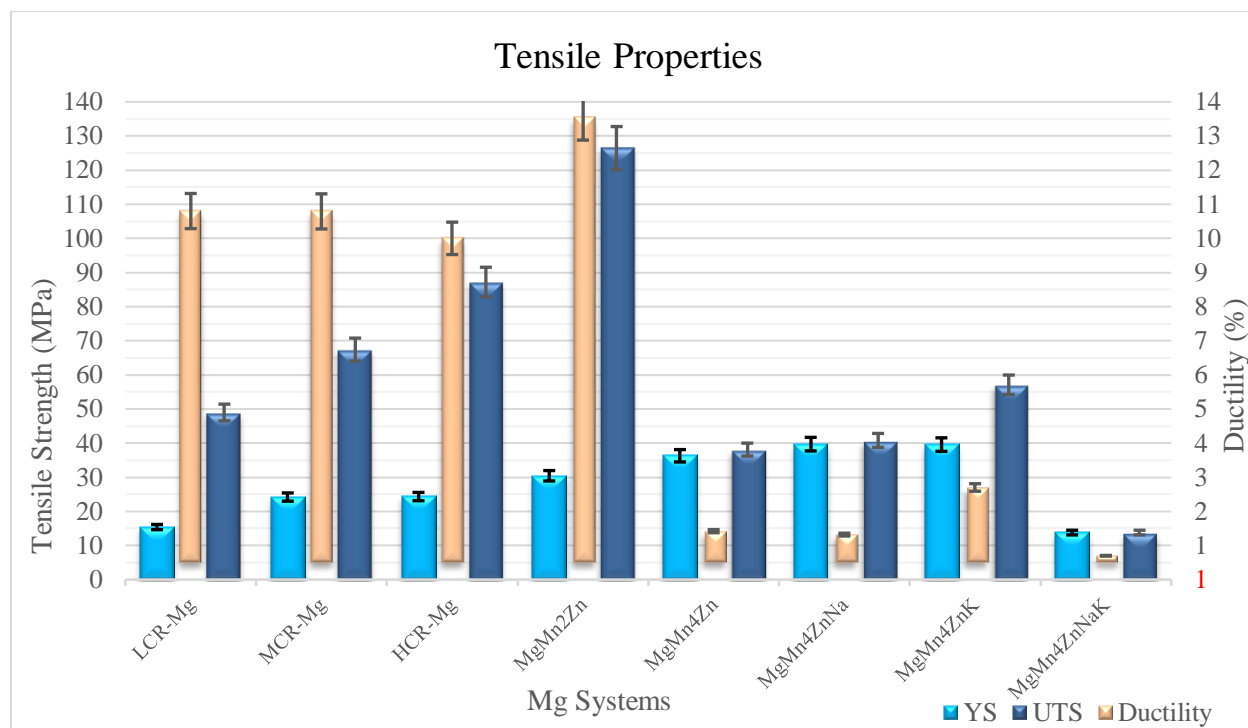


Figure 65: Tensile properties chart for all alloying systems.

The chart in Figure 65 summarizes the results of tensile tests, the results were further analyzed by looking at the correlation between the microstructure of each Mg-Mn-Zn-based alloying system and the tensile properties. The first part of the analysis covers the influence of the dendrite spacing on the mechanical properties while the second part addresses the effect of the eutectic on the properties. It was found that the yield strength increases with decreasing the dendrite spacing. However, Mg-Mn-Zn-Na-K alloying system did not follow the trend and showed a significant decrease in the yield strength, which is due to the formation of very brittle phases, as it is discussed in the SEM-EDS analysis section. Figure 66 shows the correlation between yield strength and dendrite spacing, Figure 67 and Figure 68 cover the combined analysis of the microstructure.

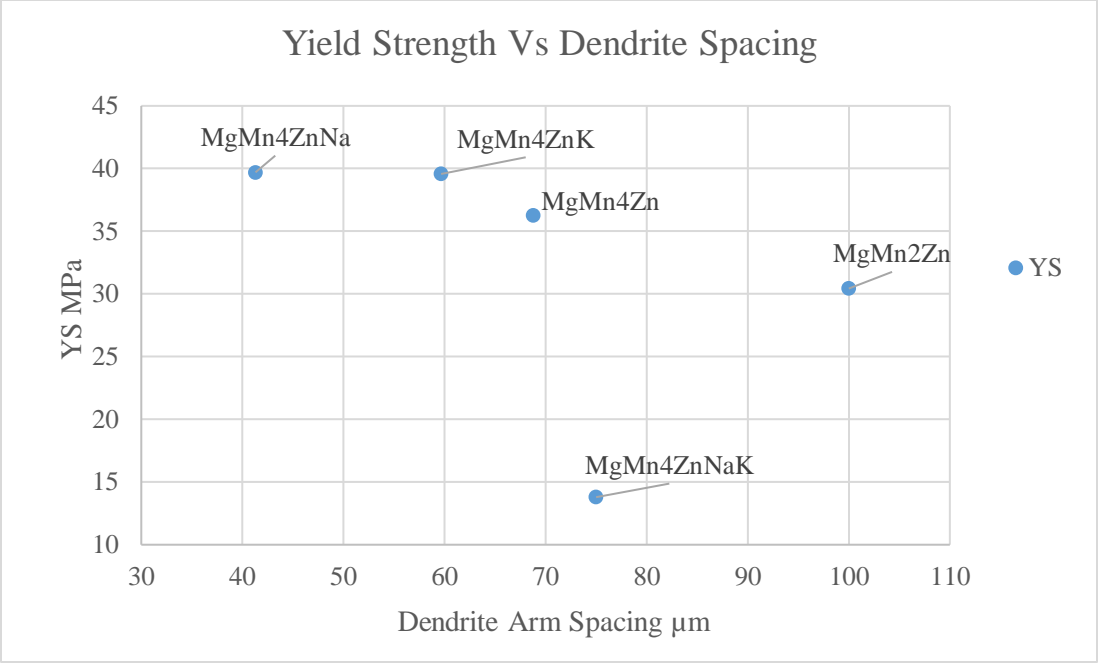


Figure 66: The correlation between yield strength and dendrite spacing of Mg-1Mn-2Zn, Mg-1Mn-4Zn, Mg-1Mn-4Zn-0.5Na, Mg-1Mn-4Zn-0.5K, and Mg-1Mn-4Zn-0.25Na-0.25K alloying systems.

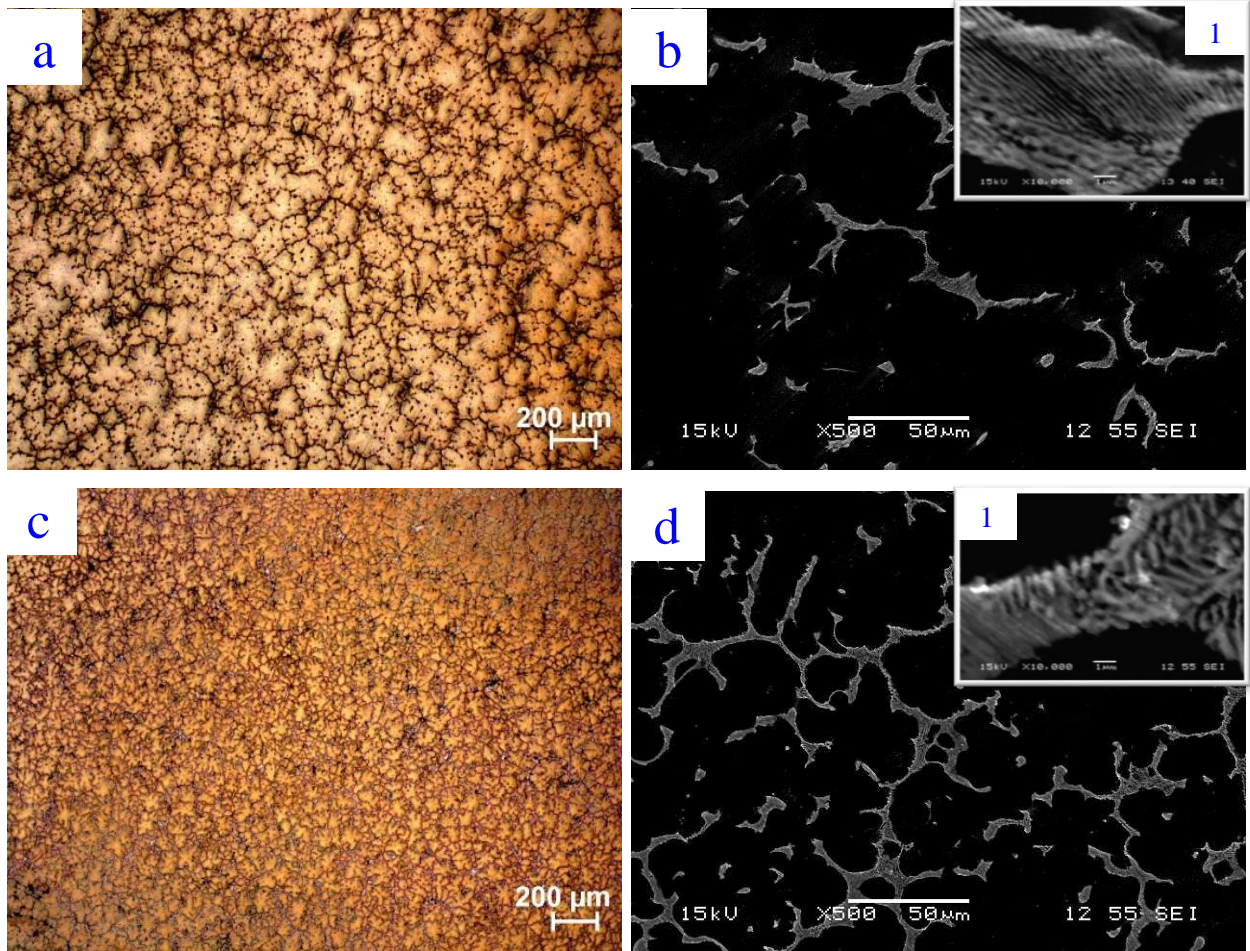
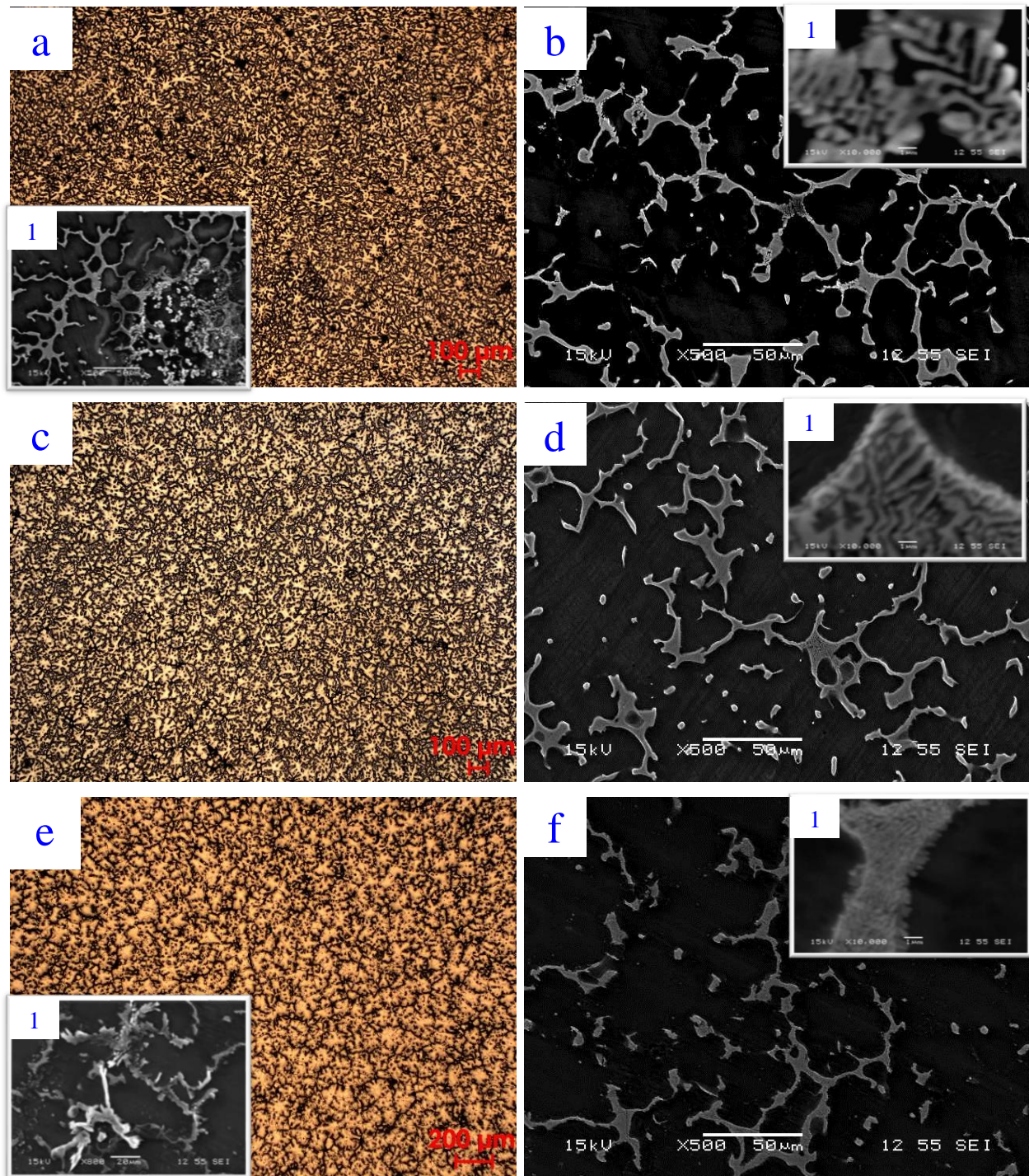


Figure 67: The optical microstructure and SEM imaging of alloying systems (a) Mg-1Mn-2Zn at 50x, (b) Mg-1Mn-2Zn at 500x and 1 is the eutectic phase at of 10000x of the system, (c) Mg-1Mn-4Zn at 50x, (d) Mg-1Mn-4Zn at 500x and 1 is the eutectic phase at of 10000x of the system.



*Figure 68: The optical microstructure and SEM imaging of alloying systems (a) Mg-1Mn-4Zn-0.5Na at 50x, (b) Mg-1Mn-4Zn-0.5Na at 500x and 1 is the eutectic phase at of 10000x of the system, (c) Mg-1Mn-4Zn-0.5K at 50x, (d) Mg-1Mn-4Zn-0.5K at 500x and 1 is the eutectic phase at of 10000x of the system, (e) Mg-1Mn-4Zn-0.25Na-0.25K at 50x, (f) Mg-1Mn-4Zn-0.25Na-0.25K at 500x and 1 is the eutectic phase at of 10000x of the system.*

The influence of dendrite spacing on other tensile properties was also investigated. The charts in [Figure 69](#) and [Figure 70](#) did not show a specific trend in the plots of the dendrite spacing versus UTS and ductility. Similarly, the correlation between the laminal thickness of the eutectic phase of the systems and the mechanical properties did not demonstrate a direct influence of this factor, as shown in [Table 17](#). After analyzing the tensile properties, it was found that there is no dominant factor that directly affects the properties. The analysis confirmed that there are multiple factors at play, which cause a combined effect and the factors can be listed as below:

- 1- The grain size and dendrite spacing.
- 2- The formation and density of sub-arms of the secondary phase.
- 3- The continuity of the primary secondary phase.
- 4- The presence and laminal thickness of the eutectic phase.
- 5- The presence and size of brittle phases.

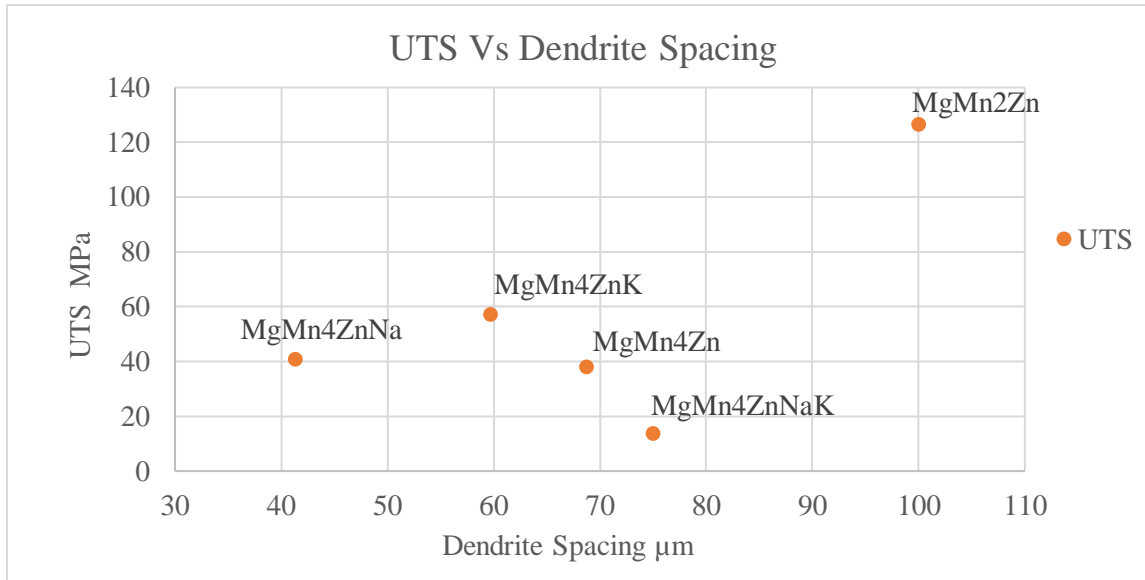


Figure 69: The correlation between ultimate tensile strength and dendrite spacing of Mg-1Mn-2Zn, Mg-1Mn-4Zn, Mg-1Mn-4Zn-0.5Na, Mg-1Mn-4Zn-0.5K, and Mg-1Mn-4Zn-0.25Na-0.25K alloying systems.

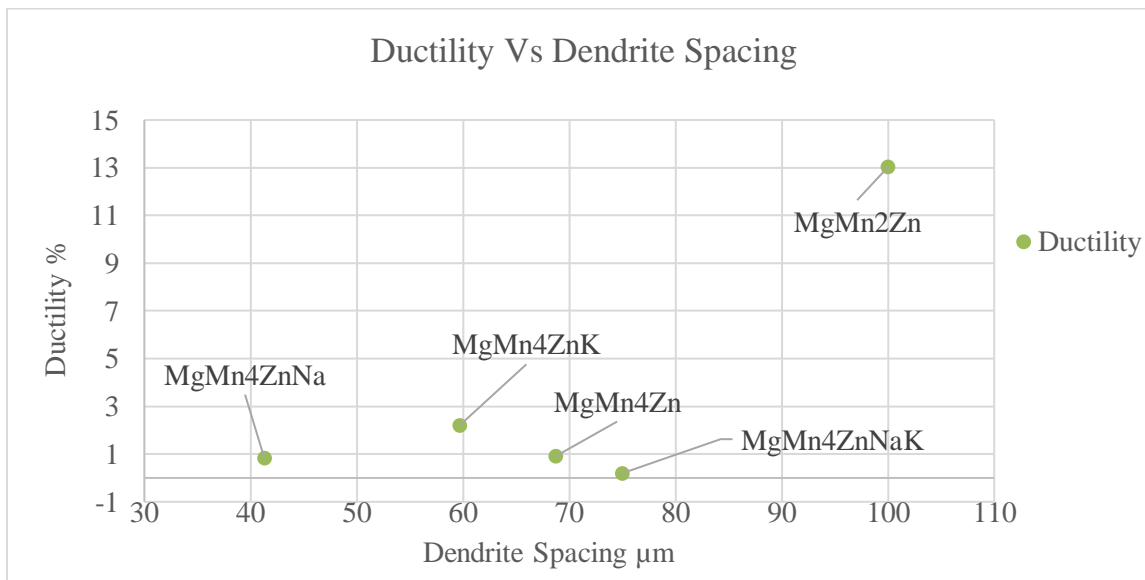


Figure 70: The correlation between the ductility and dendrite spacing of Mg-1Mn-2Zn, Mg-1Mn-4Zn, Mg-1Mn-4Zn-0.5Na, Mg-1Mn-4Zn-0.5K, and Mg-1Mn-4Zn-0.25Na-0.25K alloying systems.

Table 17: The correlation between laminal thickness of the eutectic phase and the tensile properties of Mg-1Mn-2Zn, Mg-1Mn-4Zn, Mg-1Mn-4Zn-0.5Na, Mg-1Mn-4Zn-0.5K, and Mg-1Mn-4Zn-0.25Na-0.25K alloying systems.

<b>Mg Systems</b>	<b><math>\alpha</math> Laminal Thickness <math>\mu\text{m}</math></b>	<b><math>\beta</math> Laminal Thickness <math>\mu\text{m}</math></b>	<b>YS (Mpa)</b>	<b>UTS (Mpa)</b>	<b>Ductility (%)</b>
<b>MgMn2Zn</b>	0.148	0.108	30.43	126.44	13.03
<b>MgMn4Zn</b>	0.48	0.39	36.29	38.1	0.92
<b>MgMn4ZnNa</b>	0.453	0.53	39.7	40.8	0.82
<b>MgMn4ZnK</b>	0.242	0.569	39.57	57.1	2.2
<b>MgMn4ZnNaK</b>	0.13	0.18	13.79	13.79	0.2

## 5.2.5. Microstructural Topography and Composition

### 5.1.2.1. SEM and EDS

Scanning electron microscopy (SEM) and Energy Dispersive X-ray Spectrometer (EDS) analysis were conducted to further investigate the microstructure and phases composition of the examined Mg alloying systems. The samples were machined, mounted in conductive filled mounting compound, grinded, and polished to 0.05  $\mu\text{m}$ . Wide range magnifications (500X to 20000X) were performed to get a complete analysis for the matrix and secondary phases using secondary electron imaging with account voltage of 15 KV.

The slowly cooled pure magnesium (LCR-Mg) with a cooling rate of 0.035  $^{\circ}\text{C}/\text{sec}$  was analyzed at 10000 x and 20000 x, as shown in [Figure 71](#). While microstructure and the grain size were detectable by using the optical microscope, as it was observed in [Figure 59](#), the SEM images showed a clear structure at different magnifications and wasn't able to detect the grain boundaries in both SEI and BSI. [Figure 72](#) shows the EDS elements map, and the map shows the magnesium element as a main element with the existence of oxygen distributed across the examined area. Furthermore, the sample was analyzed using the EDS spectrum to confirm the elemental content of the system. The point spectrum confirmed the presence of magnesium and oxygen with a weight percentage of 98.5 and 1.08%, respectively, as shown in [Figure 73](#).

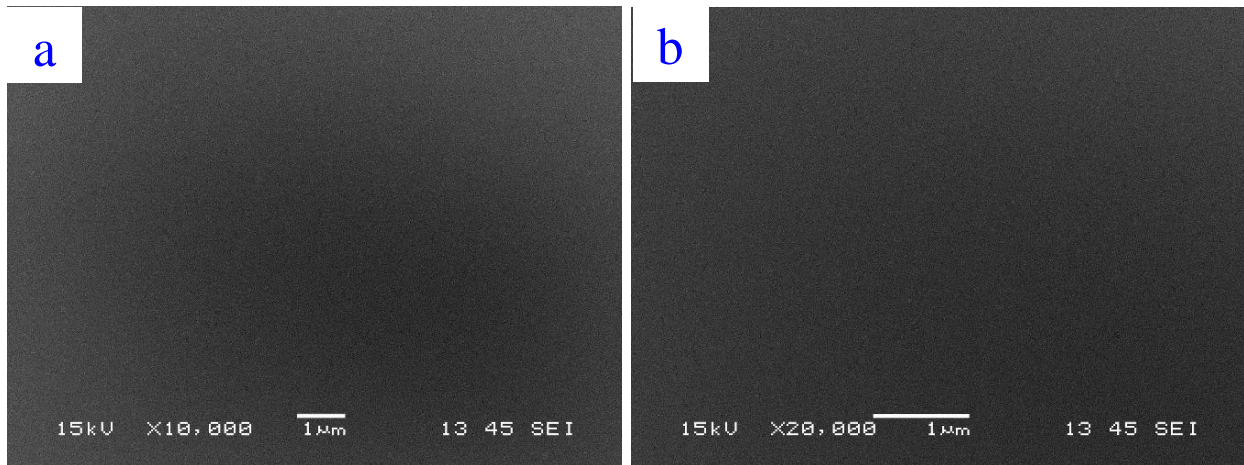


Figure 71: SEM images of pure magnesium cooled in the furnace (slow cooling rate) at different magnifications (a) at 10000 x (b) at 20000 x.

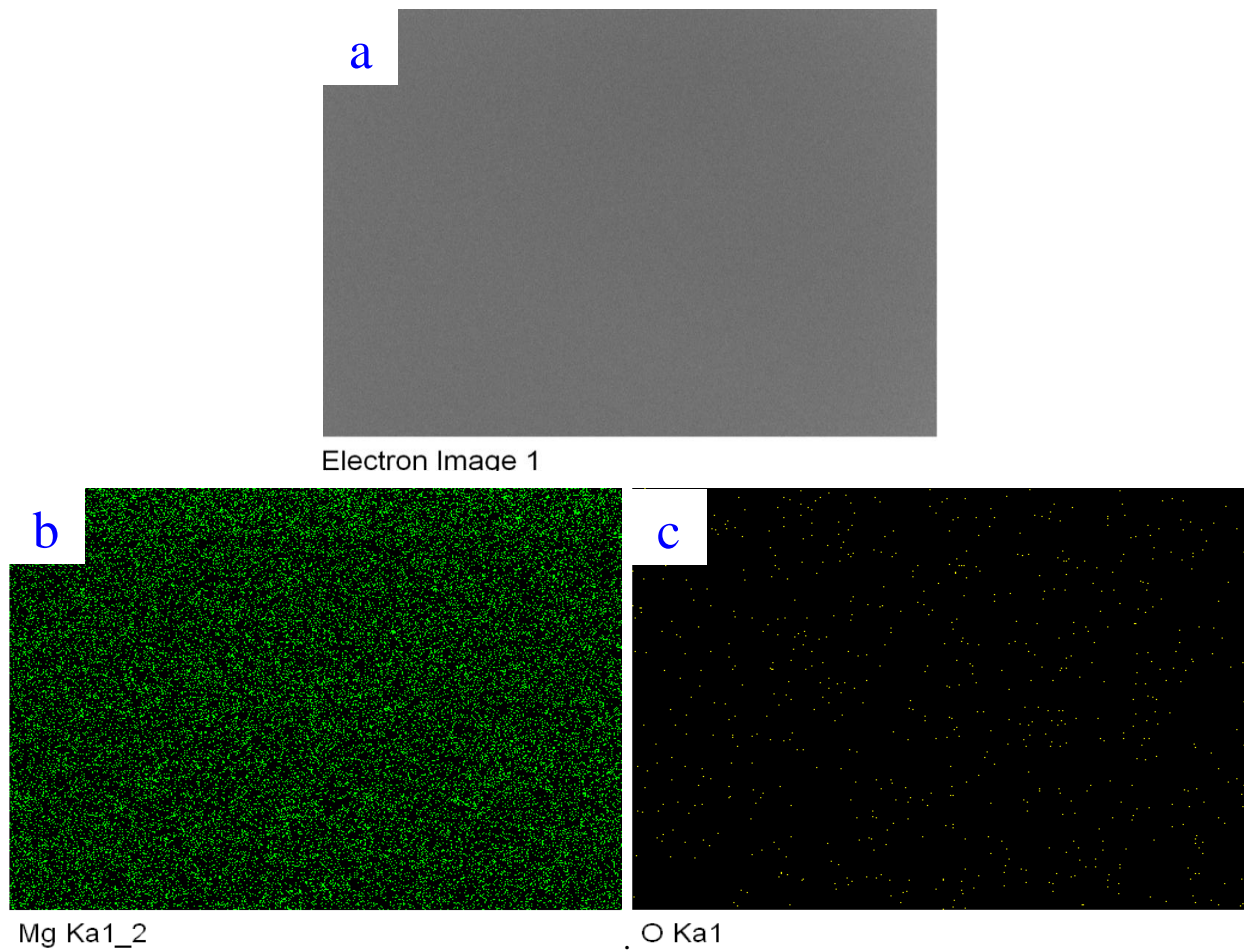
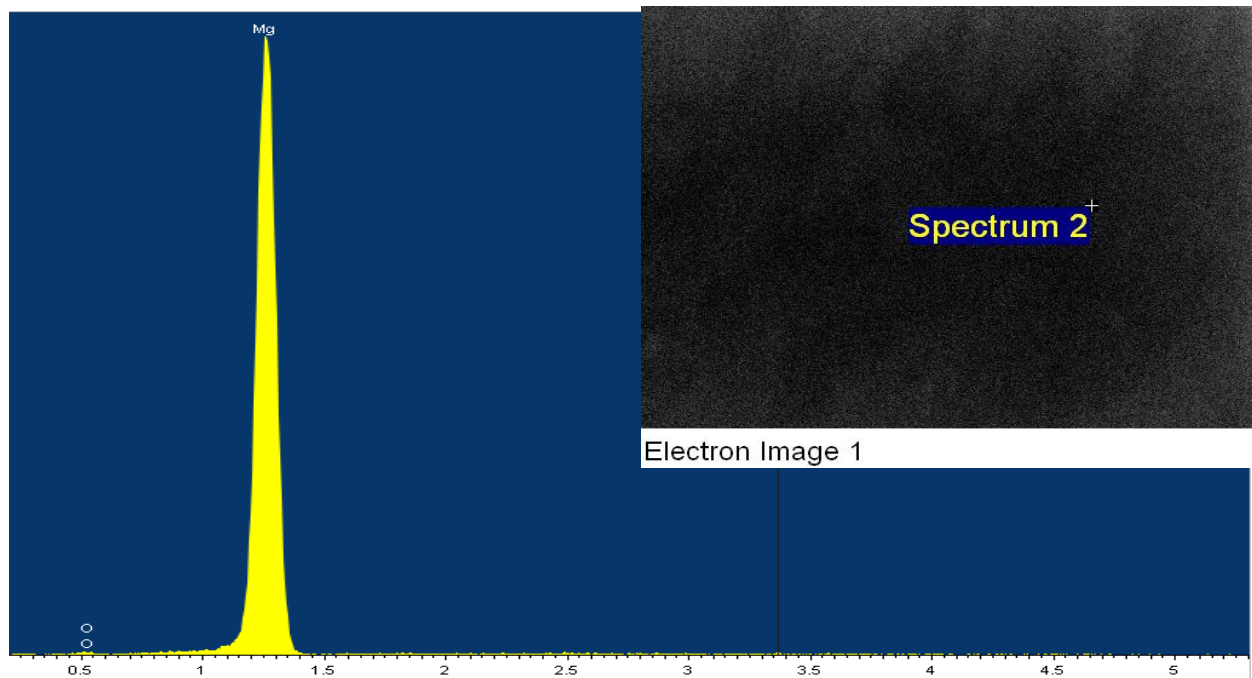


Figure 72: EDS elements map of pure magnesium cooled in the furnace (slow cooling rate) (a) area of interest (b) Magnesium map (c) Oxygen map.



*Figure 73: The EDS spectrum images of pure magnesium cooled in the furnace (slow cooling rate).*

The moderately cooled pure magnesium (MCR-Mg) with a cooling rate of 0.074 °C/Sec was analyzed at 1000 x and 10000 x, as shown in [Figure 74](#). The SEM images showed the same overall formation of pure magnesium in spite of the cooling rate with a clear structure at different magnifications and wasn't able to detect the grain boundary in both SEI and BSI. However, the microstructure and grain size were detectable by using the optical microscope as it was observed in [Figure 59](#). [Figure 75](#) shows the EDS elements map, and the map showed the magnesium element as a main element with the existence of oxygen distributed on the surface. [Figure 76](#) shows the EDS spectrum point analysis, which confirmed the elemental content of magnesium and oxygen with a weight percentage of 99.19% and 0.81 %, respectively.

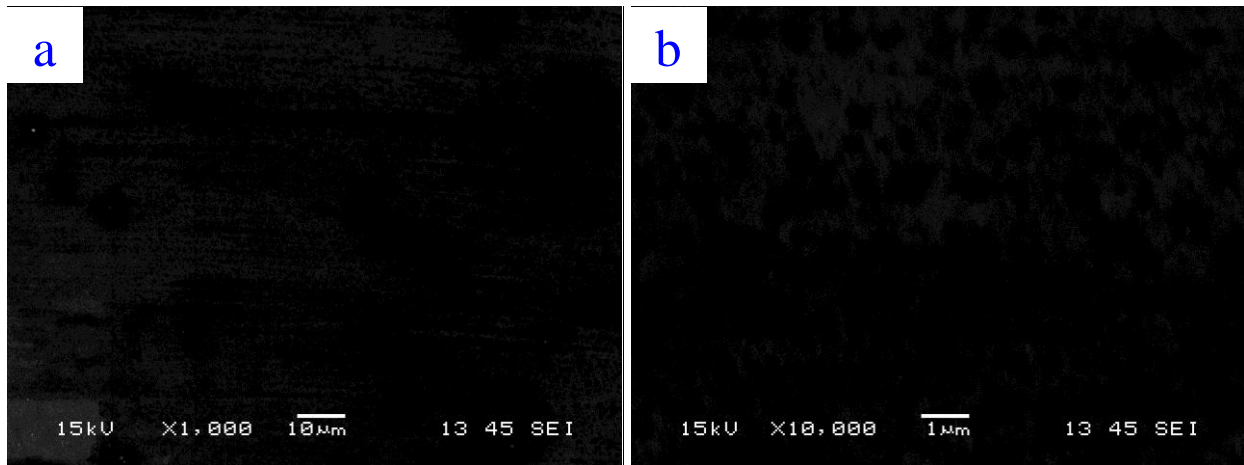


Figure 74: SEM images of pure magnesium cooled in the furnace with uninsulated-ends (moderate cooling) at different magnifications (a) at 1000 x (b) at 10000 x.

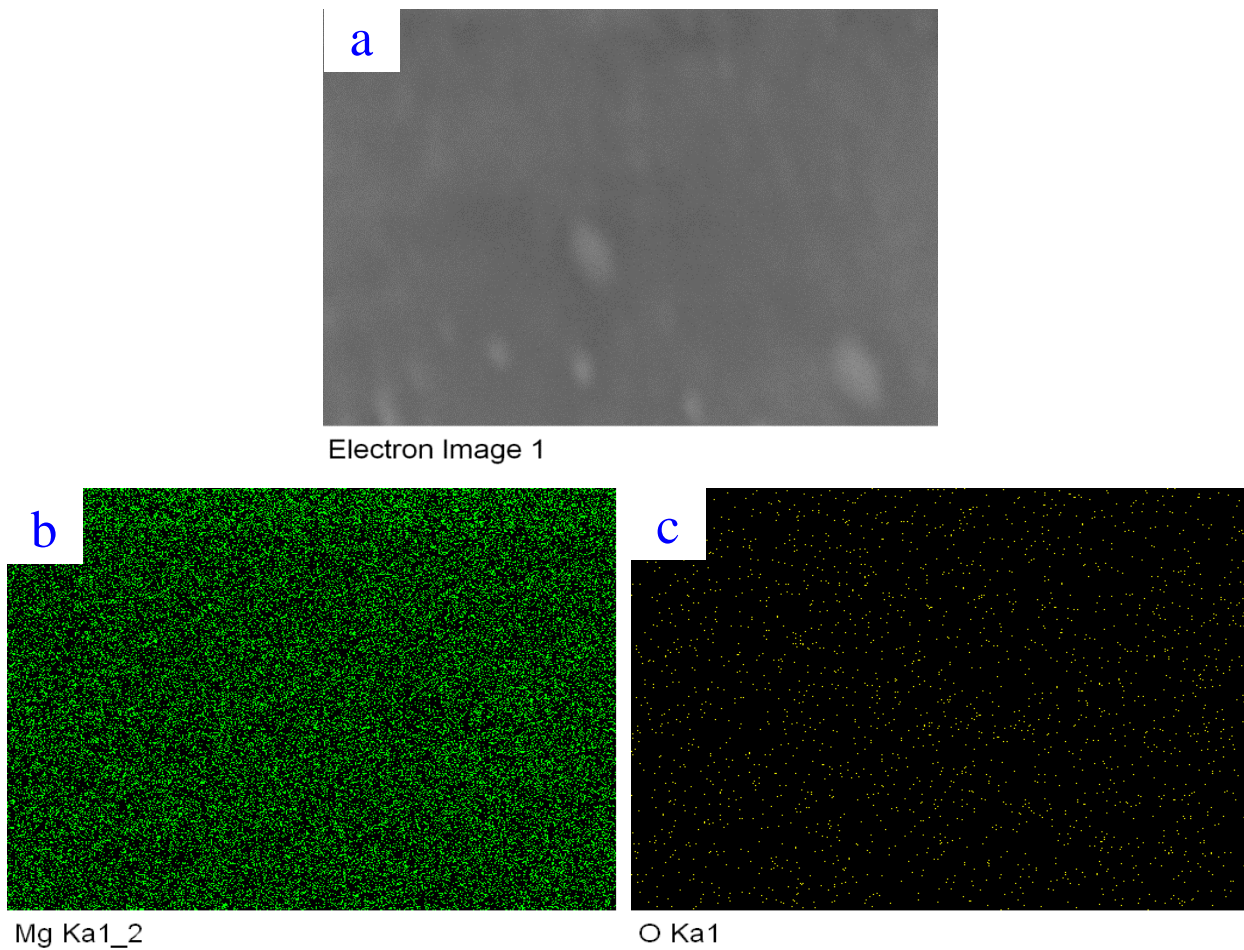
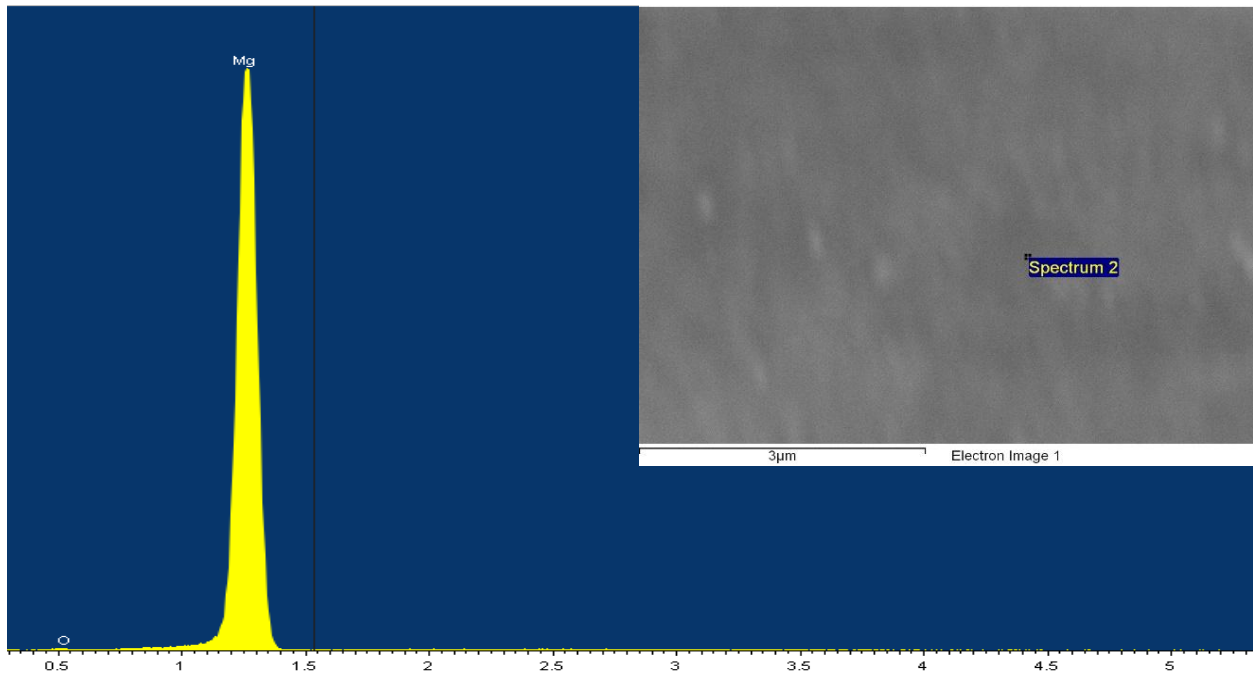


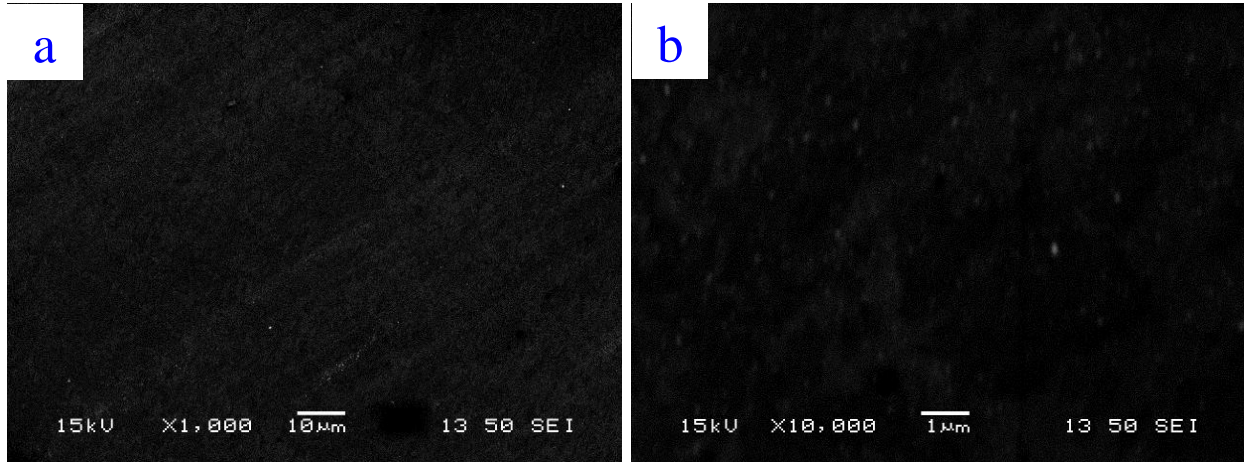
Figure 75: EDS elements map of pure magnesium moderately cooled in the furnace with uninsulated-ends (a) area of interest (b) Magnesium map (c) Oxygen map.



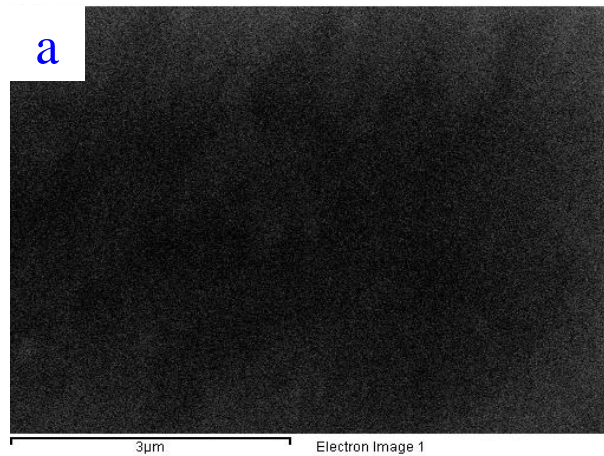
*Figure 76: The sum EDS spectrum images of pure magnesium moderately cooled in the furnace with uninsulated-ends.*

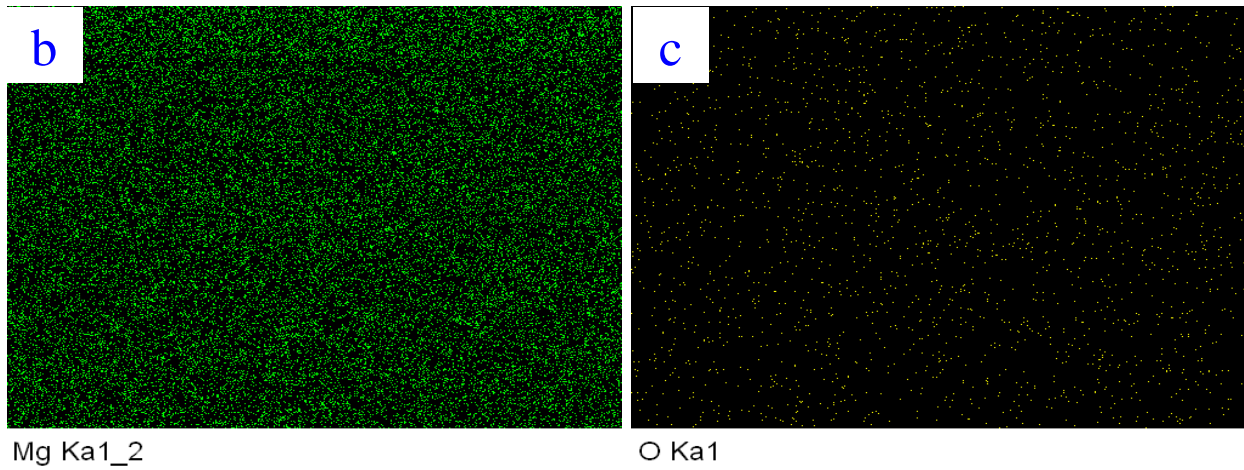
The quenched pure magnesium (HCR-Mg) with cooling rate of 13.5 °C/sec was analyzed at 1000 x and 10000 x, as shown in [Figure 77](#). The SEM images showed no difference in the structure at different magnifications in comparison with pure Mg of different solidification rates. The SEM analysis wasn't able to detect the grain boundary in both SEI and BSI. However, the grain structure was analyzed using the optical microscope as displayed in [Figure 59](#). Furthermore, the sample was analyzed using the EDS spectrum to confirm the elemental content of the system. [Figure 78](#) shows the EDS elements map, and the map showed the magnesium element as a main element with the existence of

oxygen distributed. The point spectrum confirmed presence of magnesium and oxygen with a weight percentage of 99.24% and 0.76%, respectively, as shown in [Figure 79](#).

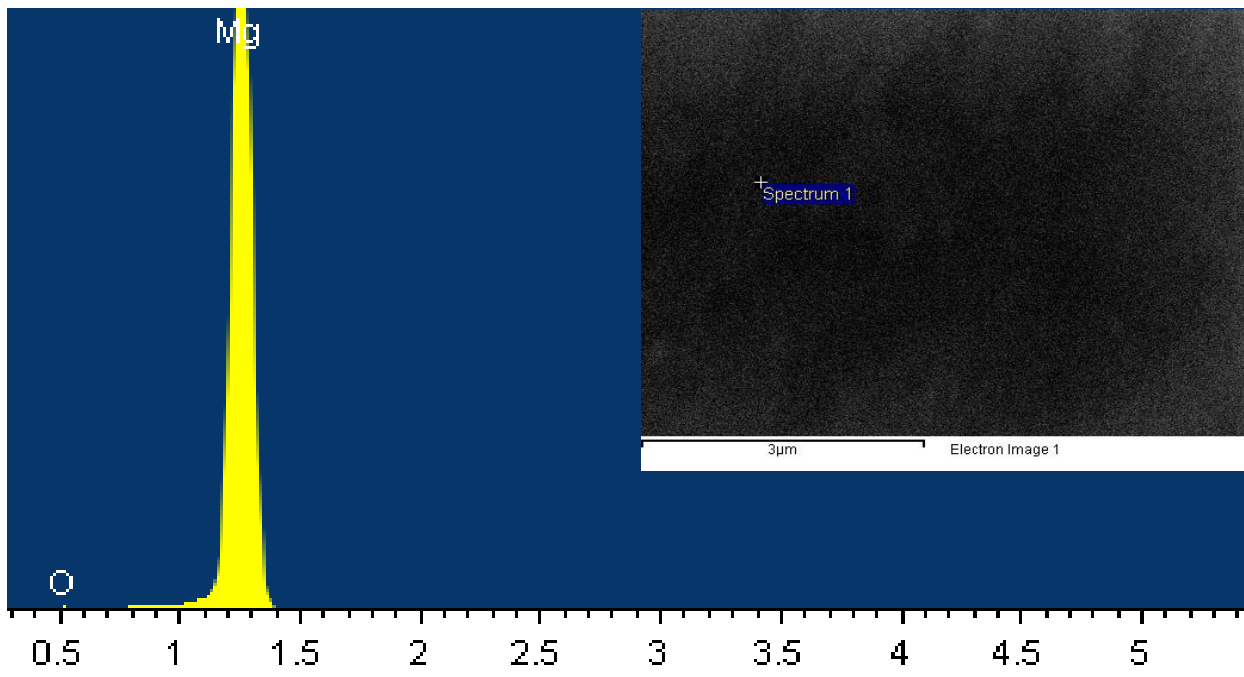


*Figure 77: SEM images of pure magnesium rapidly cooled in liquid CO<sub>2</sub> at different magnifications (a) at 1000 x (b) at 10000 x.*





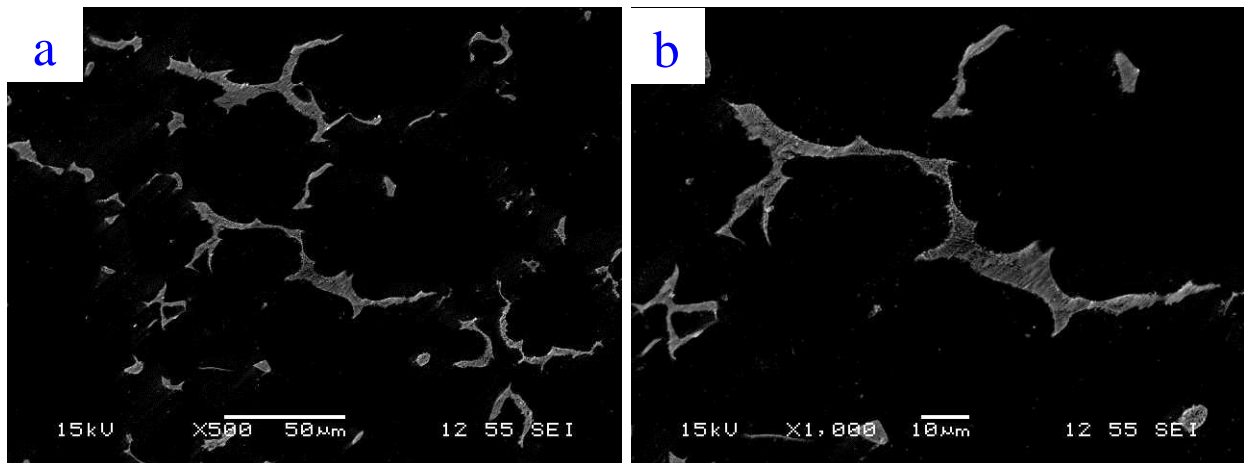
*Figure 78: EDS elements map of pure magnesium rapidly cooled in liquid CO<sub>2</sub> (a) area of interest (b) Magnesium map (c) Oxygen map.*



*Figure 79: The point EDS spectrum images of pure magnesium rapidly cooled in liquid CO<sub>2</sub>.*

The quenched Mg-1Mn-2Zn alloying system with cooling rate of 13.5 °C/sec showed  $\alpha$  phase (the dark color), which represents the matrix (magnesium), and  $\beta$  phase,

which represents the secondary phase (the light color). The distribution of the secondary phase formed a noncontinuous structure, as can be seen clearly in [Figure 80 \(a\) and \(b\)](#). [Figure 80 \(e\) and \(f\)](#) and [Figure 81 \(a-d\)](#) show the secondary phase that consists of eutectic structure ( $\alpha$  and  $\beta$  laminas) and  $\beta$  phase as a longitudinal structure and scattered nodules. The observed structure of the secondary phase showed a higher presence of eutectic than the  $\beta$  phase. Additionally, the laminal thickness of the eutectic was measured to be within an average of 0.148 and 0.108  $\mu\text{m}$  for  $\alpha$  and  $\beta$ , respectively. The formation of the interrupted secondary phase (more brittle phase) with a dendritic spacing of 100  $\mu\text{m}$ , the presence of eutectic structure, and its volume improved the hardness, yield strength, UTS, and ductility by 41%, 25%, and 45% in comparison to quenched pure magnesium. Also, the ductility was increased from 9.5% to 13.03%.



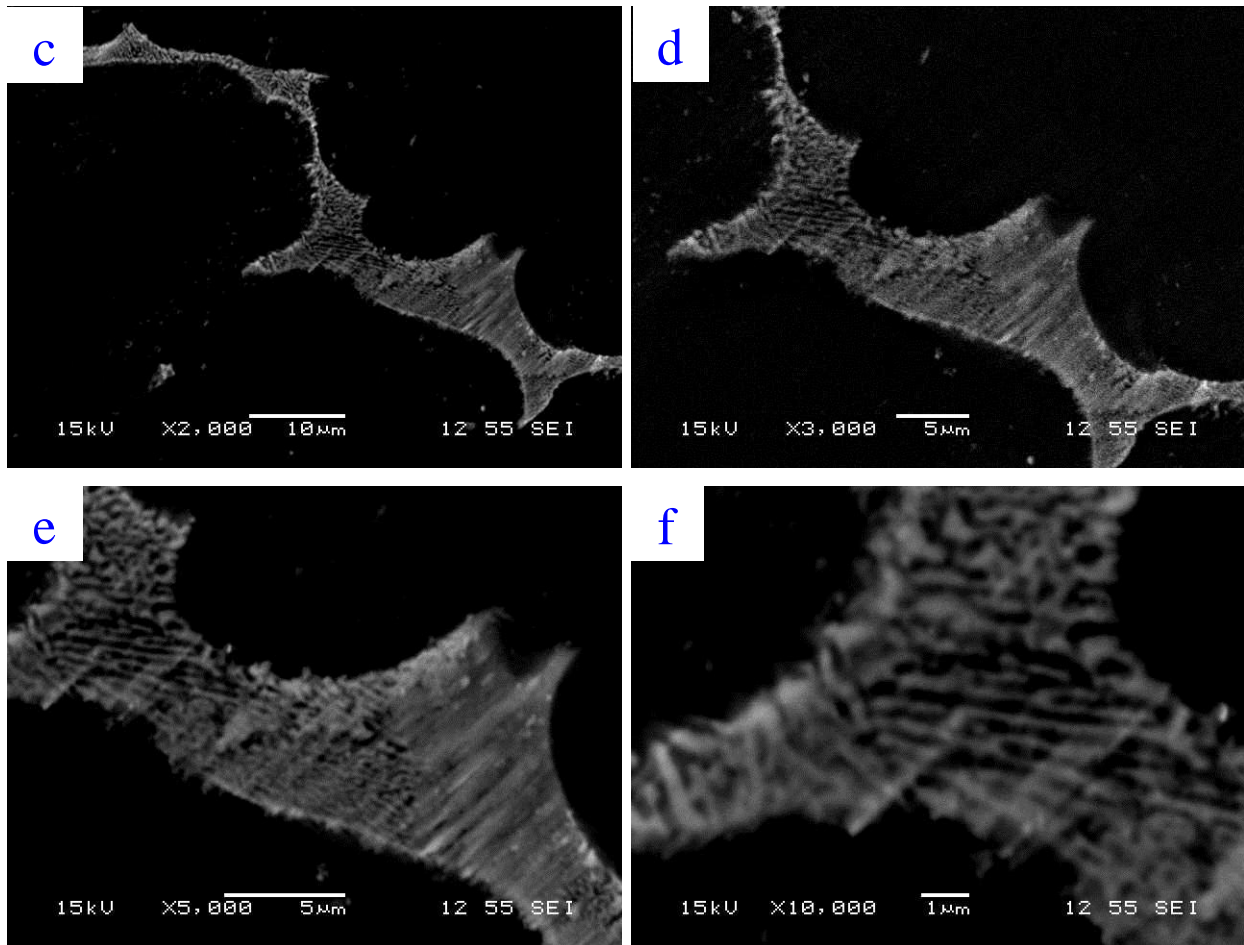
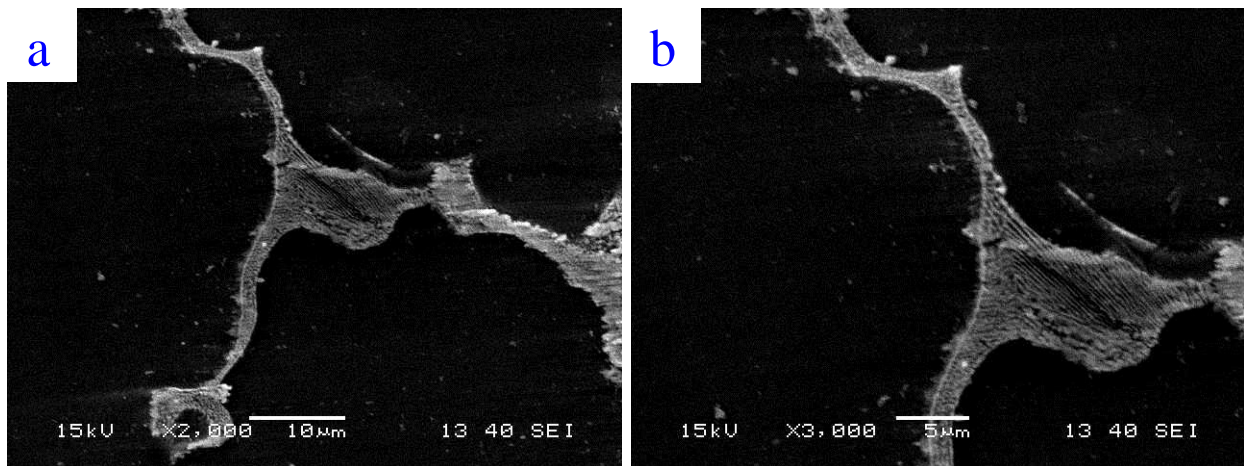
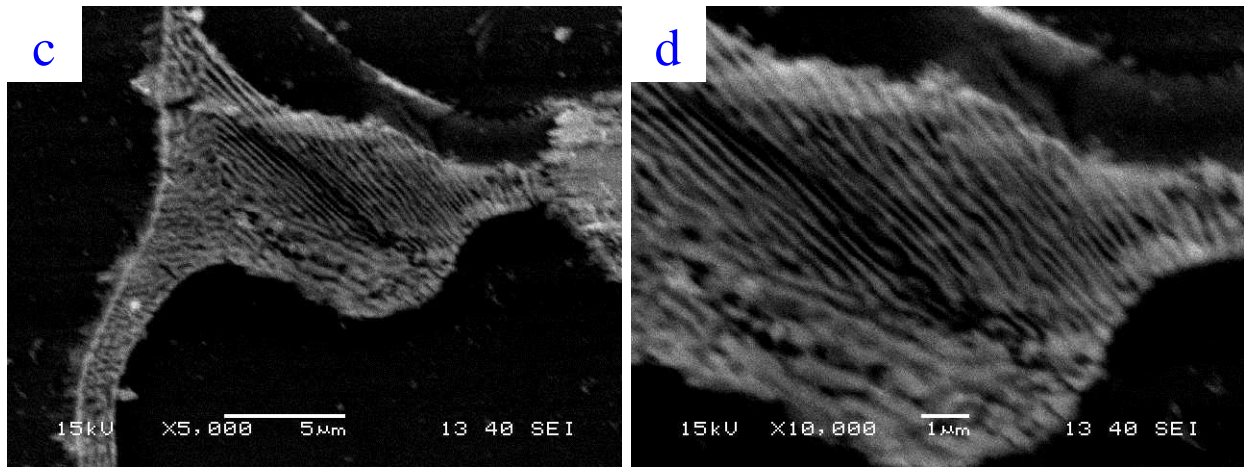


Figure 80: SEM images of Mg-1Mn-2Zn alloying system rapidly cooled in liquid CO<sub>2</sub> at different magnifications at 500 x (b) at 1000 x (c) at 2000 x (d) at 3000 x (e) at 5000 x (f) at 10000 x.





*Figure 81: SEM images of the eutectic phase of Mg-1Mn-2Zn alloying system rapidly cooled in liquid CO<sub>2</sub> at different magnifications (a) at 2000 x (b) at 3000 x (c) at 5000 x (d) at 10000 x.*

Figure 82 lays out the EDS elements map, and the map shows the structure of the  $\beta$  phase distributed in the matrix  $\alpha$  (magnesium). The map analysis detected that the secondary phase mainly consists of Zn element and Mg-Zn containing in the case of eutectic laminas. Also, manganese and oxygen were detected to be spread on the matrix and secondary phase. The map of oxygen was observed to be denser on the matrix than on the secondary phase, which could be due to the reactivity of the matrix (mainly magnesium) being higher than the secondary phase (mainly zinc). However, the accuracy of the distribution of the manganese is debatable. Furthermore, the sample was analyzed using the EDS spectrum to confirm the elemental content of the system. Figure 83 shows the sum spectrum of Mg, Zn, Mn, and O.

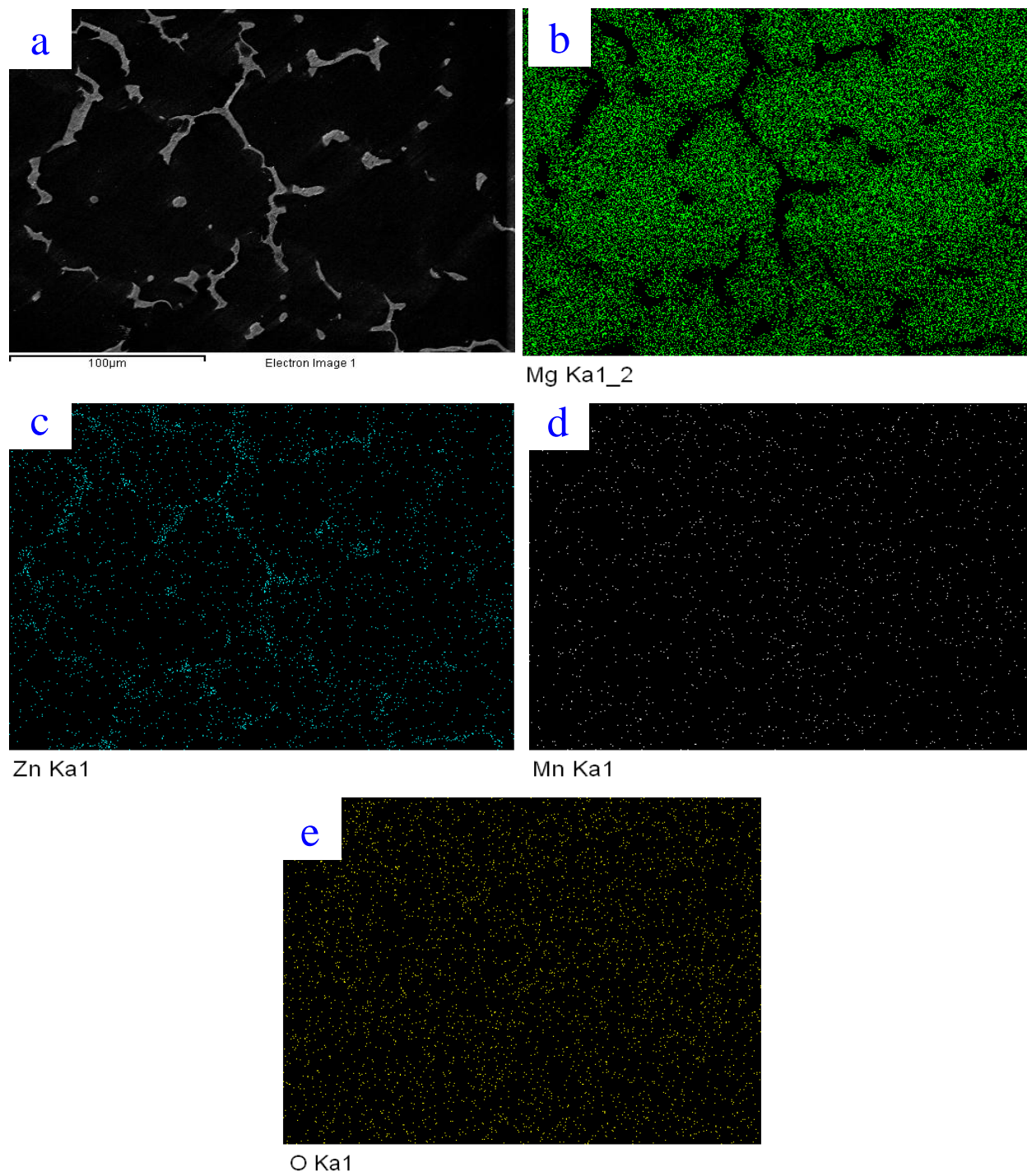
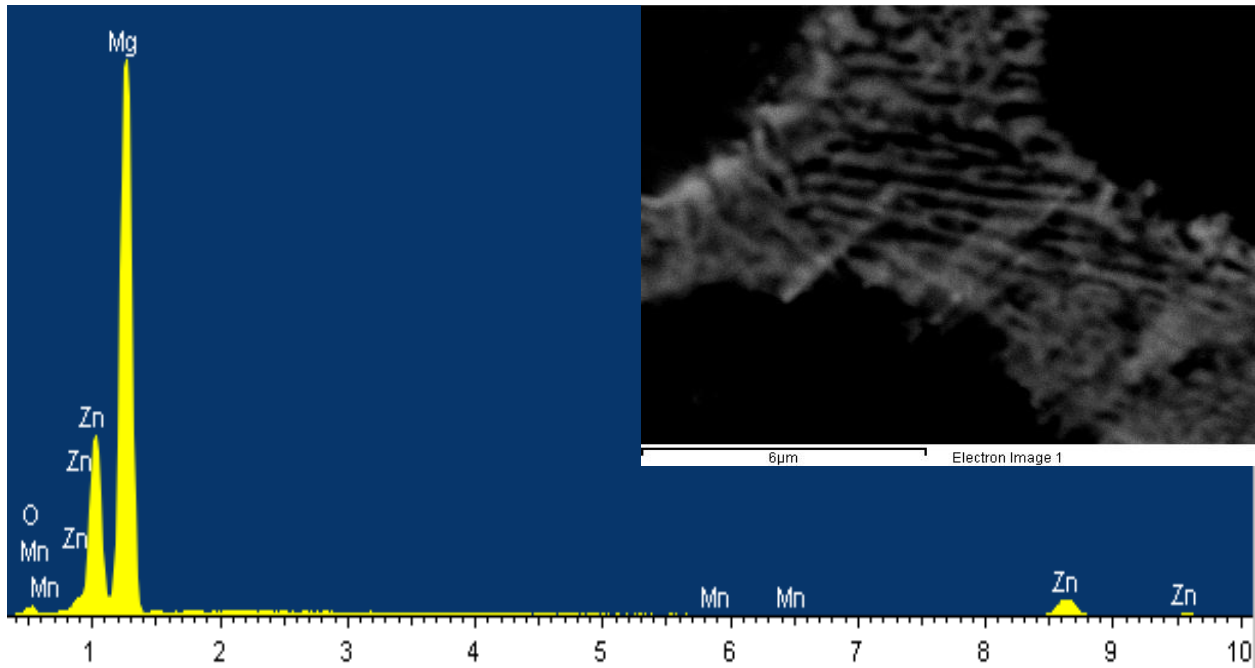


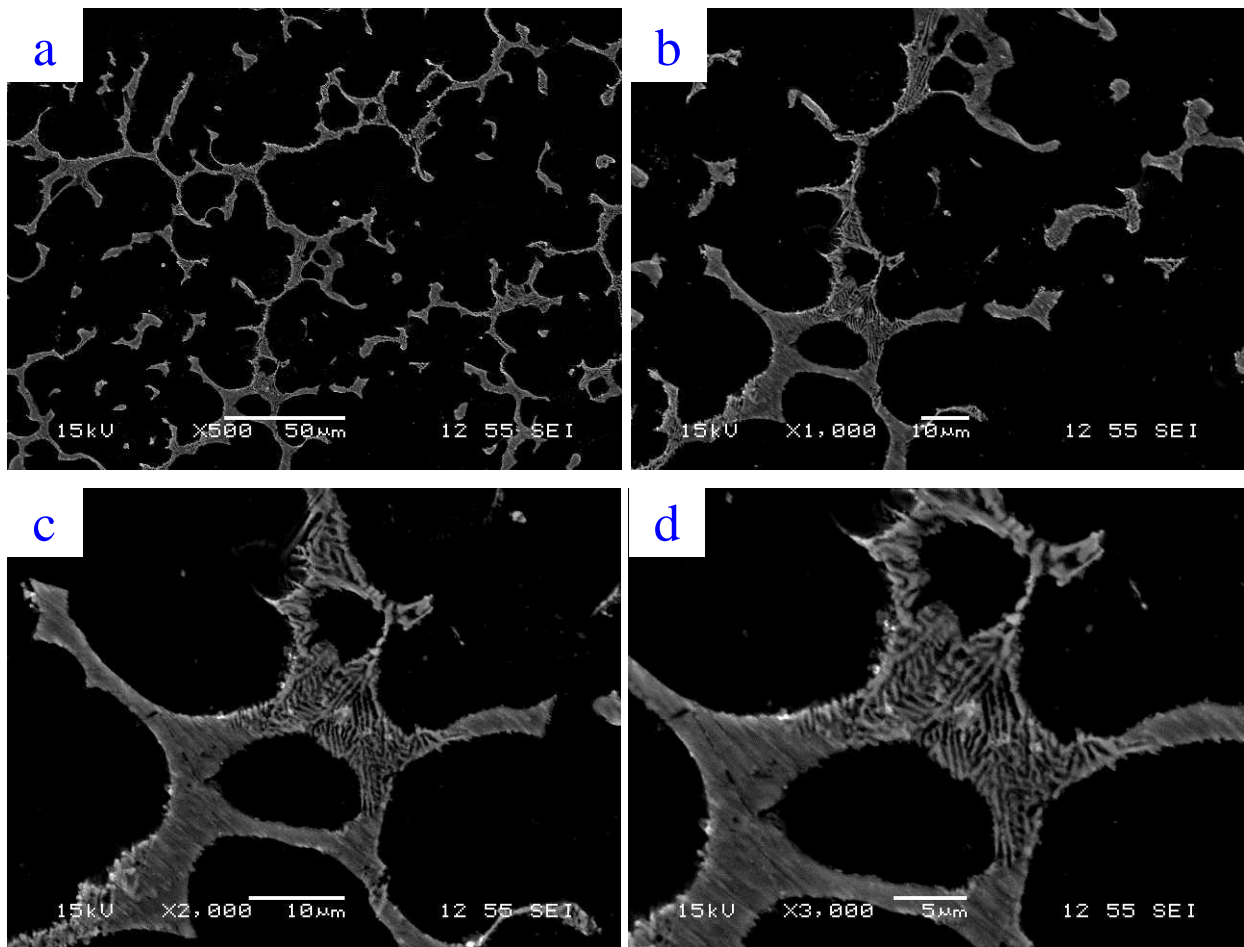
Figure 82: EDS elements map of Mg-1Mn-2Zn alloying system rapidly cooled in liquid CO<sub>2</sub> (a) area of interest (b) Magnesium map (c) Zinc map (d) Manganese map (e) Oxygen map.



*Figure 83: The sum EDS spectrum images of the primary and secondary phases Mg-1Mn-2Zn alloying system rapidly cooled in liquid CO<sub>2</sub>.*

The quenched Mg-1Mn-4Zn alloying system with cooling rate of 13.5 °C/sec showed the same phases of Mg-1Mn-2Zn alloying system where SEM analysis of the system revealed a structure of  $\alpha$  phase (the dark color), which represents the matrix (magnesium), and  $\beta$  phase which represents the secondary phase (the light color). Due to the increase of zinc content, the distribution of the secondary phase formed smaller dendritic spacing (68.75  $\mu\text{m}$ ) than Mg-1Mn-2Zn alloying system with a semi-continuous network of the secondary phase, as can be seen clearly in Figure 84 (a) and (b). Figure 84 (a-f) shows the secondary phase that consists of eutectic structure ( $\alpha$  and  $\beta$  laminas) and  $\beta$  phase as a longitudinal structure and scattered nodules.

The observed structure of the secondary phase showed a lower presence of eutectic and a higher presence of  $\beta$  phase in comparison to Mg-1Mn-2Zn alloying system. The laminal thickness of the eutectic increased and was measured to be within an average of 0.48 and 0.39  $\mu\text{m}$   $\alpha$  and  $\beta$ , respectively. The formation of a more connected secondary phase (brittle phase) with a dendritic spacing of 68.75  $\mu\text{m}$ , the increase in the number of branched arms of the secondary phase, the decrease in the presence of eutectic structure, and its volume caused the reduction in the UTS and ductility by 70% and 92%, respectively, in comparison to Mg-1Mn-2Zn alloying system. However, the hardness was increased due to the increase in the presence of the more brittle phase.



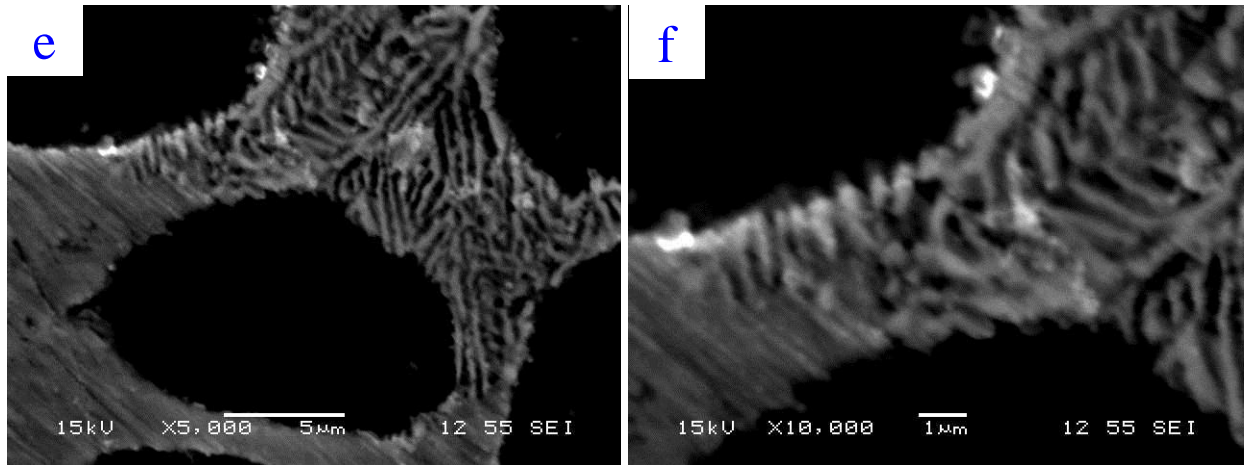


*Figure 84: SEM images of Mg-1Mn-4Zn alloying system rapidly cooled in liquid CO<sub>2</sub> at different magnifications (a) at 500 x (b) at 1000 x (c) at 2000 x (d) at 3000 x (e) at 5000 x (f) at 10000 x.*

Figure 85 shows the EDS elements map, and the map showed the structure of the  $\beta$  phase distributed in the matrix  $\alpha$  (magnesium) as dendritic structure and scattered nodules. The map analysis detected that the secondary phase mainly consists of Zn element and Mg-Zn containing. Also, manganese and oxygen were detected to be spreading on the matrix and secondary phase. However, the accuracy of the distribution of the manganese is debatable. The map of oxygen was observed to be denser in the matrix than the secondary phase, which could be due to the reactivity of the matrix (mainly magnesium) being higher than the secondary phase (mainly zinc). Furthermore, the sample was analyzed using the EDS spectrum to confirm elemental content of the system. Figure 86 shows the sum spectrum of Mg, Zn, Mn, and O.

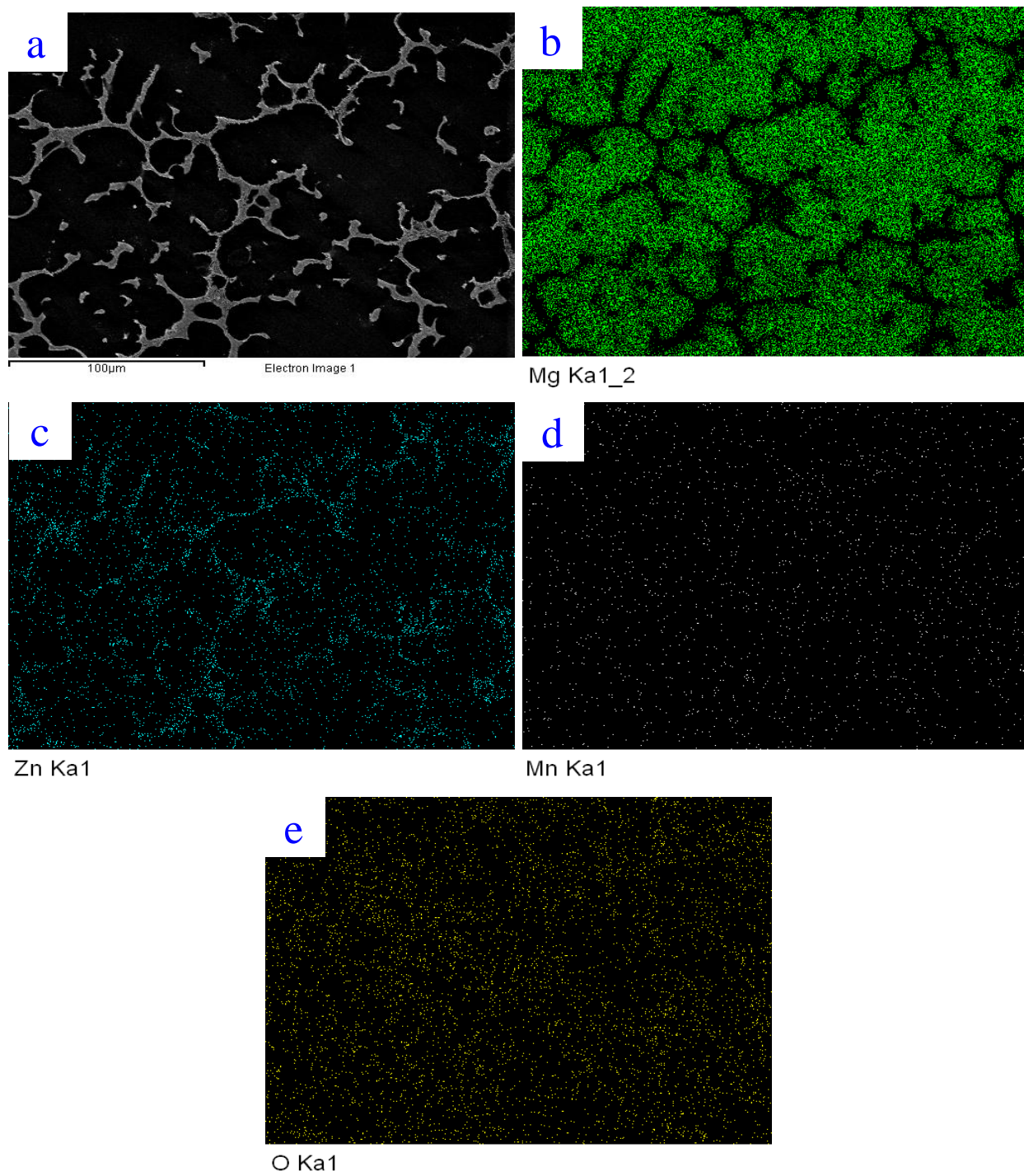
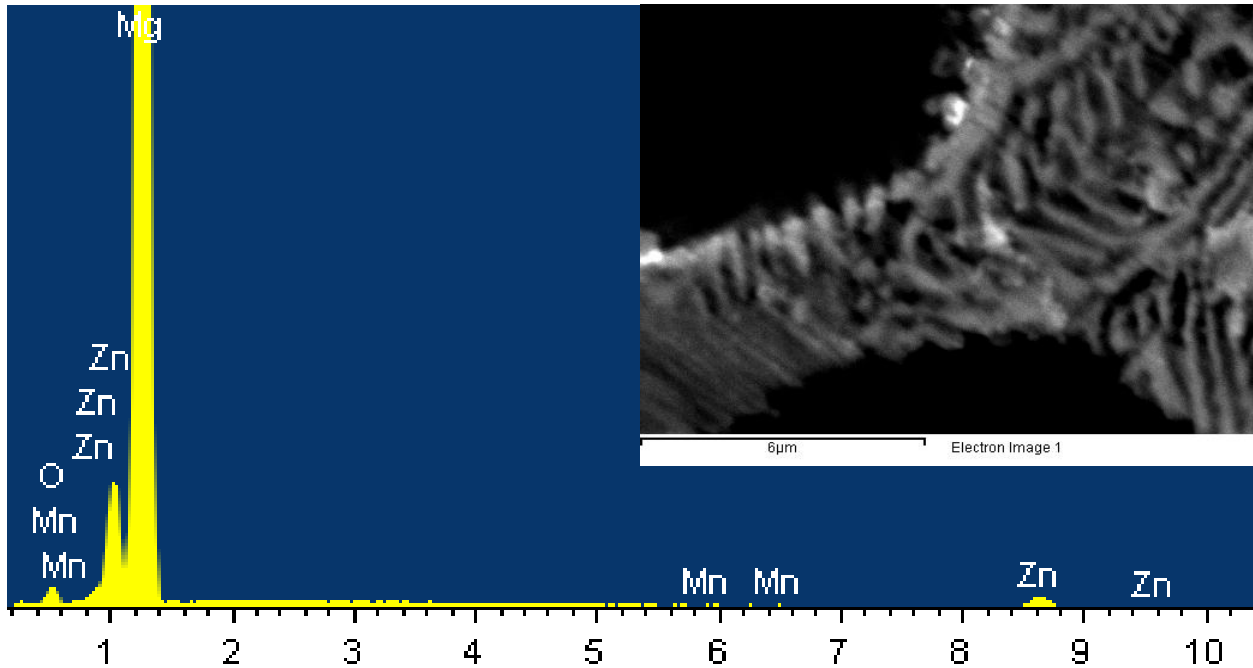


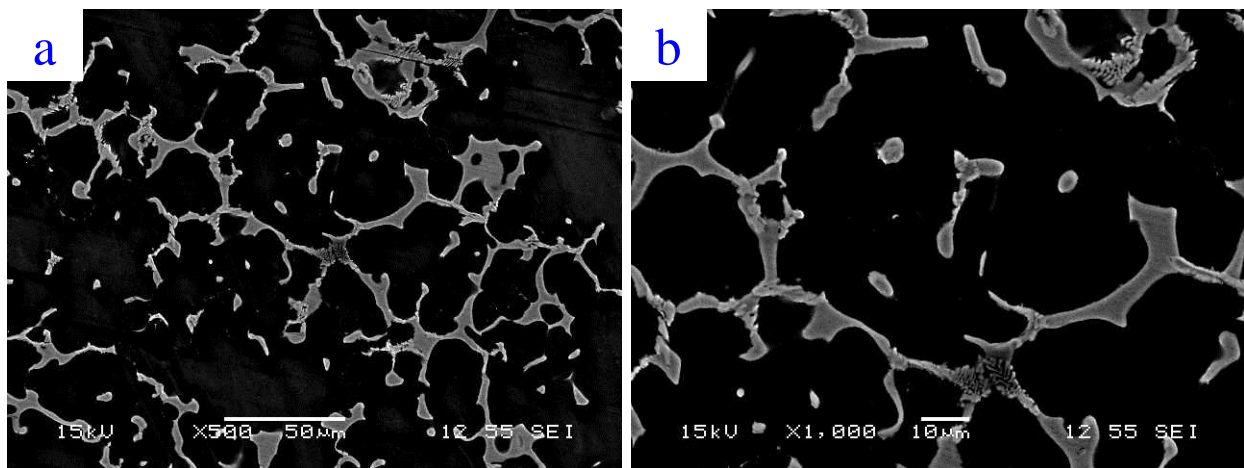
Figure 85: EDS elements map of Mg-1Mn-4Zn alloying system rapidly cooled in liquid CO<sub>2</sub> (a) area of interest (b) Magnesium map (c) Zinc map (d) Manganese map (e) Oxygen map.



*Figure 86: The sum EDS spectrum images of Mg-1Mn-4Zn alloying system rapidly cooled in liquid CO<sub>2</sub>.*

The quenched Mg-1Mn-4Zn-0.5Na alloying system with cooling rate of 13.5 °C/sec showed the same phases of Mg-1Mn-4Zn alloying system with scattered highly reactive phase. The SEM analysis of the system revealed a structure of images  $\alpha$  phase, which represents the matrix (magnesium),  $\beta$  phase (the secondary phase), and clusters of a reactive phase with size of 100  $\mu\text{m}$ . This alloying system formed the smallest spacing of 41.3  $\mu\text{m}$  in comparison with all Mg-Mn-Zn based alloys with semi-continuous network of the secondary phase, as can be seen clearly in [Figure 87 \(a\) and \(b\)](#). [Figure 87 \(a-d\)](#) shows the secondary phase that consists of eutectic structure ( $\alpha$  and  $\beta$  laminas) and  $\beta$  phase as a longitudinal structure and scattered nodules.

The observed structure of the secondary phase showed a very low presence and a short laminas eutectic and a higher presence of  $\beta$  phase in comparison to Mg-1Mn-4Zn alloying system. The laminal thickness of the short eutectic structure increased and was measured to be within an average of 0.45 and 0.53  $\mu\text{m}$   $\alpha$  and  $\beta$ , respectively. Besides the eutectic and  $\beta$  structure, there is another secondary phase that was observed to be dispersed in the matrix, which can be seen in Figure 88. The mechanical properties were affected by the formation of a scattered-brittle-reactive phase with a content of Mg-Mn-Zn-Na-O; continuous secondary phase with more brittleness effect; a dendritic spacing of 41.3  $\mu\text{m}$  in addition to increasing the branched arms of the secondary phase; a significant decrease in the presence of eutectic structure and its volume led to the increase of the hardness and reduction of the impact strength by 83% in comparison to Mg-1Mn-4Zn alloying system. However, the tensile properties did not show a significant change.



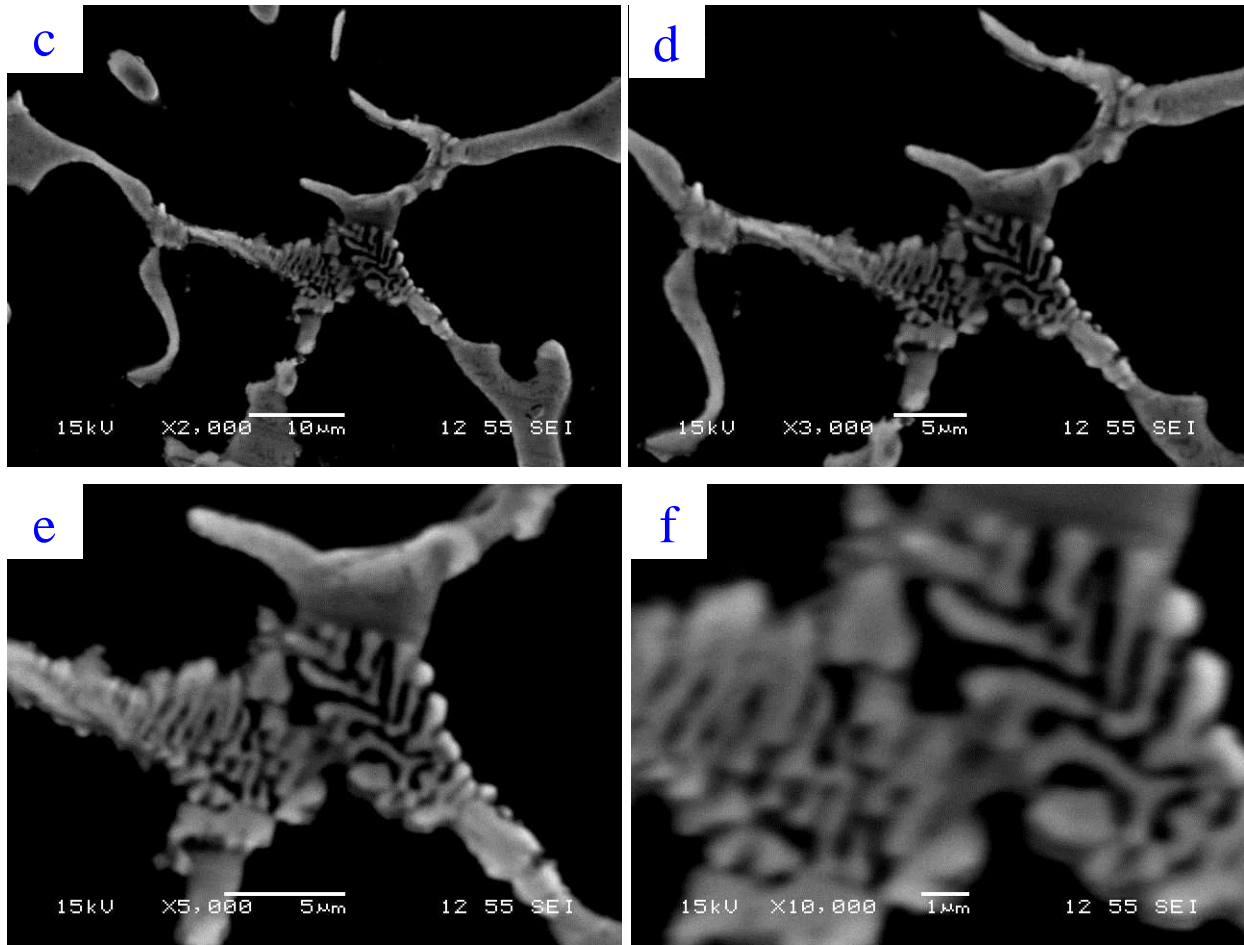
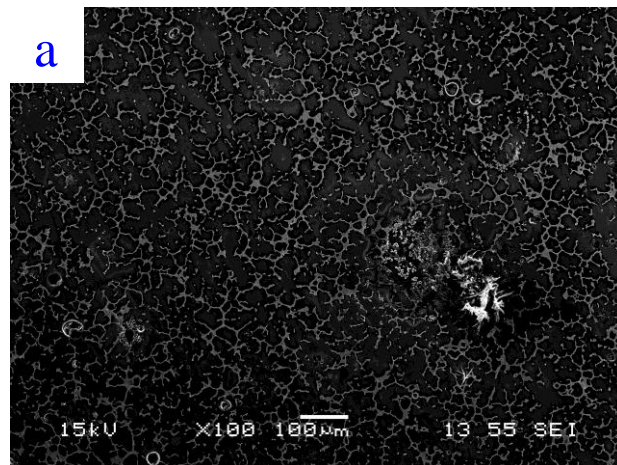
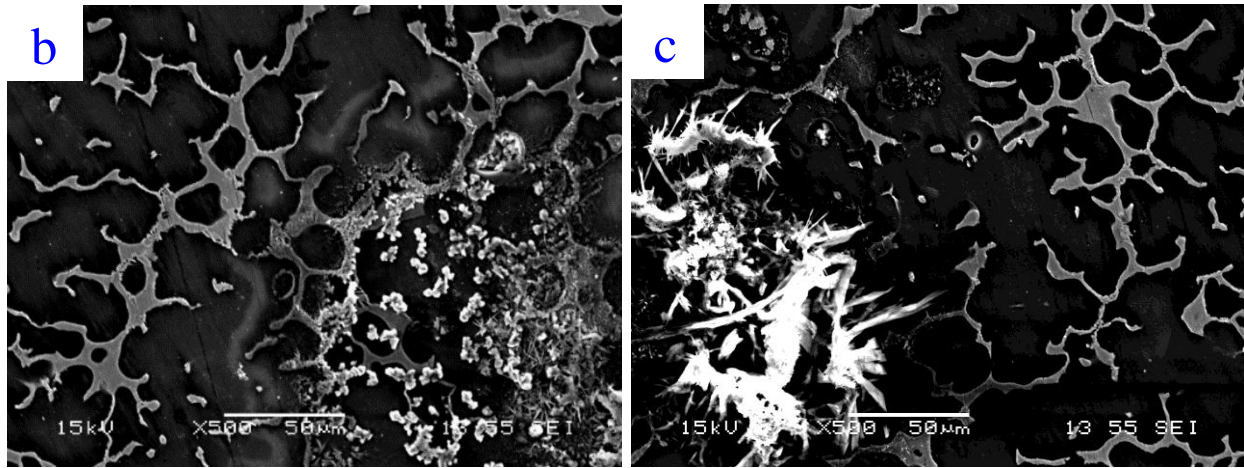


Figure 87: SEM images of Mg-1Mn-4Zn-0.5Na alloying system rapidly cooled in liquid CO<sub>2</sub> at different magnifications (a) at 500 x (b) at 1000 x (c) at 2000 x (d) at 3000 x (e) at 5000 x (f) at 10000 x.





*Figure 88: The formed scattered-brittle-reactive secondary phase in Mg-1Mn-4Zn-0.5Na.*

The alloying system was analyzed using EDS to confirm the elemental content of the system. [Figure 89](#) shows the EDS elements map, and the map showed a structure of  $\beta$  phase distributed in the matrix  $\alpha$  (magnesium) as a dendritic structure and scattered nodules of the secondary phases. The map analysis detected that the first secondary phase mainly consists of Zn element and Mg-Zn containing, which is structured in forms of eutectic ( $\alpha$  and  $\beta$  laminas) and  $\beta$  phase as a longitudinal structure and scattered nodules.

It was noticed that the manganese and oxygen were detected to be spreading in the matrix and other secondary phases. The map of oxygen was observed to be denser in the matrix and around the Mg-Zn-containing secondary phase than on the phase itself, which could be due to the reactivity of the matrix ( $\alpha$  magnesium) being higher than the secondary phase (mainly zinc). However, the oxygen formation was recorded to be heavily piled up on the top of Mg-Mn-Zn-Na-O-containing phase. This phase was spotted to be assembled in a scattered-brittle-reactive formation with a content of Mg-Mn-Zn-Na-O and size of 100

$\mu\text{m}$ . The elemental map for this phase detected heavy formation of oxide clusters at the surface, as shown in [Figure 92](#).

Furthermore, the EDS point spectrum was used to analyze the matrix and the secondary phases, as shown in [Figure 90](#) and [Figure 91](#). The analysis confirms that the matrix mainly consists of Mg while the EDS point spectrum of the main secondary phase detected the high content of magnesium and zinc in comparison to other elements: Mn, Na and O in the analyzed sample. On the other side, the sum spectrum of the reactive cluster of phase showed increased intensity of the peaks of the alloying elements. It's worth mentioning that the accuracy of the distribution of the manganese and sodium is debatable. [Figure 93](#) shows the sum spectrum of the scattered-brittle-reactive secondary phase of Mg, Zn, Mn, Na and O.

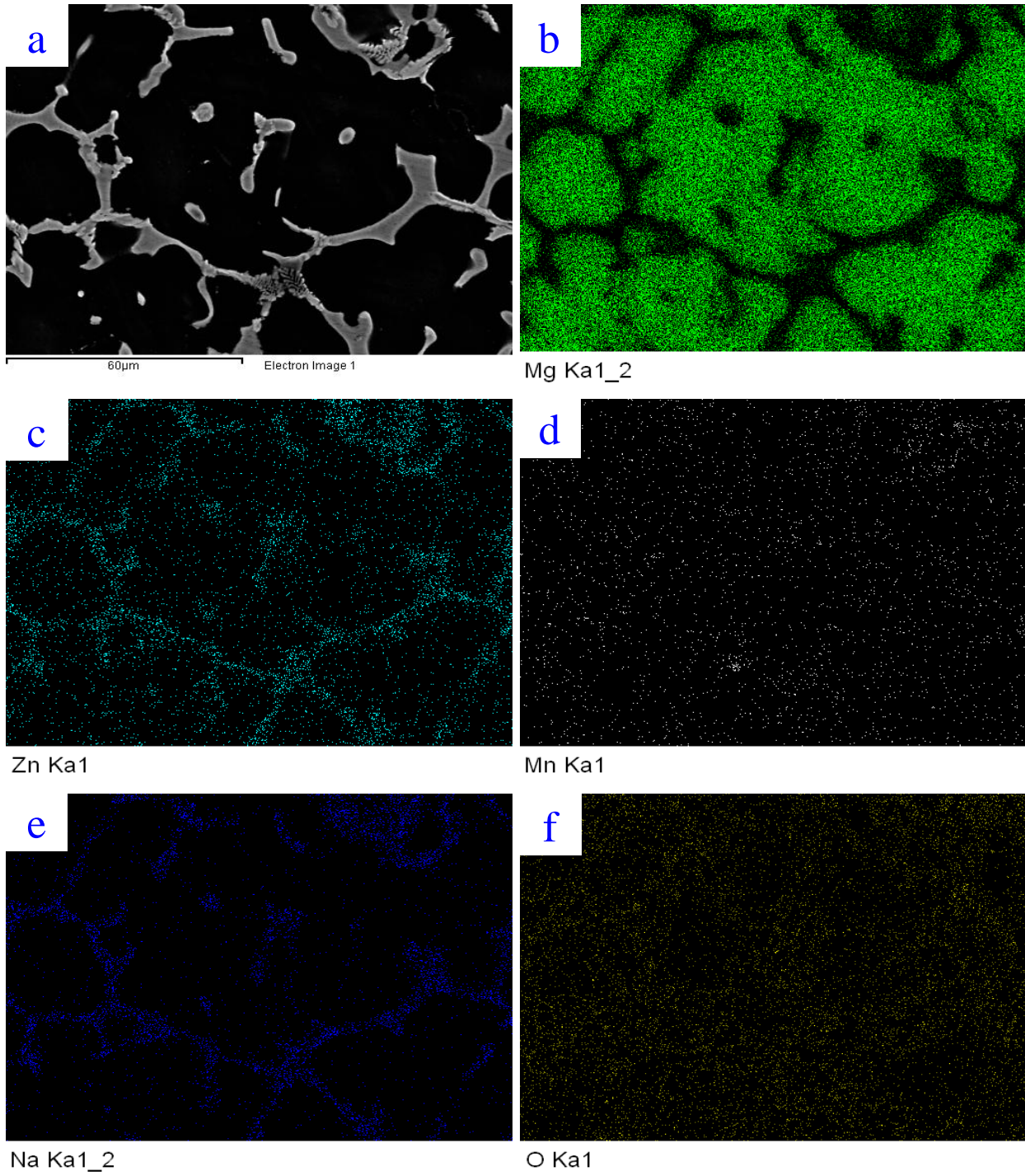


Figure 89: EDS elements map of Mg-1Mn-4Zn-0.5Na alloying system rapidly cooled in liquid CO<sub>2</sub> (a) area of interest (b) Magnesium map (c) Zinc map (d) Manganese map (e) Sodium map (f) Oxygen map.

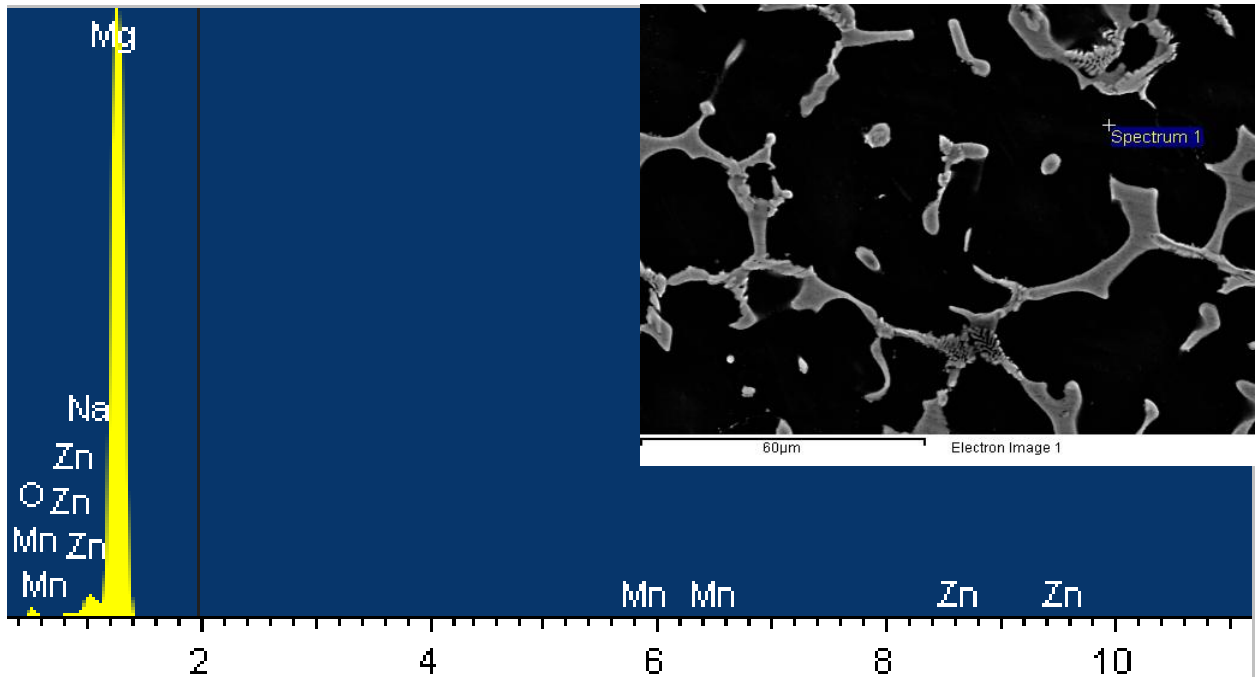


Figure 90: The point EDS spectrum image for the matrix of Mg-1Mn-4Zn-0.5Na alloying system rapidly cooled in liquid CO<sub>2</sub>.

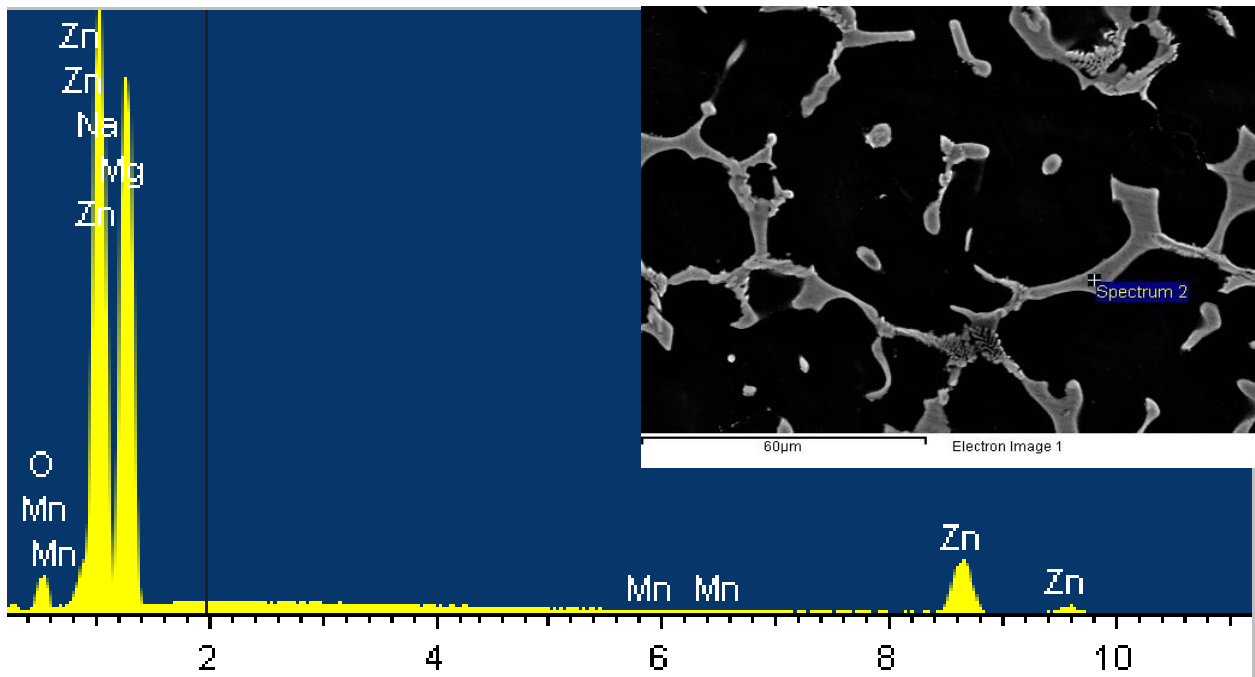
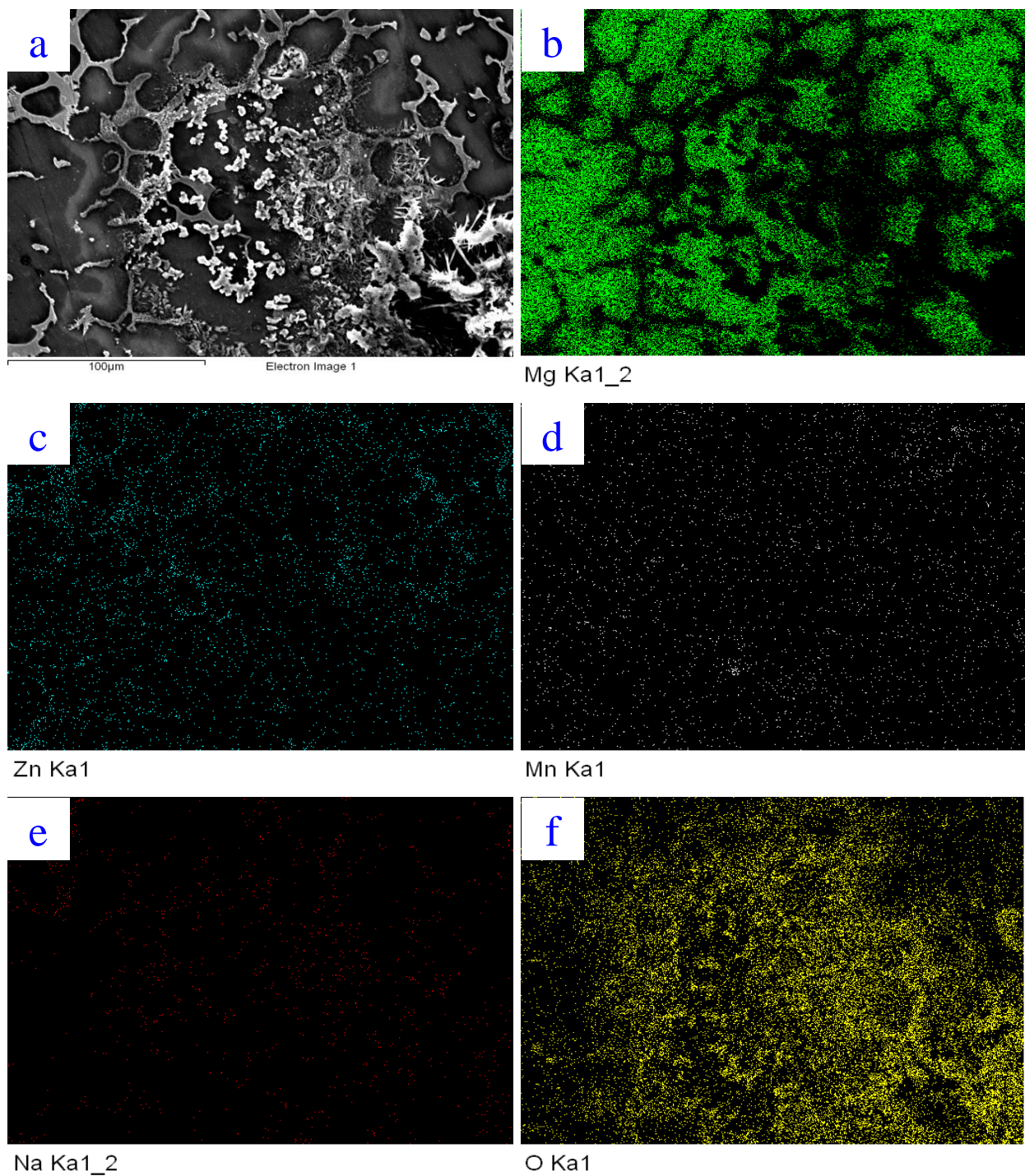
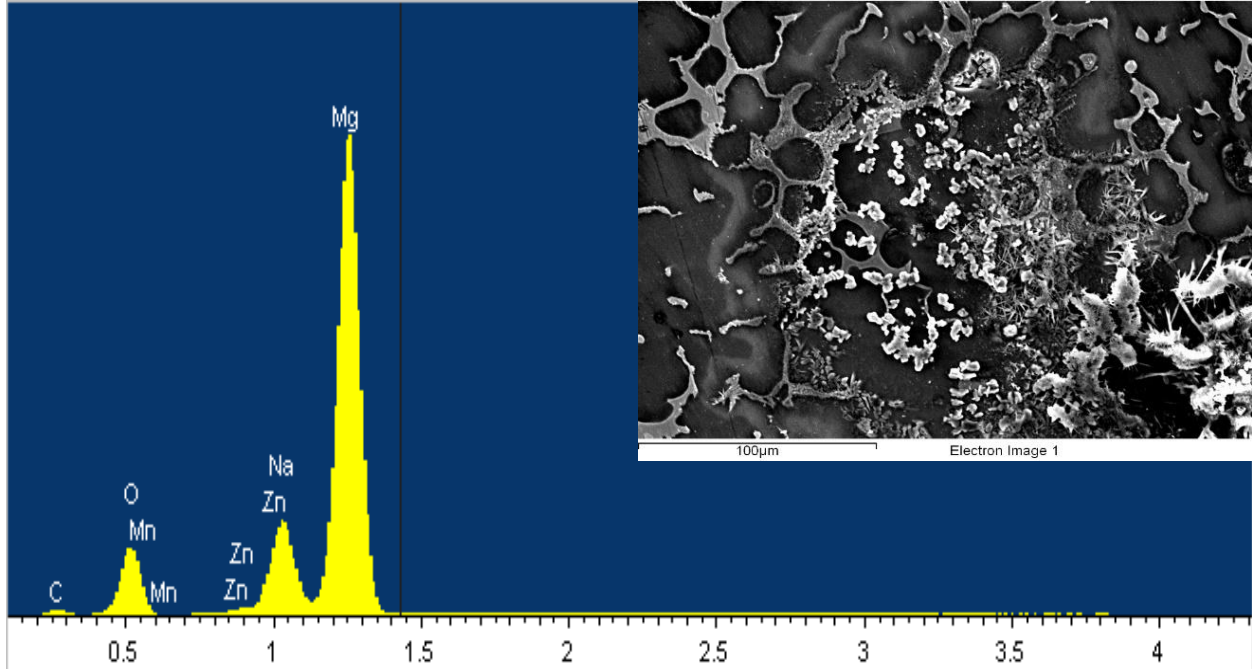


Figure 91: The point EDS spectrum image for the secondary phase of Mg-1Mn-4Zn-0.5Na alloying system rapidly cooled in liquid CO<sub>2</sub>.



*Figure 92: EDS elements map for the formed scattered-brittle-reactive secondary phase of Mg-1Mn-4Zn-0.5Na alloying system rapidly cooled in liquid CO<sub>2</sub> (a) area of interest (b) Magnesium map (c) Zinc map (d) Manganese map (e) Sodium map (f) Oxygen map.*



*Figure 93: The sum EDS spectrum image for the formed scattered-brittle-reactive secondary phase of Mg-1Mn-4Zn-0.5Na alloying system rapidly cooled in liquid CO<sub>2</sub>.*

Figure 94 shows the structure of the quenched Mg-1Mn-4Zn-0.5K alloying system with cooling rate of 13.5 °C/sec. This alloying system revealed the same phases of Mg-1Mn-4Zn alloying system with a less connected network of the secondary phase and slightly thicker  $\beta$  phase. Additionally, the formation of eutectic phase in Mg-1Mn-4Zn-0.5K alloying system was noticed to be different than the eutectic of Mg-1Mn-4Zn and Mg-1Mn-4Zn-0.5Na. However, The SEM analysis of the system revealed a same main structure of  $\alpha$  phase, which represents the matrix (magnesium), and  $\beta$  phase, which represents the secondary phase.

Figure 94 (c-f) shows the secondary phase that consists of eutectic structure ( $\alpha$  and  $\beta$  laminas) and  $\beta$  phase as a longitudinal structure and scattered nodules. This alloying

system formed a dendritic spacing of 59.67 $\mu\text{m}$ , which is smaller than the spacing of Mg-1Mn-4Zn alloying system (68.75  $\mu\text{m}$ ) and bigger than the spacing of Mg-1Mn-4Zn-0.5Na alloying system (41.3  $\mu\text{m}$ ). The difference in spacing could be due to the addition of Na, which led to the increase in the thickness of  $\beta$  in forms of a secondary phase and eutectic laminas.

The increase in  $\beta$  thickness led to the absorption of more zinc and the reduction in the formation of a continuous network of the secondary phase and its arms in the matrix, as can be seen clearly in [Figure 94 \(a\) and \(b\)](#). The laminal thickness of the eutectic structure was measured to be within an average of 0.242 and 0.569  $\mu\text{m}$   $\alpha$  and  $\beta$ , respectively. The observed structure of the secondary phase showed a presence of eutectic and thicker laminas of  $\beta$  than  $\alpha$  laminas in comparison to Mg-1Mn-4Zn, Mg-1Mn-4Zn-0.5Na, and Mg-1Mn-4Zn-0.25Na-0.25K alloying systems.

Besides the eutectic and  $\beta$  structure, no other secondary phase was observed in the matrix. The production of discontinuous secondary phase (more brittle phase) with less branched arms and dendritic spacing of 59.67  $\mu\text{m}$  besides the presence of eutectic structure increased the ultimate tensile strength and ductility by 49% and 139%, respectively. Also, it is reduced the hardness and impact strength slightly in comparison to Mg-1Mn-4Zn alloying system.

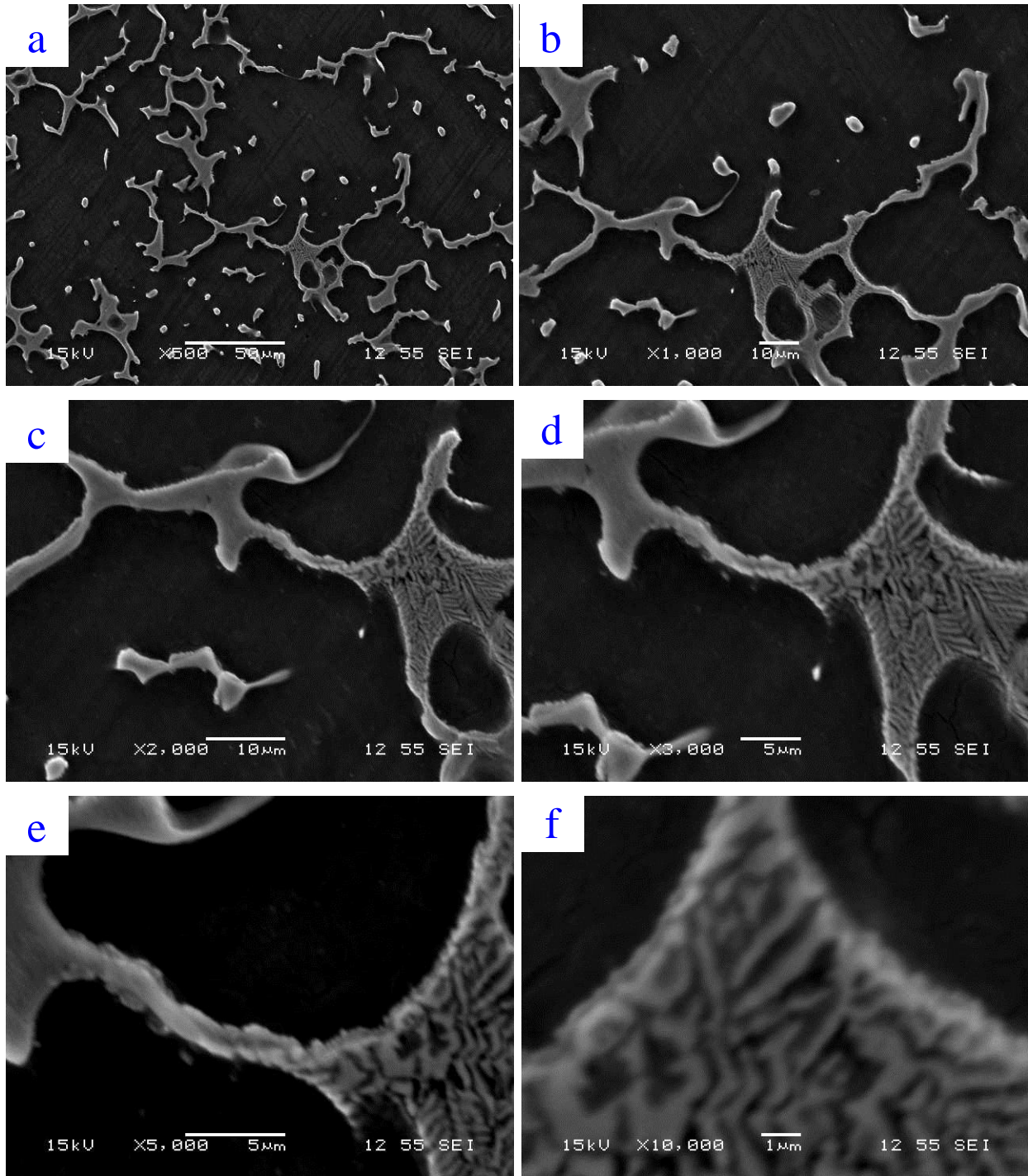
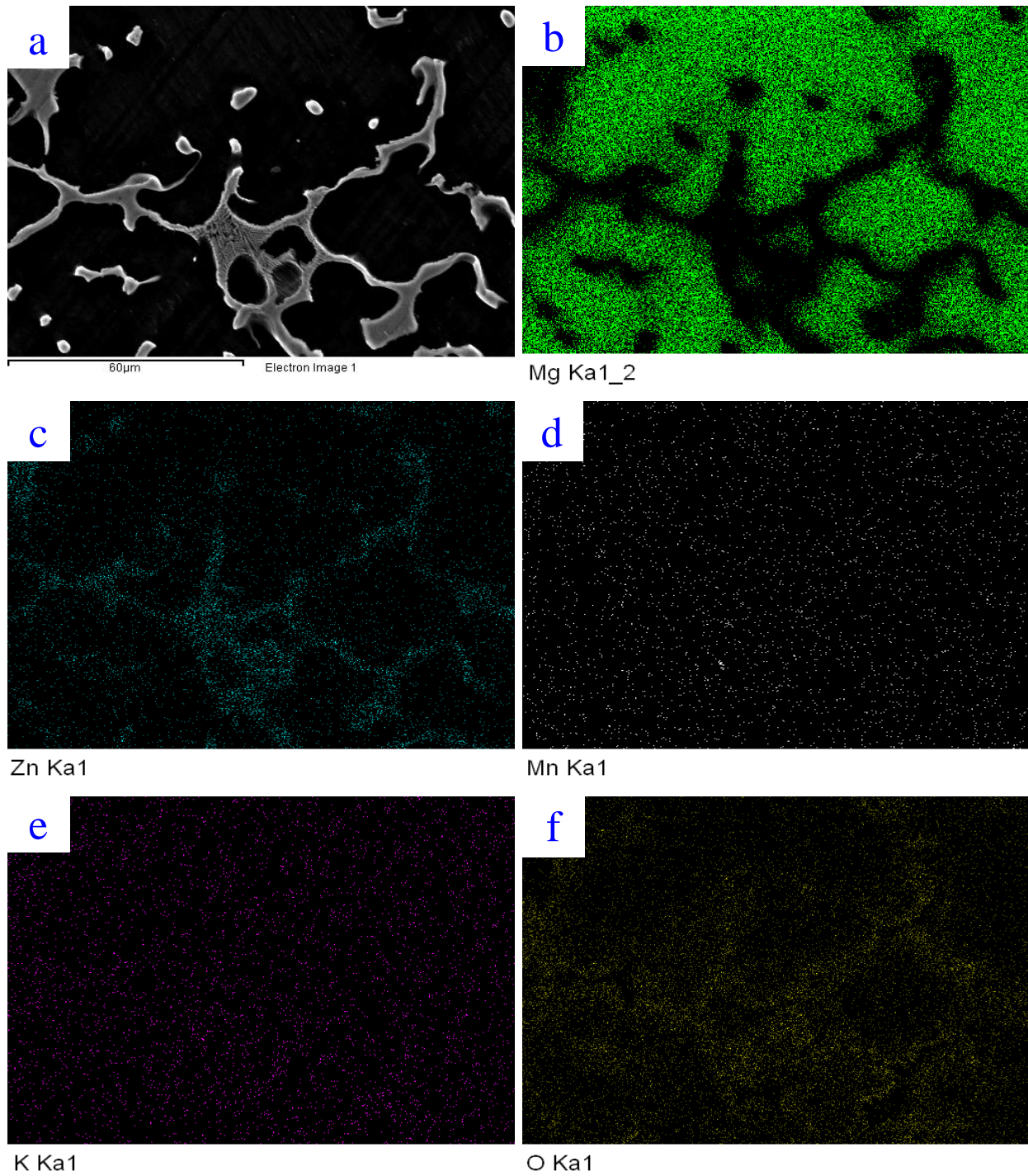


Figure 94: SEM images of Mg-1Mn-4Zn-0.5K alloying system rapidly cooled in liquid CO<sub>2</sub> at different magnifications (a) at 500 x (b) at 1000 x (c) at 2000 x (d) at 3000 x (e) at 5000 x (f) at 10000 x.

The alloying system was analyzed using EDS to confirm the elemental content of the system. [Figure 95](#) shows the EDS elements map, and the map showed a structure of the  $\beta$  phase distributed in the matrix  $\alpha$  (magnesium) as dendritic structure and scattered nodules of the secondary phases. The map analysis detected that the first secondary phase mainly consists of Zn element and Mg-Zn containing, which is structured in forms of eutectic ( $\alpha$  and  $\beta$  laminas) and  $\beta$  phase as a longitudinal structure and scattered nodules.

It was noticed that the manganese and oxygen were detected to be spreading on the matrix and the other secondary phase. The map of oxygen was observed to be denser in the matrix and denser in the adjacent surrounding of the primarily Mg-Zn-containing secondary phase than on the phase itself which could be due to the reactivity of the matrix ( $\alpha$  magnesium) being higher than the secondary phase (mainly zinc) in addition to the overall effect of potassium on the alloying system. It's worth mentioning that the accuracy of the distribution of the manganese is debatable.

Furthermore, the EDS point spectrum was used to analyze the matrix and the secondary phases. The analysis in [Figure 96](#) confirms the matrix mainly consists of Mg while the EDS point spectrum of the main secondary phase detected the high content of magnesium and zinc in comparison to other elements: Mn, K, and O in the analyzed sample, as shown in [Figure 97](#) and [Figure 98](#).



*Figure 95: The EDS elements map of Mg-1Mn-4Zn-0.5K alloying system rapidly cooled in liquid CO<sub>2</sub> (a) area of interest (b) Magnesium map (c) Zinc map (d) Manganese map (e) Potassium map (f) Oxygen map. alloying system rapidly cooled in liquid CO<sub>2</sub> at different magnifications (a) at 500 x (b) at 1000 x (c) at 2000 x (d) at 3000 x (e)*

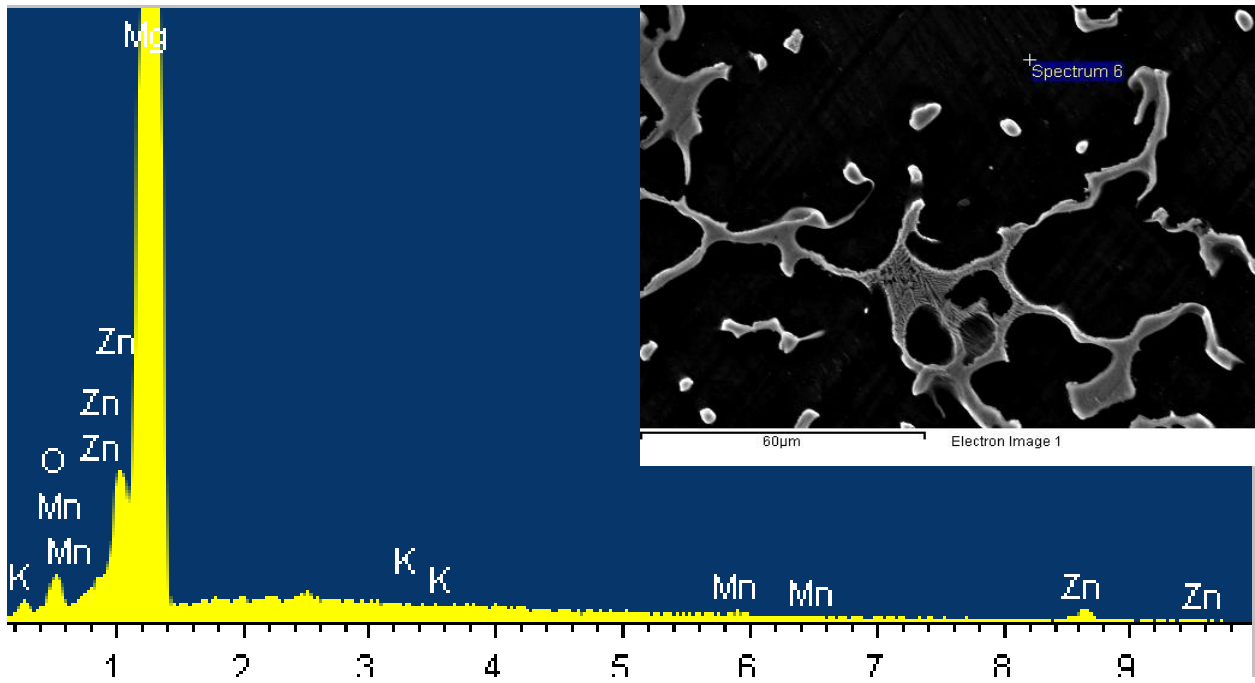


Figure 96: The point EDS spectrum image for the matrix of Mg-1Mn-4Zn-0.5Na alloying system rapidly cooled in liquid CO<sub>2</sub>.

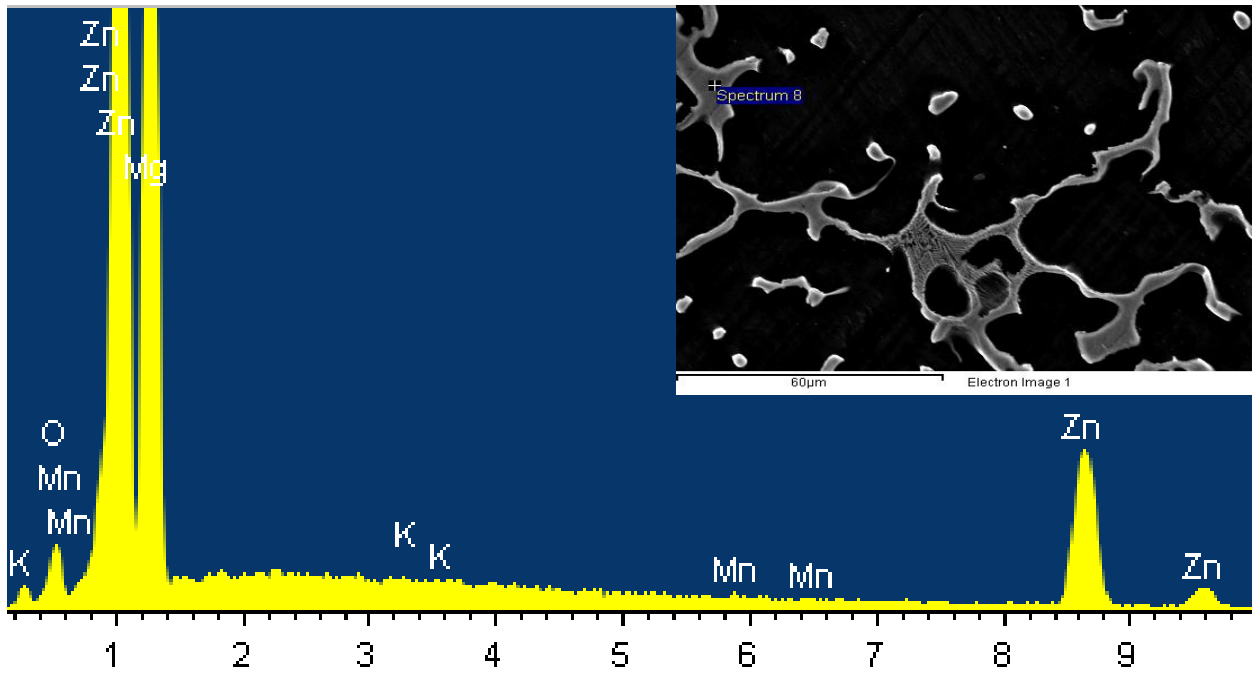


Figure 97: The point EDS spectrum image for the main secondary phase of Mg-1Mn-4Zn-0.5K alloying system rapidly cooled in liquid CO<sub>2</sub>.

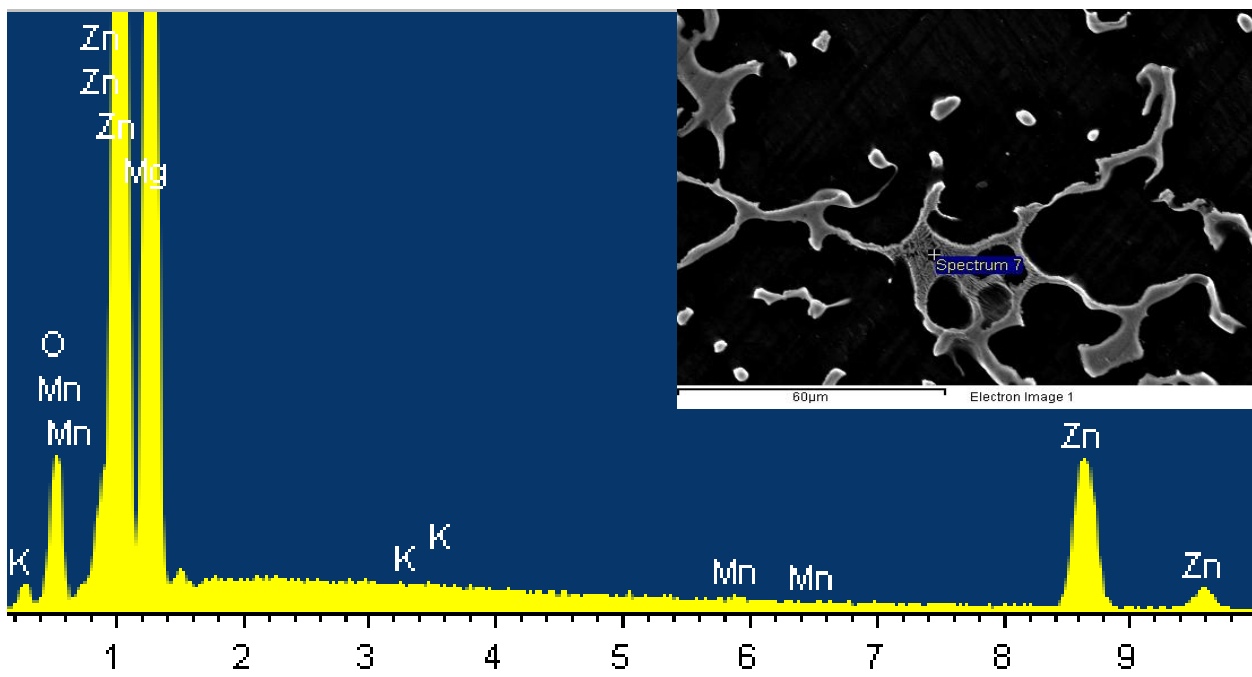
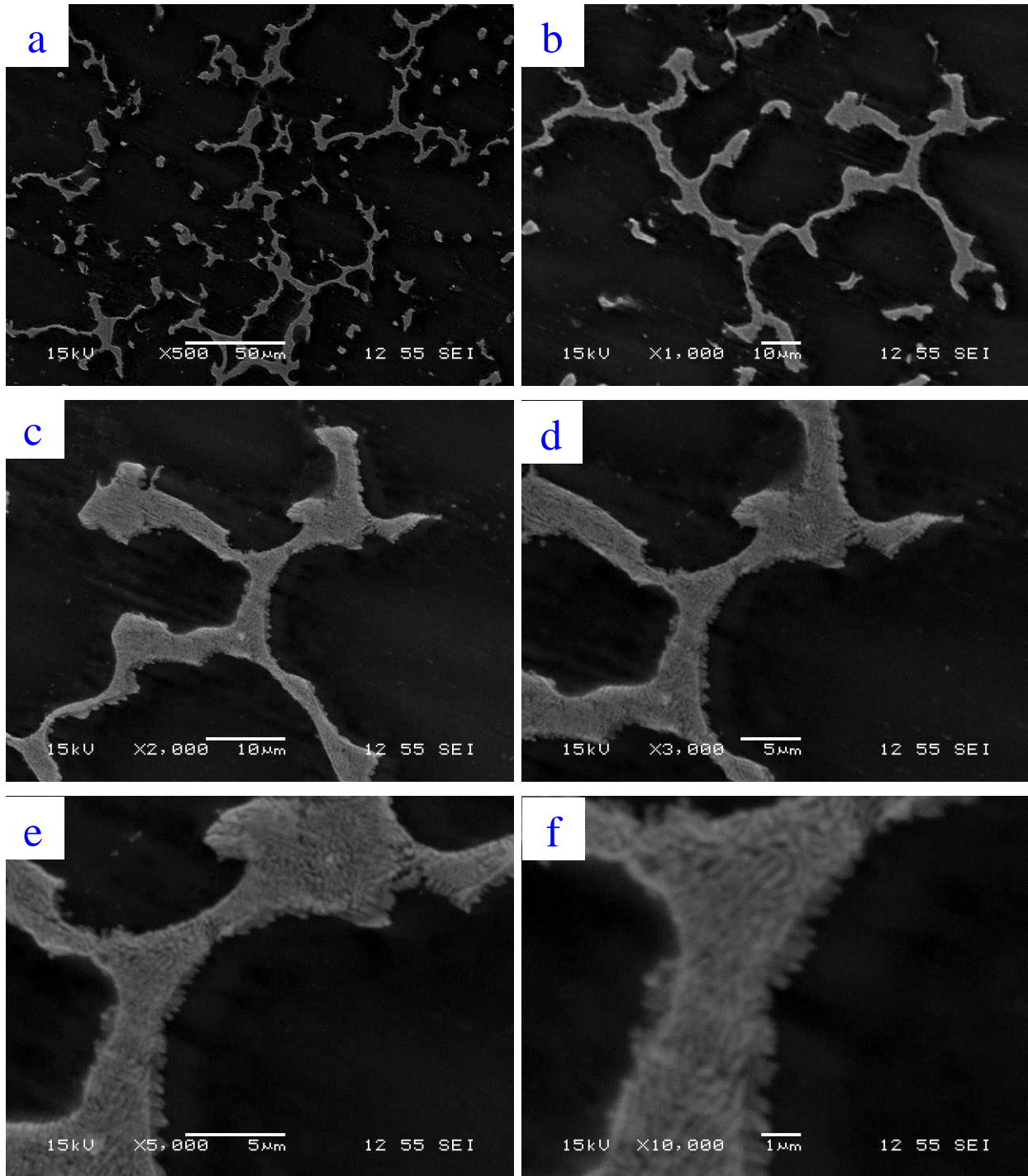


Figure 98: The point EDS spectrum image for the eutectic phase of Mg-1Mn-4Zn-0.5K alloying system rapidly cooled in liquid CO<sub>2</sub>.

The addition of sodium and potassium simultaneously to the alloying system of Mg-1Mn-4Zn was characterized further by using SEM imaging. The quenched Mg-1Mn-4Zn-0.25Na-0.25K alloying system with cooling rate of 13.5 °C/sec showed the same phases of Mg-1Mn-4Zn alloying system with a highly reactive-scattered phase diffused into the matrix, as shown in [Figure 100](#). The SEM analysis of the system revealed a structure of images  $\alpha$  phase, which is the matrix (magnesium),  $\beta$  phase is the secondary phase, and cluster of a reactive-brittle phase with size of about 160  $\mu\text{m}$  in the form of ribbons. This alloying system formed a dendritic spacing of 75  $\mu\text{m}$  with an interrupted network of the secondary phase, as can be seen clearly in [Figure 99 \(a\) and \(b\)](#).

The discontinuity in the first secondary phase of Mg-Zn could be due to the formation of another secondary phase heavily oxidized and brittle that locally absorbed more alloying elements, which led to hinder the production of a continuous Mg-Zn secondary phase. The observed structure of the first secondary phase formed the finest eutectic laminal structure among Mg-1Mn-2Zn, Mg-1Mn-4Zn, Mg-1Mn-4Zn-0.5Na, and Mg-1Mn-4Zn-0.5K. The laminal thickness of the eutectic structure was measured to be within an average of 0.13 and 0.18  $\mu\text{m}$   $\alpha$  and  $\beta$ , respectively. Besides the eutectic and  $\beta$  structure, which can be seen in [Figure 100](#), another formation of a scattered-brittle-reactive phase was detected with a content of Mg-Mn-Zn-Na-K-O that led to a significant deterioration in the tensile properties and impact strength.



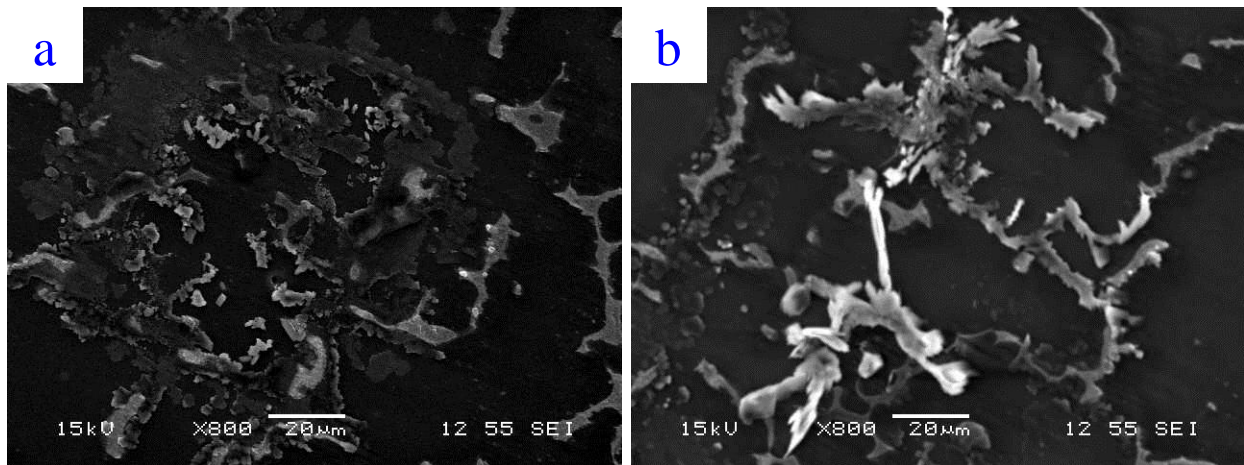
*Figure 99: SEM images of Mg-1Mn-4Zn-0.25Na-0.25K alloying system rapidly cooled in liquid CO<sub>2</sub> at different magnifications (a) at 500 x (b) at 1000 x (c) at 2000 x (d) at 3000 x (e) at 5000 x (f) at 10000 x.*

The alloying system was analyzed using EDS analysis to confirm the elemental content of the system. [Figure 101](#) shows the EDS elements map, and the map showed structure of the  $\beta$  phase distributed in the matrix  $\alpha$  (magnesium) as dendritic structure and scattered nodules of the different secondary phases. The map analysis detected that the first secondary phase mainly consists of Zn element and Mg-Zn containing, which is structured in forms of eutectic ( $\alpha$  and  $\beta$  laminas) and  $\beta$  phase as a longitudinal structure and scattered nodules.

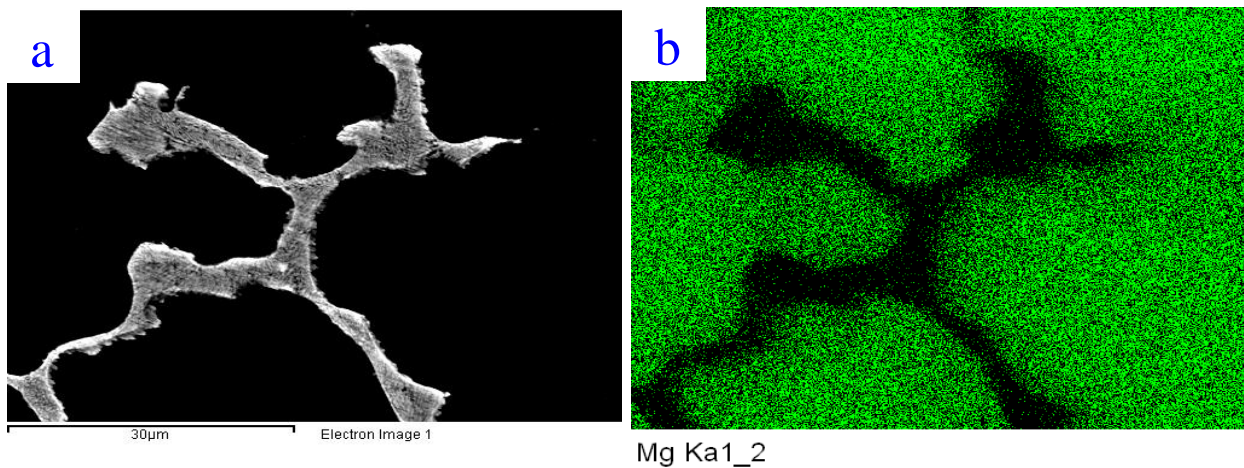
The other phase was spotted to be assembled in a scattered-brittle-reactive phase with a content of Mg-Mn-Zn-Na-K-O and size of about 160  $\mu\text{m}$ , as can be seen in the elemental map and EDS spectrum in [Figure 100](#) and [Figure 104](#). The elemental map for this phase detected a heavy formation of oxidized ribbons at the surface, as shown in [Figure 100](#). It was noticed that the manganese and oxygen were detected to be spread on the matrix and the other secondary phase.

The map of oxygen was observed to be denser in the matrix and around the Mg-Zn-containing secondary phase than on the phase itself, which could be due to the reactivity of the matrix ( $\alpha$  magnesium) being higher than the secondary phase (mainly zinc). However, the oxygen formation was heavily piled up on the top of Mg-Mn-Zn-Na-O-containing phase. It's worth mentioning that accuracy of the distribution of the manganese, sodium, and potassium is debatable. Furthermore, the EDS point spectrum was used to analyze the matrix and the secondary phases. The analysis in [Figure 103](#) confirms the

matrix mainly consists of Mg besides Zn, Mn, Na, K and O, where the EDS point spectrum of the main secondary phase detected the high content of zinc in comparison to other elements. Additionally, the peak intensity of the alloying elements and oxygen was increased for the reactive phase. Figure 105 shows the sum spectrum of the brittle reactive cluster to be with content of Mg, Zn, Mn, Na, K, and O.



*Figure 100: SEM images for the formed scattered-brittle-reactive secondary phase of Mg-1Mn-4Zn-0.25Na-0.25K alloying system rapidly cooled in liquid CO<sub>2</sub> at 800x.*



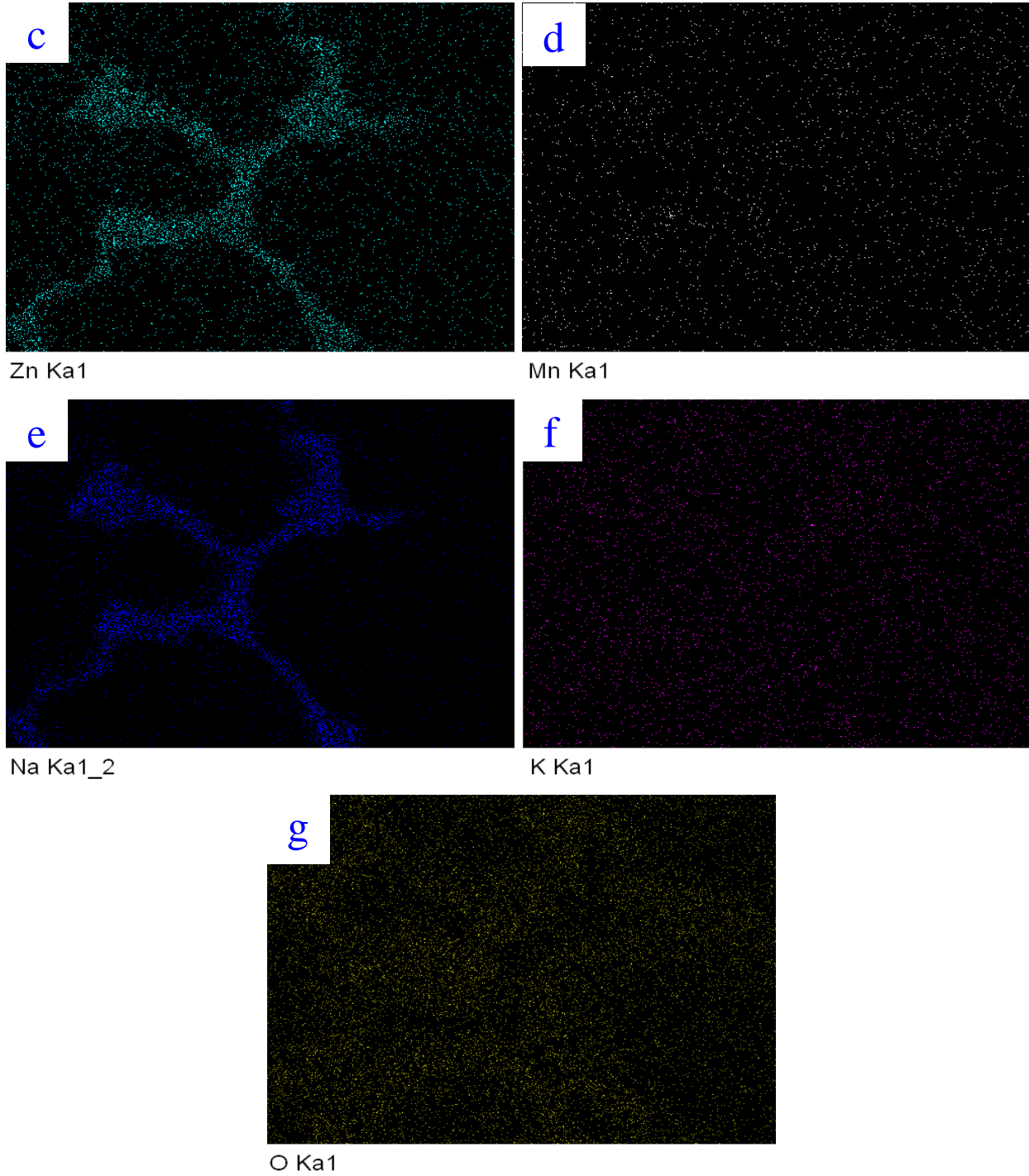
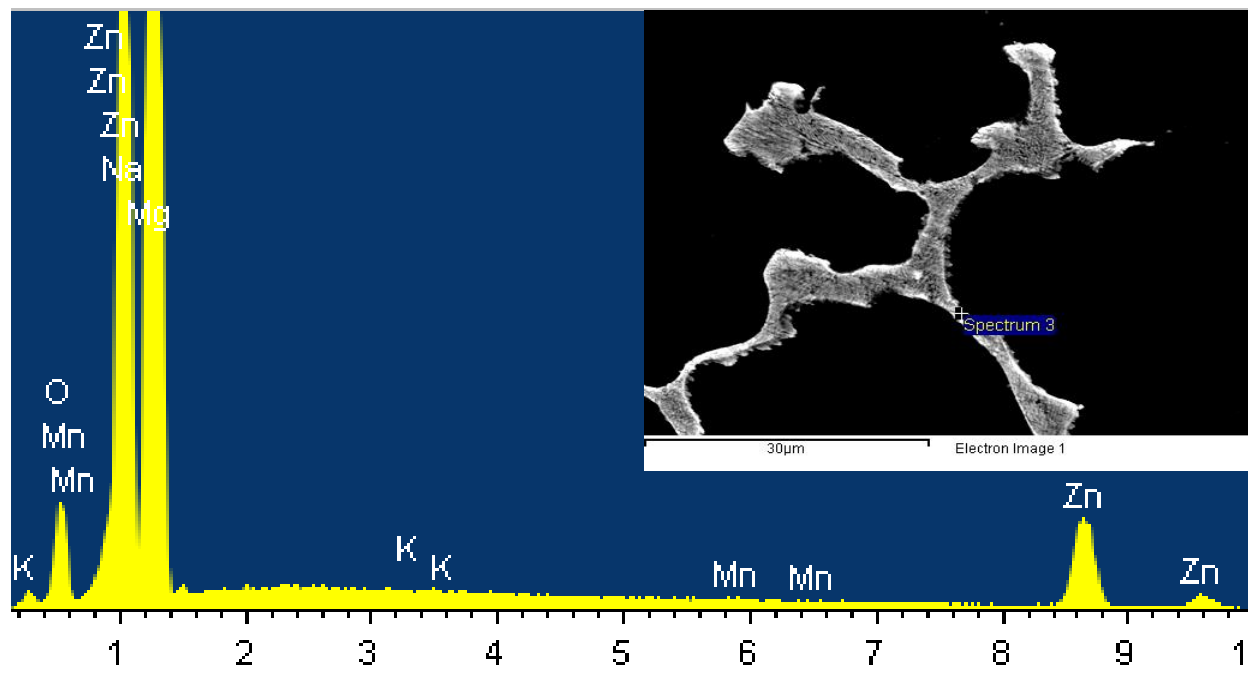


Figure 101: The EDS elements map of Mg-1Mn-4Zn-0.25Na-0.25K alloying system rapidly cooled in

*liquid CO<sub>2</sub> (a) area of interest (b) Magnesium map (c) Zinc map (d) Manganese map (e) Sodium (f) Potassium map (g) Oxygen map.*



*Figure 102: The point EDS spectrum image for the secondary phase of Mg-1Mn-4Zn-0.25Na-0.25K alloying system rapidly cooled in liquid CO<sub>2</sub>.*

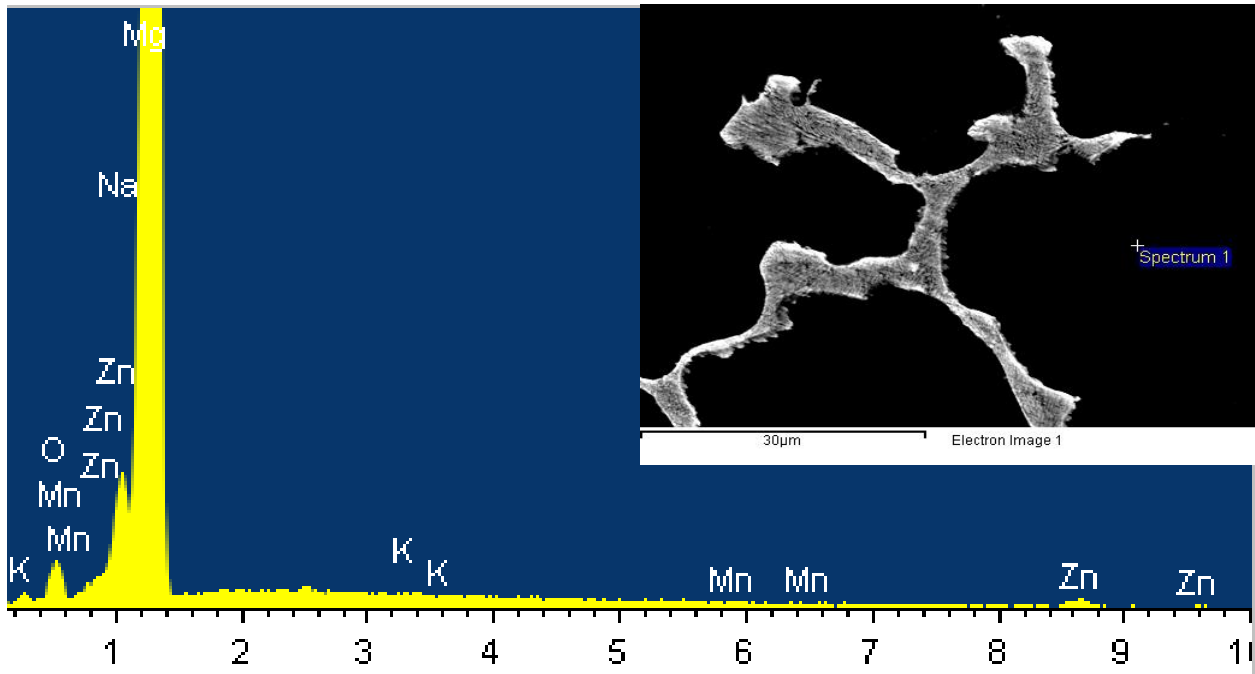
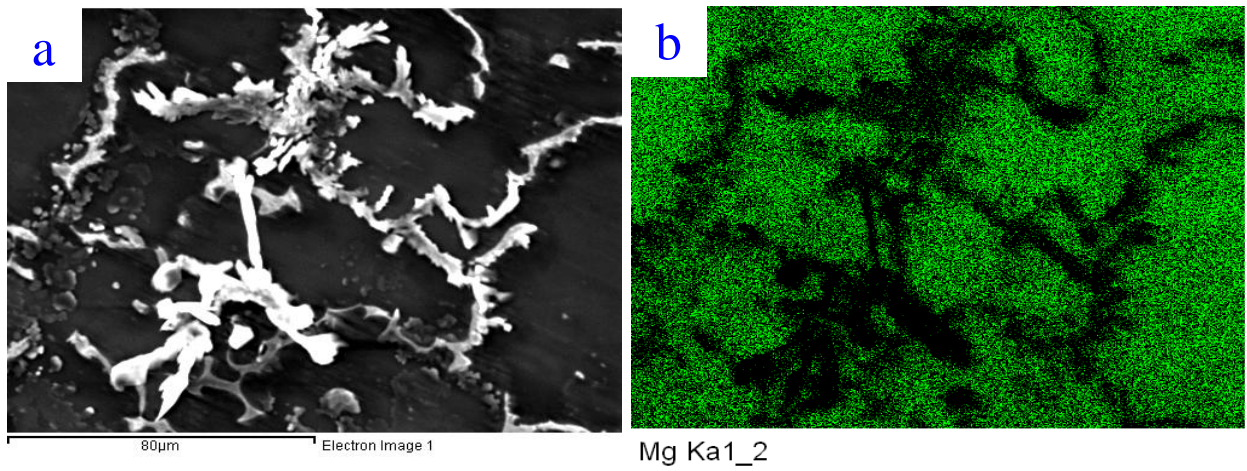
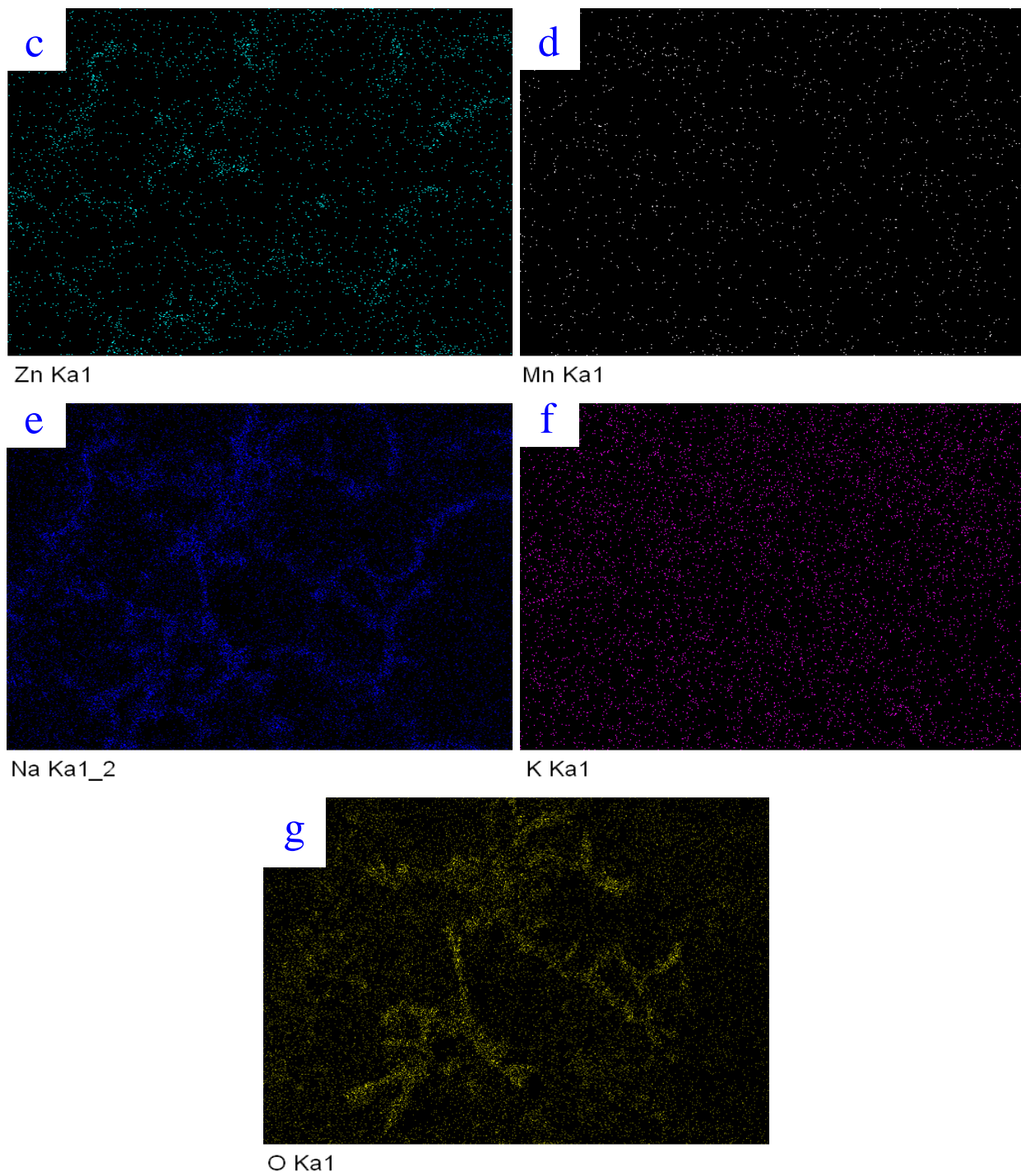
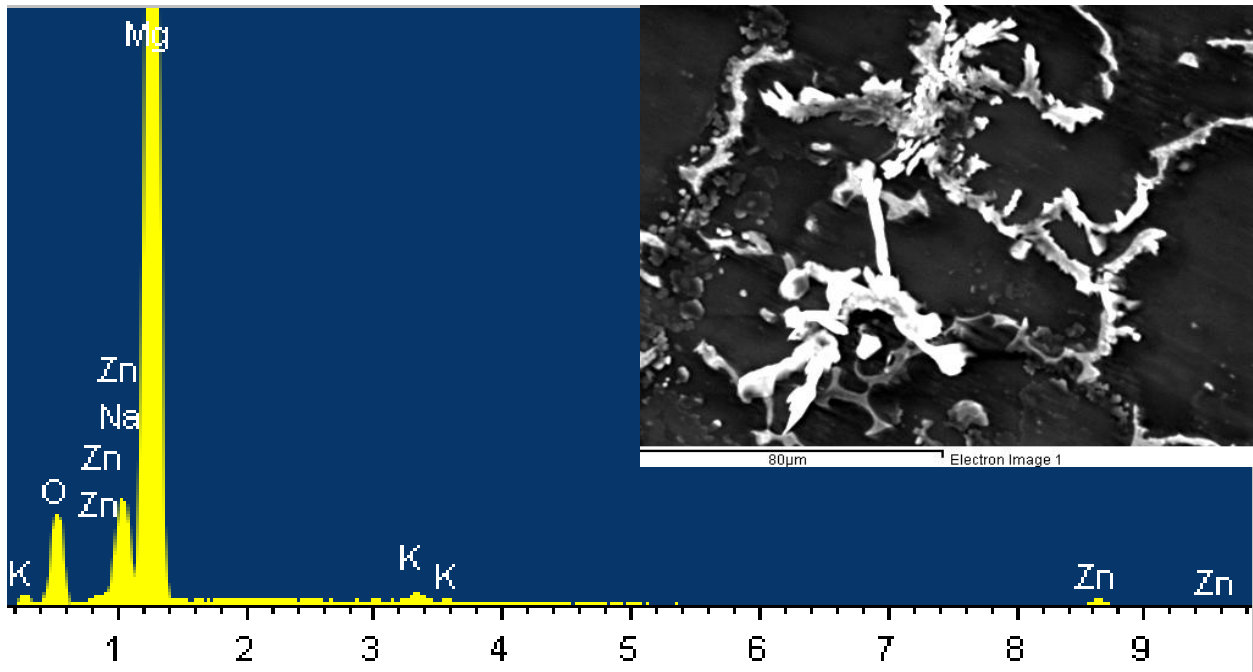


Figure 103: The point EDS spectrum image for the matrix of Mg-1Mn-4Zn-0.5Na-0.5K alloying system rapidly cooled in liquid CO<sub>2</sub>.





*Figure 104: The EDS elements map for the formed scattered-brittle-reactive secondary phase of Mg-1Mn-4Zn-0.25Na-0.25K alloying system rapidly cooled in liquid CO<sub>2</sub> (a) area of interest (b) Magnesium map (c) Zinc map (d) Manganese map (e) Sodium map (f) Potassium map (g) Oxygen map.*



*Figure 105: The sum EDS spectrum image for the formed scattered-brittle-reactive secondary phase of Mg-1Mn-4Zn-0.25Na-0.25K alloying system rapidly cooled in liquid CO<sub>2</sub>.*

The microstructure was further investigated to get a deeper understanding of the influence of the microstructure on the properties. It was observed that the microstructure of all of the Mg-Mn-Zn-based alloys consists of  $\alpha$  phase (matrix) and secondary phase. The secondary phase was noticed to be in the forms of eutectic structure ( $\alpha$  and  $\beta$  laminas),  $\beta$  phase as a longitudinal structure, and scattered nodules. Although the alloying systems shared the same main structure, the microstructure showed different characteristics in terms of the dendrite spacing, sub-branches, presence and the laminal thickness of the eutectic phase, and the presence and size of other phases.

Figure 106 characterizes the dendritic spacing of Mg-1Mn-2Zn, Mg-1Mn-4Zn, Mg-1Mn-4Zn-0.5Na, Mg-1Mn-4Zn-0.5K, and Mg-1Mn-4Zn-0.25Na-0.25K alloying systems. The dendrite spacing was found to decrease with increasing the zinc content (from 2% to 4%) by 31%, in addition to promoting the formation of a semi-continuous network of the main-secondary phase. The dendritic spacing was further refined by 39% and with the addition of 0.5% Na to Mg-1Mn-4Zn, which led to the formation of a continuous secondary phase with increasing the density of sub-branches. Furthermore, the presence and size of the eutectic phase was decreased.

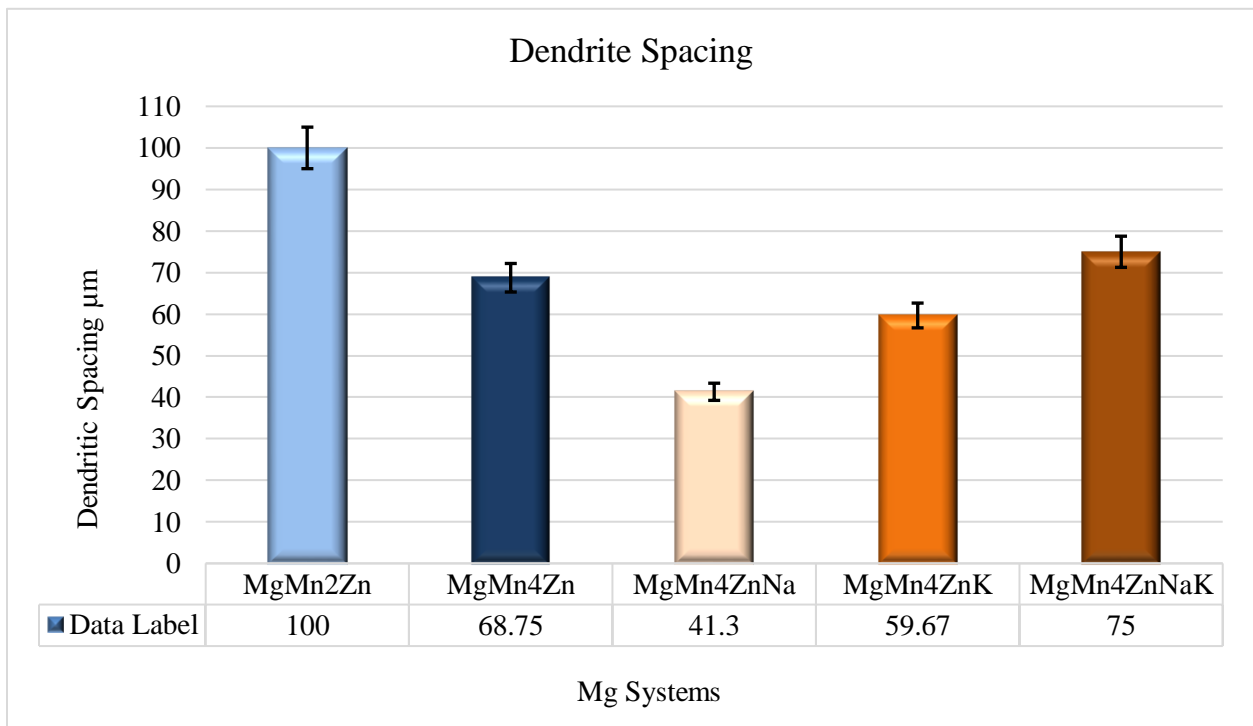


Figure 106: The dendritic spacing of Mg-1Mn-2Zn, Mg-1Mn-4Zn, Mg-1Mn-4Zn-0.5Na, Mg-1Mn-4Zn-0.5K, Mg-1Mn-4Zn-0.25Na-0.25K alloying systems

Moreover, the addition of 0.5% K to Mg-1Mn-4Zn reduced the spacing by 13%. It is believed that adding potassium led to the interruption in the secondary phase and reduction in the sub-branches due to the development of a thicker  $\beta$ . The final addition of 0.25% each of sodium and potassium together increased the spacing of Mg-1Mn-4Zn system by 9%. The increase in the spacing was concluded to be caused by forming a reactive-brittle phase with size of about 160  $\mu\text{m}$  in the form of ribbons that locally absorbed more alloying elements. Additionally, the formation of this phase drove the discontinuity of the main secondary phase and reduction of the eutectic laminas.

The other analysis was conducted on the morphology of the eutectic phase of Mg-Mn-Zn-based alloys. It was found that the structure of the eutectic changes with changing the content of zinc and adding sodium and potassium individually or simultaneously. The SEM imaging in [Figure 107](#) reveals various shapes and dimensions of the eutectic phase based on the alloying system. The formed eutectic in Mg-1Mn-2Zn was observed to have a high presence of eutectic with a laminal thickness of 0.148 and 0.108  $\mu\text{m}$  for  $\alpha$  and  $\beta$ , respectively.

The further addition of zinc (4%) increased the laminal thickness of  $\alpha$  and  $\beta$  to 0.48 and 0.39  $\mu\text{m}$ , respectively. Nevertheless, the alloying system of Mg-1Mn-4Zn-0.5Na led to the formation of an irregular-short eutectic with an average laminal thickness of 0.45 and 0.53  $\mu\text{m}$  for  $\alpha$  and  $\beta$ , respectively. However, using 0.5 K instead of Na promoted the formation of a thick  $\beta$  laminal with a measured average of 0.569  $\mu\text{m}$  along with  $\alpha$  laminal

that has an average thickness of 0.242  $\mu\text{m}$ . Finally, the addition of 0.25% Na and 0.25% K to Mg-1Mn-4Zn led to the production of an eutectic structure with an average laminal thickness of 0.13 and 0.18  $\mu\text{m}$   $\alpha$  and  $\beta$ , respectively. [Figure 108](#) lays out the laminal thickness of the alloying systems.

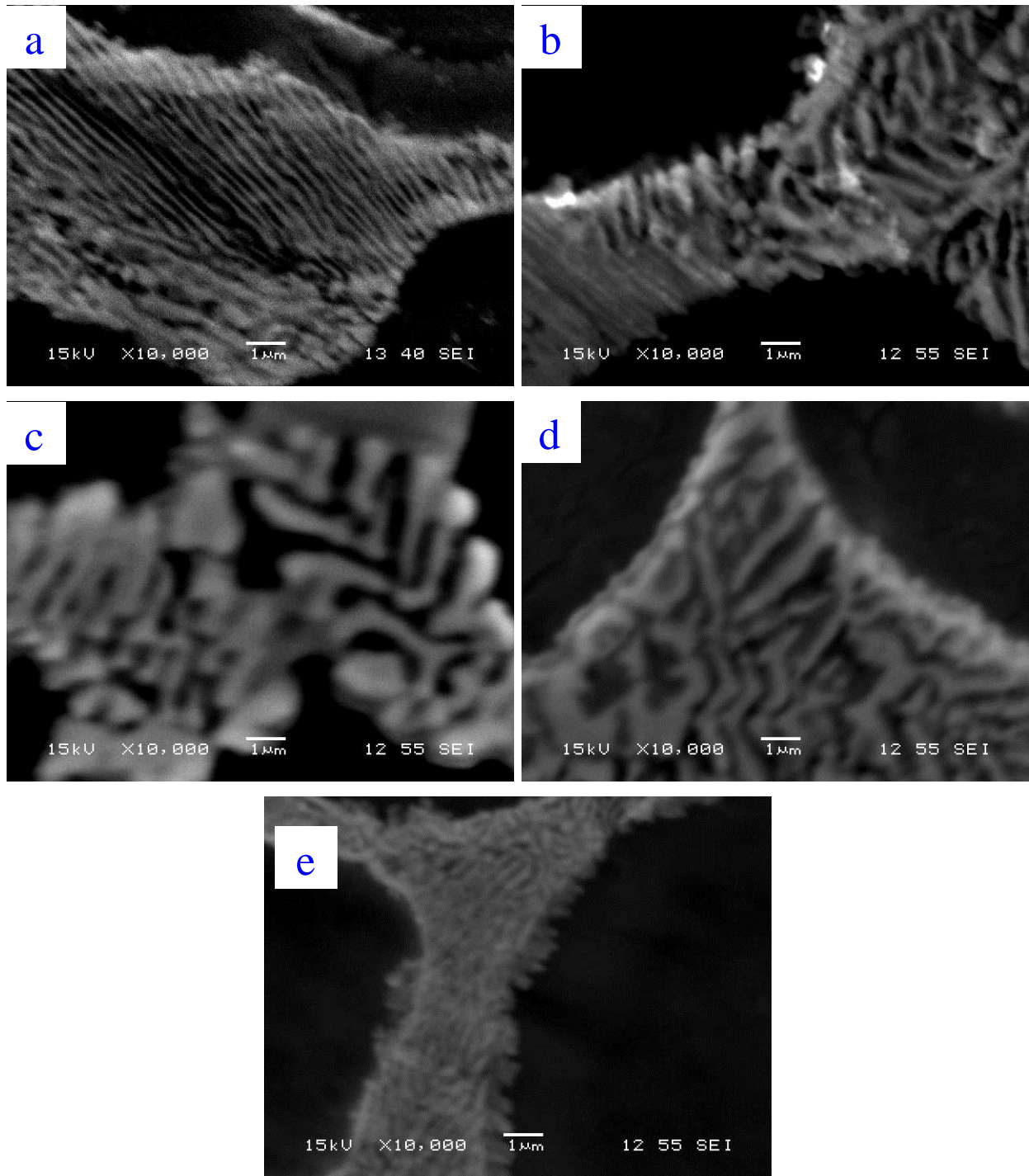
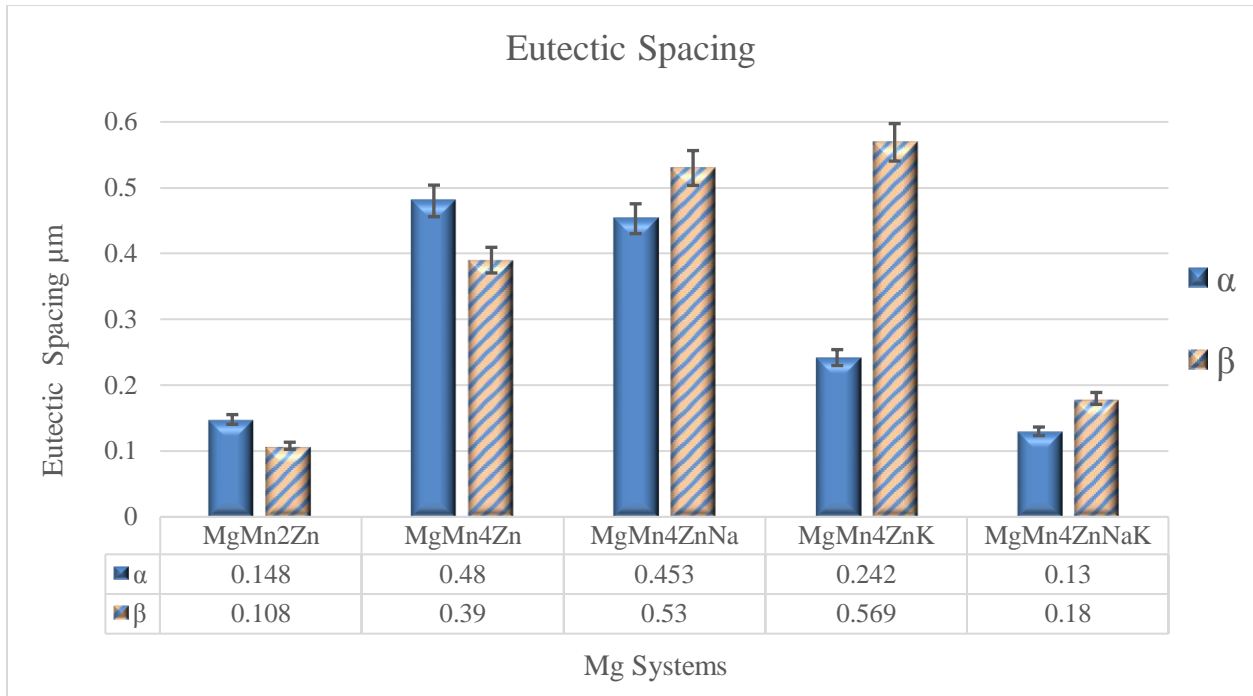


Figure 107: The difference formation of the eutectic phases of Mg-1Mn-2Zn, Mg-1Mn-4Zn, Mg-1Mn-4Zn-0.5Na, Mg-1Mn-4Zn-0.5K, Mg-1Mn-4Zn-0.25Na-0.25K alloying systems.



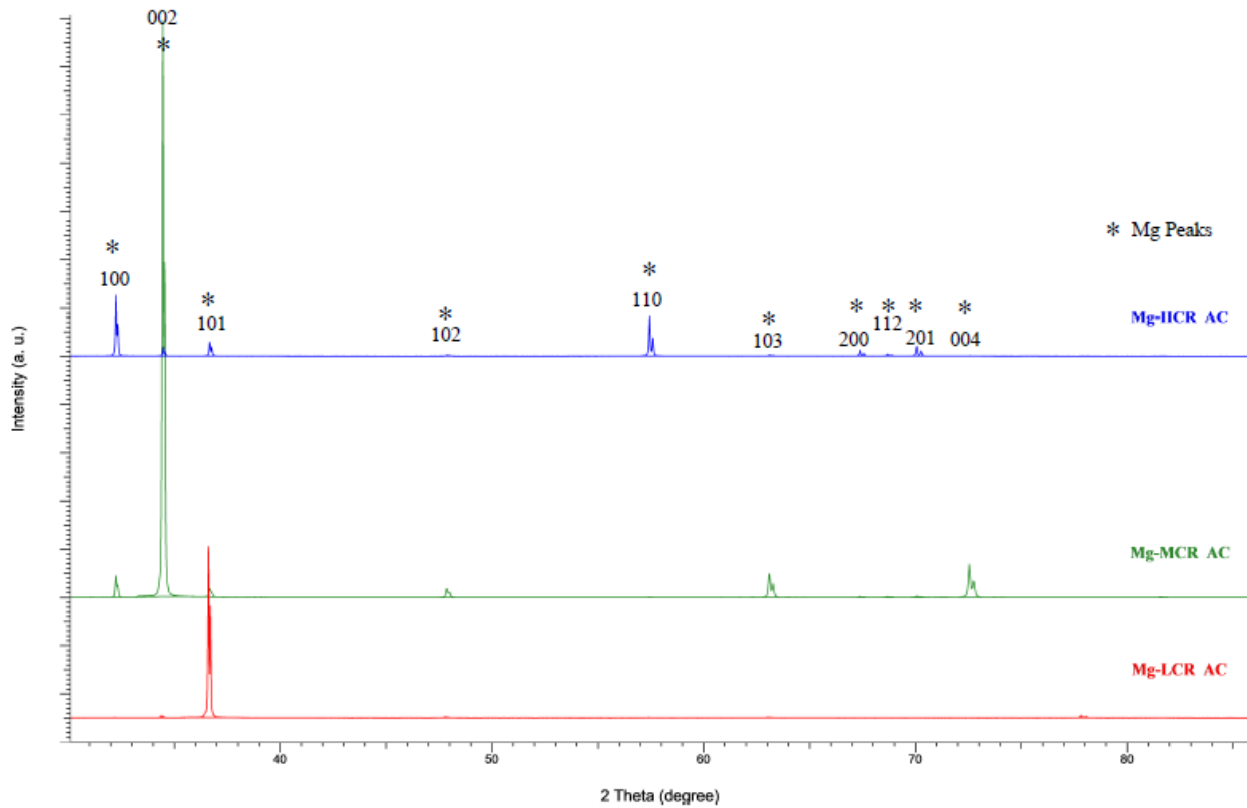
*Figure 108: The eutectic spacing of Mg-1Mn-2Zn, Mg-1Mn-4Zn, Mg-1Mn-4Zn-0.5Na, Mg-1Mn-4Zn-0.5K, Mg-1Mn-4Zn-0.25Na-0.25K alloying systems.*

### 5.1.2.2. XRD

*The X-ray diffraction analysis was used to verify the phase constitution composition of the alloying of the alloying systems. The XRD patterns were divided into three groups: pure magnesium, Mg-Mn-Zn, magnesium, Mg-Mn-Zn, and Mg-Mn-Zn-Na-k alloying systems.*

Table 18 summarizes the composition identification of the alloying systems. The first set of XRD covers the patterns of pure magnesium patterns that were cooled by different solidification rates. The patterns match the peaks of magnesium in the data base and did not show a significant difference between the diffraction peaks of pure magnesium

of different solidification rates, as shown in



However, the patterns showed a different preferred orientation at different solidification rates. The preferred orientation was detected to be associated with (101) at 2-theta of  $\approx 36$  degree for as-cast pure magnesium (Mg-LCR AC); the system was slowly solidified in a completely insulated furnace with a cooling rate of  $0.035$  °C/Sec and grain size of  $4235$   $\mu\text{m}$ . The second system (Mg-MCR AC) showed a preferred orientation with (002) and 2-theta of  $\approx 34$  degree; the moderate cooling rate ( $0.074$  °C/Sec) was achieved by cooling the casting in an uninsulated-ends furnace and the grain size was found to be  $2257$   $\mu\text{m}$ . The diffraction peak of as-cast pure magnesium (Mg-MCR AC) showed preferred orientation with (100) and 2-theta of  $\approx 32$  degree; the sample was solidified in liquid  $\text{CO}_2$  and the grain size was measured to be average range of  $6$   $\mu\text{m}$  to  $12$   $\mu\text{m}$ .

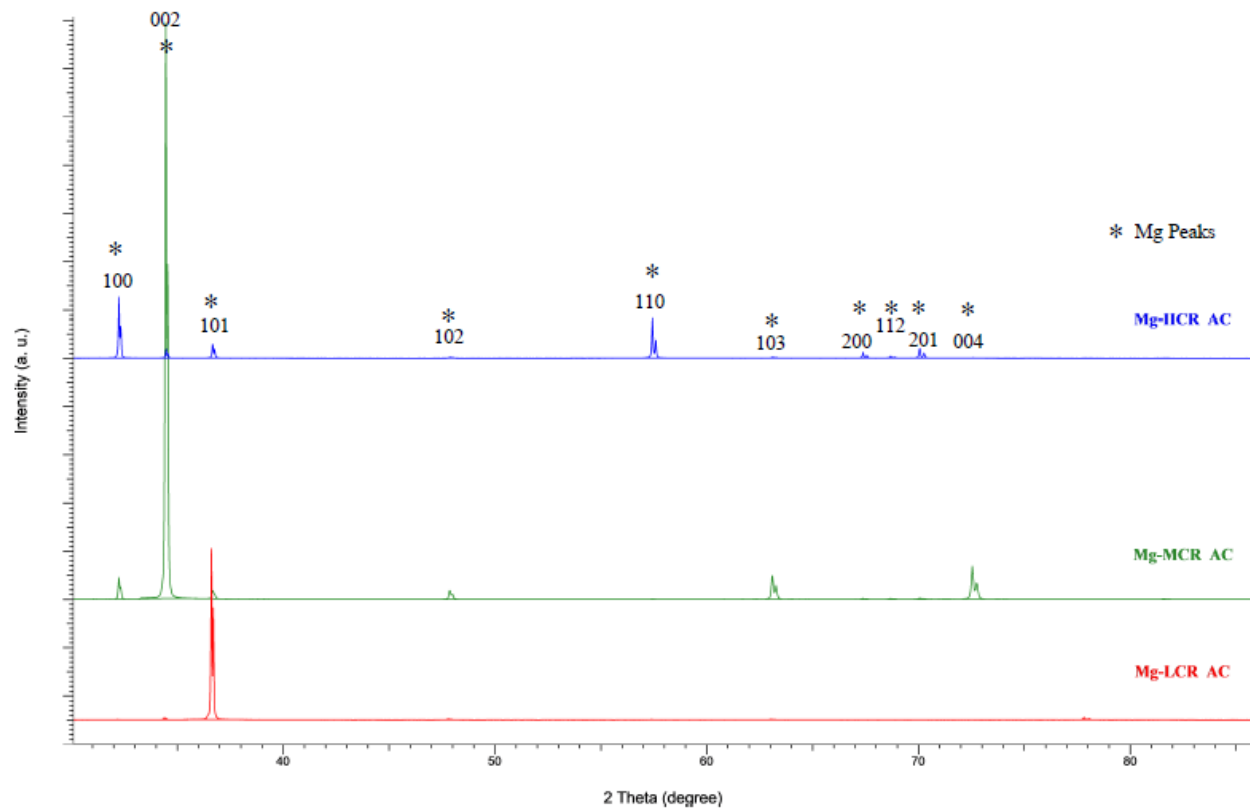
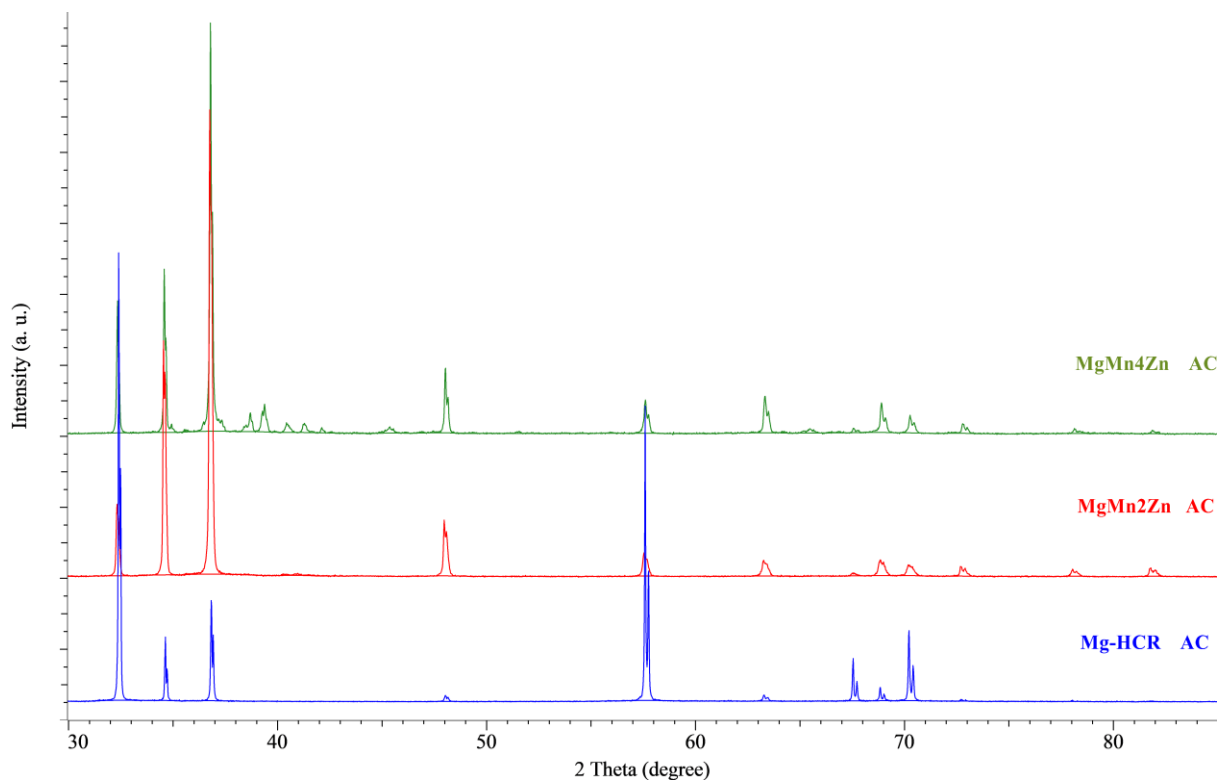
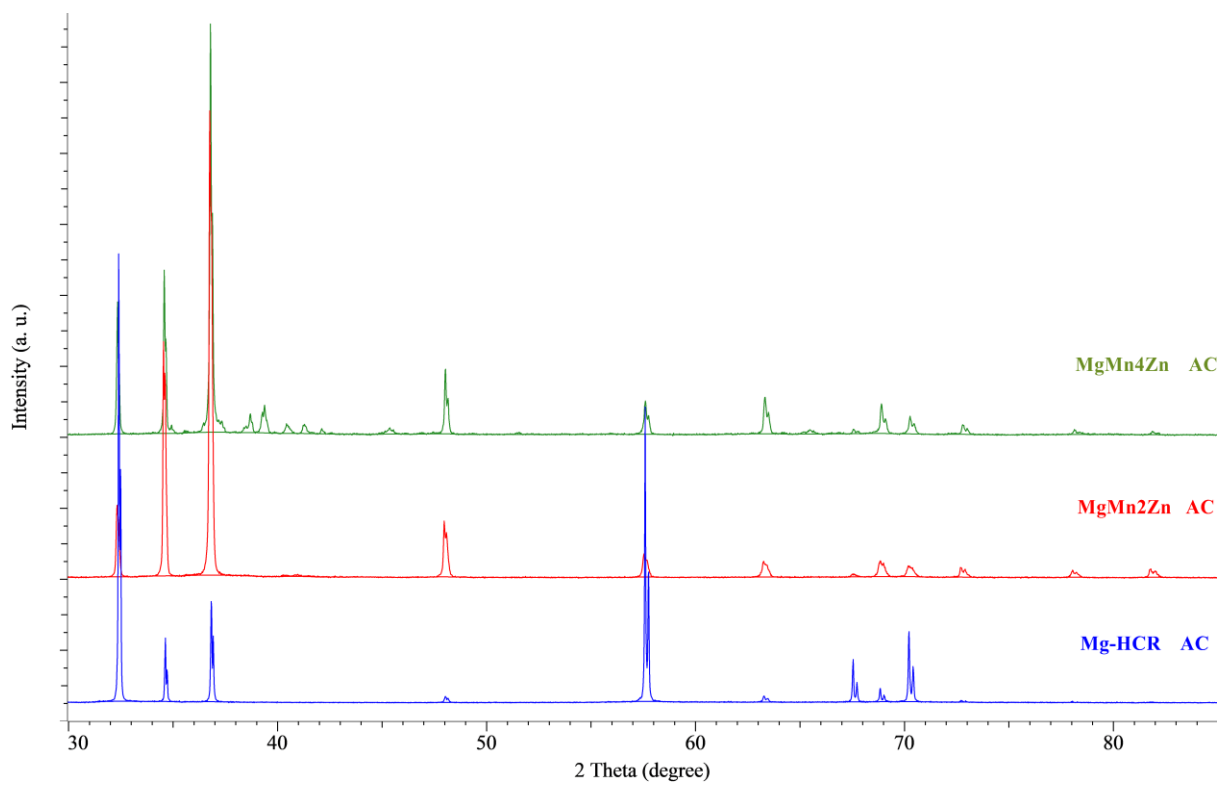


Figure 109: The XRD patterns of as cast pure magnesium that were cooled by different solidification rates.



lays out the patterns of Mg-1Mn-2Zn and Mg-1Mn-4Zn quenched alloying systems to be compared with the quenched pure magnesium. Along with magnesium peaks, the patterns show the presence of Mg 0.975 Mn 0.025, (Mg 39 Zn) 0.05, Mg 0.971 Zn 0.029, Mg 0.97 Zn 0.03, and (Mg 0.25 Zn 0.75) O in both of Mg-1Mn-2Zn and Mg-1Mn-4Zn. The phases composition (MgZn<sub>2</sub>, Mg<sub>7</sub>Zn<sub>3</sub>, zinc phosphate hydrate (Zn<sub>2</sub>P<sub>2</sub>O<sub>7</sub> · 5H<sub>2</sub>O), and ZnO) were found in only Mg-1Mn-4Zn. Figure 111 shows the XRD diffraction peaks of Mg-1Mn-4Zn, Mg-1Mn-4Zn-0.5Na, Mg-1Mn-4Zn-0.5K, and Mg-1Mn-4Zn-0.25Na-0.25K. The same phases of Mg-1Mn-4Zn was associated with MgMnZnNa, MgMnZnK, and MgMnZnNaK besides the presence of sodium hydrogen phosphate (Na<sub>3</sub>HPO<sub>4</sub>) in MgMnZnNa and MgMnZnNaK. Table 18 summarizes the phases of the alloying systems.



*Figure 110: The XRD patterns of Mg-Mn-Zn alloying systems.*

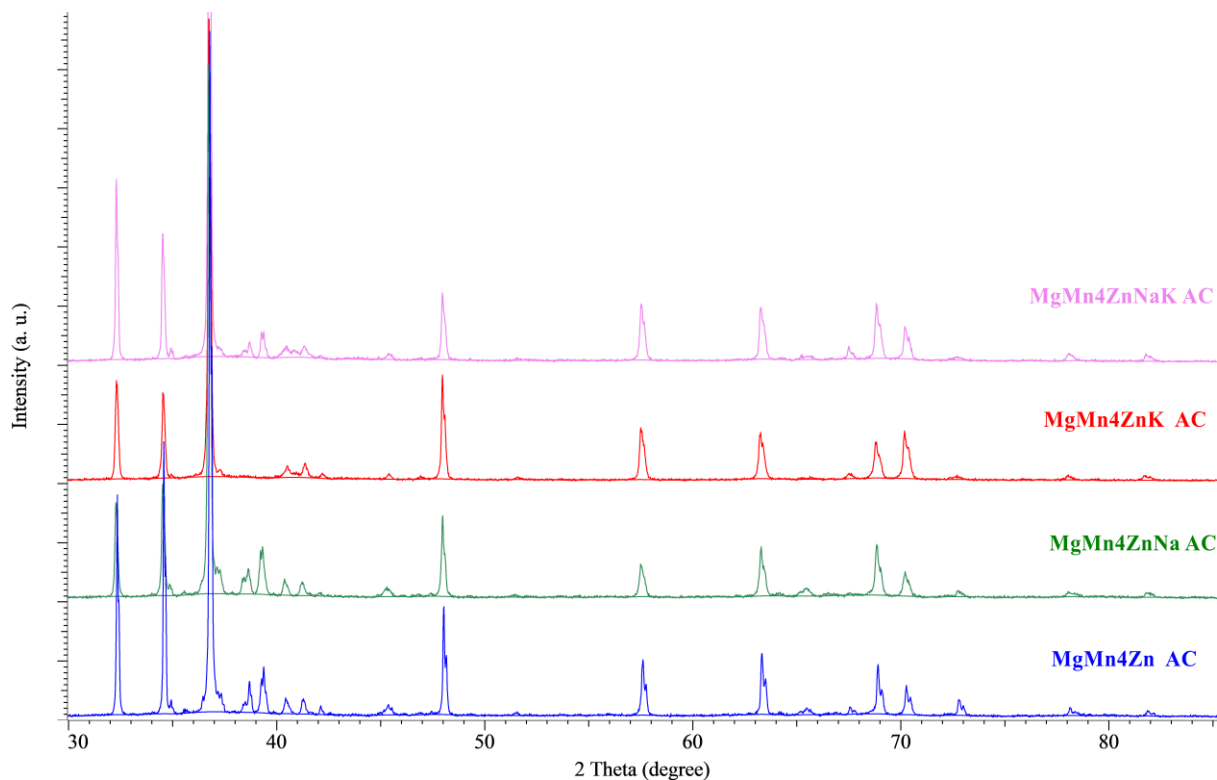


Figure 111: The XRD patterns of Mg-Mn-Zn-Na-K alloying systems.

Table 18: The phase constitution of the alloying systems.

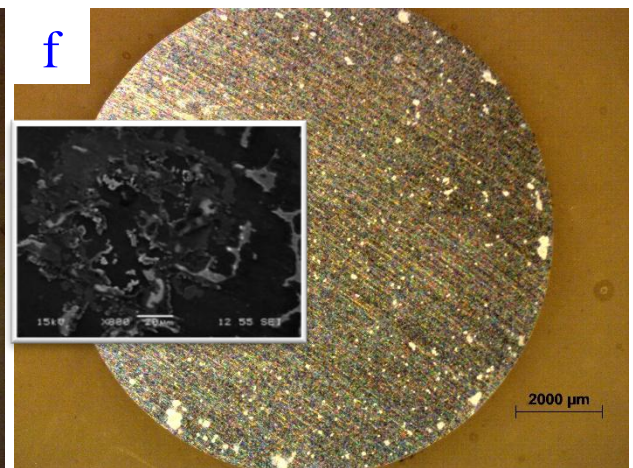
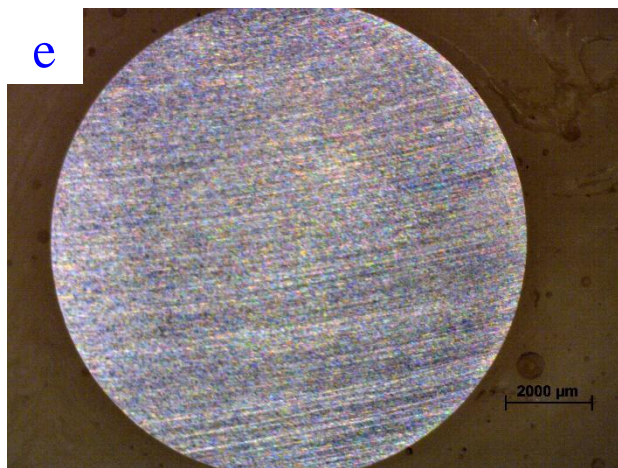
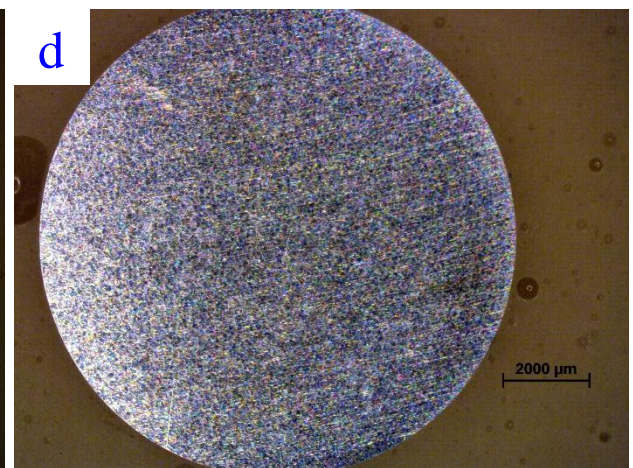
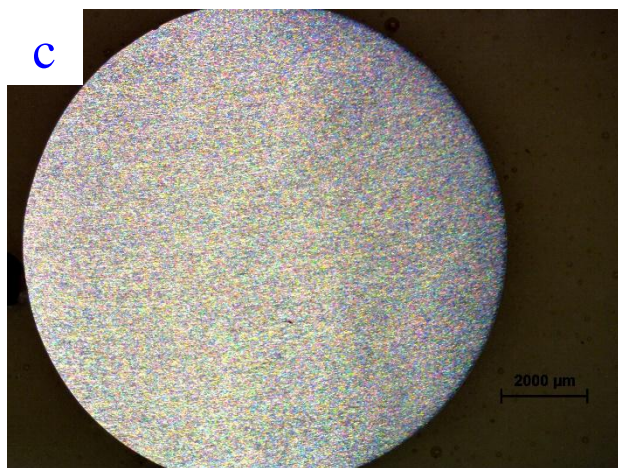
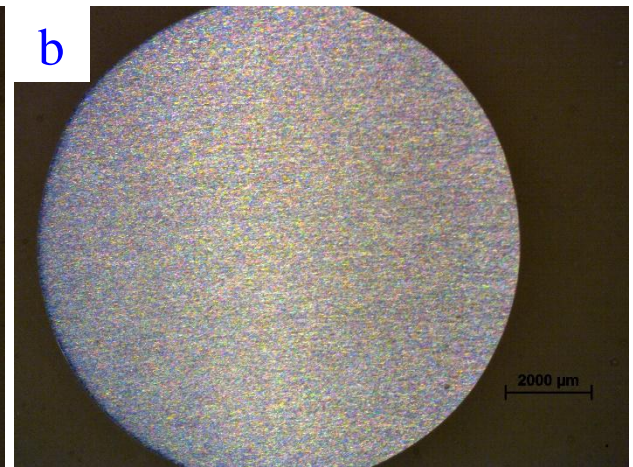
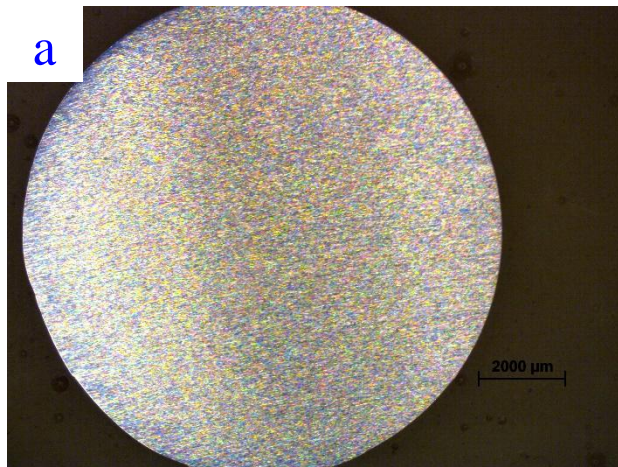
Alloying Systems	Phases-Composition										
	Mg	Mg0.975Mn0.025	(Mg39Zn)0.05	Mg0.971Zn0.029	Mg097Zn0.03	MgZn2	(Mg0.25 Zn0.75) O	Mg7Zn3	Zn2P2O7 5H2 O	ZnO	(Na3 HP2 O6)
Mg-LCR	*	-	-	-	-	-	-	-	-	-	-
Mg-MCR	*	-	-	-	-	-	-	-	-	-	-
Mg-HCR	*	-	-	-	-	-	-	-	-	-	-
MgMn2Zn	*	*	*	*	*	-	*	-	-	-	-
MgMn4Zn	*	*	*	*	*	*	*	*	*	*	-
MgMn4ZnNa	*	*	*	*	*	*	*	*	*	*	*
MgMn4ZnK	*	*	*	*	*	*	*	*	*	*	-

MgMn4ZnNaK	*	*	*	*	*	*	*	*	*	*	*
------------	---	---	---	---	---	---	---	---	---	---	---

### 5.2.6. Corrosion

The corrosion properties of the alloying systems was examined using electrochemical and immersion testing methods in addition to characterizing the interfacial surface using optical and compositional analysis. The experiments were done in Hank's Balanced Salts Solution at a temperature of 37 °C and 7.4 pH to mimic the biological environment of the human body. The samples were grinded using different grades of SiC paper: 400, 600, 800, and 1200. The grinding process was followed by a cleaning procedure starting with a quick rinse with distilled water and isopropyl alcohol and then dried by pressurized air.

Figure 112 provides initial pre-test information about the surface nature of the made alloying systems. It can be noticed that the pure magnesium and Mg-Mn-Zn system showed a clear and homogenous surface. On the other side, white spots were observed on the surface of Mg-Mn-Zn-Na and Mg-Mn-Zn-Na-K alloying systems. These spots were observed to be bigger and have more detrimental effects in Mg-Mn-Zn-Na-K than Mg-Mn-Zn-Na. Additionally, the clusters were found to be brittle-reactive minor secondary phases and were further analyzed by SEM and EDS. It's worth mentioning that the Mg-Mn-Zn-K alloying system did not suffer from the accumulations of reactive-brittle phases.



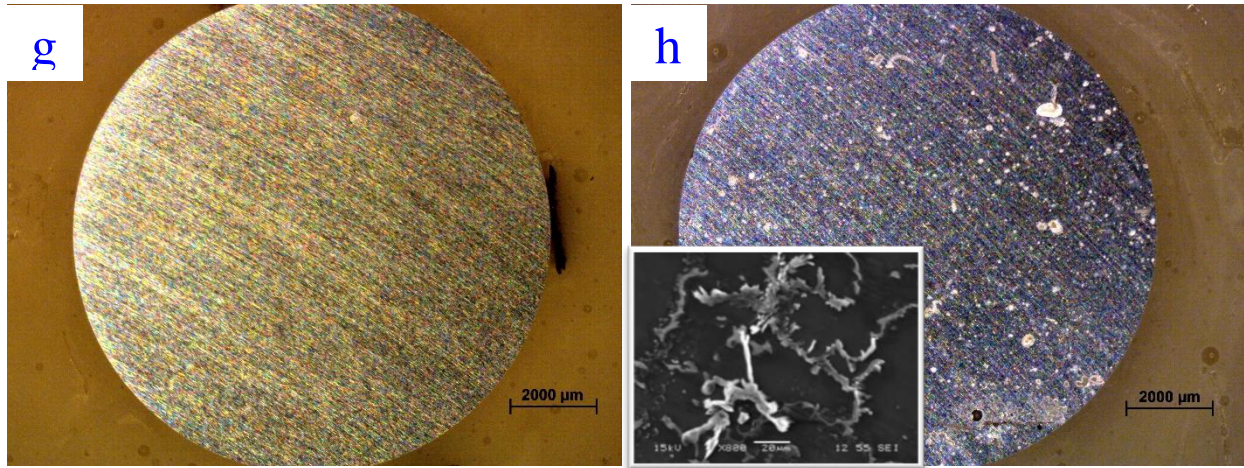


Figure 112: The surface characteristics of (a) pure magnesium cooled in the furnace (slow cooling rate) (b) pure magnesium-cooled in the furnace with uninsulated-ends (moderate cooling) (c) quenched pure magnesium (d) quenched Mg-1Mn-2Zn (e) quenched Mg-1Mn-4Zn. (f) quenched Mg-1Mn-4Zn-0.5Na (g) quenched Mg-1Mn-4Zn-0.5K (h) quenched Mg-1Mn-2Zn-0.25Na-0.25K.

### 5.2.6.1. Electrochemical Testing

The instrument was used to examine the corrosion behavior of the designed magnesium alloying systems. The first set of experiments were conducted to study the polarization curves of the alloying systems. Tafel analysis provides important information about the potential and current of corrosion in addition to describing the anodic and cathodic kinetics. The other test was conducted using electrochemical impedance spectroscopy (EIS) to get Nyquist Plot and measure the corrosion resistance. The samples were exposed to HBSS for 5 min and 8 min conditioning time for Tafel and EIS analysis, respectively.

Figure 113 illustrates the influence of the solidification rate on the polarization performance of pure magnesium. The lowest calculated corrosion rate for the pure

magnesium group was measured to be 0.044 mmpy for the rapidly solidified pure magnesium (Mg-HCR) with a current density and potential of 1.925  $\mu\text{A}/\text{cm}^2$  and -1.49 V, respectively. Additionally, Mg-HCR had the lowest anodic transition. The second lowest calculated corrosion rate in this group was measured to be 0.132 mmpy for slowly solidified pure magnesium (Mg-LCR) with a current density and potential of 5.804  $\mu\text{A}/\text{cm}^2$  and -1.79 V, respectively. Although the moderately solidified pure magnesium Mg-MCR showed a higher potential (- 1.656 V) than Mg-LCR, the other corrosion properties of Mg-MCR were measured to be 1.925  $\mu\text{A}/\text{cm}^2$  and 0.194 mmpy for corrosion current and corrosion rate, respectively.

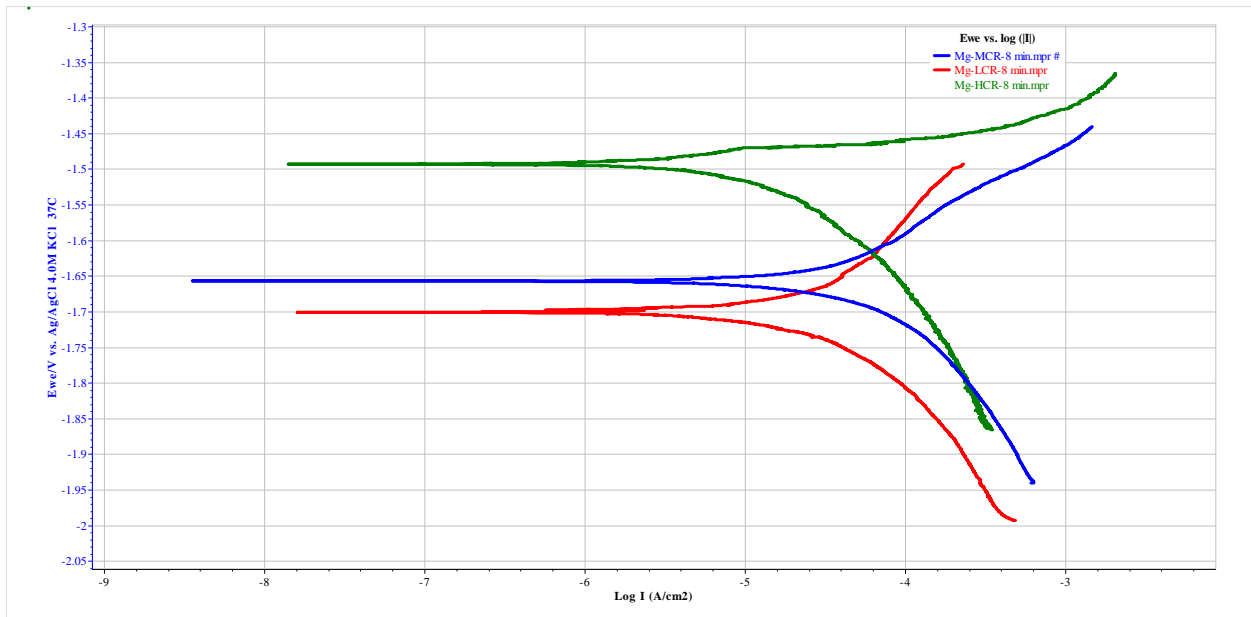


Figure 113: The polarization curves of (a) pure magnesium cooled in the furnace (slow cooling rate) (b) pure magnesium-cooled in the furnace with uninsulated-ends (moderate cooling) (c) quenched pure magnesium.

The influence of the solidification rate on the EIS performance can be seen in Figure 114. The highest corrosion resistance was found to be 941.2  $\text{ohm.cm}^2$  for the rapidly solidified pure magnesium (Mg-HCR), followed by the slowly solidified pure magnesium (Mg-LCR) with a value of 756.3  $\text{ohm.cm}^2$ . The moderately solidified pure magnesium Mg-MCR recorded the lowest corrosion resistance (575.7  $\text{ohm.cm}^2$ ) in this group.

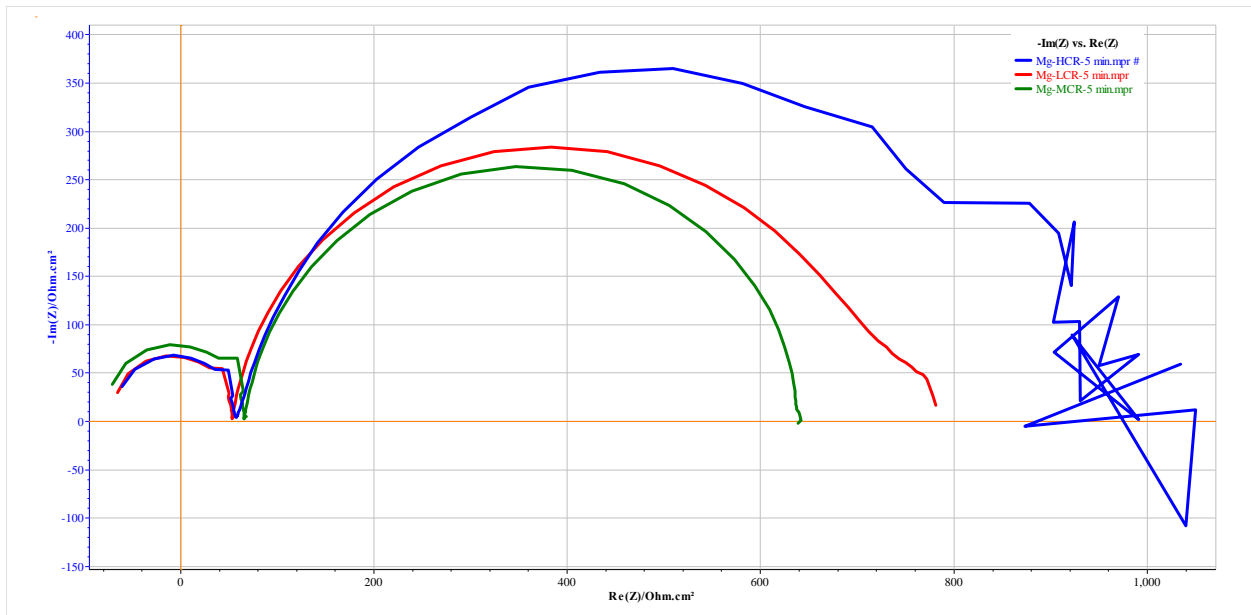


Figure 114: Nyquist curves of (a) pure magnesium cooled in the furnace (slow cooling rate) (b) pure magnesium-cooled in the furnace with uninsulated-ends (moderate cooling) (c) quenched pure magnesium.

Figure 115 shows Tafel plots for the quenched Mg-1Mn-2Zn and Mg-1Mn-4Zn alloying systems with cooling rates of 13.5  $^{\circ}\text{C}/\text{sec}$  in comparison with the rapidly solidified pure magnesium (Mg-HCR). The calculated corrosion rate for Mg-1Mn-2Zn was measured

to be 0.071 mmpy with a current density and potential of  $3.135 \mu\text{A}/\text{cm}^2$  and  $-1.47 \text{ V}$ , respectively. Additionally, Mg-HCR had the lowest anodic transition. On the other hand, the calculated corrosion rate was slightly higher for Mg-1Mn-4Zn (0.081 mmpy) than Mg-1Mn-4Zn within a current density and potential of  $3.563 \mu\text{A}/\text{cm}^2$  and  $-1.46 \text{ V}$ , respectively. The overall anodic and cathodic transitions showed a close behavior. The influence of adding 1% Mn and zinc in amounts of 2% and 4% on the EIS performance can be seen in Figure 116. The highest corrosion resistance was found to be  $1231 \text{ ohm}\cdot\text{cm}^2$  for the rapidly solidified Mg-1Mn-4Zn followed by the rapidly solidified Mg-1Mn-2Zn with a value of  $1067 \text{ ohm}\cdot\text{cm}^2$ , while the corrosion resistance for the rapidly solidified pure magnesium was found to be  $941.2 \text{ ohm}\cdot\text{cm}^2$ , as discussed above.

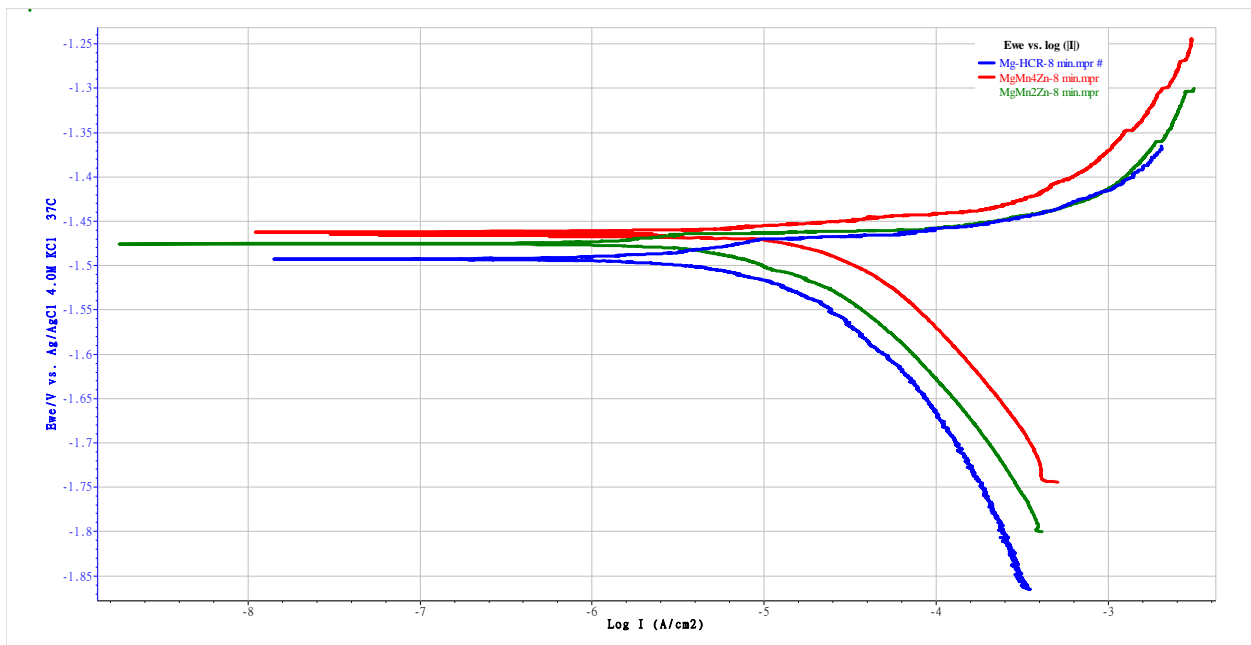


Figure 115: The polarization curves of (a) pure magnesium cooled in the furnace (b) quenched Mg-1Mn-2Zn (c) quenched Mg-1Mn-4Zn.

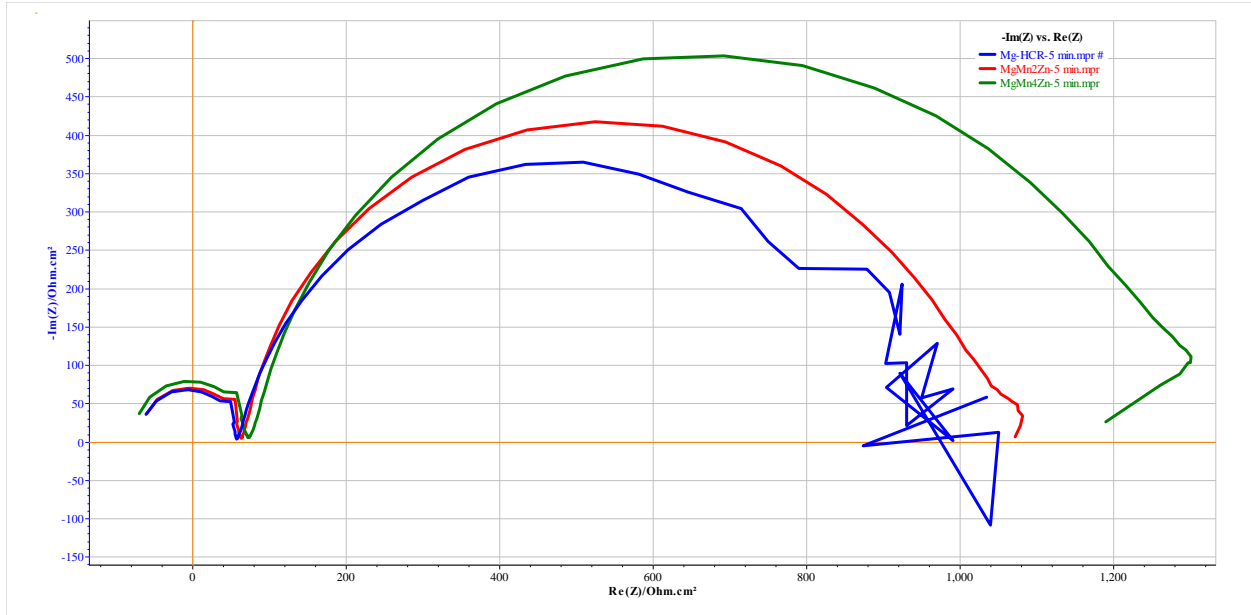


Figure 116: Nyquist curves of (a) pure magnesium cooled in the furnace (b) quenched Mg-1Mn-2Zn (c) quenched Mg-1Mn-4Zn.

The influence of adding sodium and potassium individually and simultaneously on the corrosion behavior of Mg-1Mn-4Zn can be seen in Figure 117 and Figure 118. The quenched Mg-1Mn-4Zn-0.5Na showed a dramatic increase in the calculated corrosion rate, which was measured to be 0.79 mmpy. The current density and potential were detected to be  $34.87 \mu\text{A}/\text{cm}^2$  and  $-1.46 \text{ V}$ , respectively. Additionally, the anodic transition of Mg-1Mn-4Zn-0.5Na recorded the highest corrosion rate among all other groups of alloying systems. On the other hand, the resistance for this alloy was found to be  $409.7 \text{ ohm}\cdot\text{cm}^2$ , which is the lowest among all groups.

The second tested sample was Mg-1Mn-4Zn-0.5K with a calculated corrosion rate, current density, and potential of 0.22 mmpy,  $9.7 \mu\text{A}/\text{cm}^2$ , and  $-1.485 \text{ V}$ , respectively. Although the sample showed the best corrosion behavior among the Mg-1Mn-4Zn-Na-K

alloying systems, it showed a lower corrosion resistance ( $509.9 \text{ ohm.cm}^2$ ) in comparison to the other groups of the alloying system, but higher than pure Mg-MCR. Nevertheless, the calculated corrosion rate was shifted to be  $0.23 \text{ mmpy}$  with the addition of sodium and potassium simultaneously. The current density and potential were found to be  $10.205 \text{ } \mu\text{A/cm}^2$  and  $-1.506 \text{ V}$ , respectively. Moreover, the corrosion resistance for this alloy was  $485.5 \text{ ohm.cm}^2$ .

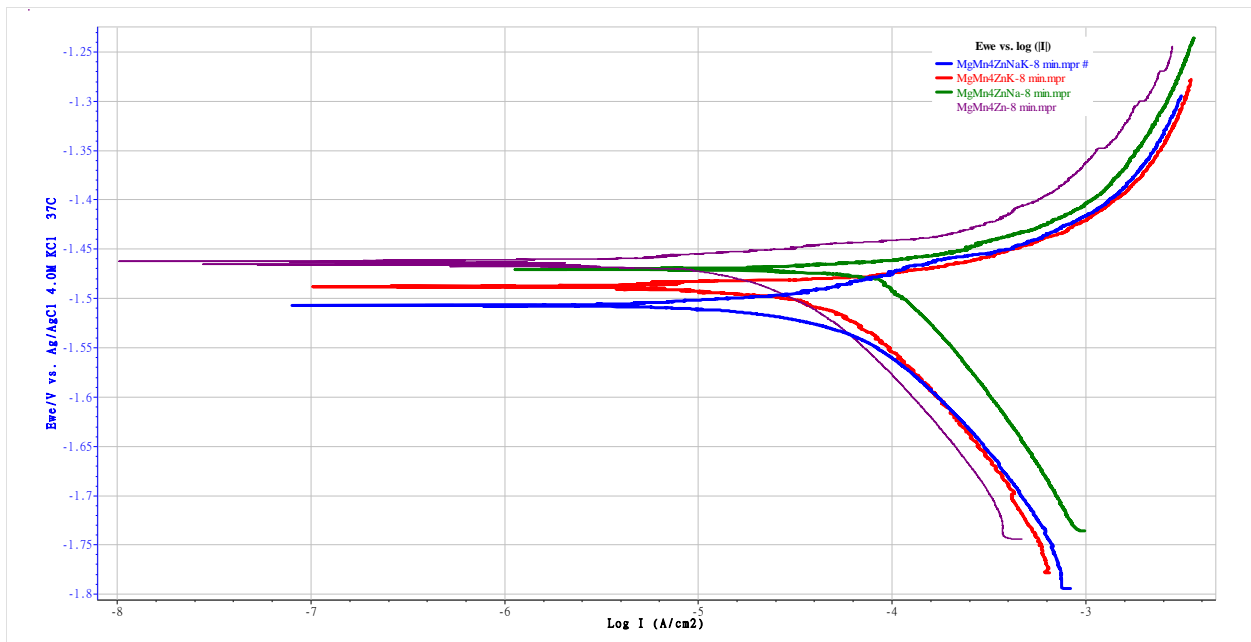


Figure 117: The polarization curves of (a) quenched Mg-1Mn-4Zn (b) quenched Mg-1Mn-4Zn-0.5Na (g) quenched Mg-1Mn-4Zn-0.5K (c) quenched Mg-1Mn-2Zn-0.25Na-0.25K.

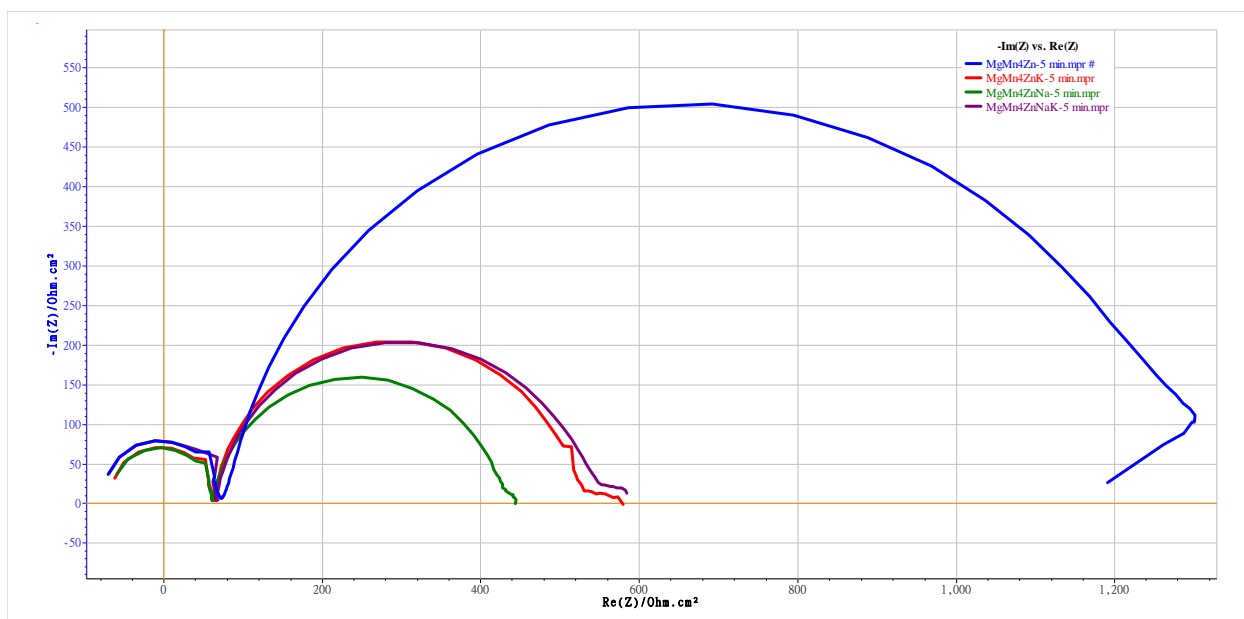


Figure 118: Nyquist curves of a) quenched Mg-1Mn-4Zn (b) quenched Mg-1Mn-4Zn-0.5Na (g) quenched Mg-1Mn-4Zn-0.5K (c) quenched Mg-1Mn-2Zn-0.25Na-0.25K.

### 5.2.6.2. Immersion Testing

This instrument was used to analyze the corrosion rate during the incubation time of ten days in Hank's Balanced Salts Solution at temperature of 37 °C and 7.4 pH. The corrosion cell was kept under a tight control to maintain the biological surrounding to obtain accurate mass loss measurements. The corrosion rate was determined according to ASTM G31-12 overtime period over 240 hours. The first group of samples was tested to investigate the effect of the solidification rate.

It was found that the rapidly solidified pure magnesium (Mg-HCR) showed the lowest corrosion rate (0.06 mm/year) with a stable oxide layer. The second lowest

corrosion rate was for slowly solidified pure magnesium (Mg-LCR) with a corrosion rate of 0.084 mm/year. On the other side, the moderately solidified pure magnesium (Mg-MCR) showed a significantly high corrosion rate of 16.19 mm/year, as shown in Figure 119 and Figure 120. It's believed that Mg-LCR showed a better corrosion rate than Mg-MCR due to the ratio of the size of grain boundaries to the cross section area of the tested sample (1 cm<sup>2</sup>), which gives Mg-LCR a nobler behavior than Mg-MCR. On the other side, refining the grain size significantly in the case of Mg-HCR refines the distribution the grain boundaries, which enhancing the production of oxide layer at the surface. In the literature review, it was reported that the corrosion rate of pure magnesium was 2.08 mm/year in Hank's solution [20].

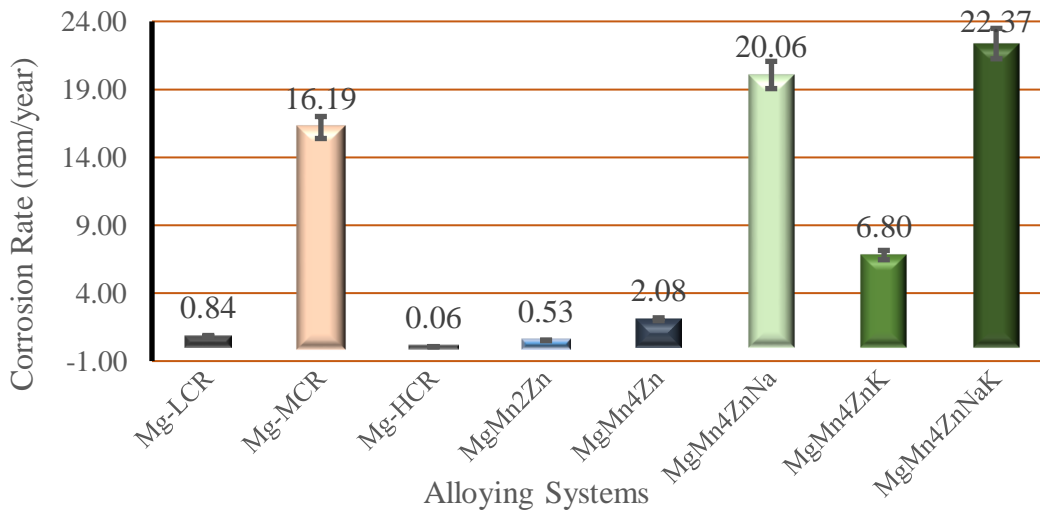


*Figure 119: Corrosion rate of the produced alloying systems over time period of 10 days in Hank's Balanced Salts Solution at temperature of 37 °C and 7.4 pH.*

The second group tested the combined effect of solidification rate and alloying system on the corrosion rate. The corrosion rates of quenched Mg-1Mn-2Zn and Mg-1Mn-

4Zn alloying systems was found to be 0.53 mm/year and 2.08 mm/year, respectively. The optical images in [Figure 120](#) show a formation of non-uniform oxide layer and the size of this layer increases with increasing the zinc content. Additionally, the presence of pitting corrosion was observed to increase with increasing the content of zinc from 2% to 4%. It was reported in the literature review that the corrosion rate of Mg-1Ca-2Zn and Mg-1Ca-4Zn was measured to be 2.38 mm/year and 4.42 mm/year in Hank's solution, respectively [20]. The third group tested the influence of adding sodium and potassium individually and simultaneously to Mg-1Mn-4Zn. It was concluded that adding sodium individually and simultaneously deteriorated the corrosion resistance. Additionally, the samples showed a significant presence of pitting corrosion, which is due to the formation of secondary brittle-reactive phases, as it was discussed in the previous sections. The addition of potassium individually showed the best corrosion rate in this group with rapid formation of a uniform oxide layer with a limited presence of pitting corrosion. This indicates that the use of more active metals leads to a modified surface.

It's worth mentioning that one corrosion test doesn't reflect the overall corrosion behavior of the sample. It's believed that the rapid changes in the corrosion properties are due to the surface modifications that occur during the exposure of the sample to the test parameters, which indicate the kinetic change on the interfacial surface. This concept can be approved by exposing the same sample to different conditioning times, which leads to the production of different outcomes by creating a modified surface for each condition.

The dominant factor in this type of corrosion is the ratio between the reaction to produce a layer on the surface and the reaction to dissolve the formed layer.

It's believed that the overall corrosion performance in this study is controlled by the ability to produce a protective layer on the surface with an adequate rate that is faster than the corrosion rate. Therefore, the fast formation at the beginning of the reaction could lead to a more stable layer by lowering the free energy at the surface, while a slow reaction at an extended time could provide a continuum to the dissolving process along with a lack of producing a protective layer at the surface. This formation can be induced by adding elements to catalyze the surface modifications such as sodium and potassium. The effectiveness of this approach starts by tweaking the composition of the alloying system to get the suitable surface kinetic to match the requirements of the corrosion environment.

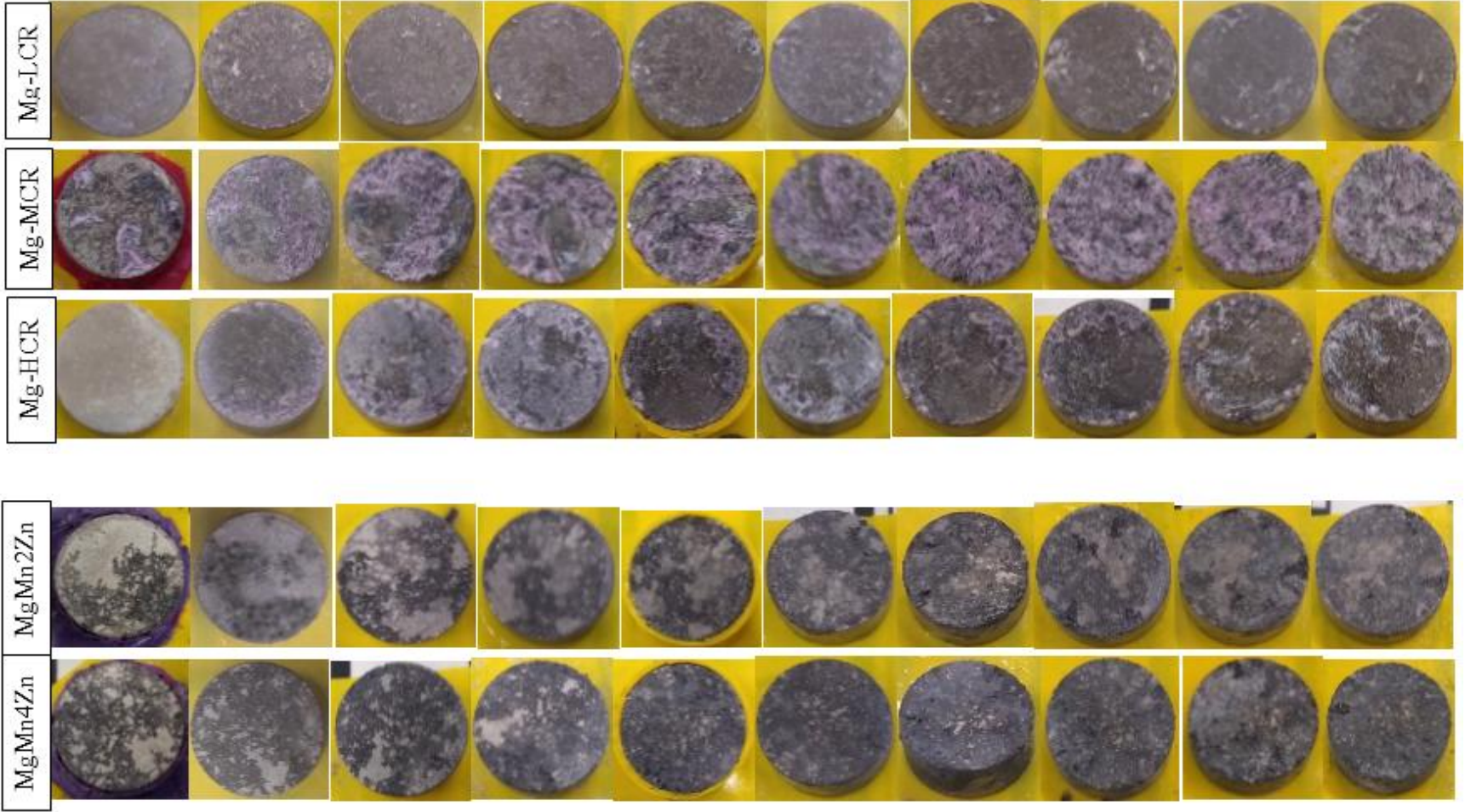
Table 19: Corrosion rate of the produced alloying systems in Hank's Balanced Salts Solution at temperature of 37 °C and 7.4 pH over a time of 240 hours.

mm/year	Day 1	Day 2	Day 3	Day 4	Day 5	Day 6	Day 7	Day 8	Day 9	Day 10
<b>Mg-LCR</b>	10.92	-12.18	-0.21	-1.05	-1.47	-1.05	0.63	-1.26	-1.05	-1.68
<b>Mg-MCR</b>	-3.78	-6.30	-16.80	-2.73	-20.79	-52.29	-9.45	-19.74	-12.81	-17.22
<b>Mg-HCR</b>	0.63	0.42	0.00	-0.42	0.21	0.21	-0.63	-0.42	-0.21	-0.42
<b>MgMn2Zn</b>	0.63	-0.84	-0.21	-1.26	-1.47	-1.05	-0.21	-1.05	-0.84	1.05
<b>MgMn4Zn</b>	0.84	-0.21	-0.84	-5.04	-2.31	-1.68	-1.89	-3.99	-0.63	-5.04
<b>MgMn4ZnNa</b>	-31.50	-23.52	-10.71	-17.43	-11.55	-15.33	-33.39	-11.76	-17.64	-27.72
<b>MgMn4ZnK</b>	-18.90	-11.34	-5.25	-5.88	-3.57	-4.62	-3.57	-4.20	-2.94	-7.77
<b>MgMn4ZnNaK</b>	-34.44	-10.75	-11.30	-23.31	-9.24	-73.50	39.27	-23.31	-41.58	-35.49

Initial Sample



Day 1    Day 2    Day 3    Day 4    Day 5    Day 6    Day 7    Day 8    Day 9    Day 10



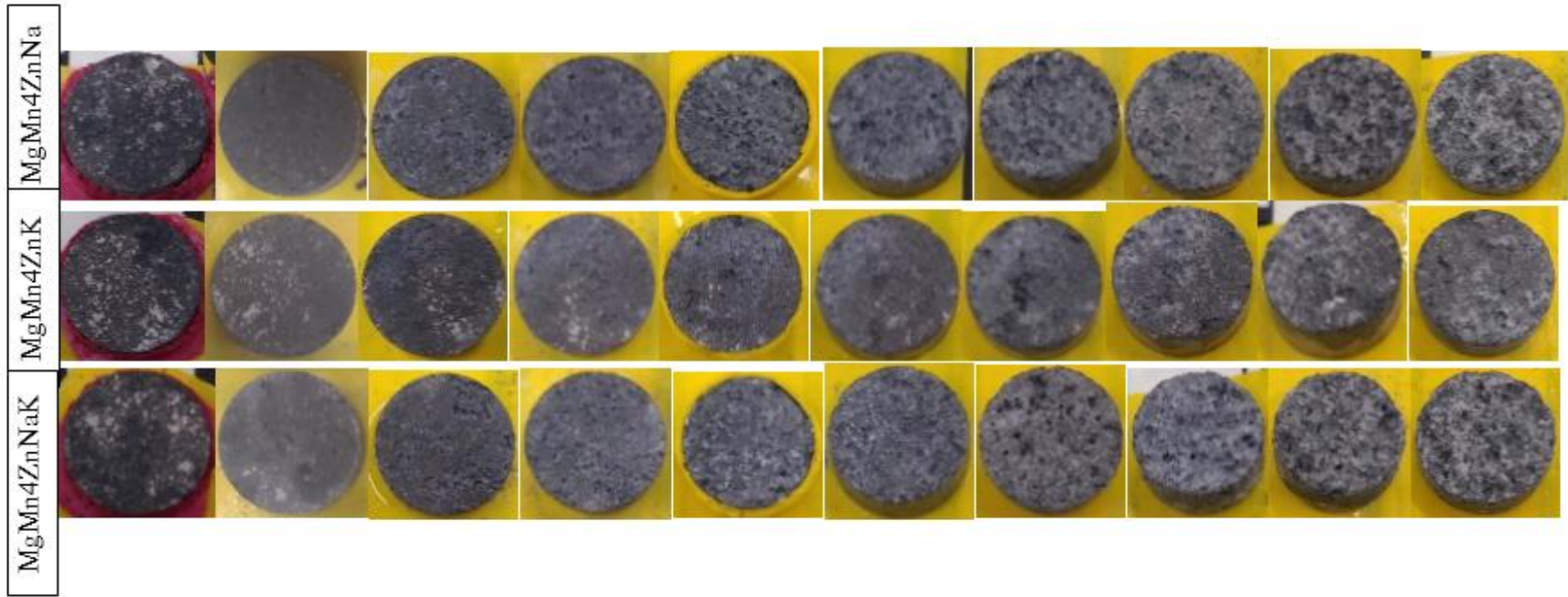


Figure 120: Optical images of exposed as-cast Magnesium alloying systems in Hank's Balanced Salts Solution at temperature of 37 °C and 7.4 pH.

### 5.2.6.3. Post-Immersion SEM and EDS

These characterization tools were used to analyze the interfacial surface during the incubation, which helps to identify and quantify the produced compounds on the interfacial. The slowly cooled pure magnesium (LCR-Mg) with a cooling rate of 0.035 °C/sec and an average grain size of 4235  $\mu\text{m}$  was analyzed post-immersion at different magnifications (500 x, 1000 x, and 3000 x), as shown in Figure 71Figure 121. The SEM images show the surface morphology of the corroded sample, which was observed to be uniformly cracked and covered with white compounds. The average size of the cracked surface of each fragment was found to be  $\sim 10 \mu\text{m}$ . The surface compounds were found to be consisted of salts, oxide, and phosphates compounds, as shown in Figure 123. Additionally, the element distribution on the corroded surface can be seen in Figure 122. While the resolution elemental map for the corroded Mg-LCR was acceptable, it was hard to get a good resolution for most of the other alloying systems due to the complexity and morphology of the corroded surface.

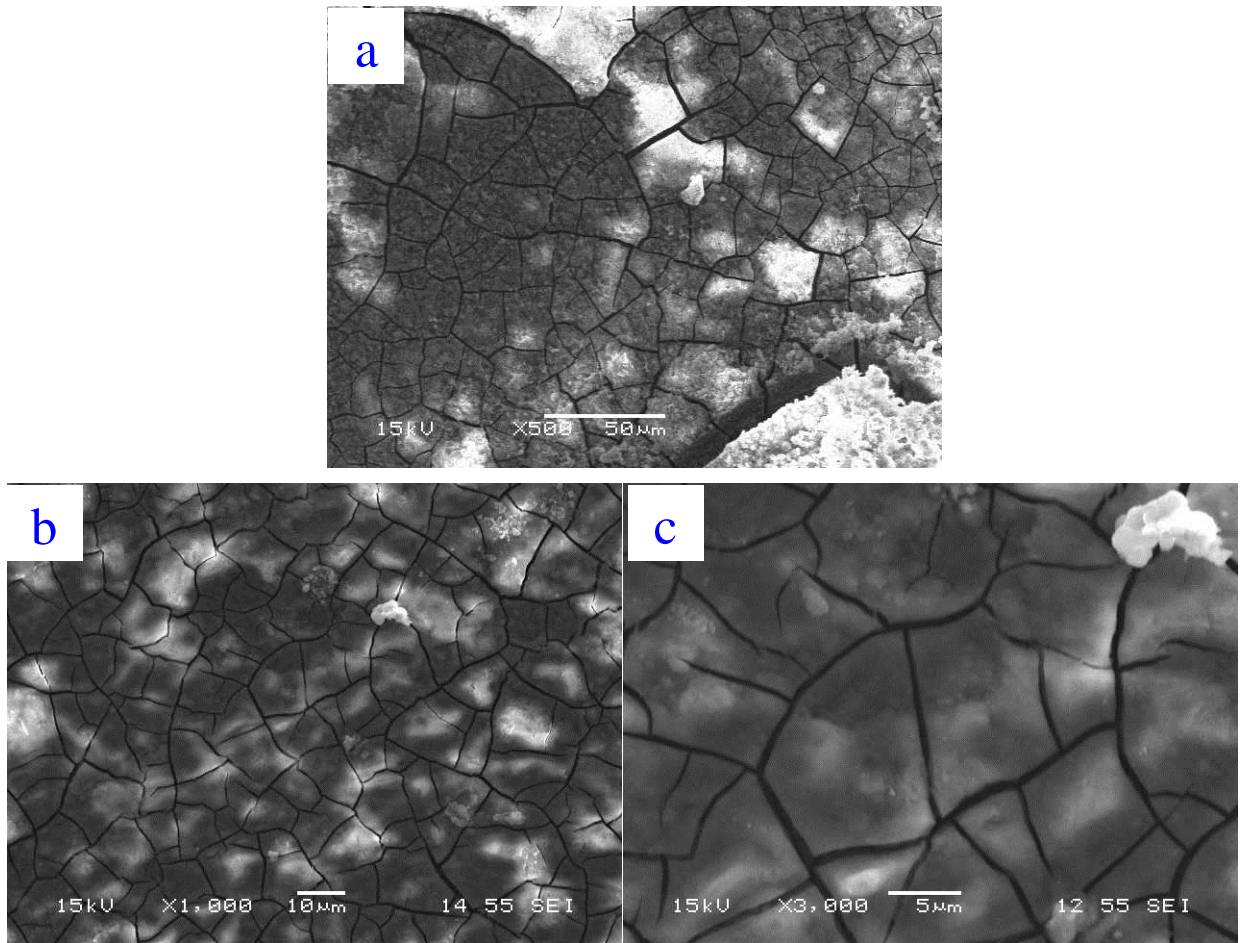
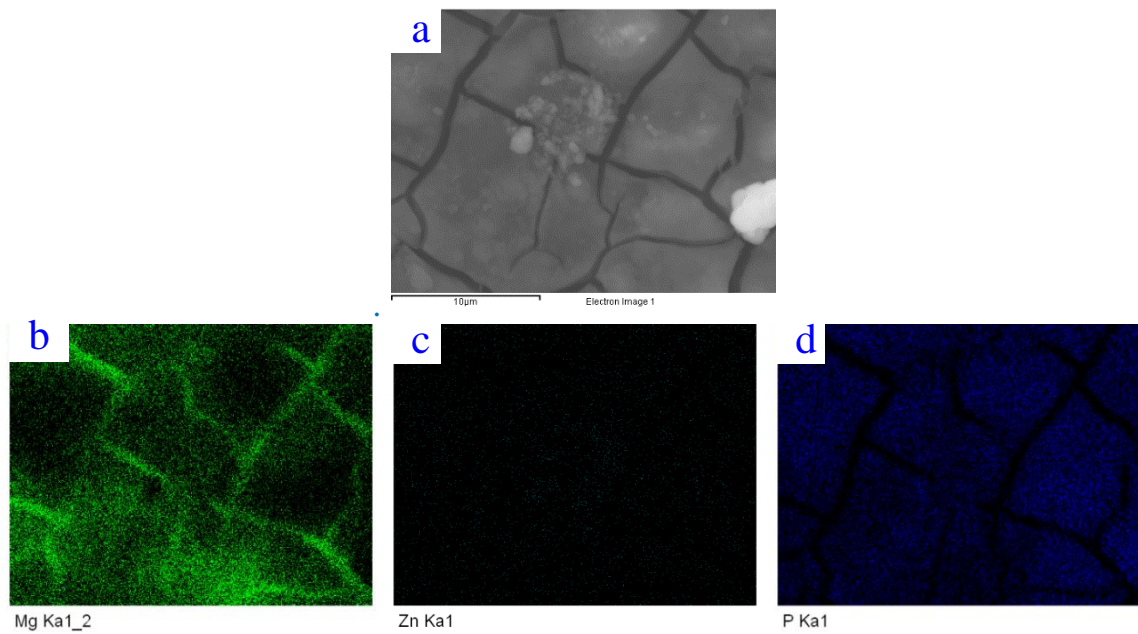


Figure 121: Post-immersion SEM images of pure magnesium cooled in the furnace (slow cooling rate) at different magnifications (a) at 500 x (b) at 1000 x (c) at 3000 x.



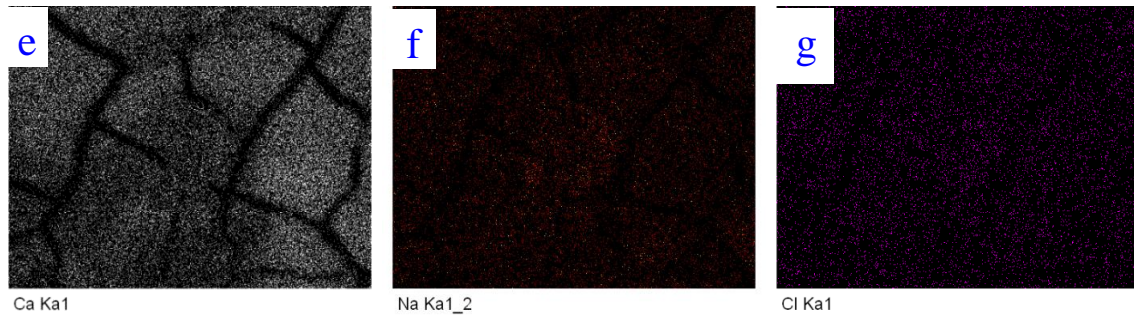


Figure 122: Post-immersion EDS elements map of pure magnesium cooled in the furnace (slow cooling rate) (a) area of interest (b) Magnesium (c) Zinc (d) P (e) Calcium (f) Sodium (g) Cl.

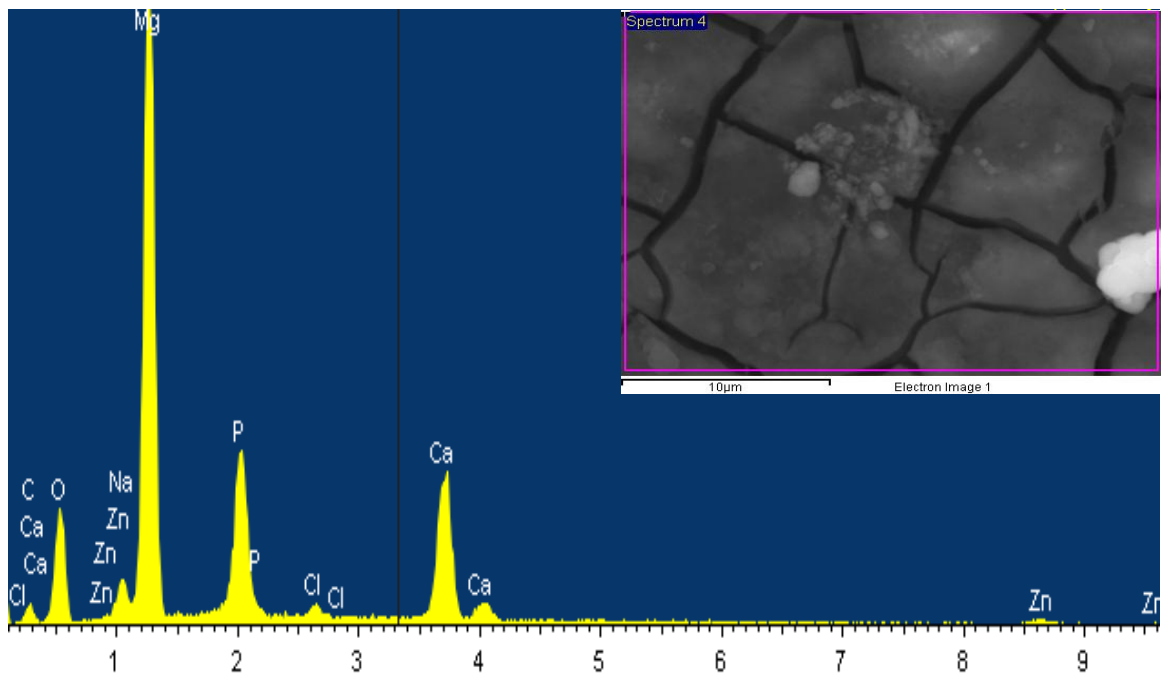
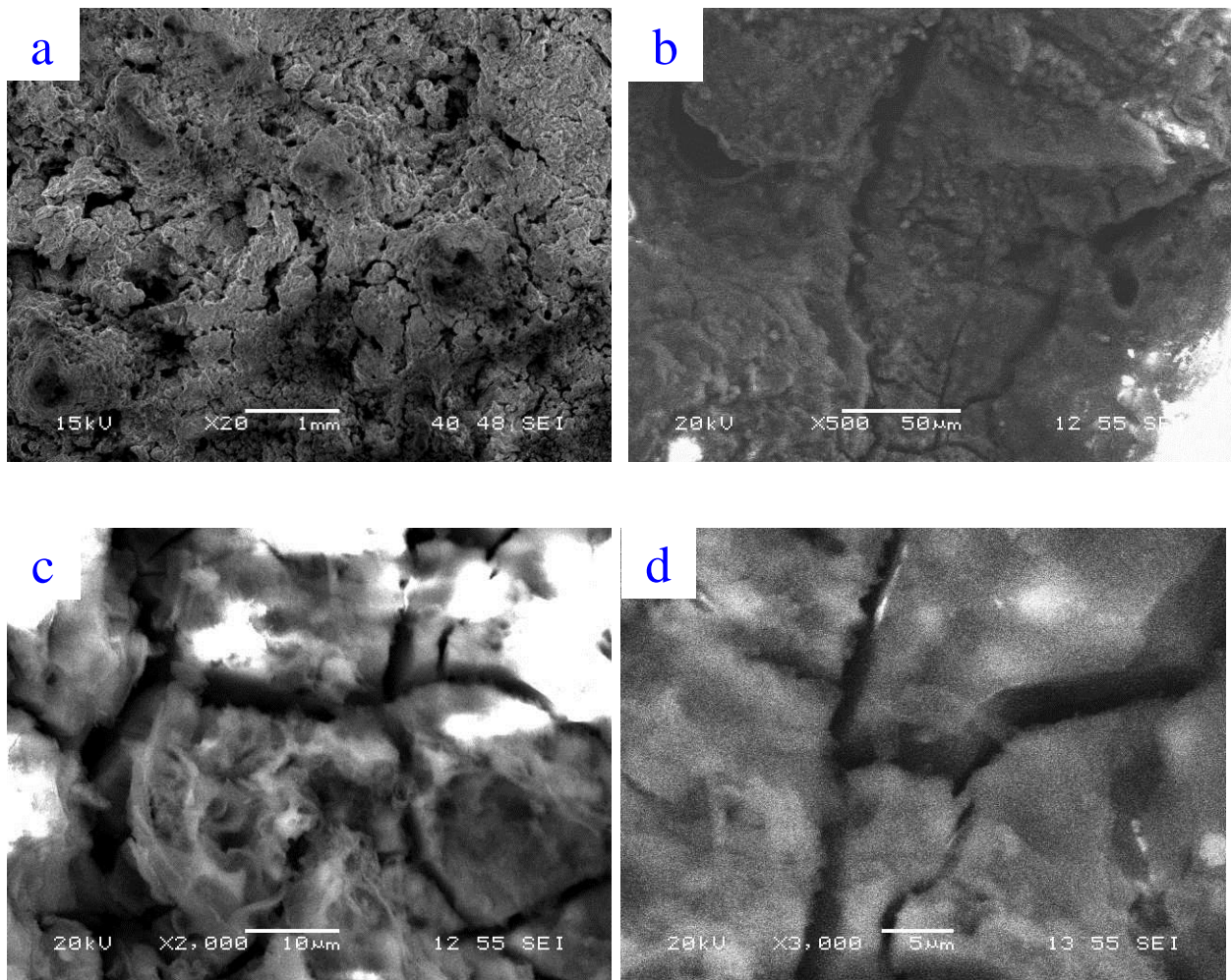


Figure 123: Post-immersion EDS spectrum images of pure magnesium cooled in the furnace (slow cooling rate).

The moderate cooled pure magnesium (MCR-Mg) with a cooling rate of 0.074 °C/Sec and an average grain size of 2257 µm was analyzed post-immersion at different magnifications (20 x, 500 x, 2000 x, and 3000 x), as shown in Figure 71Figure 124. The SEM images show the surface morphology of the corroded sample, which was observed to be heavily and unevenly corroded and covered with white compounds. The corrosion

products was accumulated on the surface. The surface compounds were found to be consisted of salts, oxide, and phosphates compounds, as shown in Figure 125. The intensity of the peaks indicates the high presence of the corrosion compounds on the surface of the sample. Additionally, the intensity of magnesium peak was observed to be lower than magnesium peak intensity of Mg-LCR sample.



*Figure 124: Post-immersion SEM images of pure magnesium cooled in the furnace with uninsulated-ends (moderate cooling) at different magnifications (a) at 20 x (b) at 500 x (c) at 2000 x (d) at 3000 x.*

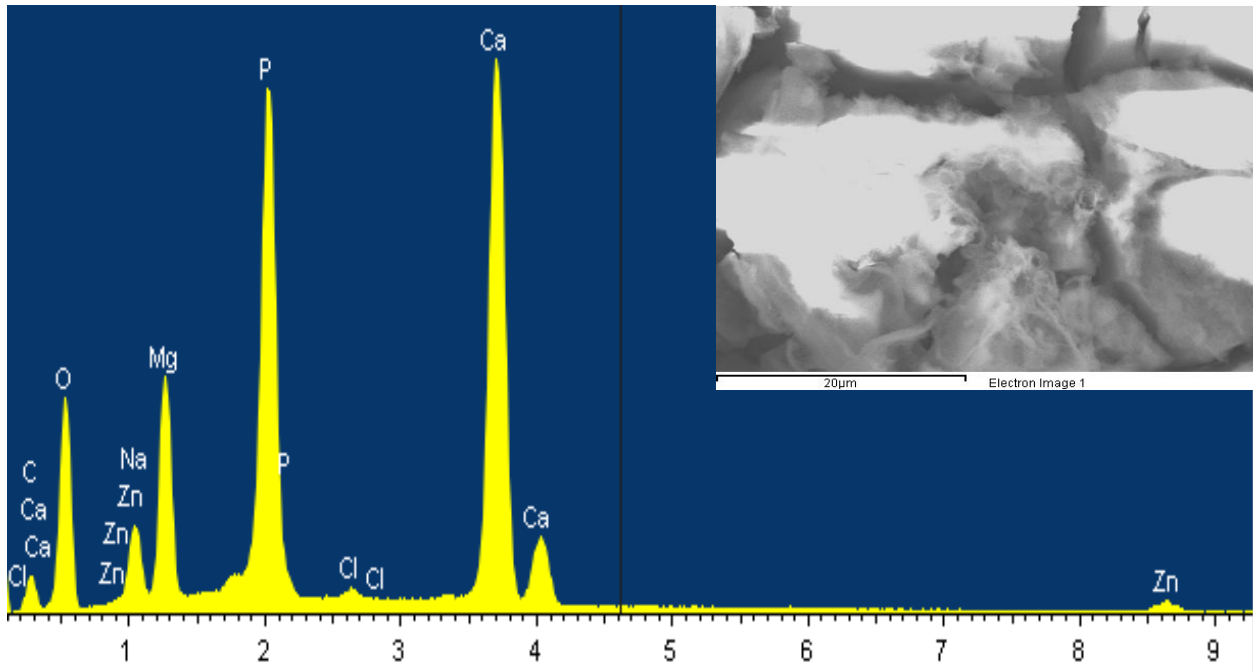


*Figure 125: Post-immersion sum EDS spectrum images of pure magnesium moderately cooled in the furnace with uninsulated-ends.*

The quenched pure magnesium (HCR-Mg) with a cooling rate of 0.035 °C/sec and an average grain size of 13 µm was analyzed post-immersion at different magnifications (100 x, 500 x, 1000 x, and 3000 x), as shown in Figure 71Figure 126. The SEM images show the surface morphology of the corroded sample, which was observed to be uniformly cracked and covered with white compounds. The average size of the cracked surface of each fragment was found to be ~ 40 µm. The surface compounds were found to be distributed evenly and consisted of salts, oxide, and phosphates compounds, as shown in Figure 127.

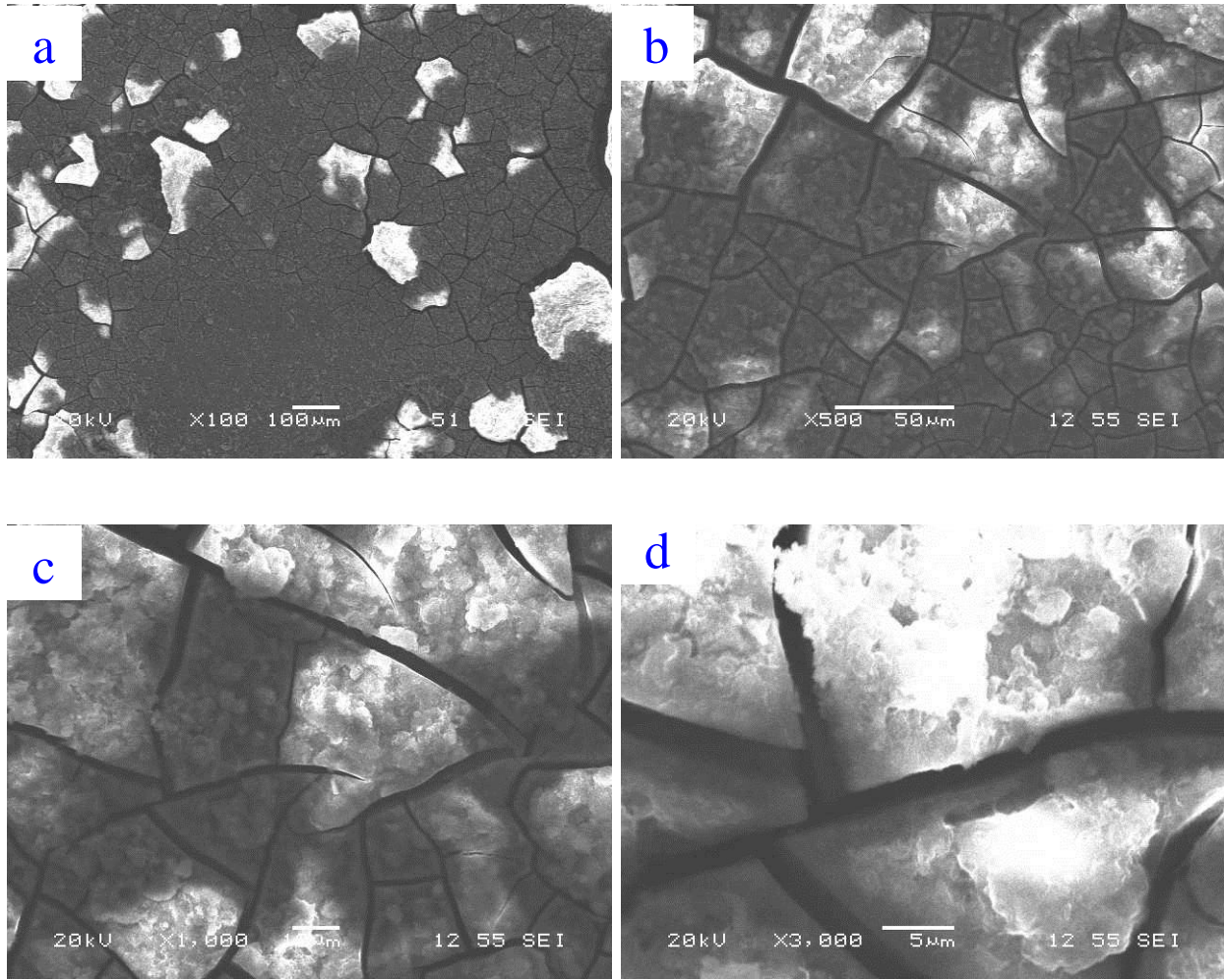


*Figure 126: Post-immersion SEM images of pure magnesium rapidly cooled in liquid CO<sub>2</sub> at different magnifications at (a) 100 x (b) 500 x (c) 1000 x (d) 3000 x.*

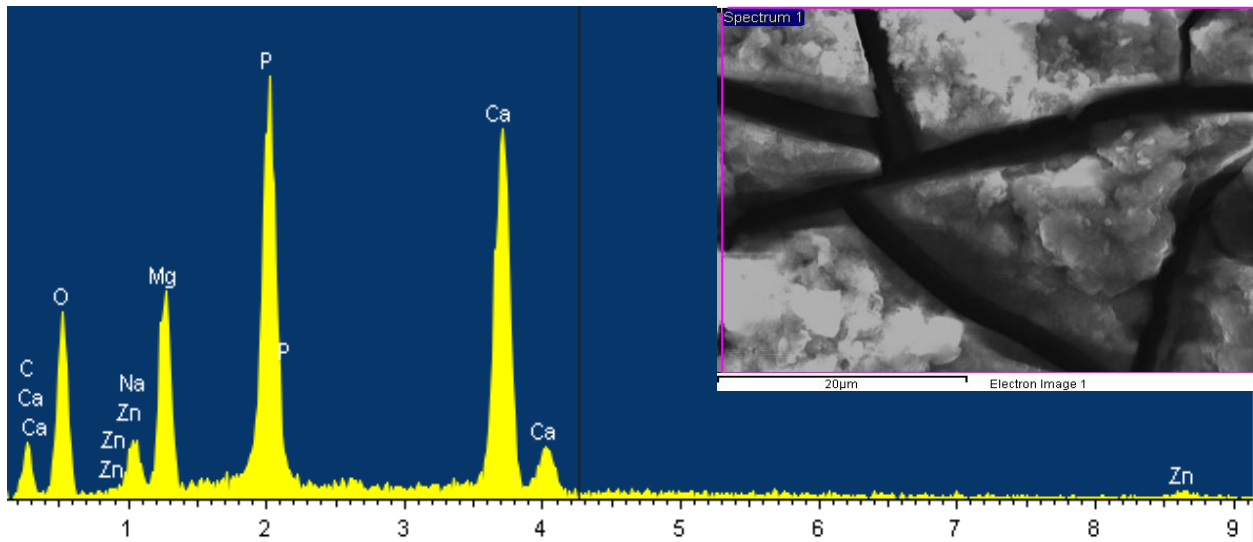


*Figure 127: Post-immersion sum EDS spectrum images of pure magnesium rapidly cooled in liquid CO<sub>2</sub>.*

The quenched Mg-1Mn-2Zn alloy was analyzed post-immersion at different magnifications (200 x, 500 x, 3000 x, and 5000 x), as shown in Figure 71Figure 128. The SEM images show the surface morphology of the corroded sample, which was observed to be uniformly cracked with a minor presence of pitting corrosion. Additionally, the surface was covered with a thicker white compound than formed on pure Mg. The average size of the cracked surface of each fragment was found to be ~ 75 µm. The surface compounds were found to be consisted of salts, oxide, and phosphates compounds, as shown in Figure 129. Additionally, the intensity of the peaks indicates the presence of a thicker uniformly formed compounds on the surface, as shown in Figure 128 d and Figure 129.

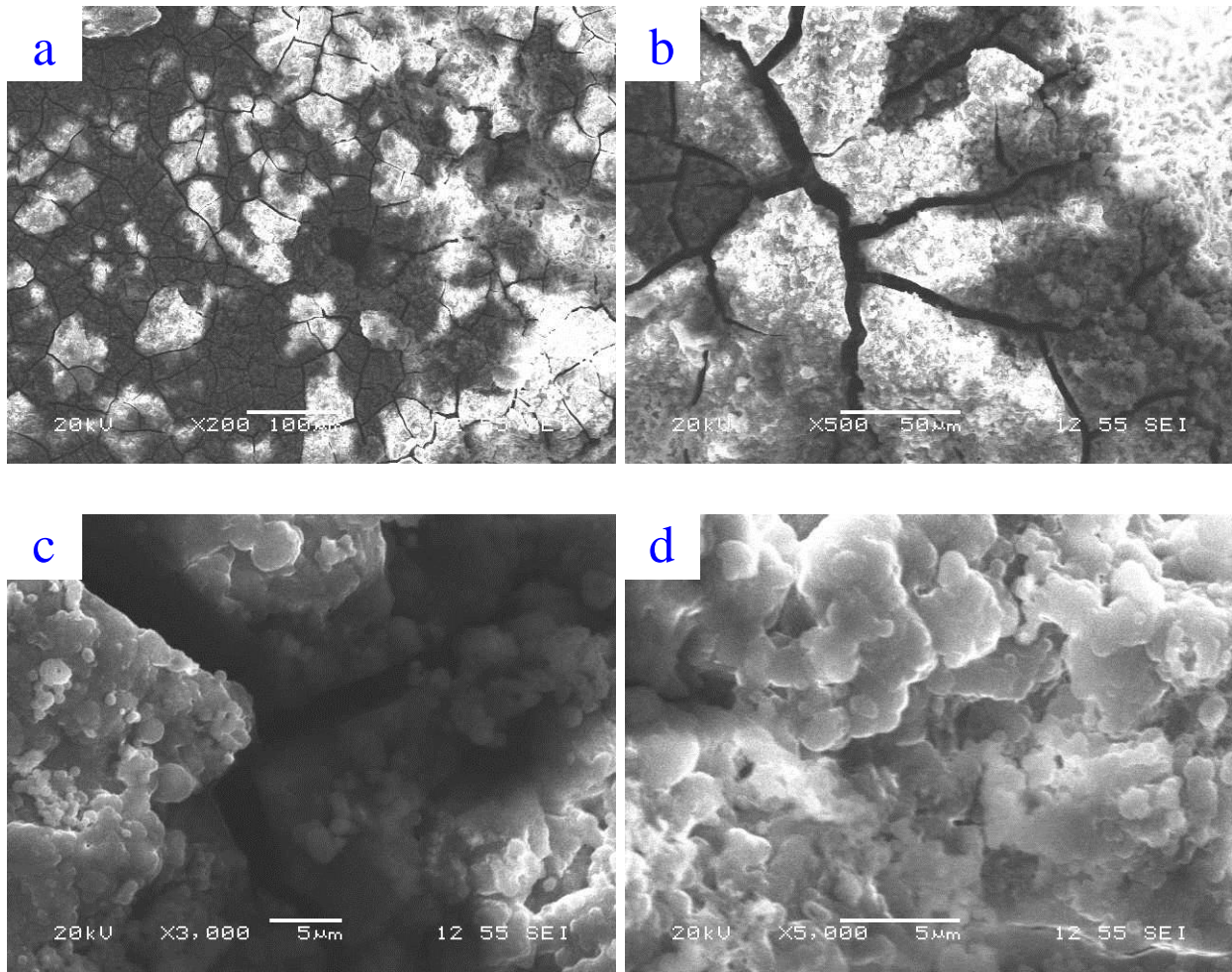


*Figure 128: Post-immersion SEM images of Mg-1Mn-2Zn alloying system rapidly cooled in liquid CO<sub>2</sub> at different magnifications at (a) at 200 x (b) at 500 x (c) at 3000 x (d) at 5000 x.*

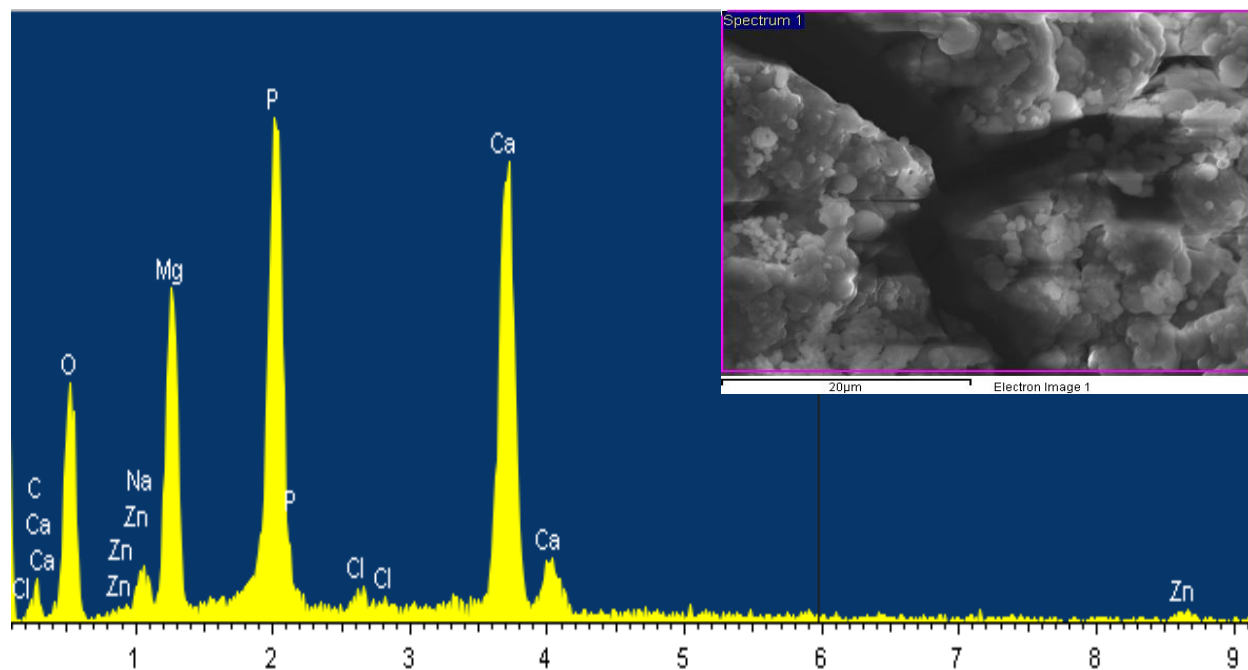


*Figure 129: Post-immersion sum EDS spectrum images of the primary and secondary phases Mg-1Mn-2Zn alloying system rapidly cooled in liquid CO<sub>2</sub>.*

The quenched Mg-1Mn-4Zn alloy was analyzed post-immersion at different magnifications (50 x, 500 x, 1000 x, 2000 x, 3000 x, and 5000 x), as shown in Figure 71Figure 130. The SEM images show the surface morphology of the corroded sample. A formation of two types of surface layers was observed, a thin evenly formed layer and thicker unevenly distributed layer with a higher presence of pitting corrosion than Mg-1Mn-4Zn, as shown in Figure 130 (a). Additionally, the thicker formation on the surface was covered with thicker white compounds. The surface compounds were found to be consisted of salts, oxide, and phosphates compounds, as shown in Figure 131. Additionally,

the intensity of the peaks indicates the presence of thicker oxide formed compounds on the surface, as shown in Figure 128 (f) and Figure 131.

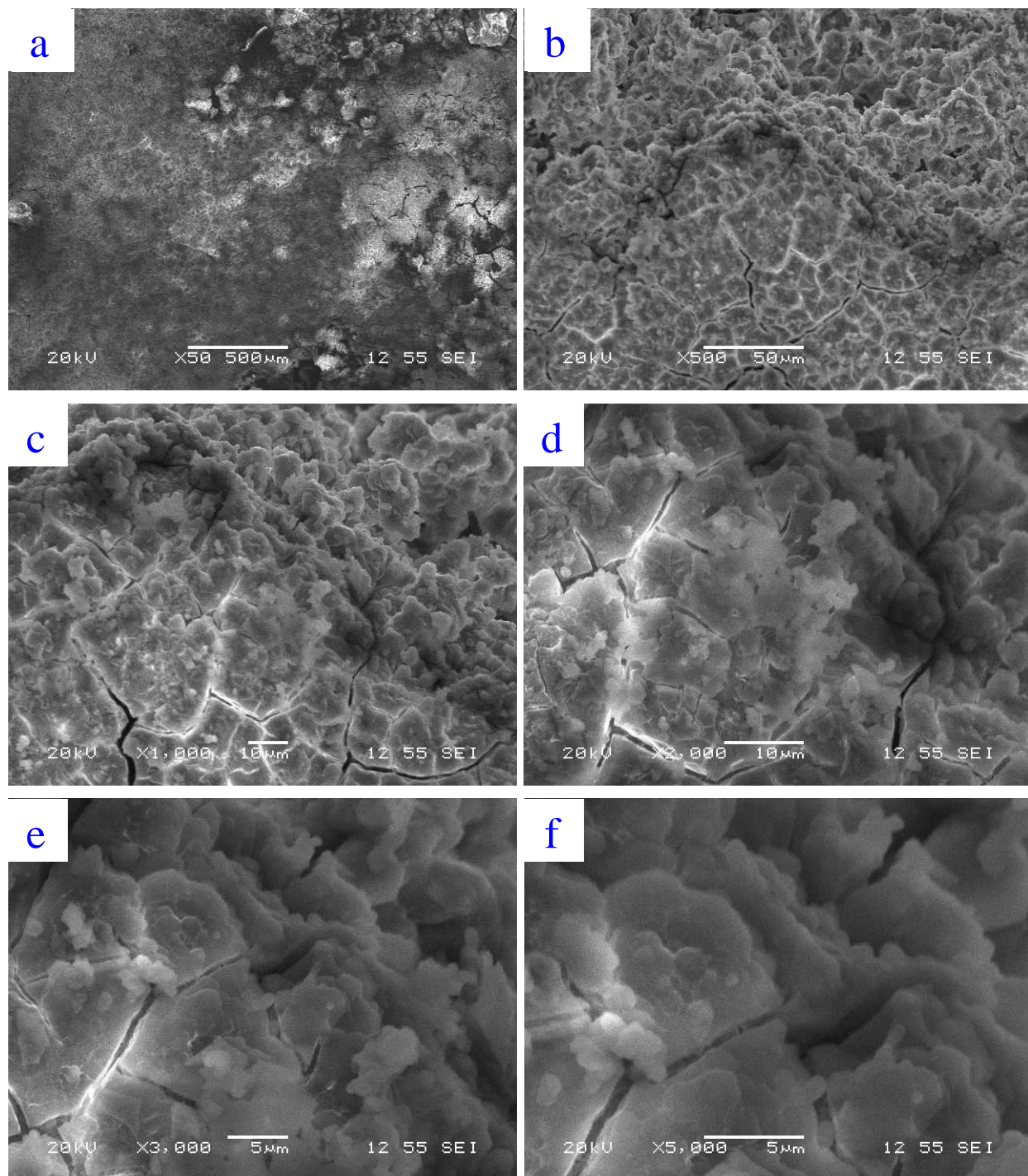


Figure 130: Post-immersion SEM images of Mg-1Mn-4Zn alloying system rapidly cooled in liquid CO<sub>2</sub> at different magnifications (a) at 500 x (b) at 1000 x (c) at 2000 x (d) at 3000 x (e) at 5000 x (f) at 10000 x.

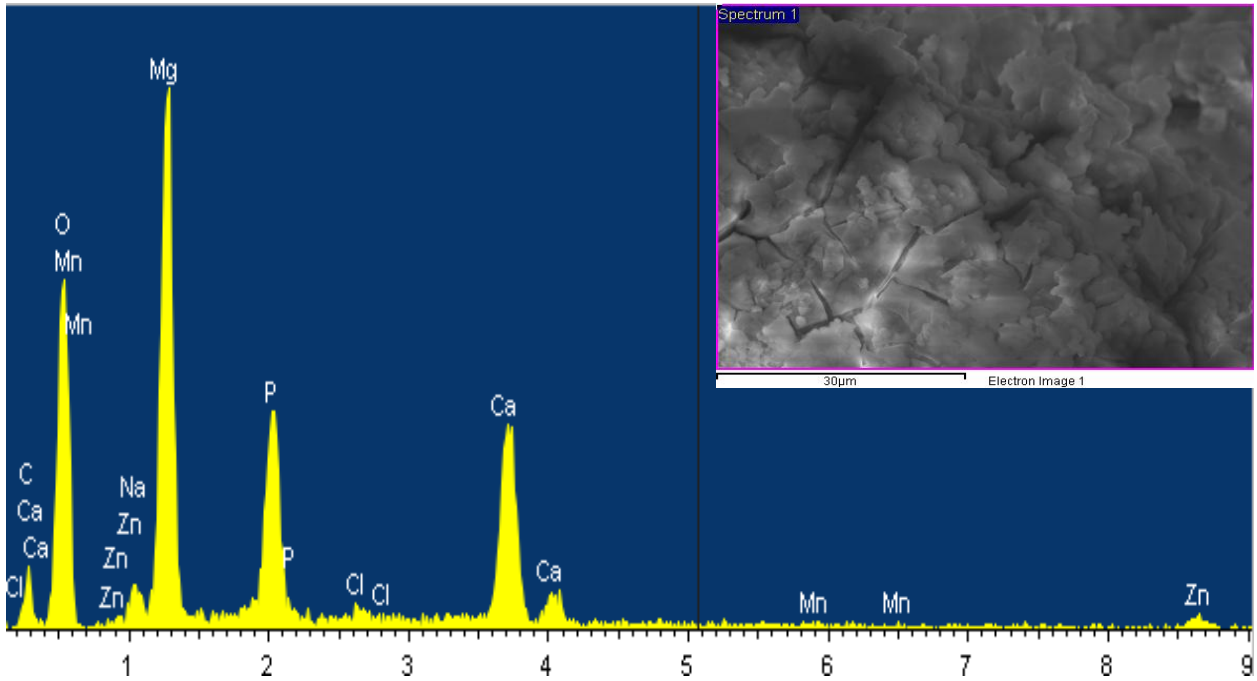
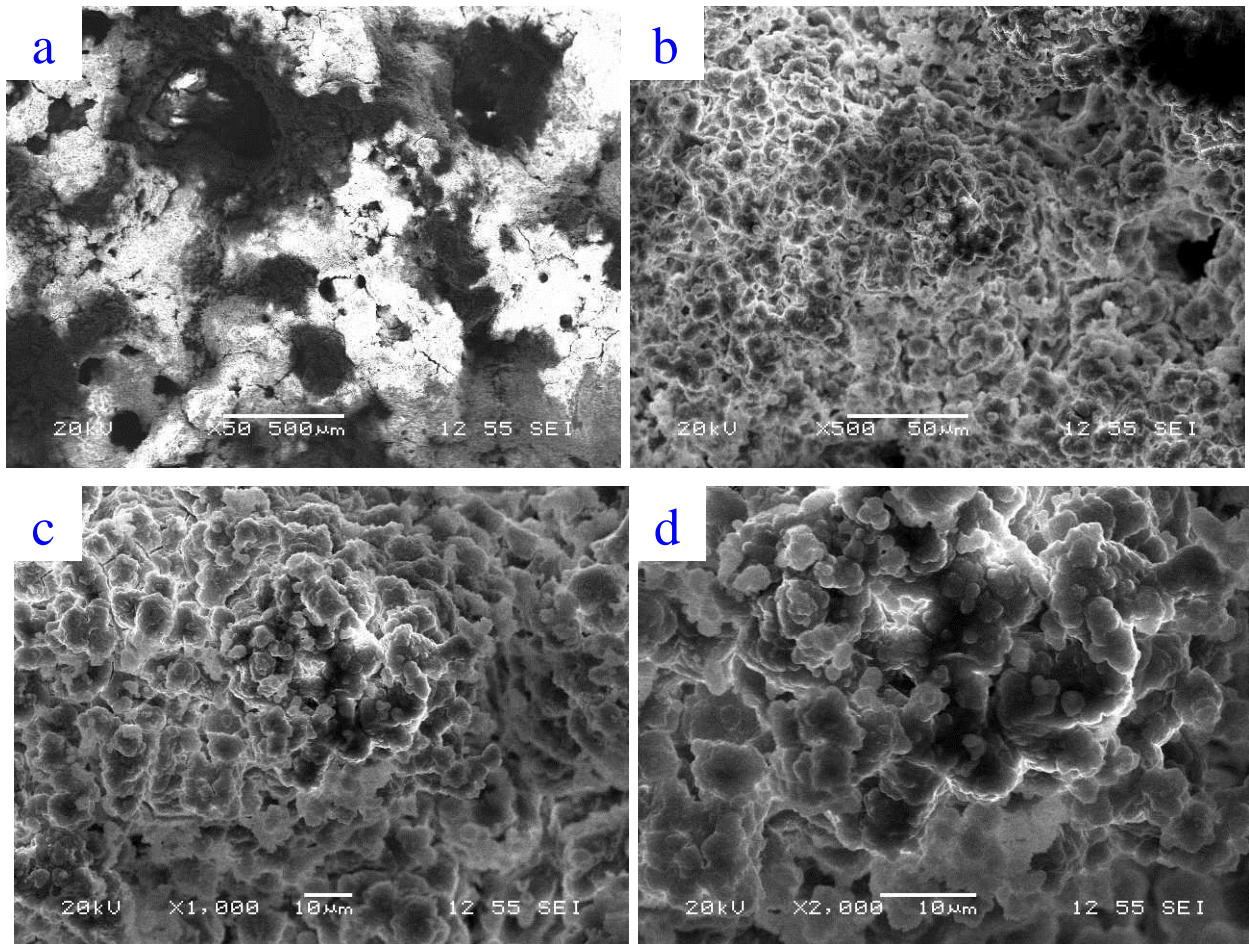


Figure 131: Post-immersion sum EDS spectrum images of Mg-1Mn-4Zn alloying system rapidly cooled in liquid CO<sub>2</sub>.

The quenched Mg-1Mn-4Zn-0.5Na alloy was analyzed post-immersion at different magnifications (50 x, 500 x, 1000 x, 2000 x, 3000 x, and 5000 x), as shown in Figure 132. The SEM images show the surface morphology of the corroded sample; a high presence of pitting corrosion was observed across the corroded surface. Nevertheless, the formed corrosion products were noticed to be in the form of separated granular particles and a thick layer attached to the corroded surface. It is believed that the separated particles are the

brittle phases that were examined in the pre-corrosion and the rounded corrosion products formed due to the reaction of these phases with the solution. The surface compounds were found to be consisted of salts, oxide, and phosphates compounds, as shown in Figure 132. Additionally, the intensity of the peaks indicates the presence of thick formed compounds on the surface.



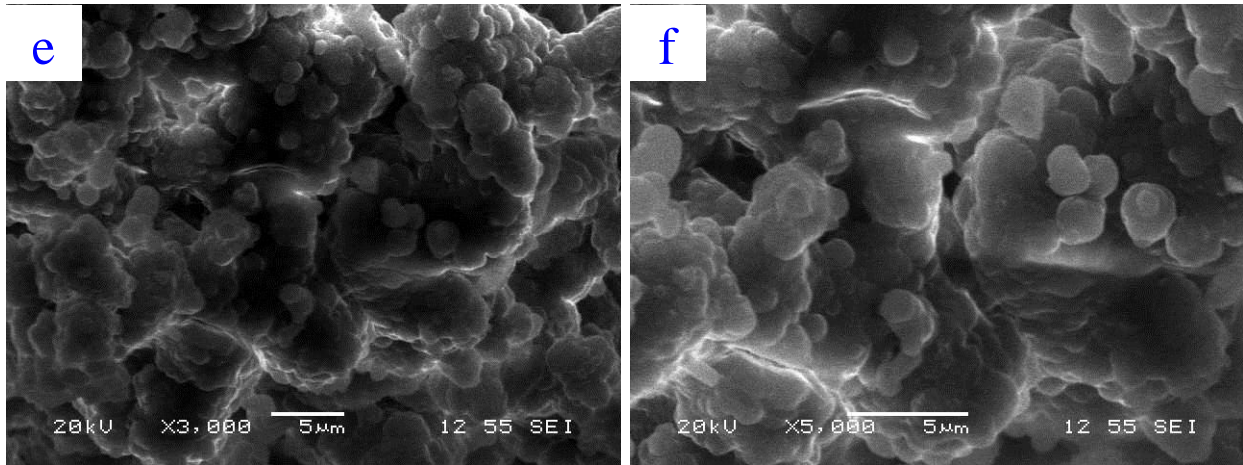


Figure 132: Post-immersion SEM images of Mg-1Mn-4Zn-0.5Na alloying system rapidly cooled in liquid CO<sub>2</sub> at different magnifications (a) at 50 x (b) at 500 x (c) at 1000 x (d) at 2000 x (e) at 3000 x (f) at 5000 x.

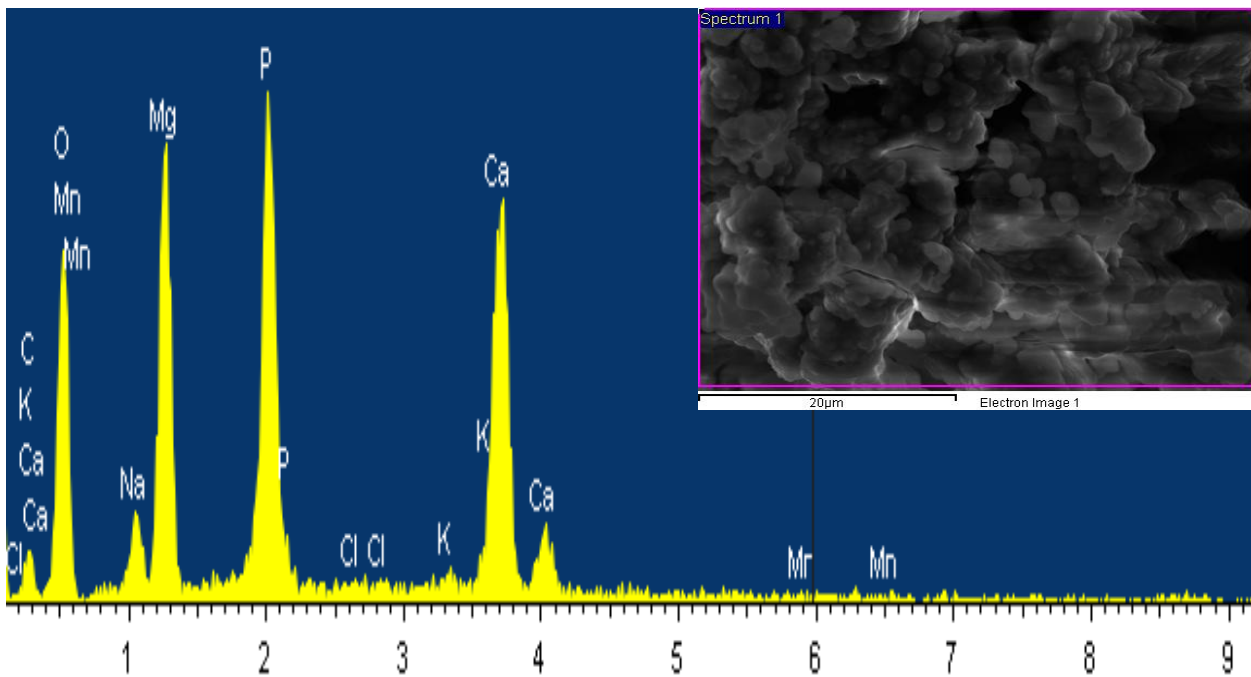
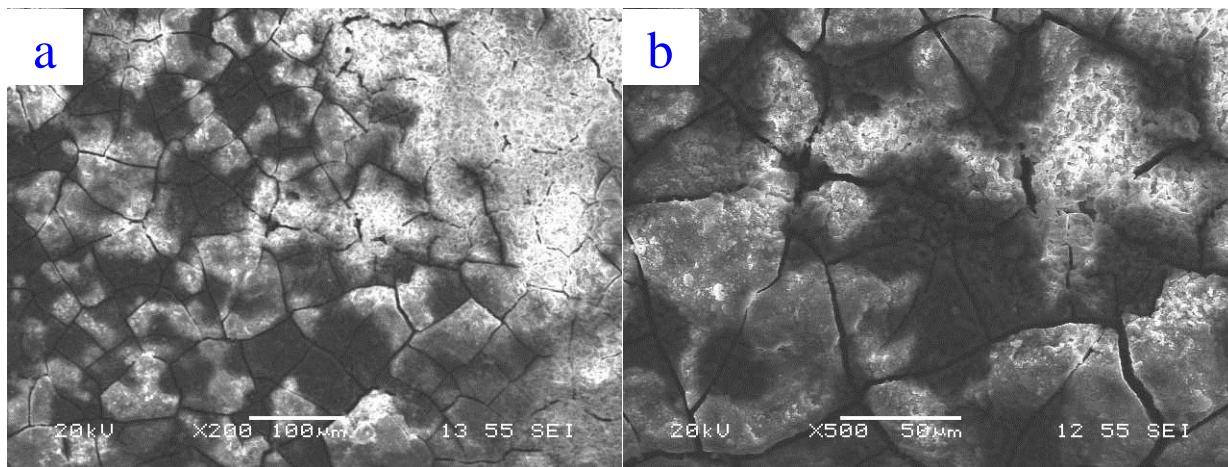
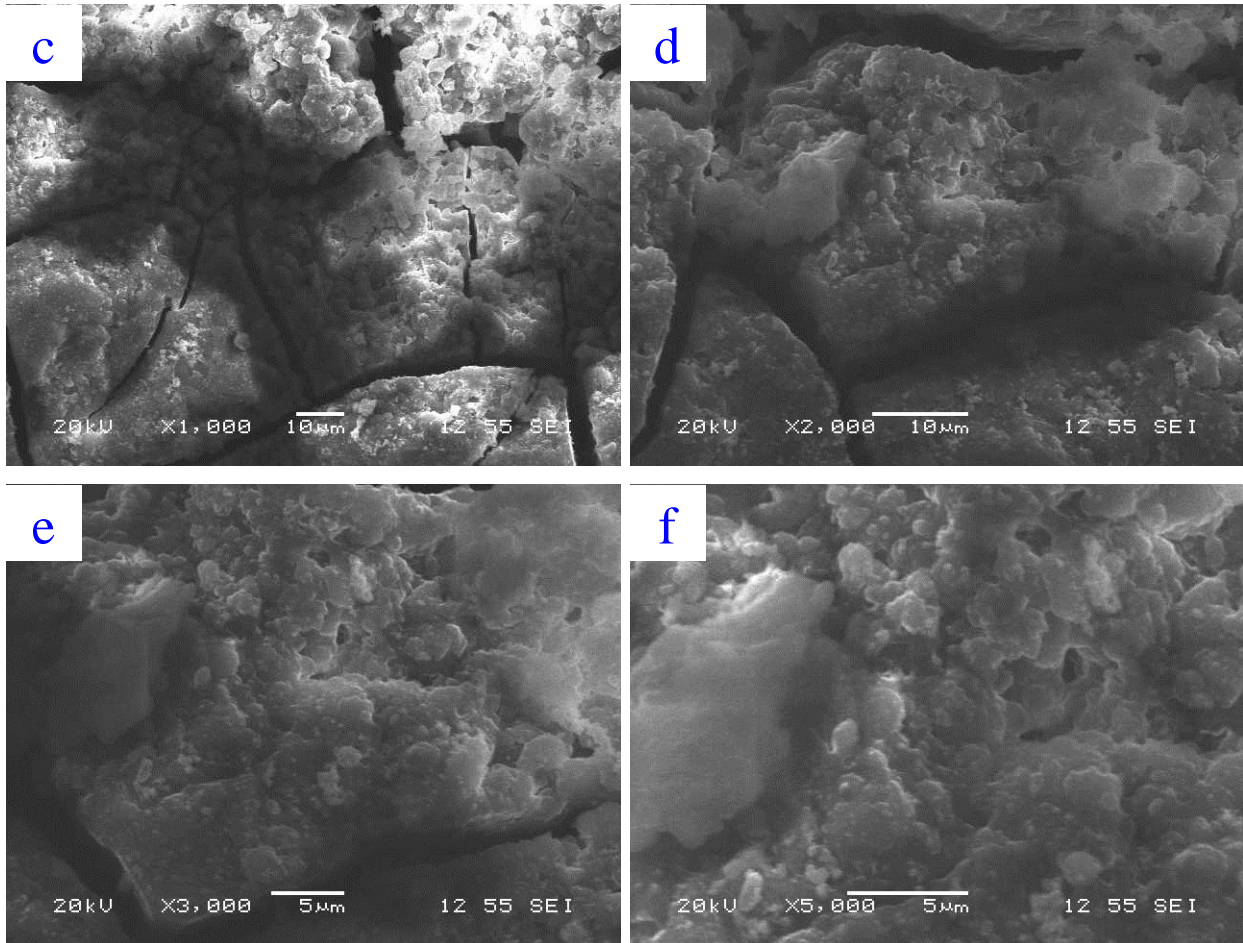


Figure 133: Post-immersion sum EDS spectrum image for the matrix of Mg-1Mn-4Zn-0.5Na alloying system rapidly cooled in liquid CO<sub>2</sub>.

The quenched Mg-1Mn-4Zn-0.5Na alloy was analyzed post-immersion at different magnifications (200 x, 500 x, 1000 x, 2000 x, 3000 x, and 5000 x), as shown in Figure 134.

The SEM images show the surface morphology of the corroded sample, which was observed to be uniformly cracked with a minor presence of pitting corrosion. Additionally, the surface was covered with thick-effective white compounds. The formation of these compounds is expected to be driven by the addition of potassium, which provided the potential force to induce the production these compounds during the reaction with solution. The average size of the cracked surface of each fragment was found to be  $\sim 50 \mu\text{m}$ . The surface compounds were found to be consisted of salts, oxide, and phosphates compounds, as shown in Figure 135. Additionally, the intensity of the peaks indicates the presence of thicker uniformly formed compounds on the surface, as shown in Figure 134 (d) and Figure 135.





*Figure 134: Post-immersion SEM images of Mg-1Mn-4Zn-0.5K alloying system rapidly cooled in liquid CO<sub>2</sub> at different magnifications (a) at 200 x (b) at 500 x (c) at 1000 x (d) at 2000 x (e) at 3000 x (f) at 5000 x.*

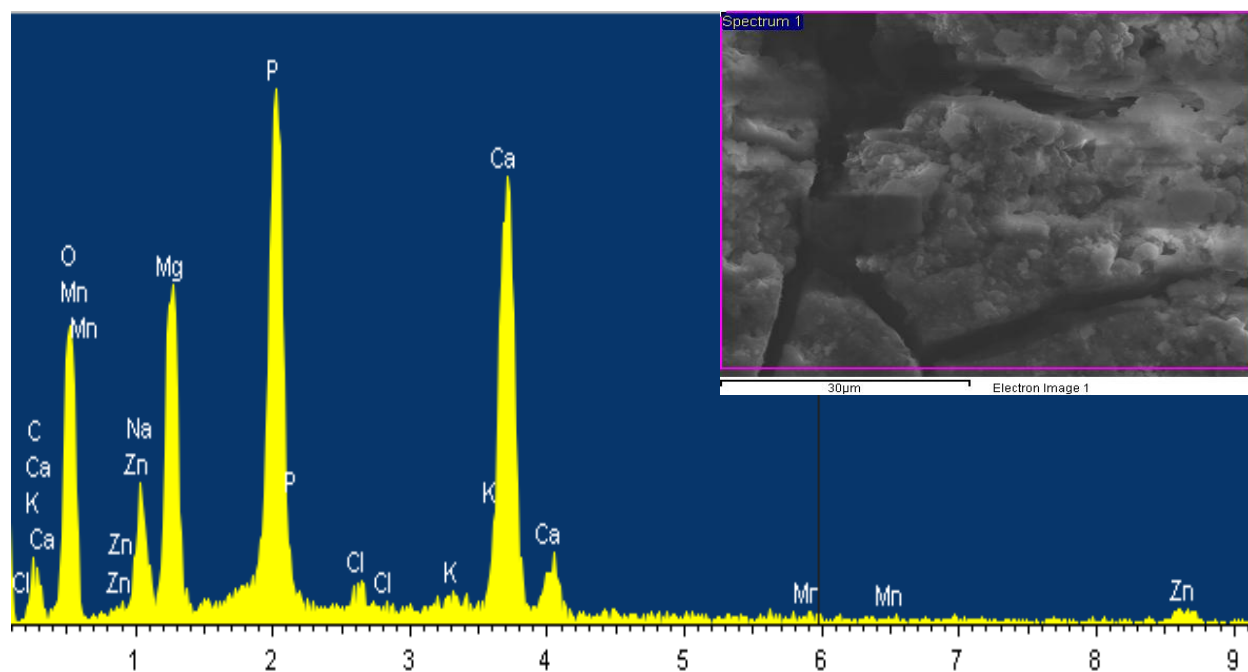


*Figure 135: Post-immersion sum EDS spectrum image for the matrix of Mg-1Mn-4Zn-0.5Na alloying system rapidly cooled in liquid CO<sub>2</sub>.*

The quenched Mg-1Mn-4Zn-0.25Na-0.25K alloy was analyzed post-immersion at different magnifications (50 x, 100 x, 500 x, 1000 x, 3000 x, and 5000 x), as shown in Figure 136. The SEM images show the surface morphology of the corroded sample; a high presence of pitting corrosion was observed across the corroded surface. Nevertheless, the formed corrosion products were noticed to be in the form of separated granular particles and a thick layer attached to the corroded surface. It is believed that the separated particles are the brittle phases that were examined in the pre-corrosion and the rounded corrosion products formed due to the reaction of these phases with the solution. The surface compounds were found to be consisted of salts, oxide, and phosphates compounds, as shown in Figure 137. Additionally, the intensity of the peaks indicates the presence of a thick formed compounds on the surface.

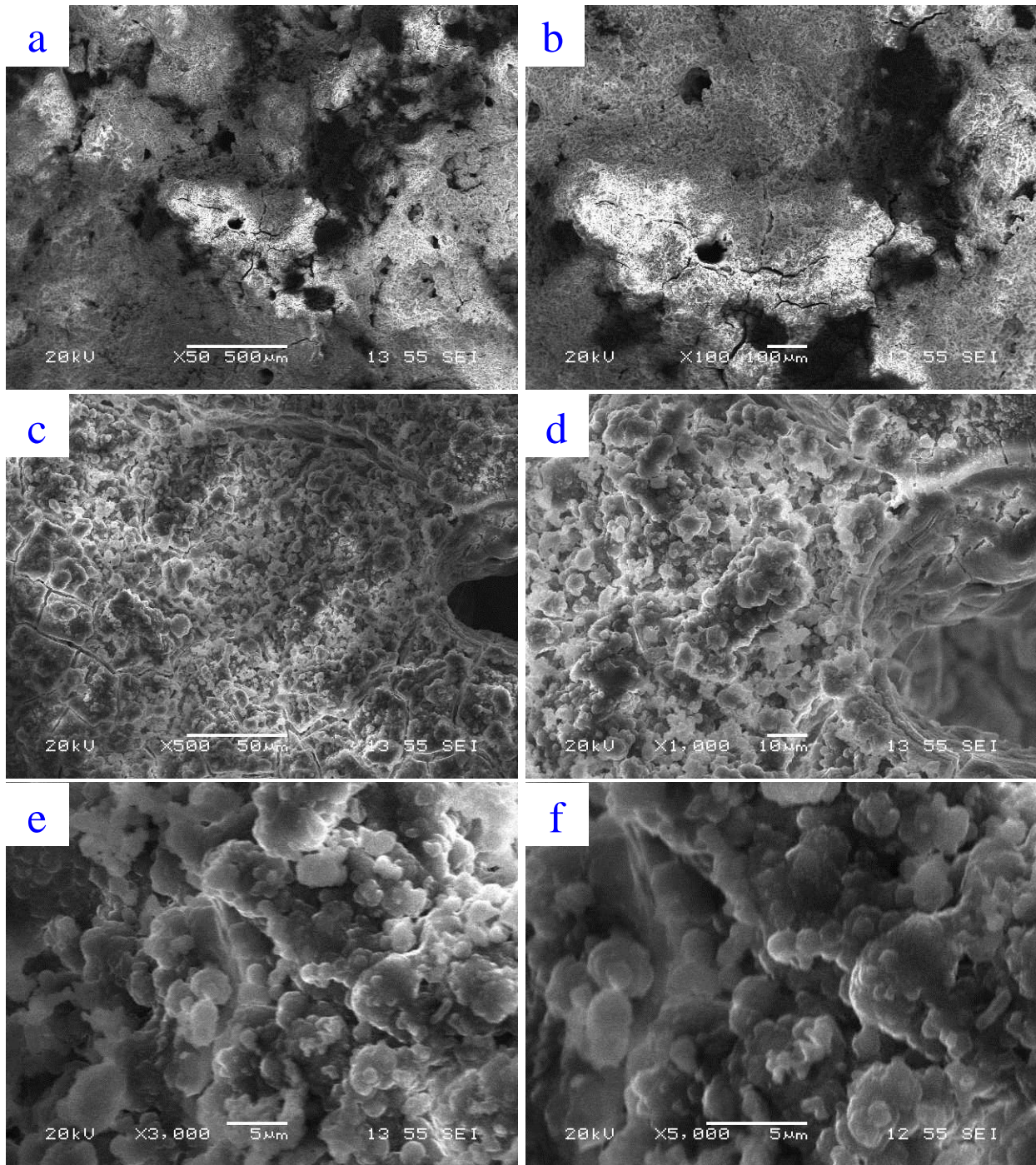


*Figure 136: Post-immersion SEM images of Mg-1Mn-4Zn-0.25Na-0.25K alloying system rapidly cooled in liquid CO<sub>2</sub> at different magnifications (a) at 50 x (b) at 100 x (c) at 500 x (d) at 1000 x (e) at 3000 x (f) at 5000 x.*

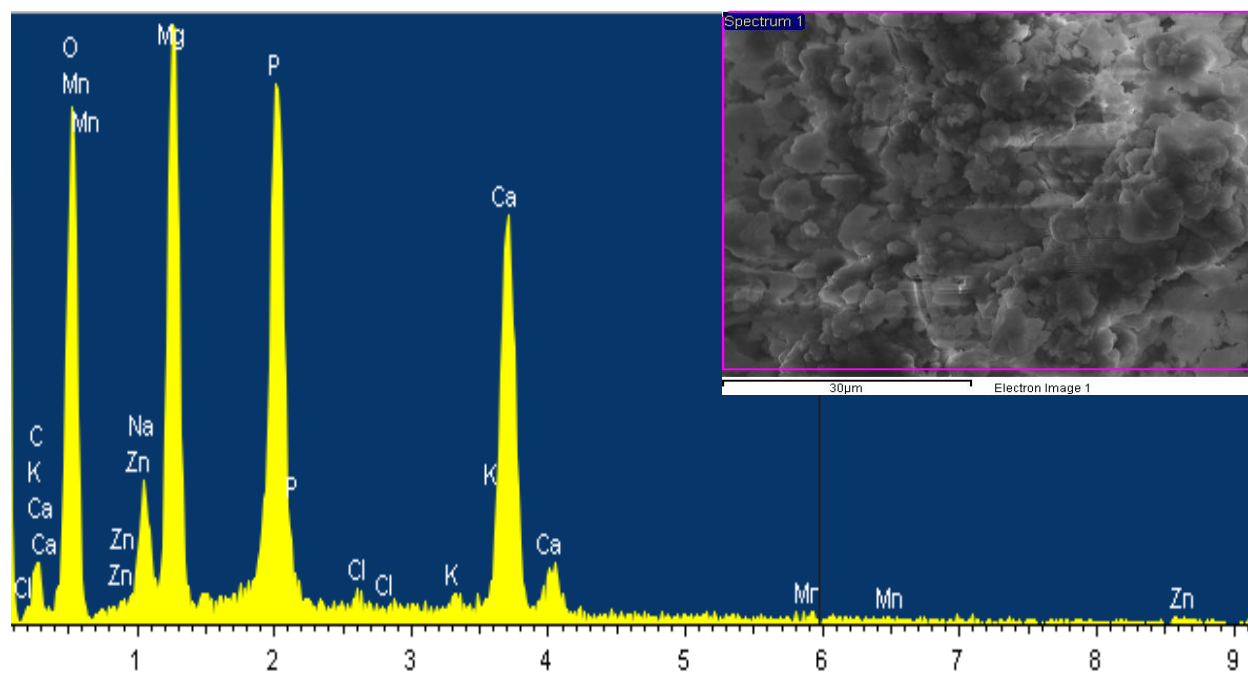


Figure 137: Post-immersion sum EDS spectrum image for the secondary phase of Mg-1Mn-4Zn-0.25Na-0.25K alloying system rapidly cooled in liquid CO<sub>2</sub>.

#### 5.2.6.4. Post-Immersion XRD

The samples were further analyzed using XRD to identify the composition of the produced compounds post-immersion test. The XRD patterns were divided into three groups: pure magnesium, Mg-Mn-Zn, and Mg-Mn-Zn-Na-k alloying systems. The first set of XRD covers the patterns of pure magnesium that were cooled by different solidification rates. The patterns of the produced peaks match the peaks of magnesium in the data base with a presence of magnesium oxide ( $\text{MgO} \cdot \text{H}_2\text{O}$ ). However, Mg-MCR post-immersion test showed high intensity peaks of magnesium hydroxide ( $\text{Mg}(\text{OH})_2$ ) that covered the base metal. Additionally, a presence of potassium fluoride phosphate ( $\text{K}_3\text{F}_2(\text{PO}_3)$ ) was detected for the Mg-HCR sample, as shown in Figure 138.

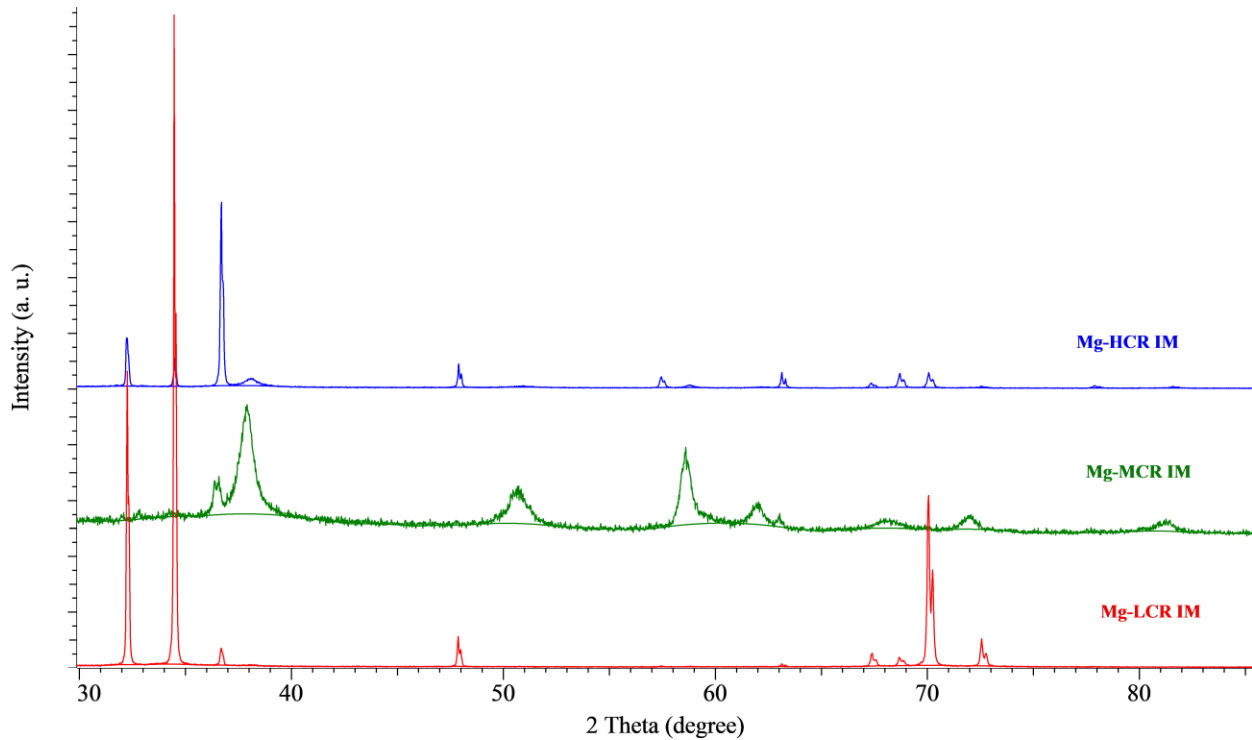


Figure 138: The XRD patterns post-immersion of pure magnesium of different solidification rates.

Figure 139 shows the patterns of post-immersion samples for Mg-1Mn-2Zn and Mg-1Mn-4Zn alloying systems compared with the quenched pure magnesium. Along with magnesium peaks, the patterns show the presence of magnesium manganese  $\text{Mg}_{0.975}\text{Mn}_{0.025}$ ,  $(\text{Mg}_{39}\text{Zn})_{0.05}$ , magnesium manganese oxide hydrate  $(\text{Mg}_{0.29}\text{Mn}_{1.42}\text{Mn}_{0.58}\text{O}_4(\text{H}_2\text{O})_{1.5})$ ,  $\text{MgZn}_2$ ,  $\text{Mg}_7\text{Zn}_3$ , zinc phosphate hydrate  $(\text{Zn}_2\text{P}_2\text{O}_7 \cdot 5\text{H}_2\text{O})$ ,  $\text{ZnO}$ , and magnesium zinc oxide  $(\text{Mg}_{0.25}\text{Zn}_{0.75})\text{O}$  in both of Mg-1Mn-2Zn and Mg-1Mn-4Zn. However, zinc phosphate hydrate has more tendency to form with increasing the zinc content from 2% to 4%.

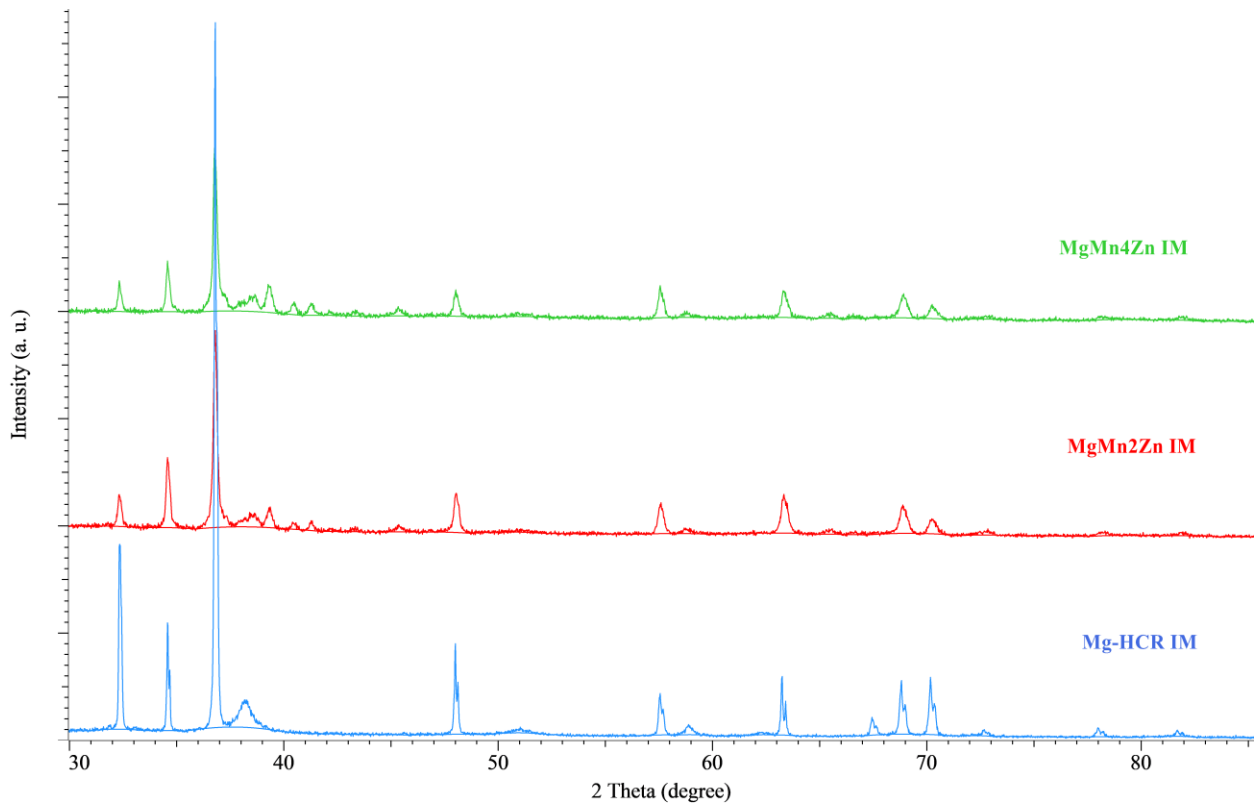


Figure 139: The XRD patterns post-immersion of Mg-Mn-Zn alloying systems.

The last compositional analysis was conducted to identify the formed compound post immersion test on Mg-1Mn-4Zn, Mg-1Mn-4Zn-0.5Na, Mg-1Mn-4Zn-0.5K, and Mg-1Mn-4Zn-0.25Na-0.25K, as shown in Figure 140. The peak of magnesium was hard to detect for Mg-1Mn-4Zn-0.5Na and Mg-1Mn-4Zn-0.25Na-0.25K due to the heavy formation of corrosion products. Additionally, high peaks intensity of hydroxide Mg (OH)<sub>2</sub> and (MgO. H<sub>2</sub>O) were detected for the same alloying system with the addition of sodium. Furthermore the compound of Mg 0.975 Mn 0.025, (Mg 39 Zn) 0.05, potassium magnesium phosphate KMg(PO<sub>3</sub>)<sub>3</sub>, and magnesium phosphate hydrate Mg<sub>3</sub>(PO<sub>4</sub>)<sub>2</sub>.H<sub>2</sub>O were found to be formed in Mg-1Mn-4Zn-0.5K alloying system. Table 20 summarizes the composition identification of the alloying systems post-immersion test.

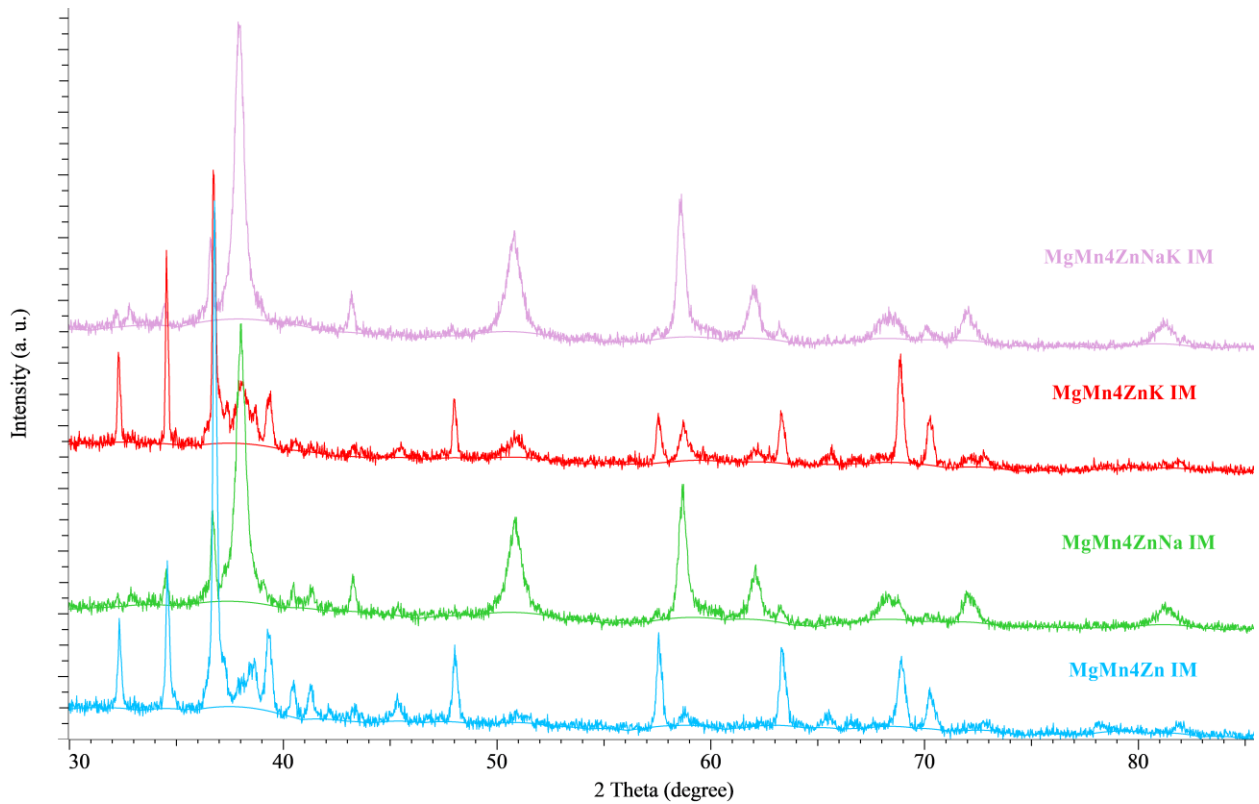


Figure 140: Figure 141: The XRD patterns post-immersion of Mg-Mn-Zn-Na-K alloying systems.

Table 20: The phase constitution of the alloying systems post-immersion test

Alloying Systems	Phases-Composition																	
	Mg	Mg (oH) <sub>2</sub>	MgO. H <sub>2</sub> O	NaMgH <sub>3</sub>	K <sub>3</sub> F <sub>2</sub> (PO <sub>3</sub> )	MgCl <sub>2</sub>	Mg0.975Mn0.025	(Mg 39 Zn) 0.05	(Mg 0.25 Zn 0.75) O	Mg0.29Mn1.42 Mn0.58O4	MgZn2	Mg <sub>3</sub> (PO <sub>4</sub> ) <sub>2</sub> /Mg <sub>3</sub> P <sub>2</sub>	KMg(PO <sub>3</sub> ) <sub>3</sub>	Mg7Zn3	Zn <sub>2</sub> P <sub>2</sub> O <sub>7</sub> 5H <sub>2</sub> O	ZnO	Mg 0.25 Zn 0.75	(Na <sub>3</sub> HP <sub>2</sub> O <sub>6</sub> )
Mg-LCR	*	-	*	-	-	-	-	-	-	-	-	-	-	-	-	-	-	-
Mg-MCR	-	*	*	-	-	-	-	-	-	-	-	-	-	-	-	-	-	-
Mg-HCR	*	-	*	-	*	-	-	-	-	-	-	-	-	-	-	-	-	-
MgMn2Zn	*	-	-	-	-	-	*	*	*	*	*	-	-	*	*	*	*	-
MgMn4Zn	*	*	*	-	*	-	*	*	*	*	*	-	-	*	*	*	*	-
MgMn4ZnNa	-	*	-	*	-	*	-	-	-	-	-	-	-	-	-	-	-	-
MgMn4ZnK	*	-	*	-	-	-	-	*	-	-	*	*	*	-	-	-	-	-
MgMn4ZnNaK	-	*	-	*	-	*	-	-	-	-	-	-	-	-	-	-	-	-

# Chapter 6

## 6.1. Conclusion

The developed casting procedure eliminated the decomposition of Mg and processing defects. Also, the established procedure reduced the fabrication cost and risk factor of casting magnesium since Mg has a high flammability and oxidation at high temperatures. Additionally, the process minimized the environmental effects of using cover gases. The other studied factor is the solidification rate; where increasing the solidification rate from 0.035 °C/Sec for Mg-LCR to 0.074 °C/Sec for Mg-MCR reduced the grain size by 46%. The change in the solidification rate improved the hardness, yield strength and UTS by 11%, 57%, and 37%, respectively. However, Mg-LCR showed a better corrosion performance than Mg-MCR. The further increase in the solidification rate to 13.5 °C/Sec to produce Mg-HCR reduced the grainsize significantly by 99% and enhanced the hardness and UTS by (57%-40%) and (78%-29%) in comparison to Mg-LCR and Mg- MCR, respectively. The fracture morphology showed less deformation with increasing the solidification cooling rate. Additionally, the corrosion performance of Mg-HCR was measured to be highest.

The combined effect of the rapid solidification (13.5 °C/Sec) and the alloying elements (manganese and zinc) on the properties showed significant improvement with the addition of 1% Mn and 2% Zn. The hardness, yield strength and the ultimate tensile

strength were increased significantly to the system by 41%, 25% and 45% in proportion to the quenched pure magnesium, respectively. It can be seen clearly that the microstructure consists of the secondary phases (Mg-Mn-Zn-containing phases) and the matrix ( $\alpha$ -Mg). Further addition of zinc (4%) reduced the dendritic spacing of the quenched alloy of Mg-1Mn-2Zn to about 70% smaller than the quenched Mg-1Mn-2Zn and promoted the formation of a thicker and more continuous secondary phases. Increasing the zinc content from 2% to 4% caused an increase of 12% in hardness, while the impact strength slightly decreased. However, the tensile properties deteriorated by 69% for the ultimate tensile strength and by 93% for the ductility. This reduction in the tensile properties is due to the increase of the formation of a continuous network of the secondary phase. Nevertheless, the addition of 4% zinc content reduced the formation of the eutectic structure and increased the laminal thickness of the eutectic phases. On the other hand, the presence of pitting corrosion and the corrosion rate were observed to increase with increasing the content of zinc from 2% to 4 %.

The effect of adding 0.5% Na and 0.5% K to the quenched alloying system of Mg-1Mn-4Zn reduced the grain size further. However, adding sodium showed more effectiveness in reducing the dendritic spacing in comparison to adding potassium individually or simultaneously with Na. The addition of 0.5% Na reduced the impact strength considerably by 83% and slightly improved the tensile properties, which could be due to the formation of brittle secondary phases and the further reduction of the dendritic spacing. The addition of sodium individually and simultaneously deteriorated the corrosion

resistance and increased the pitting corrosion significantly due to the formation of secondary brittle-reactive phases. In the case of adding potassium, it showed a positive influence on the alloying system, where the tensile strength and UTS increased significantly by 49% and 139%, respectively. This improvement was due to the effectiveness of K in interrupting the formation of the brittle secondary phases and enhancing the formation of the eutectic structure. However, the addition of sodium and potassium simultaneously led to a tremendous reduction in the impact strength, ultimate tensile strength and ductility. This reduction is due to the formation of brittle secondary phases that locally absorbed more alloying elements. Moreover, the addition of potassium individually showed the best corrosion rate in this group, with rapid formation of a uniform oxide layer with limited presence of pitting corrosion. This indicates that the use of more active metals leads to a modified surface.

Based on the overall performance of the designed nontoxic-biocompatible alloying systems, the quenched pure magnesium, Mg-1Mn-2Zn, Mg-1Mn-4Zn-0.5K showed promising results. These systems showed good mechanical properties and corrosion performance; where the impact strength was 592.1, 566.4, and 439.12 J/m, hardness was 48.53, 68.82, and 78.22 RHH, UTS was 87.18, 126.44, and 57.1 MPa, ductility was 9.5%, 13.03%, and 2.2% , and the calculated corrosion rate was 0.044, 0.071, 0.22 mmpy, respectively. Moreover, the addition of potassium to the system of Mg-1Mn-4Zn significantly enhanced the microstructure, mechanical properties, corrosion performance,

and hindered the pitting corrosion. Therefore, the study recommends adding potassium (under 0.5%) to Mg-1Mn-Zn system with using zinc content below 4%.

## 6.2. Future Plan

It is important to keep the focus on developing a biomedical-biodegradable-nontoxic Mg-Mn-Zn-K alloying system while reducing the zinc and potassium contents below 4% and 0.5%, respectively. Also, the future plan is to include a computational modeling analysis for the alloying system incorporated with a biomedical application that fuses a bone structure as an implantation device. Also, further analysis will be needed to identify the right composition to tweak the surface modification to increase the corrosion resistance. Nevertheless, tailoring this work to 3D printing can be used to produce a cellular-foam structure that can be modified to mimic the bone structure and performance.

## REFERENCES

1. Buie, Helen R. ; Bosma, Nick A. ; Downey, Charlene M. ; Jirik, Frank R. ; Boyd, Steven K. "Micro-CT evaluation of bone defects: Applications to osteolytic bone metastases, bone cysts, and fracture". *Medical Engineering and Physics*, November 2013, Vol.35(11), pp.1645-1650.
2. Ghazanfari, Amir ; Li, Wenbin ; Leu, Ming C. ; Hilmas, Gregory E. "A novel freeform extrusion fabrication process for producing solid ceramic components with uniform layered radiation drying" *Additive Manufacturing*, May 2017, Vol.15, pp.102-112.
3. Ghazanfari, Amir ; Li, Wenbin ; Leu, Ming ; Watts, Jeremy ; Hilmas, Gregory . "Mechanical characterization of parts produced by ceramic on-demand extrusion process". *International Journal of Applied Ceramic Technology*, May 2017, Vol.14(3), pp.486-494.
4. Tang, Daniel ; Tare, Rahul S. ; Yang, Liang-Yo ; Williams, David F. ; Ou, Keng-Liang ; Oreffo, Richard O.C. "Biofabrication of bone tissue: approaches, challenges and translation for bone regeneration". *Biomaterials*, March 2016, Vol.83, pp.363-382.
5. Wang, Xiaojian ; Xu, Shanqing ; Zhou, Shiwei ; Xu, Wei ; Leary, Martin ; Choong, Peter ; Qian, M. ; Brandt, Milan ; Xie, Yi Min. "Topological design and additive manufacturing of porous metals for bone scaffolds and orthopaedic implants: A review". *Biomaterials*, March 2016, Vol.83, pp.127-141.
6. Ullah, Hanif ; Wahid, Fazli ; Santos, Hélder A. ; Khan, Taous. "Advances in biomedical and pharmaceutical applications of functional bacterial cellulose-based nanocomposites". *Carbohydrate Polymers*, 5 October 2016, Vol.150, pp.330-352.
7. Jiang, Guofeng ; He, Guo. "A new approach to the fabrication of porous magnesium with well-controlled 3D pore structure for orthopedic applications". *Materials Science & Engineering C*, 1 October 2014, Vol.43, pp.317-320.
8. Li, Mingyang ; Ghazanfari, Amir ; Li, Wenbin ; Landers, Robert G. ; Leu, Ming C. "Modeling and analysis of paste freezing in freeze-form extrusion fabrication of thin-wall parts via a lumped method". *Journal of Materials Processing Tech.*, November 2016, Vol.237, pp.163-180.
9. Zhang, Xue ; Li, Xiao-Wu ; Li, Ji-Guang ; Sun, Xu-Dong. "Preparation and mechanical property of a novel 3D porous magnesium scaffold for bone tissue engineering". *Materials Science & Engineering C*, 1 September 2014, Vol.42, pp.362-367.

10. Ian H. Parkinson and Nicola L. Fazzalari, “Characterisation of Trabecular Bone Structure”, *Stud Mechanobiol Tissue Eng Biomater* (2013) 5: 31–51, DOI: 10.1007/8415\_2011\_113.
11. Yamada, Y. ; Shimojima, K. ; Sakaguchi, Y. ; Mabuchi, M. ; Nakamura, M. ; Asahina, T. ; Mukai, T. ; Kanahashi, H. ; Higashi, K., “Processing of an open-cellular AZ91 magnesium alloy with a low density of 0.05 g/cm<sup>3</sup>” *Journal of Materials Science Letters*, 1999, Vol.18(18), pp.1477-1480.
12. Kirkland, N.T ; Kolbeinsson, I ; Woodfield, T ; Dias, G.J ; Staiger, M.P, “Synthesis and properties of topologically ordered porous magnesium”, *Materials Science & Engineering B*, 2011, Vol.176(20), pp.1666-1672.
13. H. Kanahashi, T.Mukai, Y. Yamada, K. Shimojima, M. Mabuchi, T. Aizawa, K. Higashi, “Experimental study for the improvement of crashworthiness in AZ91 magnesium foam controlling its microstructure *Materials Science and Engineering*”, June 2001 DOI: 10.1016/S0921-5093(01)01199-6.
14. Emily K. Brooks ; Mark T. Ehrensberger. “Bio-Corrosion of Magnesium Alloys for Orthopaedic Applications”. *Journal of Functional Biomaterials*, 01 September 2017, Vol.8(3), p.38.
15. Liu, Xiwei ; Sun, Jianke ; Qiu, Kejin ; Yang, Yinghong ; Pu, Zhongjie ; Li, Li ; Zheng, Yufeng. “Effects of alloying elements (Ca and Sr) on microstructure, mechanical property and in vitro corrosion behavior of biodegradable Zn–1.5Mg alloy”. *Journal of Alloys and Compounds*, 15 April 2016, Vol.664, pp.444-452.
16. International Magnesium Association, <https://www.intlmag.org/>, as of January 2020.
17. Abdessameud, S ; Mezbahul-Islam, M ; Medraj, M ; Mikuli, Edward, “Thermodynamic Modeling of Hydrogen Storage Capacity in Mg-Na Alloys”, *The Scientific World Journal*, 2014, Vol.2014, 16 pages.
18. Pogorielov, Maksym ; Husak, Eugenia ; Solodivnik, Alexandr ; Zhdanov, Sergii “Magnesium-based biodegradable alloys: Degradation, application, and alloying elements.(Report)” *Interventional Medicine and Applied Science*, March, 2017, Vol.9(1).
19. Chen, Yongjun ; Xu, Zhigang ; Smith, Christopher ; Sankar, Jag. “Recent advances on the development of magnesium alloys for biodegradable implants”. *Acta Biomaterialia*, . (November 2014), Vol.10(11), pp.4561-4573. DOI:10.1016/j.actbio.2014.07.005.

20. Nan Li, Yufeng Zheng . “Novel Magnesium Alloys Developed for Biomedical Application” *Journal of Materials Science & Technology*, 6/2013, Vol.29(6), pp.489-502.
21. Atrens, Andrej ; Liu, Ming ; Zainal Abidin, Nor Ishida. “Corrosion mechanism applicable to biodegradable magnesium implants”. *Materials Science & Engineering B*, 2011, Vol.176(20), pp.1609-1636.
22. *ASM Specialty Handbook: Magnesium and Magnesium Alloys*. ASM International, edited by M. Avedesian and Hugh Baker,1999. Pp15, 51,131-144,170, 194-200.
23. Yang, Lei ; Huang, Yuanding ; Peng, Qiuming ; Feyerabend, Frank ; Kainer, Karl Ulrich ; Willumeit, Regine ; Hort, Norbert. “Mechanical and corrosion properties of binary Mg–Dy alloys for medical applications”. *Materials Science & Engineering B*, 2011, Vol.176 (20), pp.1827-183.
24. Zhang, Baoping ; Hou, Yunlong ; Wang, Xiaodan ; Wang, Yin ; Geng, Lin. ”Mechanical properties, degradation performance and cytotoxicity of Mg–Zn–Ca biomedical alloys with different compositions”. *Materials Science & Engineering C*, 2011, Vol.31(8), pp.1667-1673.
25. Lisitsyn, V. ; Ben-Hamu, G. ; Eliezer, D. ; Shin, K.S. “The role of Ca microalloying on the microstructure and corrosion behavior of Mg–6Zn–Mn–(0.5–2)Si alloys”. *Corrosion Science*, 2009, Vol.51(4), pp.776-784.
26. Ben-Hamu, G. ; Eliezer, D. ; Shin, K.S. “The role of Mg 2Si on the corrosion behavior of wrought Mg–Zn–Mn alloy”. *Intermetallics*, 2008, Vol.16(7), pp.860-867.
27. Lisitsyn, V. ; Ben-Hamu, G. ; Eliezer, D. ; Shin, K.S. “Some particularities of the corrosion behaviour of Mg–Zn–Mn–Si–Ca alloys in alkaline chloride solutions”. *Corrosion Science*, 2010, Vol.52(7), pp.2280-2290.
28. Xu, Zhigang ; Smith, Christopher ; Chen, Shuo ; Sankar, Jag. “Development and microstructural characterizations of Mg–Zn–Ca alloys for biomedical applications”. *Materials Science & Engineering B*, 2011, Vol.176(20), pp.1660-1665.
29. Zhang, Erlin ; Yin, Dongsong ; Xu, Liping ; Yang, Lei ; Yang, Ke . “Microstructure, mechanical and corrosion properties and biocompatibility of Mg–Zn–Mn alloys for biomedical application”. *Materials Science & Engineering C*, 2009, Vol.29(3), pp.987-993.
30. Yin Dongsong ; Zhang Erlin ; Zeng Songyan. “Effect of Zn content on microstructure,mechanical properties and fracture behavior of Mg-Mn alloy”. *China Foundry*, 01 February 2009, Vol.6(1), pp.43-47.

31. Kirkland, N.T. ; Birbilis, N. ; Staiger, M.P. “Assessing the corrosion of biodegradable magnesium implants: A critical review of current methodologies and their limitations” *Acta Biomaterialia*. 2011, Vol 8(3), pp925-936.
32. Ren Y, Wang H, Huang J, Zhang B, Yang K. “Study of biodegradation of pure Magnesium”. *Key Eng Mater* 2007;342–343:601–4.
33. Ding, Yunfei ; Wen, Cuie ; Hodgson, Peter ; Li, Yuncang. “Effects of alloying elements on the corrosion behavior and biocompatibility of biodegradable magnesium alloys: a review”. *Journal of Materials Chemistry B*, 2014, Vol.2(14), pp.1912-1933.
34. Trumbo, Paula; Schlicker, Sandra; Yates, Allison A.; Poos, Mary. “Dietary Reference Intakes for Energy, Carbohydrate, Fiber, Fat, Fatty Acids, Cholesterol, Protein and Amino Acids. *Journal of the American Dietetic Association*, (2002). Vol.102 (11), pp.1621-1630, DOI:10.1016/S0002-8223(02)90346-9.
35. Xin, Y. ; Hu, T. ; Chu, P.K. “In vitro studies of biomedical magnesium alloys in a simulated physiological environment: A review”. *Acta Biomaterialia*, April 2011, Vol.7(4), pp.1452-1459.
36. Van der Biest, Omer ; Marco Pelegrin, Iñigo “Degradation Testing of Magnesium and its Alloys aiming at Biodegradable Implant Applications ; Degradatietesten van magnesium en magnesium legeringen voor biologisch afbreekbare implantaten”-Dissertation, 2016-12-02, pp13.
37. Kelvii Wei Guo , “A Review of Magnesium/Magnesium Alloys Corrosion and its Protection”. *Recent Patents on Corrosion Science*, 2010, Volume 2.
38. Frank Witte “Reprint of: The history of biodegradable magnesium implants” *Acta Biomaterialia*, 1 September 2015, Vol.23, pp.S28-S40.
39. Seelig MG. “A study of magnesium wire as an absorbable suture and ligature material”. *Arch Surg* 1924;8 (2):669–80.
40. Andrews EW. “Absorbable metal clips as substitutes for ligatures in wound closure”. *JAMA* 1917;28:278–81.
41. Virtanen, Sannakaisa . “Biodegradable Mg and Mg alloys: Corrosion and biocompatibility”. *Materials Science & Engineering B*, 2011, Vol.176(20), pp.1600-1608.
42. Kirkland, N.T. ; Lespagnol, J. ; Birbilis, N. ; Staiger, M.P. “A survey of bio-corrosion rates of magnesium alloys”. *Corrosion Science*, 2010, Vol.52(2), pp.287-291.

43. Staiger, Mark P. ; Kolbeinsson, Ingólfur ; Kirkland, Nicholas T. ; Nguyen, Thanh ; Dias, George ; Woodfield, Tim B.F. “Synthesis of topologically-ordered open-cell porous magnesium”. *Materials Letters*, 2010, Vol.64(23), pp.2572-2574.
44. Luo, Alan A. “Magnesium casting technology for structural applications”. *Journal of Magnesium and Alloys*, March 2013, Vol.1(1), pp.2-22.
45. Kim, Sang-Wook; Kim, Do-Hyun; You, Byung-Don; Han, Jeong-Whan; Kim, Mok-Soon Source. “Evaporation behavior of magnesium under reduced pressure”. *Materials Science Forum*, 2003, v 439, p 238-243.
46. Abbott, Trevor & Cáceres, Carlos & Easton, Mark. “Design with Magnesium- Alloys, properties and casting processes” 2014.
47. Anbuechziyan, G. ; Muthuramalingam, T. ; Mohan, B. “Effect of process parameters on mechanical properties of hollow glass microsphere reinforced magnesium alloy syntactic foams under vacuum die casting”. *Archives of Civil and Mechanical Engineering*, September 2018, Vol.18(4), pp.1645-1650.
48. Wang, Gerry Gang ; Bos, Jeremy. “A study on joining magnesium alloy high pressure die casting components with thread forming fasteners”. *Journal of Magnesium and Alloys*, June 2018, Vol.6(2), pp.114-120.
49. Stulikova, Ivana ; Smola, Bohumil, “Mechanical properties and phase composition of potential biodegradable Mg–Zn–Mn–base alloys with addition of rare earth elements”, *Materials Characterization*, 2010, Vol.61(10), pp.952-958.
50. El-Mahallawy, Nahed ; Palkowski, Heinz ; Klingner, Anke ; Diaa, Alia ; Shoeib, Madiha, “Effect of 1.0 wt. % Zn addition on the microstructure, mechanical properties, and bio-corrosion behaviour of micro alloyed Mg-0.24Sn-0.04Mn alloy as biodegradable material”*Materials Today Communications*, September 2020, Vol.24.
51. Rosalbino, F. ; De Negri, S. ; Scavino, G. ; Saccone, A., “Microstructure and in vitro degradation performance of Mg–Zn–Mn alloys for biomedical application”, *Journal of Biomedical Materials Research Part A*, March 2013, Vol.101(3), pp.704-711.
52. Hänzi, Anja C ; Gerber, Isabel ; Schinhammer, Michael ; Löffler, Jörg F ; Uggowitzer, Peter J”, On the in vitro and in vivo degradation performance and biological response of new biodegradable Mg–Y–Zn alloys”, *Acta Biomaterialia*, 2010, Vol.6(5), pp.1824-1833.
53. Gu, Xuenan ; Zheng, Yufeng ; Zhong, Shengping ; Xi, Tingfei ; Wang, Junqiang ; Wang, Weihua, “Corrosion of, and cellular responses to Mg–Zn–Ca bulk metallic glasses”, *Biomaterials*, 2010, Vol.31(6), pp.1093-1103.

54. Li, Tao ; He, Yong ; Zhang, Hailong ; Wang, Xitao, “Microstructure, mechanical property and in vitro biocorrosion behavior of single-phase biodegradable Mg–1.5Zn–0.6Zr alloy”, *Journal of Magnesium and Alloys*, June 2014, Vol.2(2), pp.181-189.
55. Song, Yingwei ; Han, En-Hou ; Dong, Kaihui ; Shan, Dayong ; Yim, Chang Dong ; You, Bong Sun, “Effect of hydrogen on the corrosion behavior of the Mg–xZn alloys”, *Journal of Magnesium and Alloys*, September 2014, Vol.2(3), pp.208-213.
56. Song, Yingwei ; Han, En-Hou ; Shan, Dayong ; Yim, Chang Dong ; You, Bong Sun, “The effect of Zn concentration on the corrosion behavior of Mg–xZn alloys”, *Corrosion Science*, December 2012, Vol.65, pp.322-330.
57. Song, Yingwei ; Han, En-Hou ; Shan, Dayong ; Yim, Chang Dong ; You, Bong Sun, “The role of second phases in the corrosion behavior of Mg–5Zn alloy”, *Corrosion Science*, July 2012, Vol.60, pp.238-245.
58. Zhang, Erlin ; Yang, Lei ; Xu, Jianwei ; Chen, Haiyan, “Microstructure, mechanical properties and bio-corrosion properties of Mg–Si(–Ca, Zn) alloy for biomedical application”, *Acta Biomaterialia*, 2010, Vol.6(5), pp.1756-1762.
59. Liu, Xianbin ; Shan, Dayong ; Song, Yingwei ; Han, En-Hou, “Influence of yttrium element on the corrosion behaviors of Mg–Y binary magnesium alloy”, *Journal of Magnesium and Alloys*, March 2017, Vol.5(1), pp.26-34.
60. Bi, Guangli ; Li, Yuandong ; Zang, Shijun ; Zhang, Jianbin ; Ma, Ying ; Hao, Yuan. “Microstructure, mechanical and corrosion properties of Mg–2Dy–xZn (x=0, 0.1, 0.5 and 1 at.%) alloys”, *Journal of Magnesium and Alloys*, March 2014, Vol.2(1), pp.64-71.
61. Li, Daquan ; Wang, Qudong ; Ding, Wenjiang, “Effects of Ho on the microstructure and mechanical properties of Mg–Zn–Ho–Zr magnesium alloys”, *Rare Metals*, 2011, Vol.30(2), pp.131-136.
62. Sajuri, Zainuddin Bin ; Miyashita, Yukio ; Hosokai, Yasunobu ; Mutoh, Yoshiharu, “Effects of Mn content and texture on fatigue properties of as-cast and extruded AZ61 magnesium alloys”, *International Journal of Mechanical Sciences*, 2006, Vol.48(2), pp.198-209.
63. Lugo, M ; Jordon, J.B ; Solanki, K.N ; Hector, L.G ; Bernard, J.D ; Luo, A.A ; Horstemeyer, M.F, “Role of different material processing methods on the fatigue behavior of an AZ31 magnesium alloy”, *International Journal of Fatigue*, July 2013, Vol.52, pp.131-143.

64. Azeem, M.A ; Tewari, A ; Ramamurty, U, “Effect of recrystallization and grain growth on the mechanical properties of an extruded AZ21 Mg alloy”, *Materials Science & Engineering A*, 15 February 2010, Vol.527(4-5), pp.898-903.
65. Khan, Sabrina Alam ; Miyashita, Yukio ; Mutoh, Yoshiharu ; Sajuri, Zainuddin Bin, “Influence of Mn content on mechanical properties and fatigue behavior of extruded Mg alloys”, *Materials Science & Engineering A*, 25 March 2006, Vol.420(1-2), pp.315-321.
66. Nam, Nguyen Dang ; Mathesh, Motilal ; Forsyth, Maria ; Jo, Deok Su, “Effect of manganese additions on the corrosion behavior of an extruded Mg–5Al based alloy”, *Journal of Alloys and Compounds*, 25 November 2012, Vol.542, pp.199-206.
67. William H. Crosby, MD; Vilas V. Likhite, MD, PhD; Joseph E. O'Brien, MD; David Forman, “Serum Iron Levels in Ostensibly Normal People”, *JAMA*. 1974;227(3):310-312. doi:10.1001/jama.1974.03230160038009.
68. Hou, Lida ; Li, Zhen ; Pan, Yu ; Du, Li ; Li, Xinlin ; Zheng, Yufeng ; Li, Li, “In vitro and in vivo studies on biodegradable magnesium alloy”, *Progress in Natural Science: Materials International*, October 2014, Vol.24(5), pp.466-471.
69. Haghshenas, Meysam, “Mechanical characteristics of biodegradable magnesium matrix composites: A review” *Journal of Magnesium and Alloys*, June 2017, Vol.5(2), pp.189-201.
70. Liu, Xiwei ; Sun, Jianke ; Zhou, Feiyu ; Yang, Yinghong ; Chang, Rencao ; Qiu, Kejin ; Pu, Zhongjie ; Li, Li ; Zheng, Yufeng, “Micro-alloying with Mn in Zn–Mg alloy for future biodegradable metals application”, *Materials & Design*, 15 March 2016, Vol.94, pp.95-104.
71. Li, Huafang ; Zheng, Yufeng ; Qin, Ling, “Progress of biodegradable metals”, *Progress in Natural Science: Materials International*, October 2014, Vol.24(5), pp.414-422.
72. Mirco Peron ; Jan Torgersen ; Filippo Berto, “Mg and Its Alloys for Biomedical Applications: Exploring Corrosion and Its Interplay with Mechanical Failure”, *Metals*, 01 July 2017, Vol.7(7), p.252.
73. Charles Moosbrugger “Engineering Properties of Magnesium Alloys”. ASM, 2017, Chapter 1, 3.
74. Bakhsheshi-Rad, Hr ; Idris, Mh ; Abdul-Kadir, Mr ; Ourdjini, A ; Medraj, M ; Daroonparvar, M ; Hamzah, E “Mechanical and bio-corrosion properties of quaternary Mg-Ca-Mn-Zn alloys compared with binary Mg-Ca alloys” *Materials & Design*, 2014 Jan, Vol.53, pp.283-292.

75. Kelvii Wei Guo. "A Review of Magnesium/Magnesium Alloys Corrosion and its Protection". *Recent Patents on Corrosion Science*. Volume 1 , Issue 1 , 2011. DOI : 10.2174/2210683911101010072.
76. Radha, R ; Sreekanth, D, "nsight of magnesium alloys and composites for orthopedic implant applications – a review", *Journal of Magnesium and Alloys*, September 2017, Vol.5(3), pp.286-312.
77. Witte, Frank ; Hort, Norbert ; Vogt, Carla ; Cohen, Smadar ; Kainer, Karl Ulrich ; Willumeit, Regine ; Feyerabend, Frank, "Degradable biomaterials based on magnesium corrosion", *Current Opinion in Solid State & Materials Science*, 2008, Vol.12(5), pp.63-72.
78. Dietary Reference Intakes (DRIs): Estimated Average Requirements Food and Nutrition Board, Institute of Medicine, National Academies, 2014, table 3.
79. A. Elyasigorji; M. Rezaee; and A. Ghorbanpoor "Magnetic Corrosion Detection in Concrete Structures", Conference: International Conference on Sustainable Infrastructure 2019, DOI: 10.1061/9780784482650.018.
80. Zheng, Y.F ; Gu, X.N ; Witte, F, "Biodegradable metals", *Materials Science & Engineering R*, March 2014, Vol.77, pp.1-34.
81. Ricardo Augusto de Almeida Pinto, "Electrochemical Behaviour of Magnesium Alloys-Study on the influence of Rare Earths as alloying elements", Instituto Superior Técnico – Technical University of Lisbon, November 2008.
82. Esmaily, M ; Svensson, J.E ; Fajardo, S ; Birbilis, N ; Frankel, G.S ; Virtanen, S ; Arrabal, R ; Thomas, S ; Johansson, L.G, "Fundamentals and advances in magnesium alloy corrosion", *Progress in Materials Science*, August 2017, Vol.89, pp.92-193.
83. Cain, Tw ; Gonzalez-Afanador, I ; Birbilis, N ; Scully, Jr, "The Role of Surface Films and Dissolution Products on the Negative Difference Effect for Magnesium: Comparison of Cl- versus Cl- Free Solutions", *Journal Of The Electrochemical Society*, 2017, Vol.164(6), pp.C300-C311.
84. Bender, S. ; Goellner, J. ; Heyn, A. ; Schmigalla, S., "A new theory for the negative difference effect in magnesium corrosion", *Materials and Corrosion*, August 2012, Vol.63(8), pp.707-712.
85. Garcia-Garcia, Hector M ; Haude, Michael ; Kuku, Kayode ; Hideo-Kajita, Alexandre ; Ince, Hüseyin ; Abizaid, Alexandre ; Tölg, Ralph ; Lemos, Pedro Alves ; Von Birgelen, Clemens ; Christiansen, Evald Høj ; Wijns, William ; Escaned, Javier ; Dijkstra, Jouke ; Waksman, Ron, "In vivo serial invasive imaging of the second-

- generation drug-eluting absorbable metal scaffold (Magmaris — DREAMS 2G) in de novo coronary lesions: Insights from the BIOSOLVE-II First-In-Man Trial”, *International Journal of Cardiology*, 15 March 2018, Vol.255, pp.22-28.
86. Haude, Michael ; Ince, Hüseyin ; Abizaid, Alexandre ; Toelg, Ralph ; Lemos, Pedro Alves ; Von Birgelen, Clemens ; Christiansen, Evald Høj ; Wijns, William ; Neumann, Franz - Josef ; Kaiser, Christoph ; Eeckhout, Eric ; Lim, Soo Teik ; Escaned, Javier ; Onuma, Yoshinobu ; Garcia - Garcia, Hector M ; Waksman, Ron, “Sustained safety and performance of the second-generation drug-eluting absorbable metal scaffold in patients with de novo coronary lesions: 12-month clinical results and angiographic findings of the BIOSOLVE-II first-in-man trial”, *European Heart Journal*, 2016, Vol. 37(35), pp.2701-2709.
  87. Haude, Michael; Ince, Hüseyin; Abizaid, Alexandre; Toelg, Ralph ; Lemos, Pedro Alves ; Von Birgelen, Clemens ; Christiansen, Evald Høj ; Wijns, William ; Neumann, Franz-Josef ; Kaiser, Christoph ; Eeckhout, Eric ; Lim, Soo Teik ; Escaned, Javier ; Garcia-Garcia, Hector M ; Waksman, Ron, “Safety and performance of the second-generation drug-eluting absorbable metal scaffold in patients with de-novo coronary artery lesions (BIOSOLVE-II): 6 month results of a prospective, multicentre, non-randomised, first-in-man trial”, *The Lancet*, 02 January 2016, Vol.387(10013), pp.31-39.
  88. Kim, Woo-Cheol ; Han, Kwon-Hoon ; Kim, Jung-Gu ; Yang, Seok-Jo ; Seok, Hyun-Kwang ; Han, Hyung-Seop ; Kim, Young-Yul, “Effect of surface area on corrosion properties of magnesium for biomaterials”, *Metals and Materials International*, 2013, Vol.19(5), pp.1131-1137.
  89. Pathak, SS ; Mendon, Sk ; Blanton, MD ; Rawlins, JW. “Magnesium-Based Sacrificial Anode Cathodic Protection Coatings (Mg-Rich Primers) for Aluminum Alloys”. *Metals*, 2012 Sep, Vol.2(3), pp.353-376.
  90. Zeng, Rong-Chang ; Li, Xiao-Ting ; Li, Shuo-Qi ; Zhang, Fen ; Han, En-Hou .“In vitro degradation of pure Mg in response to glucose”. *Scientific reports*, 12 August 2015, Vol.5, pp.13026.
  91. Uhlig's Corrosion Handbook, Third Edition- Galvanic Corrosion, X. G. ZHANG Teck Metals Ltd., p123-140, 2011.
  92. Kuwahara, Hideyuki ; Al-Abdullat, Yousef ; Mazaki, Naoko ; Tsutsumi, Sadami ; Aizawa, Tatsuhiko, “Precipitation of Magnesium Apatite on Pure Magnesium Surface during Immersing in Hank’s Solution”, *MATERIALS TRANSACTIONS*, 2001, Vol.42(7), pp.1317-1321.

93. Zhang, Shaoxiang ; Li, Jianan ; Song, Yang ; Zhao, Changli ; Zhang, Xiaonong ; Xie, Chaoying ; Zhang, Yan ; Tao, Hairong ; He, Yaohua ; Jiang, Yao ; Bian, Yujun, “In vitro degradation, hemolysis and MC3T3-E1 cell adhesion of biodegradable Mg–Zn alloy”, *Materials Science & Engineering C*, 2009, Vol.29(6), pp.1907-1912.
94. “Electrochemical Kinetics. Theoretical and Experimental Aspects”. Klaus J. Vetter. Translated, with revisions by the author, from the German edition (Berlin, 1961) by Scripta Technica. Stanley Bruckenstein and Brian Howard, Translation Eds. Academic Press, New York, 1967.
95. “Atlas of electrochemical equilibria in aqueous solutions” by Marcel Pourbaix [and others] Translated from the French by James A. Franklin. 1966. pp.
96. G errard Eddy Jai Poinern, Sridevi Brundavanam, Derek Fawcett. “Biomedical Magnesium Alloys: A Review of Material Properties, Surface Modifications and Potential as a Biodegradable Orthopaedic Implant”. *American Journal of Biomedical Engineering*. 2014, DOI: 10.5923/j.ajbe.20120206.02.
97. Guan Ling Song, Andrej Atrens. “Corrosion mechanisms of magnesium alloys” . (1999) 249–273.
98. Noviana, Deni ; Paramitha, Devi ; Ulum, Mokhamad Fakhrul ; Hermawan, Hendra “The effect of hydrogen gas evolution of magnesium implant on the postimplantation mortality of rats”. *Journal of Orthopaedic Translation*, April 2016, Vol.5, pp 9-15.
99. Clarke, E G ; Hickman, J. “An investigation into the correlation between the electrical potentials of metals and their behaviour in biological fluids”. *The Journal of bone and joint surgery*. British volume, August 1953, Vol.35-B(3), pp.467-73.
100. Witte, F. ; Ulrich, H. ; Rudert, M. ; Willbold, E. “Biodegradable magnesium scaffolds: Part 1: Appropriate inflammatory response”. *Journal of Biomedical Materials Research Part A*, 01 June 2007, Vol.81(3), pp.748-756.
101. Li, Zijian ; Gu, Xunan ; Lou, Siqun ; Zheng, Yufeng. “The development of binary Mg–Ca alloys for use as biodegradable materials within bone”. *Biomaterials*, 2008, Vol.29(10), pp.1329-1344.
102. Fontenier G, Freschard R, Mourot M. Study of the corrosion in vitro and in vivo of magnesium amodes involved in an implantable bioelectric battery. *Med Biol Eng* 1975;13(5):683–9.
103. Xue-Nan GU, Yu-Feng Zheng. “A review on magnesium alloys as biodegradable materials”. *Frontiers of Materials Science*. June 2010, DOI: 10.1007/s11706-010-0024-1.

104. Yin, Dong-Song ; Zhang, Er-Lin ; Zeng, Song-Yan. "Effect of Zn on mechanical property and corrosion property of extruded Mg-Zn-Mn alloy". Transactions of Nonferrous Metals Society of China, 2008, Vol.18(4), pp.763-768.
105. Burkhardt Arthur, Knabe Richard. "Magnesium alloy". Feb 1948, US2231881 A.
106. Guo, Gh ; Song, D ; Jiang, Jh ; Ma, AB ; Zhang, Lw ; Li, C. "Effect of Synthesizing Temperature on Microstructure and Electrochemical Property of the Hydrothermal Conversion Coating on Mg-2Zn-0.5Mn-Ca-Ce Alloy". Metals, 2016 Mar, Vol.6(3).
107. Hornberger, H. ; Virtanen, S. ; Boccaccini, A.R. "Biomedical coatings on magnesium alloys – A review". Acta Biomaterialia, July 2012, Vol.8(7), pp.2442-2455.
108. Witte, F. ; Ulrich, H. ; Palm, C. ; Willbold, E. "Biodegradable magnesium scaffolds: Part II: Peri-implant bone remodeling". Journal of Biomedical Materials Research Part A, 01 June 2007, Vol.81(3), pp.757-765.
109. Zhang, Fan ; MA, Aibin ; Song, Dan ; Jiang, Jinghua ; Lu, Fumin ; Zhang, Liuyan ; Yang, Donghui ; Chen, Jianqing. "Improving in-vitro biocorrosion resistance of Mg-Zn-Mn-Ca alloy in Hank's solution through addition of cerium". Journal of Rare Earths, January 2015, Vol.33(1), pp.93-101.
110. Gu, X.N. ; Xie, X.H. ; Li, N. ; Zheng, Y.F. ; Qin, L. "In vitro and in vivo studies on a Mg-Sr binary alloy system developed as a new kind of biodegradable metal". Acta Biomaterialia, July 2012, Vol.8(6), pp.2360-2374.
111. Bornapour, M ; Muja, N ; Shum-Tim, D ; Cerruti, M ; Pekguleryuz, M. "Biocompatibility and biodegradability of Mg-Sr alloys: the formation of Sr-substituted hydroxyapatite". Acta biomaterialia, February 2013, Vol.9(2), pp.5319-30.
112. Gu, Xuenan ; Zheng, Yufeng ; Cheng, Yan ; Zhong, Shengping ; Xi, Tingfei "In vitro corrosion and biocompatibility of binary magnesium alloys", Biomaterials, 2009, Vol.30(4), pp.484-498.
113. Song, Guangling, "Control of biodegradation of biocompatible magnesium alloys", Corrosion Science, 2007, Vol.49(4), pp.1696-1701.
114. Guan, Ren-Guo ; Cipriano, Aaron F ; Zhao, Zhan-Yong ; Lock, Jaclyn ; Tie, Di ; Zhao, Tong ; Cui, Tong ; Liu, Huinan, "Development and evaluation of a magnesium-zinc-strontium alloy for biomedical applications — Alloy processing, microstructure, mechanical properties, and biodegradation", Materials Science & Engineering C, October 2013, Vol.33(7), pp.3661-3669.

115. Zhang, Shaoxiang ; Zhang, Xiaonong ; Zhao, Changli ; Li, Jianan ; Song, Yang ; Xie, Chaoying ; Tao, Hairong ; Zhang, Yan ; He, Yaohua ; Jiang, Yao ; Bian, Yujun ,“Research on an Mg–Zn alloy as a degradable biomaterial”, *Acta Biomaterialia*, 2010, Vol.6(2), pp.626-640.
116. Yuen, C.K ; Ip, W.Y, “Theoretical risk assessment of magnesium alloys as degradable biomedical implants”, *Acta Biomaterialia*, 2010, Vol.6(5), pp.1808-1812
117. Cha, Pil-Ryung ; Han, Hyung-Seop ; Yang, Gui-Fu ; Kim, Yu-Chan ; Hong, Ki-Ha ; Lee, Seung-Cheol ; Jung, Jae-Young ; Ahn, Jae-Pyeong ; Kim, Young-Yul ; Cho, Sung-Youn ; Byun, Ji Young ; Lee, Kang-Sik ; Yang, Seok-Jo ; Seok, Hyun-Kwang ; Cha, Pil-Ryung (correspondence author) ; Cha, Pil-Ryung, “Biodegradability engineering of biodegradable Mg alloys: tailoring the electrochemical properties and microstructure of constituent phases”, *Scientific reports*, 2013, Vol.3, p.2367.
118. Ibrahim, Hamdy ; Klarner, Andrew D. ; Poorganji, Behrang ; Dean, David ; Luo, Alan A. ; Elahinia, Mohammad. “Microstructural, mechanical and corrosion characteristics of heat-treated Mg-1.2Zn-0.5Ca (wt%) alloy for use as resorbable bone fixation material”. *Journal of the Mechanical Behavior of Biomedical Materials*, May 2017, Vol.69, pp.203-212.
119. Nyberg Eric A ; Agnew Sean R ; Neelameggham Neale R ; Pekguleryuz Mihriban O . “Applicability of Existing Magnesium Alloys as Biomedical Implant Materials”. TMS (The Minerals, Metals & Materials Society) ; 2009.
120. Sun, Yu; Zhang, Baoping; Wang, Yin; Geng, Lin; Jiao. “Preparation and characterization of a new biomedical Mg–Zn–Ca alloy”. *Materials and Design*, February 2012, v 34, p 58-64.
121. Gao, J.H. ; Guan, S.K. ; Ren, Z.W. ; Sun, Y.F. ; Zhu, S.J. ; Wang, B. “Homogeneous corrosion of high pressure torsion treated Mg–Zn–Ca alloy in simulated body fluid”. *Materials Letters*, 2011, Vol.65(4), pp.691-693.
122. Dilip Chandrasekaran. “Grain Size and Solid Solution Strengthening in Metals- Doctoral Dissertation”. 2003, pp13, 49.
123. Zhang, Erlin ; Yang, Lei. “Microstructure, mechanical properties and bio-corrosion properties of Mg–Zn–Mn–Ca alloy for biomedical application”. *Materials Science & Engineering A*, 2008, Vol.497(1), pp.111-118.
124. Dilip Chandrasekaran . “Grain Size and Solid Solution Strengthening in Metals”, A Theoretical and Experimental Study. 2003. pp5-13.

125. Callister Jr, William D. "Materials Science and Engineering - An Introduction", Eighth Edition, 2010. Pp212-225.
126. Mohammad Mezbahul-Islam; Ahmad Omar Mostafa; Mamoun Medraj. "Essential Magnesium Alloys Binary Phase Diagrams and Their Thermochemical Data" Journal of Materials, 01 January 2014, Vol.2014.
127. Agarwal, Sankalp ; Curtin, James ; Duffy, Brendan ; Jaiswal, Swarna, "Biodegradable magnesium alloys for orthopaedic applications: A review on corrosion, biocompatibility and surface modifications", Materials Science & Engineering C, 01 November 2016, Vol.68, pp.948-963.
128. Li, Xia ; Liu, Xiangmei ; Wu, Shuilin ; Yeung, K.W.K ; Zheng, Yufeng ; Chu, Paul K, "Design of magnesium alloys with controllable degradation for biomedical implants: From bulk to surface", Acta Biomaterialia, November 2016, Vol.45, pp.2-30.
129. Zhang, Ding-Fei ; Shi, Guo-Liang ; Dai, Qing-Wei ; Yuan, Wei ; Duan, Hong-Ling. "Microstructures and mechanical properties of high strength Mg-Zn-Mn alloy". Transactions of Nonferrous Metals Society of China, 2008, Vol.18, pp.s59-s63.
130. Zhang, Ding-Fei ; Shi, Guo-Liang ; Zhao, Xia-Bing ; Qi, Fu-Gang. "Microstructure evolution and mechanical properties of Mg- x%Zn-1%Mn ( x=4, 5, 6, 7, 8, 9) wrought magnesium alloys". Transactions of Nonferrous Metals Society of China, 2011, Vol.21(1), pp.15-25.
131. Zhang, Erlin ; Xu, Liping ; Yu, Guoning ; Pan, Feng ; Yang, Ke, "In vivo evaluation of biodegradable magnesium alloy bone implant in the first 6 months implantation", Journal of Biomedical Materials Research Part A, 01 September 2009, Vol.90(3), pp.882-893.
132. Xu, Liping ; Yu, Guoning ; Zhang, Erlin ; Pan, Feng ; Yang, Ke, "In vivo corrosion behavior of Mg-Mn-Zn alloy for bone implant application", Journal of Biomedical Materials Research Part A, 01 December 2007, Vol.83(3), pp.703-711.
133. Huang, Dandan ; Liu, Shuhong ; Xu, Honghui ; Du, Yong. "Phase equilibria of the Mg-Mn-Zn system at 593 K (320 °C)". Journal of Alloys and Compounds, 15 December 2016, Vol.688, pp.1115-1124.
134. Pang, Song ; Wu, Guohua ; Liu, Wencai ; Sun, Ming ; Zhang, Yang ; Liu, Zhijie ; Ding, Wenjiang. "Effect of cooling rate on the microstructure and mechanical properties of sand-casting Mg-10Gd-3Y-0.5Zr magnesium alloy". Materials Science & Engineering A, 1 February 2013, Vol.562, pp.152-160.

135. Candan, S. ; Celik, M. ; Candan, E. “Effectiveness of Ti-micro alloying in relation to cooling rate on corrosion of AZ91 Mg alloy”. *Journal of Alloys and Compounds*, 5 July 2016, Vol.672, pp.197-203.
136. Izumi, Shogo ; Yamasaki, Michiaki ; Kawamura, Yoshihito. “Relation between corrosion behavior and microstructure of Mg–Zn–Y alloys prepared by rapid solidification at various cooling rates”. *Corrosion Science*, 2009, Vol.51(2), pp.395-402.
137. A Closer Look at Magnesium-Chris Berry, Aug 2015. [www.discoveryinvesting.com/blog/2015/8/10/a-closer-look-at-magnesium](http://www.discoveryinvesting.com/blog/2015/8/10/a-closer-look-at-magnesium), as of Jan 2020.
138. Brady, Michael P ; Joost, William J ; David Warren, C ; Oak Ridge National Lab. (Ornl), Oak Ridge, Tn (United States) (Corporate Author), ”Insights from a Recent Meeting: Current Status and Future Directions in Magnesium Corrosion Research”, *Corrosion*, 17 November 2016, Vol.73(5).
139. D. Sameer Kumar, C. Tara Sasanka , K. Ravindra , K.N.S. Suman, “Magnesium and Its Alloys in Automotive Applications – A Review”, *American Journal of Materials Science and Technology*, (2015) Vol. 4 No. 1 pp. 12-30, doi:10.7726/ajmst.2015.1002.
140. Magnesium Metal Production-U.S. Geological Survey <https://prd-wret.s3-us-west-2.amazonaws.com/assets/palladium/production/atoms/files/mcs-2019-mgcom.pdf>, as of Jan 2020.
141. Magnesium Compounds Production-U.S. Geological Survey <https://prd-wret.s3-us-west-2.amazonaws.com/assets/palladium/production/atoms/files/mcs-2019-mgmet.pdf>, as of Jan 2020.
142. Media and Balanced Salt Solutions Preparation from Powder and Concentrates “[https://assets.thermofisher.com/TFS-Assets/LSG/manuals/powdered\\_mediaprep\\_man.pdf](https://assets.thermofisher.com/TFS-Assets/LSG/manuals/powdered_mediaprep_man.pdf)”, as of January 2020.
143. Erdem Karakulak “A review: Past, present and future of grain refining of magnesium castings”. *Journal of Magnesium and Alloys*, 2019 vol. 7 (3), pp. 355.
144. Herbert J. Weber “Air Pollution Problems of the Foundry Industry”, *Journal of the Air Pollution Control Association*, vol. 11:4, pp157-172, DOI: 10.1080/00022470.1961.10467985.
145. G. Petzow “Metallographic etching: metallographic and ceramographic methods for revealing microstructure”. 5th edition, American Society for Metals, 1978,pp72-74.

146. Basharat Mubeen, Ikhlas Ahmed, Azher Jameel “Study of Mechanical Properties of Bones and Mechanics of Bone Fracture”, Proceedings of 60th Congress of ISTAM (<http://istam.iitkgp.ac.in>) Held at : MNIT, Jaipur-302017, Rajasthan, India, Dec. 16-19, 2015.
147. Prasad, Somasundaram ; Wong, Raymond Chung Wen “Unraveling the mechanical strength of biomaterials used as a bone scaffold in oral and maxillofacial defects”, Wiley Oral science international, 2018-07, Vol.15 (2), p.48-55.
148. Liu, Chen ; Ren, Zheng ; Xu, Yongdong ; Pang, Song ; Zhao, Xinbing ; Zhao, Ying ; Passeri, Daniele “Biodegradable Magnesium Alloys Developed as Bone Repair Materials: A Review”England: Hindawi Limited Scanning, 2018, Vol.2018, p.1-15.

# CURRICULUM VITAE

**Murtatha M. Jamel**

## **EDUCATION**

- ✓ PhD Candidate in Materials Science and Engineering, UWM, USA, Dec 2020
- ✓ Minor in Manufacturing and Industrial Science and Engineering
  - ✓ Dissertation: DESIGNING AND INVESTIGATING A NOVEL BIODEGRADABLE-NONTOXIC MG-MN-ZN-NA-K ALLOYING SYSTEM
- ✓ Master's Degree in Materials Engineering, UWM, USA, May 2015
  - ✓ Thesis: THE EFFECT OF E-GLASS FIBERS AND PHLOGOPITE MICA ON THE MECHANICAL PROPERTIES AND DIMENSIONAL STABILITY OF RIGID PVC FOAMS
- ✓ Bachelor Degree in Materials Engineering, UOB, Iraq, 2009
  - ✓ Senior Design: STEEL CORROSION AND INHIBITORS IN DIFFERENT SOLUTIONS AND TEMPERATURE
- ✓ Associate Degree in Mechanical Equipment Technology, BPI, Iraq, 2004

## **WORK EXPERIENCE**

UW-Milwaukee, USA      Lab Manager, Researcher Teaching Assistant, Aug 2013–Dec 2020

- Lab Manager- processing and characterization-330 lab
- Teaching assistant for Materials Engineering 201 lab and Processes and Manufacturing 330 lab
- Instructor assistant for Materials Laboratory course 411 and Senior Design Projects course 490
- Composites materials research projects with a focus on advanced alloys and polymers
- Reinforcing matrices with fibers and particles for different applications
- Metal casting, manufacturing techniques, testing, thermal analysis, failure analysis, and characterization
- Involved in Joining and welding studies
- Biomedical, recyclable, and biodegradable applications
- Corrosion and electrochemical testing
- Supported additive manufacturing 3D printing studies
- Professional, technical, and safety training
- Developing procedures, reports, and funding proposal writing
- Installing, calibrating and maintaining lab equipment

Gossen Company, USA

Engineering Researcher(through the R&D), 1/2014–1/2015

- Worked for the R&D, strove to improve the quality of the products
- Recognized for developing efficient Design Of Experiment (DOE) to improve quality and quantity performance
- Made compounds of composites and formed new products
- Tested and characterized composite products for their properties

## **TECHNICAL, LABORATORY & ANALYTICAL SKILLS**

- **Characterization Techniques:** SEM, EDS, XRD, Optical Microscope, Laser Microscope, Polymer Rheology, DSC, TGA, FTIR, Raman, and DMA
- **Manufacturing Techniques:** Casting, Forging, Cold and Hot Rolling, Welding, Heat Treatment, Machining, Injection, Extrusion, and other Materials Forming and Joining techniques
- **Materials Mechanical Testing:** Hardness, Tensile, Compressive, Flexural, and Impact
- **Products Defects and Inspection Techniques:** Visual, Fluid Pressure (leak), Liquid Penetrant (dye), Magnetic Particle, Eddy Current, Ultrasonic, Radiography
- **Corrosion/Erosion:** Analysis, causes, and protection techniques

## **PROFESSIONAL MEMBERSHIPS**

- Iraqi Engineers Association, **Iraq**
- American Society for Metals **ASM-US**
- Association for Iron & Steel Technology **AIST-US**
- The American Ceramic Society **ACerS-US**
- Foundry Educational Foundation **FEF-US**
- The Minerals, Metals and Materials Society **TMS-US**
- American Foundry Society **AFS-US**
- Society of Plastics Engineers **SPE-US**
- Institute of Industrial Engineers **IIE**
- Order Of The Engineer-**US**
- Arab American Association of Engineers and Architects **AAEA-US**
- Biomedical Engineering Society **UWM- US**
- International Teaching Assistants' Community **UWM- US**
- Engineers Without Borders-**US**

## **PARTICIPATION AND VOLUNTEER ACTIVITIES**

- Participated in The 81st AFS Annual Wisconsin Regional Foundry Conference & Exposition Potawatomi, February 13-15, 2019
- Participated in The 80th AFS Annual Wisconsin Regional Foundry Conference & Exposition Potawatomi, February 14-16, 2018
- Participated in Hosting ASM Materials Camp, UWM Summer 2014 and 2015
- Participated in Hosting Cub Scouts, UWM Spring 2014
- Participated in Hosting Elkhorn High School, UWM spring 2014
- Served as a Judge for UW system symposium Spring 2015

## **AWARDS AND HONORS**

- H.H. Harris Foundation-Scholarship Award, 2019, 2020, USA
- PACK International Research Experience Fellowship Penn State US-The American Ceramic Society-University of Kiel Germany Funded by National Science Foundation, 2020
- UWM Advanced Opportunity Program (AOP) Fellowship 2017-2020, USA
- Foundry Educational Foundation (FEF) Scholarship Feb. 2018, 2020, USA
- AFS Northeastern Wisconsin Scholarship 2020, USA
- American Institute of Mining, Metallurgical, and Petroleum Engineers (AIME) and The Minerals, Metals & Materials Society (TMS) Award-the Henry DeWitt Smith Scholarship 2020, USA
- AIST-Training funding, Long Products Rolling – A Practical Training Seminar 11–13 February 2020, Jacksonville, FL, USA
- UWM College of Engineering & Applied Science-Research Grant Summer 2019, USA
- Department award for graduate-research, poster competition 2019, USA
- AFS Northeastern Wisconsin Scholarship 2019, USA
- George J. Barker Memorial Scholarship 2019, USA
- Leadership Program, Focus on The Future, Spring 2018, USA
- UWM Chancellor Award Fall 2013, Spring 2014, Spring 2016, 2020, USA

## **CONFERENCES AND WORKSHOPS**

- TMS 2020 Annual Meeting & Exhibition, February 23–27 in San Diego, CA USA
- AIST-Long Products Rolling – A Practical Training Seminar 11–13 February 2020, Jacksonville, FL USA
- Rockwell Automation Fair, Nov 20-21 2019 McCormick Place West, Chicago, IL USA
- ASM-Milwaukee- Raised Grain Company, Corrosion and Failure Analysis, September 12 2019
- ASM-Milwaukee's-The 60th H.R. Bergmann Memorial Seminar, Enhanced Productivity Through Computational Modeling April 9 2019 at MSOE, WI USA
- AFS Northeastern Wisconsin Chapter, Project Presentations April 8 2019 at MSOE, WI USA
- ASM-Milwaukee -The 60th H.R. Bergmann Memorial Seminar, Advances in Material Characterization April 10 2018 at MSOE, WI USA
- ASM-Milwaukee, Vacuum Furnaces were meant for Additive Manufacturing
- November 14, 2017 at UW-Milwaukee, WI USA
- ASM-Milwaukee, Advances in High Pressure Gas Quenching
- November 14, 2017 at UW-Milwaukee, WI USA
- SME Medical Additive Manufacturing and 3D Printing
- November 28, 2017 at RSNA Annual Conference McCormick Place Chicago, Illinois USA
- NETZSCH, Thermal Analysis of Polymers and Coatings
- November 12, 2013, Hilton MKE City Center, WI-USA

## **PUBLICATIONS**

1. Enhancement of Dimensional Stability of Rigid PVC Foams using E-Glass Fibers  
Murtatha M. Jamel, Parisa Khoshnoud, Subhashini Gunashekar, Nidal Abu-Zahra  
Journal of Minerals and Materials Characterization and Engineering, published in March 2015  
DOI: [10.4236/jmmce.2015.32009](https://doi.org/10.4236/jmmce.2015.32009)
2. Mechanical Properties and Dimensional Stability of Rigid PVC Foam Composites Filled with High Aspect Ratio Phlogopite Mica  
Murtatha M. Jamel, Parisa Khoshnoud, Subhashini Gunashekar, Nidal Abu-Zahra  
Journal of Minerals and Materials Characterization and Engineering, published in June 2015  
DOI: [10.4236/jmmce.2015.34026](https://doi.org/10.4236/jmmce.2015.34026)
3. Effect of E-Glass Fibers and Phlogopite Mica on the Mechanical Properties and Dimensional Stability of Rigid PVC Foams  
Murtatha M. Jamel, Parisa Khoshnoud, Subhashini Gunashekar, Nidal Abu-Zahra  
Journal of Polymer-Plastics Technology and Engineering, published in June 2015
4. Comparative Analysis of Rigid PVC Foam Reinforced with Class C and Class F Fly Ash  
Parisa Khoshnoud, Subhashini Gunashekar, Murtatha M. Jamel, Nidal Abu-Zahra  
Journal of Minerals and Materials Characterization and Engineering, published in November 2014.  
DOI: [10.4236/jmmce.2014.26057](https://doi.org/10.4236/jmmce.2014.26057).
5. Evaluating the Performance of Class-F Fly Ash Reinforced PVC Foam Composites  
Parisa Khoshnoud, Murtatha M. Jamel, Subhashini Gunashekar, Nidal Abu-Zahra  
International Journal of Innovative Research in Science, Engineering and Technology, published in September 2015.  
DOI: [10.15680/IJIRSET.2015.0404043](https://doi.org/10.15680/IJIRSET.2015.0404043).

## **CONFERENCE PAPERS**

1. ICSIM 2016 : 18th International Conference on Surface and Interface of Materials in Copenhagen, Denmark  
<http://waset.org/Publications/enhanced-dimensional-stability-of-rigid-pvc-foams-using-glass-fibers/10000154>
2. ICTCME 2015 : 17th International Conference on Textile Composites, Materials and Engineering in Penang, Malaysia  
<http://waset.org/Publications/enhanced-thermal-properties-of-rigid-pvc-foams-using-fly-ash/10000155>
3. ICMCE 2015: XIII International Conference on Materials and Chemical Engineering in Jeddah  
<https://www.waset.org/abstracts/18461>  
<http://www.waset.org/abstracts/18474>